

**NASA  
Technical  
Paper  
2457**

0.2

**December 1985**

**Installation Effects of  
Long-Duct Pylon-Mounted  
Nacelles on a Twin-Jet  
Transport Model With  
Swept Supercritical Wing**

**Edwin E. Lee, Jr., and  
Odis C. Pendergraft, Jr.**

PROPERTY OF U.S. AIR FORCE  
AEDC TECHNICAL LIBRARY

**TECHNICAL REPORTS  
FILE COPY**

**NASA**

1985

Installation Effects of  
Long-Duct Pylon-Mounted  
Nacelles on a Twin-Jet  
Transport Model With  
Swept Supercritical Wing

Edwin E. Lee, Jr., and  
Odis C. Pendergraft, Jr.

*Langley Research Center  
Hampton, Virginia*



National Aeronautics  
and Space Administration

Scientific and Technical  
Information Branch

## SUMMARY

The aerodynamic performance of a long-duct, turbofan nacelle installed with two different pylon shapes has been evaluated in the Langley 16-Foot Transonic Tunnel using a twin-engine transport model with a supercritical wing swept  $30^\circ$ . The primary objective of this investigation was to determine the installation interference characteristics of advanced turbofan nacelles mounted under the wing in the near-sonic flow field of the supercritical airfoil. Wing, pylon, and nacelle pressures and overall model force data were obtained at Mach numbers from 0.70 to 0.83 and nominal angles of attack from  $-2^\circ$  to  $4^\circ$  at an average unit Reynolds number of  $11.9 \times 10^6$  per meter. Both engine installations used the same axisymmetric flow-through nacelles, pylon mounted under the wing at 37 percent semispan, with exits at approximately 38 percent of the local chord. Two symmetrical pylon designs were investigated which had relatively flat-topped crowns at different heights above the nacelles, creating both lower surface and conventional leading-edge junctures of the pylon with the wing.

The results show that adding the long-duct nacelles to the supercritical wing changed the magnitude and direction of flow velocities over the entire span, significantly reduced cruise lift, and caused large interference drag on the nacelle afterbody. Both wing-pylon juncture designs created local flow separation in the juncture region. The lower surface juncture separated most strongly with a noticeable increase in wing drag, while the leading-edge juncture exhibited mild shock-induced separation with only a modest increase in wing drag.

These results indicate that more clearance than is usually necessary between wing and nacelles will be required to minimize interference for installations involving shorter, separate, flow-through nacelles. Also, strongly indicated is the need to minimize curvature at the sides of the pylon leading edges and along the wing lower surface at the pylon junctures in order to reduce local velocities and avoid separation.

## INTRODUCTION

The National Aeronautics and Space Administration has in progress major research efforts aimed at improving the fuel efficiency of subsonic jet transports. One of the main thrusts in aerodynamics seeks to improve wing performance by applying supercritical airfoil technology and by increasing aspect ratio (refs. 1, 2, and 3). In the propulsion field, improvements are being sought in the performance of large turbofan engines, partly by increasing bypass ratio and partly by internally mixing the core and fan exhausts to augment thrust (ref. 4). The impact of advancing technology on the shape and relative size of these major components results in wings that have thicker airfoil sections and shorter chords than past designs, and in nacelles that may further increase in size relative to the wing.

While these changes are a necessary part of major component improvement, they are also cause for concern that, when the components are integrated into an aircraft design, wing-nacelle aerodynamic interference may increase. For example, higher velocities are generated by the supercritical airfoils than by older sections, which may intensify local interference in regions where the propulsion system joins the

wing. Also, continued enlargement of the engine nacelles relative to the wing tends to disturb the flow over a greater area of the wing. As chord length decreases relative to nacelle size, the wing becomes increasingly sensitive to flow changes imposed by the nacelles in the vertical direction, thereby strongly affecting lift and drag.

If overall aircraft performance and efficiency are to benefit fully from advancing wing and engine technology, a better understanding of the nature and cause of interference must be provided by airframe-propulsion-integration research in order to properly design the wing-nacelle combination to reduce this interference. These objectives are being pursued through a comprehensive research program underway in the Propulsion Aerodynamics Branch at the Langley 16-Foot Transonic Tunnel to assess relative installation effects from a variety of schemes for mounting large turbofan nacelles on thick, supercritical wings. Initial exploratory investigations have been carried out for both underwing and overwing nacelle installations at Mach numbers from 0.70 to 0.83 using a full-span, twin-jet, research transport model specifically developed for this work. Highlights of the current research have already been presented in reference 5. The purpose of the present investigation was twofold: First, to evaluate the interference caused by pylon-mounted long-duct nacelles under a thick, supercritical wing, with particular emphasis on the results at a cruise Mach number of 0.80; and second, to determine the relative interference effects for two different pylon leading-edge profiles, one intersecting the wing lower surface and the other intersecting the wing leading edge.

#### SYMBOLS

$c$	local chord, cm
$\bar{c}$	mean aerodynamic chord, cm
$c_{av}$	average chord (trapezoidal planform), cm
$c_n$	wing section normal-force coefficient, $\int_0^{1.0} [(C_p)_{\text{Lower}} - (C_p)_{\text{Upper}}] d(x/c)$
$C_D$	drag coefficient, $\frac{\text{Drag}}{q_\infty S}$
$C_{D,I}$	total internal drag coefficient for two nacelles
$C_L$	lift coefficient, $\frac{\text{Lift}}{q_\infty S}$
$C_m$	pitching-moment coefficient, $\frac{\text{Pitching moment}}{q_\infty S \bar{c}}$
$C_p$	pressure coefficient, $\frac{p - p_\infty}{q_\infty}$
$(\Delta C_D)_{\text{NAC}}$	increment of installation drag coefficient produced by a single pylon and nacelle, $\frac{1}{2}[(C_D)_{\text{Nacelles on}} - (C_D)_{\text{Clean wing}}]$
$M_\infty$	free-stream Mach number
$p$	local static pressure, Pa



$p_{\infty}$	free-stream static pressure, Pa
$q_{\infty}$	free-stream dynamic pressure, Pa
S	wing reference area (trapezoidal planform), 3416.66 cm <sup>2</sup>
t	maximum local wing-section thickness, cm
x	streamwise distance from leading edge parallel to wing reference plane, positive rearward, cm
z	vertical distance normal to wing reference plane, positive upward, cm
$\alpha$	angle of attack, deg
$\delta_h$	horizontal-tail incidence angle, positive leading edge up, deg
$\epsilon$	angle between wing reference plane and a straight line through local section leading-edge and average trailing-edge ordinates, positive leading edge up, deg
$\eta$	fraction of semispan
$\phi$	meridian angle about axis of symmetry of left nacelle (advances clockwise from zero at top of nacelle when looking upstream), deg

#### Abbreviations:

BL	butt line, cm
FS	fuselage station, cm
LER	leading-edge radius
MHB	maximum half-breadth, cm
NS	nacelle station, cm
NWL	nacelle water line, cm
R	radius, cm
WL	water line, cm
WRP	wing reference plane

#### Model configurations:

UWS-A	underwing symmetrical nacelle with pylon A
UWS-B	underwing symmetrical nacelle with pylon B

## APPARATUS AND PROCEDURE

### Wind Tunnel and Model Support

The present investigation was conducted in the Langley 16-Foot Transonic Tunnel. This facility is a single-return, continuous-flow, atmospheric wind tunnel with a slotted test section of octagonal cross section. The slots, located at the corners of the octagon, vent the test section to a surrounding plenum to provide transonic capability. Test-section airspeed is continuously variable between Mach numbers of 0.20 and 1.30. The model was sting mounted and held near the test-section centerline at all angles of attack by the support-system arrangement. Further information on the wind tunnel and model support equipment can be found in reference 6.

### Model

The sketch in figure 1 gives the overall dimensions of the basic research transport model in the clean-wing configuration without nacelles. The photographs of figure 2 show the model complete with underwing flow-through nacelles installed in the tunnel test section. This model, resembling a wide-body logistics transport, represents an aircraft weighing approximately 946 000 N designed to cruise at an altitude of 10 668 m at  $M_\infty = 0.80$  and  $C_L = 0.45$ . The propulsion system consists of twin, mixed-flow turbofans with a sea-level static thrust of 226 860 N each housed in 274.3-cm-diameter nacelles.

The model was designed for powered testing, both with inlets faired over and with inlets flowing. In the latter case, the nacelles must accommodate the turbine-powered simulators (ref. 6, pp. 140-143). This simulator design sized the maximum nacelle diameter and resulted in a model scale of 1/24.

The choice of the high-wing configuration offered the opportunity to study interference effects on a wide variety of nacelle installations, including upper-surface-mounted nacelles, without unduly restricting conventional underwing-mounting capability. The tails were configured as shown in order to maintain adequate clearance between the horizontal stabilizer and nacelle exhaust paths for any anticipated nacelle position on the wing.

Fuselage.- Features of the basic fuselage geometry and the descriptive coordinates are shown in figure 3. The shape is comprised of an ellipsoidal nose section, cylindrical midsection, and an upswept afterbody of locally circular cross section closed at the rear by a spherical cap.

The values of  $z$  shown in the coordinate table for the afterbody (fig. 3(a)) locate the line of centers (mean line) of the circular cross sections relative to the axis of symmetry of the forward fuselage (WL 0.0). Between stations FS 34.290 and FS 154.623, where the spherical cap begins, the fuselage crown is a straight line coincident with WL 11.430. The full afterbody keel profile is shown in figure 3(a), whereas the actual profile is relieved somewhat by removal of material for the sting cavity. (See photograph in fig. 2 and sketch in fig. 3(b).)

Wing.- Figure 4 shows the planform geometry of the model wing that had a span of 160.327 cm, an aspect ratio of 7.52, and a quarter-chord sweep of 30°. Dihedral and incidence angles were both 0°, and the wing reference plane (WRP) intersected the vertical plane of symmetry of the model at WL 8.255. (See fig. 1.) The wing shape was defined by the airfoil sections located at the fuselage side ( $\eta = 0.127$ ), the

planform break ( $\eta = 0.410$ ), and the tip ( $\eta = 1.000$ ), all of which are shown in figure 5. Maximum thickness ratios of the fuselage side, planform break, and tip sections were 0.144, 0.12, and 0.10, respectively. The corresponding streamwise coordinates relative to the wing reference plane are given in table I. At each value of  $x/c$ , the ordinates of all airfoils between adjacent defining sections can be obtained by spanwise linear interpolation. These defining airfoil shapes are the same as those used in the high-aspect-ratio wings of reference 1.

The airfoil at the fuselage side is a modified section incorporating some supercritical features but has reduced curvature over the rear upper surface in order to maintain isobar sweep and reduce shock strength at the wing-fuselage juncture. The airfoils at the planform break and tip stations are unmodified NASA supercritical sections. The leading-edge points of all sections are collinear, and maximum thickness ratio and twist vary with semispan location as shown in figure 6, which indicates a total "washout" of approximately  $3.7^\circ$ . The variation of airfoil shape and twist gives the trailing edge a somewhat "gulled" appearance typical of most transport wings. (See oblique rear view of fig. 2.)

Wing-fuselage juncture fairings.- Figure 7 shows the geometry of the fairings used to provide smooth shape transitions and control boundary-layer growth in the wing-fuselage juncture. The forward fairing (leading-edge fillet) was kept to a minimal size sufficient to provide smooth flow from fuselage to wing without separating the fuselage boundary layer (fig. 7(b)). Under the rear of the wing, the fuselage surface above the MHB curves inboard as it approaches the bottom of the wing (fig. 7(c)). In the same region, the undersurface of the wing rises to form the cove (rear camber), and the combined surface shapes form a deep cavity. The rear fairing (figs. 7(c) and (d)) serves to fill this cavity and prevent undue thickening of the boundary layer (corner flow) in the presence of the strong positive pressure gradient on the wing. Both fairings were made removable in case future size and shape changes might be required.

Tail surfaces.- Figure 8 shows the dimensional details of the vertical tail and its symmetrical airfoil coordinates. The full profile shape of the tail-plane intersection, "bullet" fairing, is also shown. The nose and closure of the fairing are ogives with the same profile radius and length. The horizontal tail, shown in figure 9, was a one-piece, all movable, negatively cambered surface whose airfoil section coordinates are also shown in the figure. The negative-loading feature was needed to more effectively counteract the increased nose-down pitching moment of the supercritical wing relative to conventional designs. The horizontal stabilizer was hinged in pitch from the top of the vertical tail. By removing the partially hollow bullet fairing, the horizontal stabilizer could be manually set and locked at incidence angles from  $-2^\circ$  to  $2^\circ$ .

Nacelle-pylon installations.- The geometric details are shown in figure 10 for the three-piece, axisymmetric flow-through nacelles used in this investigation. In the design of the inlet section, designated NACA 1-83-75, the data of reference 7 were used to match the flow requirements at  $M_\infty = 0.80$  for the turbine-powered simulator unit referred to previously (ref. 6, pp. 140-143). The ratio of highlight diameter to maximum diameter is 0.83, and the ratio of external length to maximum diameter is 0.75. The ratio of highlight area to throat area (contraction ratio) is 1.09. The removable center section of the nacelle, referred to as the transition section, provides for smooth internal bore changes between inlet and afterbody as well as for future length changes, adaptation for powered testing, etc.

The nacelle afterbody has a shallow, circular-arc profile with a fineness ratio of approximately 1.87. The closure ratio, or ratio of exit diameter to maximum diameter, is 0.7, which is generally representative of medium bypass turbofan installations for subsonic cruise speeds. These features were selected on the basis of the isolated afterbody test results of reference 8, which indicate that such shapes have very low drag levels and minimal drag divergence at high subsonic speeds when operating at ratios of total pressure to free-stream static pressure at flow-through conditions. The interior of the afterbody is shaped to provide a shallow, conically convergent nozzle.

The overall fineness ratio of the nacelle is 3.5, somewhat longer than mixed flow designs currently being considered (i.e., ref. 4). This additional length resulted from the desirability of obtaining comparative interference data on different installations of the same size, thereby requiring the present underwing installation to have the same length as the upper surface installations shown in reference 5. The latter would generally require longer ducts than would an underwing installation of the same engine. Also, maintaining as much as possible of the nacelle geometry common to all configurations facilitated maximum reuse of model components when constructing the various installations.

Details of the pylon components used to mount the axisymmetric nacelles under the wing are given in figure 11. The leading-edge shapes of figures 11(a) and (b) were interchanged on the common strut and trailing-edge section of figure 11(c) so that two pylon configurations were generated. These differed only in profile height and cross-sectional shape along the leading edge. Both configurations were slab sided and had a common thickness ratio of 6.4 percent.

The low-profile and high-profile configurations are designated pylon A (fig. 11(a)) and pylon B (fig. 11(b)), respectively. Pylon A provides a profile more representative of full-scale requirements and gives a somewhat traditional "hockey-stick" side view. In this case, the crown line at the top of the pylon changes sweep angle and intersects the wing lower surface noticeably below the actual wing leading edge and approximately 8 percent of the local chord behind it. Pylon B, with its raised crown, represents the shape required to provide the nacelles with added instrumentation and high-pressure air for jet simulation during future powered tests. The straight-line portion of the crown follows a nacelle water line to the wing intersection point, which occurs virtually at the leading edge, longitudinally, and is approximately 2 percent of local chord below the leading edge, vertically. Thus, pylons A and B afforded an opportunity to study the effect of changing the location of the wing leading-edge juncture.

The forward part of each pylon had swept, symmetrical, streamwise sections generated by applying the given airfoil coordinates along specified water lines as shown in figures 11(a) and (b). From the rear of the circular-arc portion of the crown line to the wing leading edge, the locally perpendicular cross-sectional shapes of the crowns were semi-elliptical as typified by station-plane cross sections A-A. These shapes were chosen in an effort to maximize the pylon internal volume and facilitate instrumentation routing from nacelle to wing, etc. Over the region where the circular arcs define the crown lines, the swept leading-edge shape was smoothly faired into the semi-elliptical crowns, as is generally done at a wing tip. The locus of tangent points between the curved and flat surfaces of each leading-edge piece is shown by the "phantom" (broken) lines within each planform (figs. 11(a) and (b)). On pylon A the tangent line turns upward, parallel to the crown at the leading-edge break, and coincides with the parting line of the leading edge and strut until intersecting with the wing. For both leading-edge profiles, the area below the

tangent line is flat and has the same constant thickness as the mating strut (fig. 11(c)).

The common closure shape used on all pylons had a trapezoidal, constant-chord planform swept at approximately  $33^\circ$ . The streamwise airfoil section between the parting line and trailing edge was also constant over the vertical distance from nacelle to wing. The typical section outline shape and its coordinates are shown in figure 11(c). The entire closure was attached to the pylon strut, and its upper and lower ends were contoured to match the wing and nacelle shapes, respectively. On the lower end, where the closure overhangs the nacelle exit, the underside was made concave to provide a "runout" for the exhaust flow. This surface had circular-arc station-plane cross sections with radii about the nacelle axis that matched the inside radius of the afterbody at the exit, then decreased linearly to 3.810 cm at the trailing edge. Note that all pylon dimensions in figure 11 are given with respect to the local nacelle reference system.

The location of the pylon-nacelle installation on the model wing is shown in figure 12. The center of the nacelle exit was positioned at FS 76.921, BL 29.660, and WL -1.905. The assembly was then pitched down  $0.5^\circ$  and toed in  $1.0^\circ$  about the exit center point without rolling the installation, thereby maintaining the vertical symmetry plane of the pylon-nacelle combination perpendicular to the model water-line planes. These cant angles aligned the installation with the general flow direction approaching the wing and were established from a pretest wing-fuselage flow-field analysis at  $M_\infty = 0.70$  using the inviscid, subsonic panel method discussed in reference 9.

The location of the exit was chosen to position the installation spanwise at  $\eta = 0.37$  or slightly inboard of the trailing-edge break ( $\eta = 0.41$ ). In the longitudinal direction, the exit occurred at 37.6 percent of the local chord and was intended to generally match the core exit location of a separate flow installation with the fan exit placed near the wing leading edge. The vertical spacing between the exit center and the wing reference plane was made approximately 40 percent of the local chord to represent a full-scale channel height between wing and nacelle of almost 1 m. Although this spacing may be larger than the spacings of past design practice, more channel area was desired because of the long-duct volume extending under the wing and because of higher airfoil velocities anticipated relative to older, conventional sections. Throughout the remainder of this report, the two configurations of figure 12 are identified as UWS-A and UWS-B. These designations indicate that both installations were of the underwing type (UW), had symmetrical nacelles and pylons (S), and incorporated either the low (-A) or high (-B) pylon leading-edge profile discussed previously.

## INSTRUMENTATION

The airplane model was completely metric and contained a conventional six-component strain-gage balance that measured overall aerodynamic forces and moments.

Chordwise pressure distributions were measured on the upper and lower wing surfaces at nine spanwise stations and along the top of the fuselage over the virtual chord length of the wing at  $\eta = 0$ . Figure 13(a) shows the spanwise locations of the orifice rows, and table II provides the chordwise orifice locations at each span station. Each entry in table II denotes the presence of an orifice at the corresponding values of  $x/c$  and  $\eta$ , whereas the entry itself gives the fuselage-station location

of the orifice relative to the model nose. This information aids in spatially relating wing and pylon-nacelle pressures since the latter are located by fuselage station throughout this report. At  $\eta = 0.328$  and  $0.440$  in table II, the annotated entries and corresponding values of  $x/c = 0.5620$  and  $0.4140$  are actual locations of orifices displaced from standard chordwise positions to avoid a parting line between mechanical components of the wing.

Most of the orifices were located between the side of the fuselage and midspan where the greatest influence of any test nacelle installation might be expected. Orifice rows from  $\eta = 0.154$  to  $0.550$  contained 45 taps - 1 at the leading edge and 22 on each of both surfaces. On the outer portion of the wing from  $\eta = 0.750$  to  $0.950$ , reducing the number of orifices in each row was necessary because of decreasing mechanical thickness due to taper. As a means of facilitating the routing of instrumentation through the available space within the wing, the orifice rows from  $\eta = 0.154$  to  $0.440$  were located on the left inboard panel and those from  $\eta = 0.550$  to  $0.950$  were installed on the right outboard section. (See fig. 2.)

Pylon-nacelle surface pressures were measured only on the left side of the model. Two rows of orifices differing in vertical position were installed along either side of the pylon as indicated in figure 11(c). The nacelle was instrumented over its length with six longitudinal orifice rows lying in the key meridian planes shown in figure 13(b). Notice that the meridian angle  $\phi$  advances clockwise from  $0^\circ$  at the top of the nacelle when viewing the left engine installation from the rear. At  $\phi = 0^\circ$ , the presence of the pylon limited the instrumentation to those few orifices ahead of the pylon leading edge. In the rear-view sketch of figure 13(b), the position of the wing and pylon orifice rows adjacent to the nacelle are also shown for convenient reference. Internal static pressures were obtained in the inlet throat at NS 6.350 by four orifices positioned  $90^\circ$  apart circumferentially.

All pressure measurements on the wing, pylon, and nacelle were made by 12 pressure scanning units mounted in the hollow, removable nose section of the model. Each scanning unit which contained a transducer was capable of measuring 47 pressures sequentially. The units, mounted in groups of six on two individual stepping devices, were electrically actuated, simultaneously. This instrumentation arrangement kept the model orifices and transducers sufficiently close together to virtually eliminate "tube lag;" also, this arrangement required only soft, flexible, electrical lead wires to be routed across the balance and through the support system, avoiding any significant mechanical restraint.

Pressures were measured at 16 positions in the fuselage sting cavity by individual transducers located outside the tunnel test section. The small metal tubes that transmitted cavity pressures to the transducers were fastened to the external surface of the sting (see fig. 2), including that portion inside the fuselage. Within the cavity, the tube ends were positioned where desired and left open to serve as orifices. Adequate clearance was maintained between tube ends and model surfaces to avoid balance interference.

## TESTS

This investigation was conducted at Mach numbers from  $0.70$  to  $0.83$  and nominal angles of attack from  $-2^\circ$  to  $4^\circ$ . The unit Reynolds number averaged over all test conditions was  $11.9 \times 10^6$  per meter.

Aerodynamic force and pressure data were obtained for the clean-wing model (fig. 1), complete except for nacelles, and for the model with UWS-A and UWS-B pylon-nacelle installations added (fig. 12). The major part of this investigation was comprised of tests of these three configurations, during which the tail surfaces were always installed and the horizontal stabilizer was set at  $\delta_h = 0^\circ$ .

Force data only were taken at fewer Mach numbers for the model without nacelles, during which the horizontal tail was either set at  $\delta_h = 1^\circ$  or both tail surfaces were removed entirely. Whenever these force-data results appear in this report, the status of the tails is appropriately noted. These data were obtained to assess trimming effectiveness for possible future use. However, during the present investigation, no deliberate attempt was made to trim the model.

Boundary-layer transition was fixed on the model by 0.25-cm-wide strips of silicon carbide grit, sized and positioned by the considerations of references 10 and 11. Strips of No. 100 grit were applied at 2.54 cm behind the fuselage nose, at 2.54 cm behind the forward tip of each pylon, and along  $x/c = 0.10$  on both tail surfaces. Strips of No. 120 grit were placed at 2.54 cm behind the nose of the "bullet" tail fairing and at 0.95 cm behind the nacelle leading edges on both inside and outside surfaces.

Transition was fixed on the wing upper and lower surfaces as indicated by the sketches in figure 14. The transition strips are located farther rearward than usual in an effort to more nearly simulate the aerodynamic behavior of the wing at full-scale Reynolds numbers. (See ref. 11.)

#### DATA REDUCTION

All data from the model and wind tunnel were recorded on magnetic tape and were used to compute standard aerodynamic force and moment coefficients. The trapezoidal planform area of the wing and the mean aerodynamic chord  $\bar{c}$  were used as reference area and length, respectively. Resulting model force and moment coefficients were referred to the stability axis system with moment reference center located at FS 75.522 and WL 0.0 (fig. 1). The longitudinal position of this point corresponds to 25 percent of the mean aerodynamic chord.

The angle of attack of the model was obtained by correcting the recorded pitch angles of the main support strut for sting deflections under aerodynamic loading. The necessary deflection characteristics were determined by pretest static force loadings on the model, balance, and sting support system assembled in the tunnel test section.

Normal, axial, and pitch force data were corrected for internal sting cavity forces generated by local differences between cavity and free-stream static pressures. These tares were computed by assigning appropriately weighted areas and moment arms to each measured cavity pressure. Model force data with nacelles installed were corrected for the axial force produced by the internal flow ( $C_{D,I}$ ) in passing from the free stream through the nacelles to the exits. These internal corrections were computed by one-dimensional flow analysis at each test Mach number and angle of attack. The measured tunnel conditions and average static pressure at the inlet throat were used to determine the internal mass-flow rate and the duct Mach number and pressure distributions. Pressure forces on the entering stream tube and nacelle duct were then obtained by momentum analysis and pressure integration, respectively. Duct skin friction was computed using the nacelle internal wetted area and friction

coefficients for turbulent, compressible, flat-plate boundary-layer flow. (See ref. 12, p. 1110, eq. 27.66a.) The calculation of friction coefficients was based on the duct length and the average internal Mach number taken over that length.

The resulting total internal drag was attributed almost entirely to skin friction, did not vary significantly with Mach number or angle of attack, and averaged approximately 5 counts per nacelle (1 drag count is equivalent to  $C_D = 0.0001$ ). Consequently, the total measured drag of configurations with nacelles was reduced by approximately 10 counts as indicated in figure 15. Data are shown for both pylon configurations, although the internal drag increments are nearly identical for the data shown. The average computed mass-flow ratio for each nacelle was approximately 0.685.

## PRESENTATION OF RESULTS

All the aerodynamic force data taken during the investigation are presented and shown graphically. Although it was possible to present only part of the pressure data actually obtained, the amount of plotted pressure data presented is sufficient to provide an adequate graphical sampling of the results. In addition, sufficient pressure data are presented from which to assess flow conditions on the various configurations and locate installation effects. These pressure plots have been limited to the two Mach numbers of primary interest, namely, 0.70 and 0.80, the latter being the assumed cruise condition. Supplementary pressure-coefficient data for the wing and pylon-nacelle installations may be obtained by contacting the authors at the Propulsion Aerodynamics Branch, NASA Langley Research Center, Hampton, Virginia 23665-5225. These results are available for each configuration at Mach numbers of 0.70, 0.75, 0.78, 0.79, 0.80, 0.81, and 0.82 and at nominal angles of attack from  $-2^\circ$  to  $4^\circ$  ( $C_L \approx 0$  to 0.8).

Unless otherwise noted, data were obtained with tail surfaces installed and with the incidence angle of the horizontal stabilizer set at  $0^\circ$ .

The major results of the investigation are presented in the following figures:

Figure

### Aerodynamic force data:

Configuration with clean wing .....	16
Configurations UWS-A and UWS-B compared with clean-wing configuration .....	17

### Chordwise pressure distributions:

Clean-wing configuration	
$M_\infty = 0.70$ ; $\eta = 0$ to 0.950 .....	18
$M_\infty = 0.80$ ; $\eta = 0$ to 0.950 .....	19
Configuration UWS-A	
$M_\infty = 0.70$ ; $\eta = 0.154$ to 0.550 .....	20
$M_\infty = 0.80$ ; $\eta = 0.154$ to 0.550 .....	21
Configuration UWS-B	
$M_\infty = 0.70$ ; $\eta = 0.154$ to 0.550 .....	22
$M_\infty = 0.80$ ; $\eta = 0.154$ to 0.550 .....	23



## Pressure coefficient characteristics:

Clean-wing configuration; $M_{\infty} = 0.70$ .....	24
Clean-wing configuration; $M_{\infty} = 0.80$ .....	25
Influence of pylon-nacelle installations on wing surface pressures:	
Configuration UWS-A; $M_{\infty} = 0.70$ .....	26
Configuration UWS-A; $M_{\infty} = 0.80$ .....	27
Configuration UWS-B; $M_{\infty} = 0.70$ .....	28
Configuration UWS-B; $M_{\infty} = 0.80$ .....	29
Local effects of nacelle installations on wing lower surface pressures:	
Constant lift coefficient; $M_{\infty} = 0.70$ and $0.80$ .....	30
Various angles of attack; $M_{\infty} = 0.80$ .....	31
Effects of pylon shape on pylon-nacelle pressures:	
$M_{\infty} = 0.70$ ; $\alpha = 2.18^\circ$ .....	32
$M_{\infty} = 0.80$ ; various angles of attack .....	33
Effects of pylon-nacelle installations on total lift and drag .....	34
Influence of pylon-nacelle installations on spanwise load distributions of wing at cruise conditions .....	
	35
Variation of model drag with Mach number at $C_L = 0.45$ , with and without nacelles .....	
	36
Variation of pylon-nacelle installation drag with Mach number at $C_L = 0.45$ .....	
	37
Integrated pressure drag of pylon and nacelle closures at $M_{\infty} = 0.70$ and $0.80$ .....	
	38

## DISCUSSION

## Pressure Data

Clean wing.— The airplane model used in this investigation was designed as a test vehicle for measuring the aerodynamic effects caused by different wing-mounted nacelle installations. (See ref. 5 also.) An important design objective was that the wing should provide a flow environment for the nacelles representative of future transports using advanced subsonic wing designs. The diagrams of figures 24 and 25 show that the general pressure characteristics of the wing are quite typical of swept, supercritical designs and that the above objective was met quite satisfactorily.

At  $M_{\infty} = 0.80$  a very mild secondary expansion appears on the rear upper surface around the trailing-edge break. (See fig. 25(a),  $\eta = 0.328$  to  $0.440$ .) This was caused by the combination of twist and upper surface curvature development as the airfoil shapes changed from modified root section to the standard section at the break station. However, this anomaly was considered weak enough not to compromise in any way the validity of the installation effects being sought. Consequently, no

attempt was made to reduce the upper surface curvature of the finished wing in that region.

Wing with nacelles installed.- Figures 26 to 29 compare wing pressures of each pylon-nacelle configuration with those of the clean wing at constant angle of attack and Mach numbers of 0.70 and 0.80. The angles of attack selected for these comparisons correspond to test points for which pressure-coefficient data were available and the clean-wing lift coefficient was near  $C_L = 0.45$ , the assumed requirement for cruise at  $M_\infty = 0.80$ . At  $\eta = 0.370$ , the nacelle mounting station, no pressure data are shown on the lower surface because the pylons covered the entire chordwise orifice row at that location.

These results indicate extensive adverse interference of the large pylon-nacelle installations with the wing. Velocity reduction occurred on the upper surface from  $\eta = 0.250$  to  $0.550$ , the region spanning the nacelle. Although minor at  $M_\infty = 0.70$ , the velocity suppression became quite noticeable at  $M_\infty = 0.80$ , showed no marked dependence on pylon leading-edge profile, and was presumably related to the large size of the installation as a whole. (Compare figs. 27(a) and 29(a).) Along the outboard panel, from nacelle to wing tip, the effective angle of attack was reduced, as noted by the decrease in leading-edge pressure peaks and slightly increased suction on the lower surface. Outboard of  $\eta = 0.440$ , the lower surface is seen to be generally free of any major interference.

As expected, the most severe interference is evident on the lower inboard surface between the nacelle and the side of the fuselage. This occurrence resulted mainly from the flow accelerating longitudinally (overspeeding) around the pylon-nacelle installation. The largest overspeed peaks on the lower surface are noted at  $\eta = 0.328$ , just inboard of the pylon, and occur typically where the pylon obstructs the flow turning spanwise at the wing leading edge.

The local installation effects on lower surface pressures are shown in more detail in figures 30 and 31. The given fractions of semispan correspond to positions approximately halfway between pylon and fuselage ( $\eta = 0.250$ ), 2 cm inboard of the pylon ( $\eta = 0.328$ ), and 4 cm outboard of the pylons ( $\eta = 0.440$ ). In figure 30, the data are compared at cruise lift coefficient and are shown for Mach numbers of 0.70 and 0.80. At  $M_\infty = 0.70$ , the results show strong, normal recovery along the underside of the cambered trailing edge (cove) and no significant interference at  $\eta = 0.440$ , indicating generally good alignment of the pylon with the flow. However, the peak pressure coefficients at  $\eta = 0.328$  are noted as rather high, relative to the critical value for configurations whose desired cruise speed is  $M_\infty = 0.80$ . As the free-stream Mach number was increased from 0.70 to 0.80, shocks and boundary-layer separation developed in the inboard channel for both pylon-nacelle installations (fig. 30(b)).

The reversal in relative levels of the inboard channel pressure peaks between Mach numbers of 0.70 and 0.80 was due to a difference in separation characteristics of pylons A and B, which can be seen in figure 31. There, installation effects on local wing lower surface pressures are shown for each of a number of angles of attack at  $M_\infty = 0.80$ . Pylon A, with low profile leading edge and underwing juncture ( $x/c \approx 0.08$  at  $\eta = 0.370$ ), exhibits fundamental shape separation characteristics at angles of attack from  $0.25^\circ$  to  $1.74^\circ$  (figs. 31(a) to (d)). At  $\eta = 0.328$  in figure 31(b), the pressure distribution for configuration UWS-A flattens and indicates separation at  $x/c = 0.10$ . This value corresponds to a position approximately halfway between the pylon and wing leading edges at  $\eta = 0.370$ , the nacelle mounting station. The flow separating ahead of the pylon leading edge apparently fills the

inboard side of the pylon juncture with the wing and obscures the physical curvature of the inboard shoulder. Consequently, no interference expansion occurs in the wing pressure distribution. As the angle of attack increases, the separation point moves rearward, and the severity and extent of the separated flow diminishes (notice trailing-edge pressure coefficients at  $\eta = 0.250$ ). In the inboard juncture, the flow reattaches and begins to follow the physical surfaces again. The interference peak begins to rise at  $\alpha = 1.74^\circ$  (fig. 31(d)) and reaches a maximum value at  $\alpha = 2.23^\circ$  (fig. 31(e)). Over the angle-of-attack range from  $0.25^\circ$  to  $2.23^\circ$ , pylon B produces interference peaks up to  $C_p = -0.8$  in the inboard channel and shock-induced separation. With a further increase in angle of attack, the general decrease in velocity under the leading edge causes the negative peaks at  $\eta = 0.328$  to decrease and the flow to reattach to the rear lower surface of the wing. At  $\alpha = 4.22^\circ$  (fig. 31(f)), the results indicate strong recovery in the cove and flow in the inboard channel which, though slightly supercritical, is essentially shock free. Moreover, the peak pressure coefficient of approximately  $-0.5$  must be tentatively considered as the maximum negative value allowable in the inboard channel at the desired cruise conditions if underwing pylons are to be successfully integrated with the present wing.

One of the major factors contributing to the flow separation at the pylons is that the present supercritical airfoil shapes generally produce higher velocities along the forward lower surface than do the older, conventional airfoil sections. On the older sections, the leading-edge radius was not only smaller but was followed by a very flat profile that maintained surface velocities below free-stream value for a greater percentage of the chord. Thus, the leading-edge disturbances of pylon and wing could be superposed and still maintain acceptable velocity levels. Since the introduction in the 1950's of turbojet-powered aircraft with nacelles pylon mounted under the wings, the importance of this feature to the successful integration of pylons with transport wings cannot be overemphasized. With the newer, thicker supercritical sections, surface velocities under the leading edge are much higher; therefore, this surface may have to be modified to reduce velocities locally around the pylon.

Reference 13, for example, shows the inboard channel pressures ( $\eta = 0.320$ ) for a transport model with long-duct nacelles and a wing similar to the present model except for having conventional airfoils. At  $M_\infty = 0.82$  and  $C_L = 0.45$ , pressure coefficients in the forward inboard channel of the model in reference 13 correspond closely to those of the present model at  $\eta = 0.328$  in figure 31(d). For the clean wing of reference 13, the pressure coefficient was zero at  $x/c \approx 0.10$  to  $0.15$ , and the peak value with nacelle installed was  $-0.5$ . For similar cruise conditions ( $M_\infty = 0.80$  and  $C_L \approx 0.45$ ), the corresponding pressure coefficients for the clean, supercritical wing ( $\eta = 0.328$ ) are those in figure 31(b) or figure 31(c). At  $x/c = 0.15$ , the level of  $-0.30$  indicates a 15-percent velocity increase over the conventional wing at the same location. This increase is also reflected in the interference peak when the nacelles are added (configuration UWS-B) and the flow in the inboard channel becomes supersonic, with resulting shock formation and/or boundary-layer separation.

Consequently, the present results show that the higher velocities in the lower leading-edge region of the thick, supercritical airfoils can severely aggravate pylon interference from the underwing pylon-nacelle installations. For the present wing, this problem might be partly overcome by means of "wing contouring" whereby the forward lower surface of airfoil profiles near the pylons would be flattened and steepened to reduce local velocities.

The juncture position of pylon A, as well as the leading-edge cross-section shapes of both pylon configurations, also contributed significantly to the flow-separation problems encountered. The leading edge of pylon A was set behind that of the wing in an effort to relieve juncture interference. Ironically, this was achieved to a limited extent, but only then because of flow separation. Presumably, any pylon leading-edge shape intersecting the forward lower surface of the present wing would tend to jeopardize the flow integrity, a feature which the airfoil sections cannot tolerate. Also, the superposition of any disturbance from the pylon tends to occur farther rearward on the wing where its velocities and compressibility effects become larger. Based on these results, therefore, the underwing juncture of pylon A is considered unsuitable for use with the present supercritical airfoils in combination with the long-duct nacelles in their present position.

The rather flat-topped shapes chosen for the pylon crowns or leading-edge cross sections (fig. 11) were based on model and possible full-scale requirements for maximum internal pylon volume. However, these shapes also produced highly curved shoulders at the sides of the pylons, over which the flow had to pass when accelerating downward and around the lower leading edge of the wing near the juncture. Generally, increasing curvature and velocity together would be expected to worsen compressibility effects and interference, and this did occur very noticeably in the inboard channel ( $\eta = 0.328$ ) at both  $M_\infty = 0.70$  (fig. 30(a)) and  $M_\infty = 0.80$  (figs. 31(e) and 31(f)), where little or no separation occurred. Notice that the peak pressure coefficient of pylon A is more negative by  $\Delta C_p = -0.2$  than that of pylon B, a result of the relatively small change in shape. Thus, the sensitivity of this already high interference region to the side curvature of the pylons suggests that flat-topped crown shapes may not be desirable when the nacelle afterbody is largely located under the thick, supercritical wing.

Based on these results, it should be possible to reduce the present pylon interference by reducing the shoulder curvature. This could be done most effectively by using a crown shape whose curvature decreases continuously from the top of the pylon to the sides. This shape limits the maximum curvature of the pylon cross section to a single region located along the pylon crown or leading edge. The leading edge of the pylon should then join that of the wing where the airfoil surface velocities are minimal, thereby avoiding combinations of high curvature and velocity that result in separation, as in the case of the present pylons. Consequently, the "standard" leading-edge juncture should still afford the best opportunity to minimize the peak level and chordwise extent of the pylon disturbance superposed on the wing. Provided the pylon crown is well rounded, such junctures should also be less susceptible to separation in the presence of strong crossflows generated by the thick, swept-wing leading edge. Reference 14 provides an interesting example of how revising the pylon crown curvature, as cited above, eliminated a crossflow separation problem on the outboard side of a pylon joining a swept wing.

Nacelle effects on the lower inboard wing surface at  $M_\infty = 0.80$  can be seen by comparing data for configuration UWS-A and the clean-wing configuration at  $\eta = 0.250$  in figures 31(b) and (c). For these conditions, the flow separation on the inboard-side juncture region between pylon A and the wing maintained pressures in the inboard channel ( $\eta = 0.328$ ) closely matched to those of the clean wing over approximately 40 percent of the local chord. Since no strong interference disturbance was propagated inboard, as in the case of pylon B, the pressure difference on the lower inboard wing surface at  $\eta = 0.250$  between configuration UWS-A and the clean wing appears to be due to flow acceleration around the nacelle afterbody. This more extensive effect can be seen in figure 27(b), which shows that the nacelles reduced the pressures over approximately 40 percent of the lower surface on the inboard wing

panel. Consequently, a significant loss of inboard lift can be anticipated. Also, note that the nacelle disturbances did not diminish noticeably at low values of semi-span positions, indicating a modest channeling effect between nacelles and fuselage.

Pylon-nacelle pressures.- The longitudinal distributions of pressure coefficients measured along the inboard and outboard sides of the two pylon-nacelle installations are compared, on facing pages, in figures 32 and 33 at  $M_\infty = 0.70$  and  $0.80$ , respectively. The upper and lower wing surface pressures immediately adjacent to the installations are repeated in these figures for spatial references. Comparing the pressure recovery on the wing lower surface just inboard and outboard of the nacelle readily indicates the condition of the inboard channel flow because the lower-surface data at  $\eta = 0.440$  follow closely those of the clean wing. Interference on the nacelle surface can be assessed by comparing local pressure levels to those along  $\phi = 180^\circ$  at the same fuselage station. The latter provide a near-isolated reference condition because the orifice row is farthest from the wing. Also, as a convenience when comparing pressure levels, the data for  $\phi = 180^\circ$  are repeated with the other data for each side of the installations.

From the data for  $M_\infty = 0.70$  and cruise lift conditions, the flow around the pylons and nacelles is seen to be subcritical, attached, and recovering normally in the inboard channel (fig. 32). At  $M_\infty = 0.80$ , the onset of flow separation at the pylons is quite evident in the inboard data for angles of attack from  $1.25^\circ$  to  $2.23^\circ$  (figs. 33(a), (b), and (c)). Also, the inboard pylon pressures vary with configuration and attitude changes similar to the wing-lower-surface data discussed previously (fig. 31).

Nacelle pressures on the afterbody surface under the wing exhibit adverse interference over the entire upper inboard quadrant ( $\phi = 30^\circ$  to  $90^\circ$ ), thereby indicating a very definite increase in installed drag relative to isolated conditions for  $M_\infty = 0.70$  and  $0.80$ . (See figs. 32 and 33.) Although the pressures in some areas on the nacelle afterbodies are different, implying significant drag differences, it will be shown that the differences between inboard channel pressures due to changing pylon leading-edge shape have relatively minor effects on the afterbody drag of these configurations. A comparison of figures 33(c) and (d) shows that the flow reattaches to the wing and pylons between  $\alpha \approx 2^\circ$  and  $\alpha \approx 4^\circ$  and that afterbody interference decreases. Thus, a general reduction in pressure drag with increasing attitude is indicated.

#### Force Data

Complete-model lift and drag characteristics.- Effects of the large nacelle installations on configuration aerodynamics are summarized in figures 34 to 36, which compare lift and drag for the model with and without nacelles. Large adverse lift and drag interferences are evident throughout these results, as anticipated from previous considerations of the pressure data. For cruise angles of attack of  $1^\circ$  or  $2^\circ$ , figure 34 shows that both nacelle configurations reduced lift about 16 percent at  $M_\infty = 0.70$  and 24 percent at  $M_\infty = 0.80$ , based on the cruise value of  $C_L = 0.45$ . Local flow separation in the inboard channels apparently had little effect on lift since there was no rapid shift in level corresponding to the abrupt slope changes in the drag polars which denote separation or reattachment.

The extensive region of adverse lift interference caused by the large nacelle installations is illustrated in figure 35 by the span loads diagrams for the test configurations at a cruise Mach number of  $0.80$  and  $\alpha \approx 1.25^\circ$  (approximate design

lift condition for clean wing). The large lift reductions inboard of the nacelles are presumably related to the high-wing position and channeling effect between the pylon-nacelle installations and the fuselage because the pressure data showed this region to be dominated by increased velocity over approximately 40 percent of the local chords. A more surprising result was the extent of reduced loading on the outboard panel, manifested in the pressure data as a loss of leading-edge suction. This effect is currently attributed to the downward motion of the flow over the nacelle afterbody which caused a reduction in the local angle of attack as the wing leading edge swept rearward over the installation.

The poor installed lift performance seen in figure 34 could presumably be improved somewhat by moving the nacelles farther outboard to minimize the channeling effect. Because of the extensive disturbance created by the large nacelles, major lift improvements will probably require the addition of a leading-edge extension inboard of the nacelles and local twist revisions to raise the section angles of attack in the vicinity of the engine installations. Such features, usually applied to compensate for the addition of engines, were not incorporated initially in the present configuration because the near-term research objective is to first try minimizing nacelle interference by means of installation shape and position before considering possible wing design changes.

In figure 36, total drag coefficients as a function of Mach number are compared at cruise lift with and without nacelles installed. The sum of the clean-wing-model drag and the skin friction drag of the nacelle installations is also shown, making the pressure drag and compressibility effects of the nacelles readily visible. Actual drag divergence is assumed to occur when  $\partial C_D / \partial M_\infty = 0.1$ , which, by choice of figure scales, corresponds to the point on each curve where the slope is 45°. It can be seen that the drag divergence Mach number was 0.81 for the clean-wing model and decreased to approximately 0.78 when either nacelle installation was added. Thus, poor installed drag performance is indicated by the development of strong compressibility effects and premature drag divergence, which occurred noticeably below the desired cruise Mach number of 0.80.

Nacelle installation drag.- All drag values that follow are increments associated with one pylon, nacelle, and model wing panel. The installed drag increment  $(\Delta C_D)_{NAC}$  is defined as half of the difference between total model drag values with and without nacelles when compared at the same Mach number and lift coefficient. Values of  $(\Delta C_D)_{NAC}$  from the force balance measurements appear as a function of  $M_\infty$  in figure 37 for  $C_L = 0.45$ , the assumed value for cruise at  $M_\infty = 0.80$ . Drag obtained by integrating measured pressures on one pylon trailing edge and nacelle boattail (closure drag) is given in figure 38 as a function of angle of attack at  $M_\infty = 0.70$  and  $0.80$ . In the pylon data, the rapid drag reduction (fig. 38(a)) or slope change (fig. 38(b)) indicates where the initially separated inboard channel flow reattached as angle of attack increased.

At  $M_\infty = 0.70$  to  $0.80$ , the "isolated" parasite drag of the pylon and nacelle is estimated to be approximately 21 counts, of which 15 counts are skin friction (see fig. 37) and 6 counts are pressure drag. The latter consists of 3 counts each of nacelle spillage and afterbody drag (pylon pressure drag assumed negligible). Inlet spillage drag was obtained for the actual test shape by the computational method of reference 15 and was verified by experimental data (after removing skin friction) for similar inlets in reference 7. Afterbody drag was taken from reference 8 at values of the ratio of total pressure to free-stream static pressure corresponding to the tunnel Mach numbers (i.e., flow-through pressure ratio). The above estimate of isolated drag (21 counts) agrees well with the force measurements of figure 37 at

$M_\infty = 0.70$ , indicating little or no net interference for either nacelle installation at that condition.

Figure 37 shows that the installation drag of configuration UWS-A became noticeably higher than that of configuration UWS-B with increasing Mach number, a difference which can be attributed to increased wing drag. In order to determine the levels of interference drag on the wing, it was first necessary to estimate the pylon leading-edge drag. Since the "nose" of each pylon was not instrumented in this test, pressures along the nacelle orifice rows at  $\phi = 30^\circ$  and  $330^\circ$  at each side of the pylon were averaged and applied to the area progression of the nose. The average drag for  $M_\infty = 0.70$  to  $0.80$  was approximately -3 counts, or equal and opposite to the inlet spillage drag. Thus, the external pressure drag associated with the entering stream tube, inlet cowl, and pylon nose region was essentially zero. This means that the installation pressure drag in figure 37 (increment above skin-friction level) was principally the sum of the closure drags (fig. 38) and the wing interference drag.

Values of closure drag corresponding to  $C_L = 0.45$  and Mach numbers of  $0.70$  and  $0.80$  occur at  $\alpha = 2.0^\circ$  and  $1.73^\circ$ , respectively, in figure 38. (See lift curves of fig. 34, also.) Subtracting these results from the pressure drag increments at corresponding Mach numbers in figure 37, the reader can verify that the wing interference of configuration UWS-A increased from roughly -3 counts at  $M_\infty = 0.70$  to 5 counts at  $M_\infty = 0.80$ , an increase of 8 counts. The corresponding increase in wing interference drag for configuration UWS-B was from -4 counts to -1 count (a 3-count increase).

The following table summarizes the results of the preceding discussion and presents the equation used to derive the wing interference drag:

Configuration	$M_\infty$	①	②	③	④	⑤
		Measured ( $\Delta C_D$ ) <sub>NAC</sub> * (fig. 37)	Calculated pylon-nacelle skin friction (fig. 37)	Integrated closure drag		Wing interference drag
				Nacelle boattail (fig. 38)	Pylon trailing edge (fig. 38)	
UWS-A	0.70	23	16	13	-3	-3
	.80	38	15	15	3	5
UWS-B	0.70	21	16	12	-3	-4
	.80	31	15	16	1	-1
Wing-interference drag: ⑤ = [(① - ②)] - [(③ + ④)]						

\*( $\Delta C_D$ )<sub>NAC</sub> is principally the sum of closure drags and wing interference if spillage drag and pylon leading-edge suction cancel each other.

These results show that the adverse pressure gradient separation produced by locating the leading edge of pylon A behind that of the wing caused higher wing drag

at  $M_\infty = 0.80$  than produced by pylon B. Therefore, the "relieved," or lower, surface juncture is considered unsuitable for use with supercritical wings because of the supersonic environment on the forward lower surface. By comparison, the conventional leading-edge juncture of pylon B caused only a modest drag "creep" between  $M_\infty = 0.70$  and  $0.80$  and almost no wing interference drag at cruise conditions (-1 count estimated). Apparently, the expansion causing shock-induced separation in the inboard channel also generated compensating wing leading-edge thrust that retarded the drag rise. (Compare pressure data at  $\eta = 0.328$  in fig. 30(b).) Consequently, joining the pylon and wing leading edges directly causes less tendency toward increased wing interference drag at high subsonic speeds and still appears to offer the most suitable procedure. Reducing the curvature at the shoulders of the pylon crown as well as on the lower inboard wing should help eliminate flow separation and reduce installation drag.

Figure 38 shows that the pylon closure drag was -3 counts with flow attached at  $M_\infty = 0.70$  and cruise lift ( $\alpha = 2^\circ$ ). Approximately the same level is indicated at  $M_\infty = 0.80$  ( $\alpha = 1.73^\circ$ ) if the data for the attached flow at  $\alpha = 3^\circ$  and  $4^\circ$  are extrapolated to  $\alpha = 1.73^\circ$ . When compared with the actual levels, the results show an average drag penalty due to pylon trailing-edge separation of about 6 counts for pylon A and about 4 counts for pylon B at cruise. (See dotted lines on fig. 38 at  $M_\infty = 0.80$ .) Also, with attached flow, the pylon would have produced an installed component drag of -6 counts, including the leading-edge value of -3 counts estimated earlier. This major favorable interference (isolated pylon pressure drag negligible) equals and opposes the "isolated" pressure drag of the nacelle (6 counts). Therefore, the installation pressure drag can potentially reach zero (viscous drag alone) provided the large afterbody drags evident in figure 38 can be reduced. The latter are seen to be about 15 to 16 counts at cruise conditions, compared to an isolated level of 3 counts. Thus, the results show an adverse interference drag on the nacelle afterbody of approximately 12 counts at  $M_\infty = 0.80$ .

The following table summarizes the effect of flow separation on the pylon closure drag. (Values are listed in drag counts where 1 drag count equals 0.0001 in drag coefficient.)

Configuration	$M_\infty$	Pylon leading-edge estimated drag count	Pylon closure drag count	Pylon total drag count
UWS-A	0.70	-3	-3 (attached flow)	-6
	.80	-3	3 (separated flow)	0
	.80	-3	-3 (estimated attached flow)	-6
UWS-B	0.70	-3	-3 (attached flow)	-6
	.80	-3	1 (separated flow)	-2
	.80	-3	-3 (estimated attached flow)	-6

Comparison of the afterbody drag curves in figure 38 shows a difference of only about 2 counts between configurations UWS-A and UWS-B. Therefore, the afterbody drag was not strongly dependent on local peak pressure differences measured on the wing in the inboard channel, differences which were substantial at times. (See  $\eta = 0.328$ ,



fig. 30.) This suggests that locally improving the inboard juncture shape may eliminate flow separation but may not greatly reduce afterbody drag. Rather, the high levels of boattail drag coefficient at cruise conditions appear more generally dependent on flow acceleration around the combined shape of wing and pylon, as well as nacelle position. Further research will be required to examine these general features in more detail in an effort to improve the installed performance of long-duct nacelles with supercritical wings.

#### CONCLUDING REMARKS

The aerodynamic performance of a long-duct, turbofan nacelle installed with two different pylon shapes has been determined with a twin-engine transport model having a supercritical wing swept  $30^\circ$  mounted in the Langley 16-Foot Transonic Tunnel. Pressure and force data were obtained at Mach numbers from 0.70 to 0.83 and nominal angles of attack from  $-2^\circ$  to  $4^\circ$  at an average unit Reynolds number of  $11.9 \times 10^6$  per meter. Both installations used the same axisymmetric flow-through nacelles, pylon mounted under the wing at 37 percent semispan, with exits at approximately 38 percent of the local chord. The two symmetrical pylon designs investigated had relatively flat-topped leading edges at different heights above the nacelle, creating both lower surface and leading-edge junctures with the wing. At a cruise Mach number of 0.80, the test results lead to the following conclusions:

1. Adding the long-duct nacelles to the supercritical wing changed the magnitude and direction of flow velocities over the entire span and significantly reduced cruise lift. Large interference drag also occurred on the nacelle afterbodies as a result of their underwing location and exposure to strong local flow accelerations from the thick wing and pylons. On the whole, these results indicate that considerably more clearance than is usually necessary between wing and nacelles will be required to minimize interference for installations involving shorter, separate flow nacelles.

2. The underwing location of the nacelle afterbodies, coupled with wing-ylon thickness effects, produced high velocities and local flow separation for both wing-ylon junctures investigated. The lower surface juncture separated most strongly and caused the wing drag to increase noticeably. The lower surface juncture, therefore, appears to be unsuitable for use with thick, supercritical wings. By comparison, the more conventional leading-edge juncture exhibited relatively mild shock-induced separation, with only a modest increase in wing drag generally characteristic of compressibility effects. Thus, the leading-edge juncture appears more desirable since it affords lower wing drag and its compressibility effects can be reduced by local shaping modifications. These results indicate the need to minimize curvature at the sides of the pylon leading edges and along the wing lower surface at the pylon junctures in order to reduce local velocities and avoid separation.

NASA Langley Research Center  
Hampton, VA 23665-5225  
July 2, 1985

# REFERENCES

1. Bartlett, Dennis W.: Wind-Tunnel Investigation of Several High Aspect-Ratio Supercritical Wing Configurations on a Wide-Body-Type Fuselage. NASA TM X-71996, 1977.
2. Steckel, Doris K.; Dahlin, John A.; and Henne, Preston A.: Results of Design Studies and Wind Tunnel Tests of High-Aspect-Ratio Supercritical Wings for an Energy Efficient Transport. NASA CR-159332, 1980.
3. Henne, Preston A.; Dahlin, John A.; Peavey, Charles C.; and Gerren, Donna S.: Configuration Design Studies and Wind Tunnel Tests of an Energy Efficient Transport With a High-Aspect-Ratio Supercritical Wing. NASA CR-3524, 1982.
4. Macioce, Lawrence E.; Schaefer, John W.; and Saunders, Neal T.: A Status Report on the Energy Efficient Engine Project. NASA TM-81566, 1980.
5. Henderson, William P.; and Patterson, James C., Jr.: Propulsion Installation Characteristics for Turbofan Transports. AIAA Paper 83-0087, Jan. 1983.
6. Peddrew, Katherine H., compiler: A User's Guide to the Langley 16-Foot Transonic Tunnel. NASA TM-83186, 1981.
7. Re, Richard J.: An Investigation of Several NACA 1-Series Axisymmetric Inlets at Mach Numbers From 0.4 to 1.29. NASA TM X-2917, 1974.
8. Reubush, David E.: Effects of Fineness and Closure Ratios on Boattail Drag of Circular-Arc Afterbody Models With Jet Exhaust at Mach Numbers up to 1.30. NASA TN D-7163, 1973.
9. Gillette, W. B.: Nacelle Installation Analysis for Subsonic Transport Aircraft. AIAA Paper 77-102, Jan. 1977.
10. Braslow, Albert L.; and Knox, Eugene C.: Simplified Method for Determination of Critical Height of Distributed Roughness Particles for Boundary-Layer Transition at Mach Numbers From 0 to 5. NACA TN 4363, 1958.
11. Blackwell, James A., Jr.: Preliminary Study of Effects of Reynolds Number and Boundary-Layer Transition Location on Shock-Induced Separation. NASA TN D-5003, 1969.
12. Shapiro, Ascher H.: The Dynamics and Thermodynamics of Compressible Fluid Flow. Volume II. Ronald Press Co., c.1954, p. 1110.
13. Patel, S. P.; and Donelson, J. E.: Investigation of the Interference Effects of Mixed-Flow Long-Duct Nacelle on a DC-10 Wing. NASA CR-159202, 1980.
14. Pauley, G.: Interim Note on Tests With a Wing-Mounted Fan Nacelle With the Fan Jet Simulated by Cold Air Blowing and Alternatively by a Gas Generator Shroud. ARC CP No. 1111, Her Majesty's Stationery Off., 1970.
15. Ferguson, D. R.; and Keith, J. S.: Modifications to the Streamtube Curvature Program. Volume I - Program Modifications and User's Manual. NASA CR-132705, 1975.

TABLE I.- WING STREAMWISE AIRFOIL COORDINATES

(a)  $\eta = 0.127$  (Fuselage side)

x/c	z/c	
	Upper surface	Lower surface
0	-.0016	-.0016
.002	.0104	-.0136
.005	.0164	-.0196
.010	.0229	-.0266
.020	.0304	-.0351
.030	.0359	-.0401
.040	.0394	-.0446
.050	.0419	-.0486
.060	.0441	-.0521
.070	.0460	-.0553
.080	.0477	-.0581
.090	.0492	-.0607
.100	.0506	-.0632
.110	.0518	-.0655
.120	.0529	-.0676
.130	.0539	-.0695
.140	.0548	-.0713
.150	.0556	-.0730
.160	.0563	-.0746
.170	.0570	-.0760
.180	.0576	-.0773
.190	.0582	-.0785
.200	.0587	-.0796
.210	.0591	-.0805
.220	.0593	-.0813
.230	.0595	-.0820
.240	.0596	-.0826
.250	.0596	-.0832
.260	.0596	-.0837
.270	.0595	-.0842
.280	.0593	-.0846
.290	.0591	-.0850
.300	.0588	-.0853
.310	.0585	-.0856
.320	.0581	-.0858
.330	.0577	-.0860
.340	.0572	-.0862
.350	.0567	-.0863

x/c	z/c	
	Upper surface	Lower surface
.360	.0561	-.0864
.370	.0555	-.0864
.380	.0548	-.0863
.390	.0541	-.0862
.400	.0534	-.0860
.410	.0526	-.0858
.420	.0518	-.0855
.430	.0510	-.0852
.440	.0501	-.0848
.450	.0492	-.0843
.460	.0483	-.0838
.470	.0473	-.0832
.480	.0463	-.0825
.490	.0453	-.0817
.500	.0442	-.0809
.510	.0431	-.0800
.520	.0420	-.0790
.530	.0408	-.0779
.540	.0396	-.0767
.550	.0384	-.0754
.560	.0371	-.0741
.570	.0358	-.0727
.580	.0345	-.0713
.590	.0331	-.0698
.600	.0317	-.0683
.610	.0303	-.0668
.620	.0289	-.0652
.630	.0274	-.0636
.640	.0259	-.0620
.650	.0244	-.0604
.660	.0229	-.0588
.670	.0213	-.0573
.680	.0197	-.0558
.690	.0181	-.0543
.700	.0164	-.0529
.710	.0147	-.0515
.720	.0130	-.0502
.730	.0113	-.0489

TABLE I.- WING STREAMWISE AIRFOIL COORDINATES - Continued

(a)  $\eta = 0.127$  (Fuselage side) - Concluded

x/c	z/c	
	Upper surface	Lower surface
.740	.0095	-.0477
.750	.0077	-.0465
.760	.0059	-.0454
.770	.0041	-.0444
.780	.0022	-.0434
.790	.0003	-.0425
.800	-.0016	-.0417
.810	-.0036	-.0410
.820	-.0056	-.0404
.830	-.0076	-.0399
.840	-.0096	-.0394
.850	-.0116	-.0390
.860	-.0136	-.0387
.870	-.0156	-.0385
.880	-.0176	-.0384
.890	-.0196	-.0385
.900	-.0216	-.0387
.910	-.0236	-.0390
.920	-.0256	-.0394
.930	-.0276	-.0400
.940	-.0296	-.0407
.950	-.0316	-.0415
.960	-.0336	-.0424
.970	-.0356	-.0435
.980	-.0376	-.0447
.990	-.0396	-.0460
1.000	-.0416	-.0476
c = 37.899 cm $\epsilon = 2.462^\circ$ t/c = .144		

TABLE I.- WING STREAMWISE AIRFOIL COORDINATES - Continued

(b)  $\eta = 0.410$  (Planform break)

x/c	z/c	
	Upper surface	Lower surface
0	-.0044	-.0044
.002	.0049	-.0131
.005	.0099	-.0181
.010	.0148	-.0230
.020	.0210	-.0290
.030	.0253	-.0329
.040	.0286	-.0360
.050	.0312	-.0386
.060	.0336	-.0408
.070	.0357	-.0427
.080	.0376	-.0444
.090	.0393	-.0459
.100	.0409	-.0473
.110	.0424	-.0487
.120	.0436	-.0499
.130	.0448	-.0510
.140	.0460	-.0520
.150	.0471	-.0529
.160	.0481	-.0538
.170	.0491	-.0546
.180	.0500	-.0554
.190	.0508	-.0561
.200	.0516	-.0567
.210	.0523	-.0573
.220	.0530	-.0579
.230	.0537	-.0584
.240	.0543	-.0588
.250	.0548	-.0593
.260	.0554	-.0597
.270	.0559	-.0600
.280	.0563	-.0603
.290	.0568	-.0605
.300	.0571	-.0607
.310	.0575	-.0609
.320	.0577	-.0611
.330	.0580	-.0612
.340	.0582	-.0612
.350	.0585	-.0612

x/c	z/c	
	Upper surface	Lower surface
.360	.0587	-.0611
.370	.0589	-.0610
.380	.0590	-.0609
.390	.0590	-.0608
.400	.0591	-.0606
.410	.0591	-.0603
.420	.0591	-.0601
.430	.0591	-.0597
.440	.0591	-.0593
.450	.0590	-.0589
.460	.0588	-.0584
.470	.0587	-.0578
.480	.0585	-.0572
.490	.0584	-.0562
.500	.0582	-.0558
.510	.0579	-.0549
.520	.0577	-.0541
.530	.0573	-.0531
.540	.0570	-.0520
.550	.0567	-.0508
.560	.0563	-.0496
.570	.0559	-.0482
.580	.0555	-.0468
.590	.0550	-.0454
.600	.0544	-.0438
.610	.0539	-.0422
.620	.0534	-.0405
.630	.0528	-.0387
.640	.0522	-.0369
.650	.0515	-.0351
.660	.0509	-.0332
.670	.0500	-.0314
.680	.0493	-.0294
.690	.0485	-.0275
.700	.0476	-.0255
.710	.0467	-.0235
.720	.0458	-.0215
.730	.0448	-.0195

TABLE I.- WING STREAMWISE AIRFOIL COORDINATES - Continued

(b)  $\eta = 0.410$  (Planform break) - Concluded

x/c	z/c	
	Upper surface	Lower surface
.740	.0438	-.0175
.750	.0427	-.0155
.760	.0415	-.0135
.770	.0404	-.0116
.780	.0391	-.0098
.790	.0378	-.0081
.800	.0365	-.0064
.810	.0351	-.0048
.820	.0336	-.0034
.830	.0320	-.0020
.840	.0304	-.0008
.850	.0288	.0003
.860	.0271	.0011
.870	.0253	.0017
.880	.0235	.0021
.890	.0215	.0024
.900	.0195	.0025
.910	.0174	.0023
.920	.0152	.0019
.930	.0130	.0011
.940	.0107	.0001
.950	.0083	-.0012
.960	.0058	-.0027
.970	.0033	-.0046
.980	.0005	-.0067
.990	-.0025	-.0092
1.000	-.0056	-.0120
c = 23.249 cm $\epsilon = 0.256^\circ$ t/c = .12		

TABLE I.- WING STREAMWISE AIRFOIL COORDINATES - Continued

(c)  $\eta = 1.000$  (Tip)

x/c	z/c	
	Upper surface	Lower surface
0	-.0175	-.0175
.002	-.0095	-.0240
.005	-.0053	-.0284
.010	-.0012	-.0323
.020	.0041	-.0367
.030	.0079	-.0397
.040	.0109	-.0420
.050	.0134	-.0439
.060	.0157	-.0455
.070	.0177	-.0468
.080	.0195	-.0480
.090	.0213	-.0491
.100	.0229	-.0500
.110	.0245	-.0509
.120	.0258	-.0516
.130	.0272	-.0523
.140	.0284	-.0530
.150	.0296	-.0535
.160	.0308	-.0540
.170	.0318	-.0544
.180	.0329	-.0548
.190	.0339	-.0551
.200	.0349	-.0554
.210	.0357	-.0557
.220	.0366	-.0559
.230	.0374	-.0561
.240	.0382	-.0562
.250	.0390	-.0563
.260	.0397	-.0563
.270	.0404	-.0564
.280	.0410	-.0564
.290	.0417	-.0563
.300	.0422	-.0563
.310	.0428	-.0561
.320	.0433	-.0560
.330	.0437	-.0558
.340	.0442	-.0556
.350	.0446	-.0553

x/c	z/c	
	Upper surface	Lower surface
.360	.0451	-.0551
.370	.0455	-.0548
.380	.0459	-.0544
.390	.0462	-.0541
.400	.0465	-.0536
.410	.0468	-.0532
.420	.0470	-.0527
.430	.0473	-.0522
.440	.0475	-.0516
.450	.0478	-.0510
.460	.0479	-.0503
.470	.0481	-.0495
.480	.0482	-.0488
.490	.0483	-.0479
.500	.0484	-.0471
.510	.0484	-.0462
.520	.0485	-.0451
.530	.0485	-.0441
.540	.0486	-.0429
.550	.0485	-.0418
.560	.0485	-.0405
.570	.0484	-.0392
.580	.0484	-.0378
.590	.0482	-.0364
.600	.0481	-.0348
.610	.0479	-.0333
.620	.0477	-.0316
.630	.0475	-.0299
.640	.0472	-.0281
.650	.0470	-.0264
.660	.0467	-.0245
.670	.0464	-.0227
.680	.0460	-.0208
.690	.0457	-.0189
.700	.0452	-.0170
.710	.0448	-.0150
.720	.0443	-.0131
.730	.0437	-.0111

TABLE I.- WING STREAMWISE AIRFOIL COORDINATES - Concluded

(c)  $\eta = 1.000$  (Tip) - Concluded

x/c	z/c	
	Upper surface	Lower surface
.740	.0432	-.0092
.750	.0426	-.0072
.760	.0420	-.0052
.770	.0413	-.0034
.780	.0406	-.0015
.790	.0398	.0003
.800	.0391	.0020
.810	.0382	.0037
.820	.0372	.0052
.830	.0362	.0067
.840	.0351	.0081
.850	.0340	.0094
.860	.0328	.0104
.870	.0316	.0113
.880	.0302	.0119
.890	.0288	.0123
.900	.0273	.0127
.910	.0258	.0127
.920	.0241	.0126
.930	.0224	.0122
.940	.0207	.0114
.950	.0188	.0104
.960	.0168	.0091
.970	.0146	.0076
.980	.0123	.0057
.990	.0097	.0036
1.000	.0069	.0012
c = 10.521 cm $\epsilon = -1.229^\circ$ t/c = .10		



TABLE II.- LOCATION OF WING PRESSURE ORIFICES BY FUSELAGE STATION

Chordwise orifice locations, cm, at $\eta$ of -													
x/c	0.0	0.154	0.250	0.328	0.370	0.440	0.550	0.750	0.850	0.950	0.750	0.850	0.950
	Upper surface	Upper and lower surfaces							Upper surface			Lower surface	
0.0000		56.202	61.180	65.224	67.381	71.065	76.687	87.019	92.187	97.352	87.417	92.531	97.642
.0125		56.658	61.574	65.568	67.697	71.347	76.940						
.0250		57.114	61.968	65.911	68.014	71.630	77.192	87.417	92.531	97.642	88.213	93.219	98.222
.0500	50.483	58.027	62.756	66.599	68.647	72.194	77.698	87.815	92.875	97.932	88.611	93.563	98.512
.0750	51.594	58.940	63.545	67.286	69.281	72.759	78.204				89.406	94.251	99.092
.1000	52.705	59.853	64.333	67.973	69.914	73.323	78.710	88.611	93.563	98.512	90.202	94.939	99.672
.1500	54.928	61.678	65.909	69.347	71.180	74.452	79.721	89.406	94.251	99.092	90.998	95.627	100.252
.2000	57.150	63.503	67.486	70.721	72.447	75.581	80.733	90.202	94.939	99.672	91.794	96.315	100.832
.2500	59.373	65.329	69.063	72.096	73.713	76.710	81.744	90.998	95.627	100.252	92.590	97.003	101.412
.3000	61.595	67.154	70.639	73.470	74.980	77.839	82.756	91.794	96.315	100.832	92.590	97.003	101.412
.3500	63.817	68.979	72.216	74.844	76.246	78.967	83.768	92.590	97.003	101.412	94.181	98.379	102.572
.4000	66.040	70.805	73.792	76.218	77.512	80.411	84.779	93.385	97.691	101.992	94.181	98.379	102.572
.4500	68.263	72.630	75.369	77.593	78.779	81.225	85.791	94.181	98.379	102.572	94.181	98.379	102.572
.5000	70.485	74.455	76.945	78.967	80.045	82.354	86.802	94.977	99.067	103.152	95.773	99.755	103.732
.5500	72.708	76.281	78.522	*80.670	81.312	83.483	87.814	95.773	99.755	103.732	95.773	99.755	103.732
.6000	74.930	78.106	80.099	81.715	82.578	84.612	88.825	96.569	100.443	104.312	97.364	101.130	104.892
.6500	77.153	79.932	81.675	83.090	83.845	85.741	89.837	97.364	101.130	104.892	97.364	101.130	104.892
.7000	79.375	81.757	83.252	84.464	85.111	86.870	90.848	98.160	101.818	105.472			
.7500	81.598	83.582	84.828	85.838	86.378	87.999	91.860						
.8000	83.820	85.408	86.405	87.213	87.644	89.128	92.872	99.752	103.194	106.632	99.752	103.194	106.632
.8500	86.043	87.233	87.982	88.587	88.910	90.257	93.883				101.343	104.570	107.792
.9000	88.265	89.058	89.558	89.961	90.177	91.385	94.895	102.139	105.258				
.9500	90.487	90.884	91.135	91.335	91.443	92.514	95.906						

\*x/c = 0.5620.

†x/c = 0.4140.

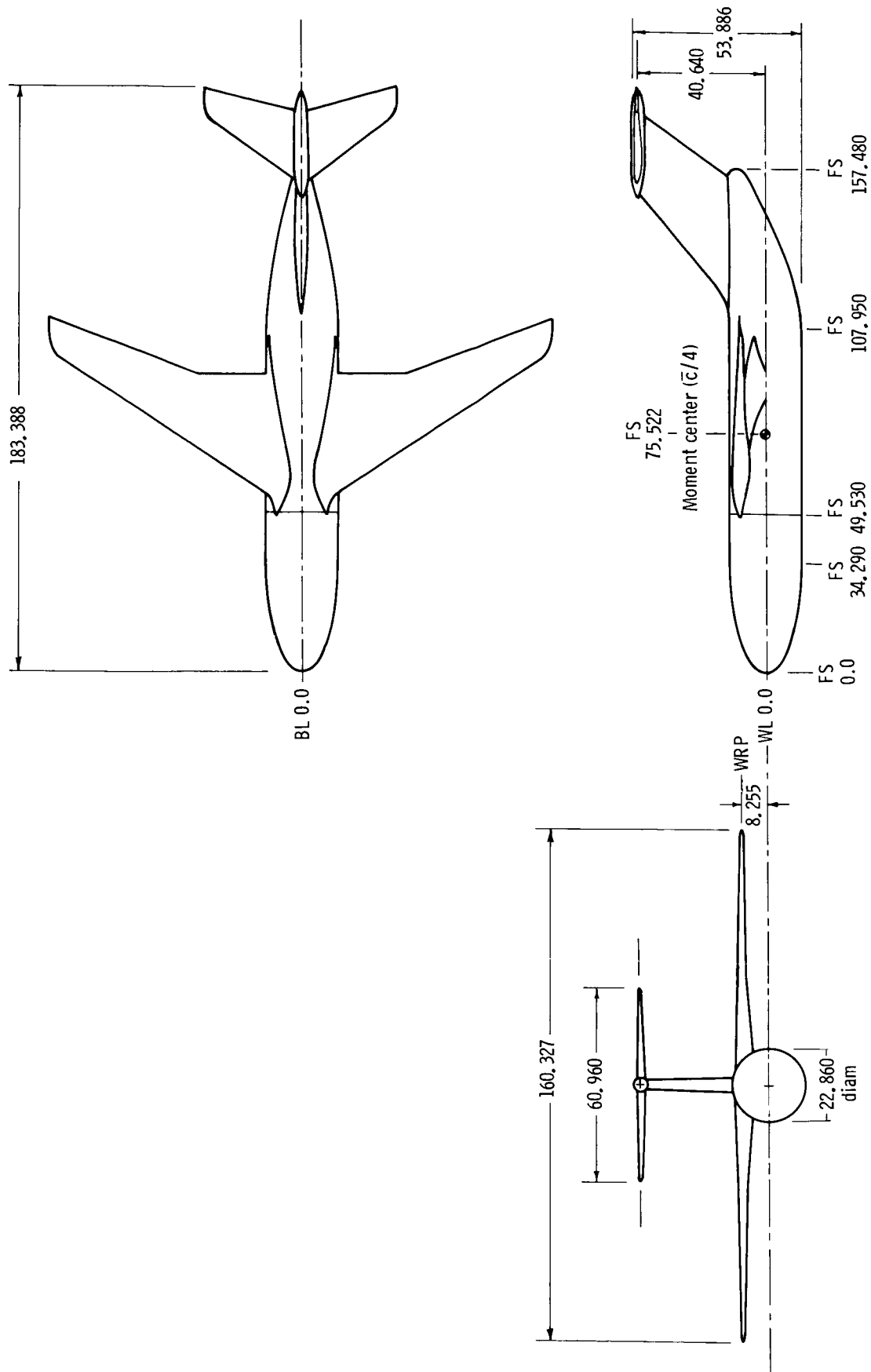
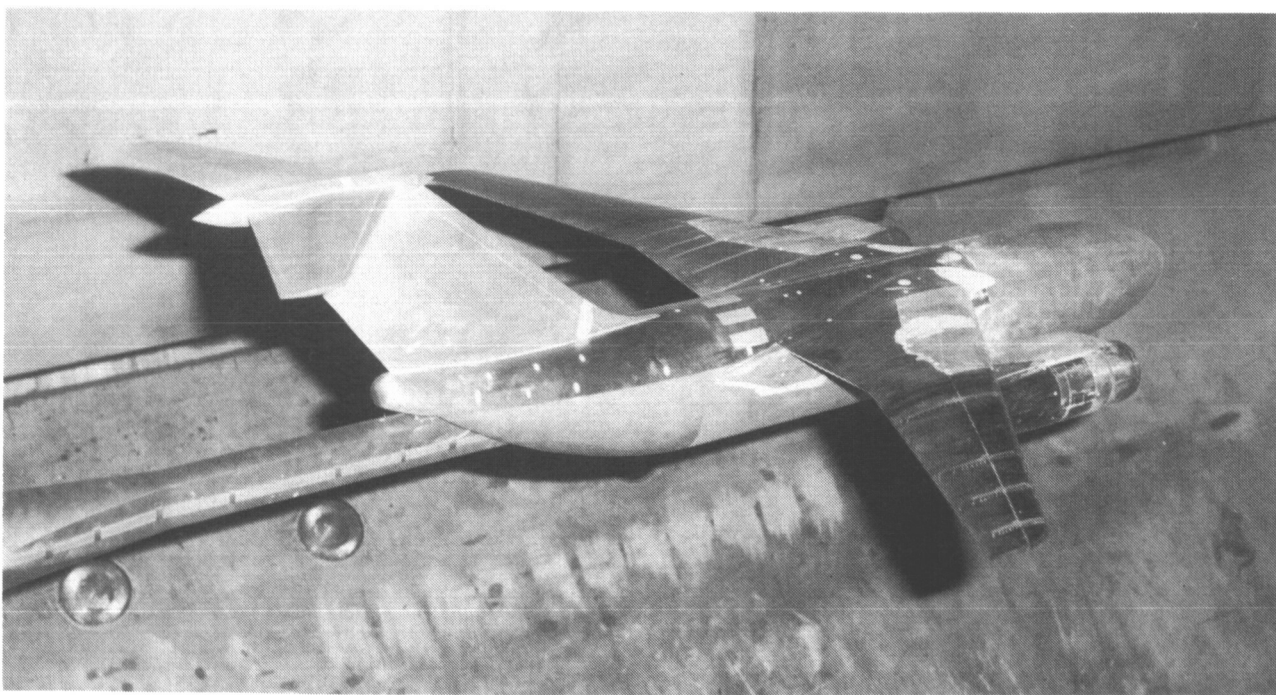


Figure 1.- Basic transport model with clean wing. Linear dimensions are in centimeters.

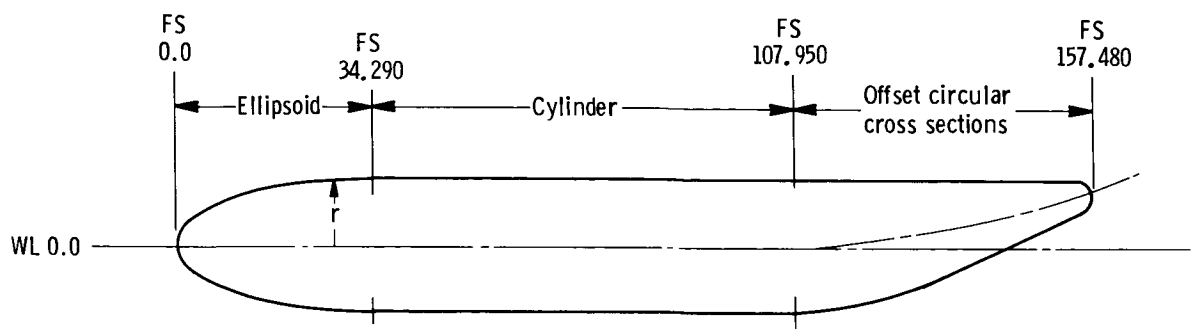


L-79-3940

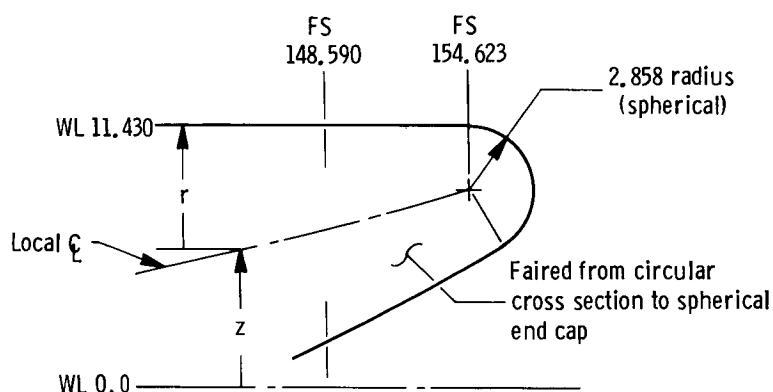


L-79-3937

Figure 2.- Model with pylon-mounted nacelles (configuration UWS-B) installed in Langley 16-Foot Transonic Tunnel.



#### Closure detail

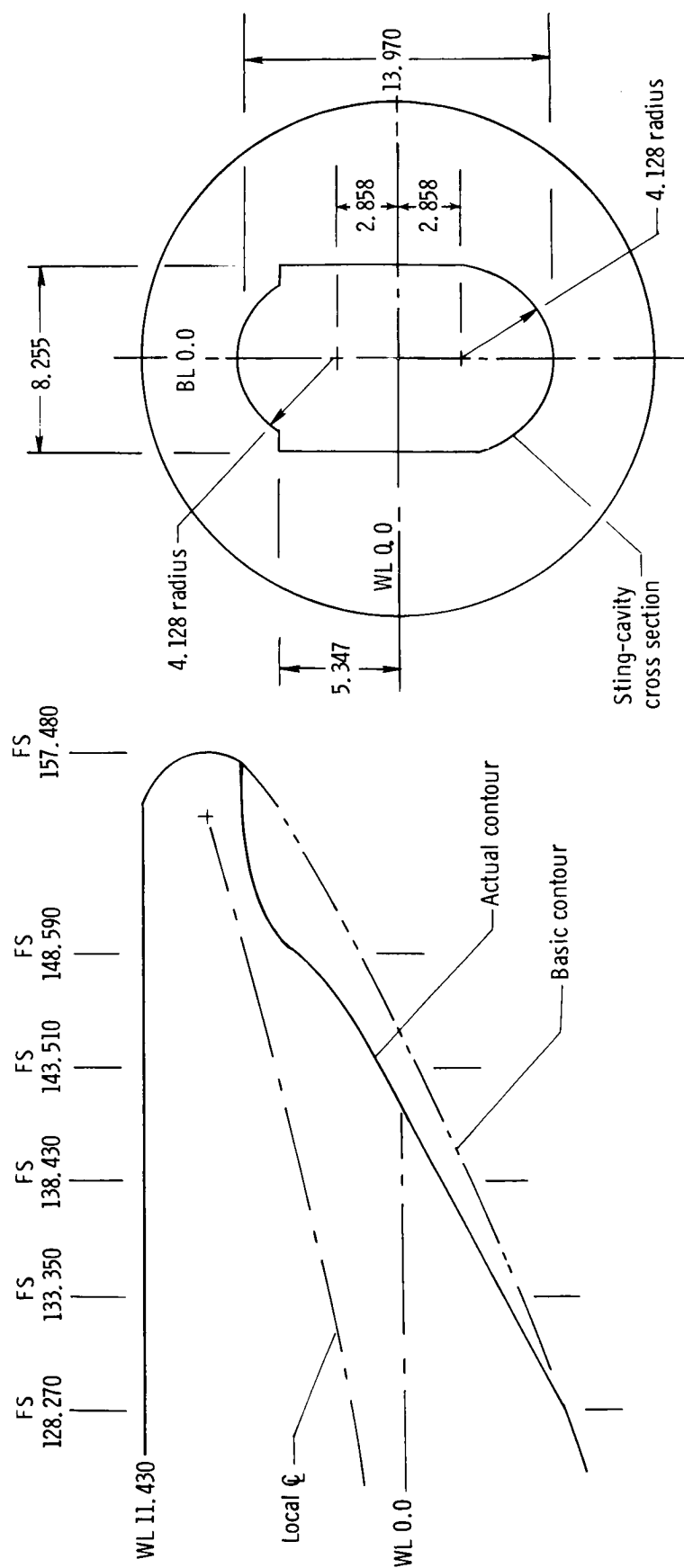


Ellipsoidal nose coordinates	
FS	r
0	0
.254	1.389
.508	1.961
.635	2.189
.952	2.675
1.270	3.081
1.905	3.757
2.540	4.318
3.175	4.803
3.810	5.237
5.080	5.987
6.350	6.627
8.890	7.678
11.430	8.519
13.970	9.208
16.510	9.774
19.050	10.239
24.130	10.917
29.210	11.303
34.290	11.430

Afterbody coordinates		
FS	z	-r
107.950	0	11.430
113.030	.254	11.176
118.110	.711	10.719
123.190	1.397	10.033
128.270	2.184	9.246
133.350	3.112	8.319
138.430	4.216	7.214
143.510	5.410	6.020
148.590	6.731	4.699
154.622	8.573	2.858

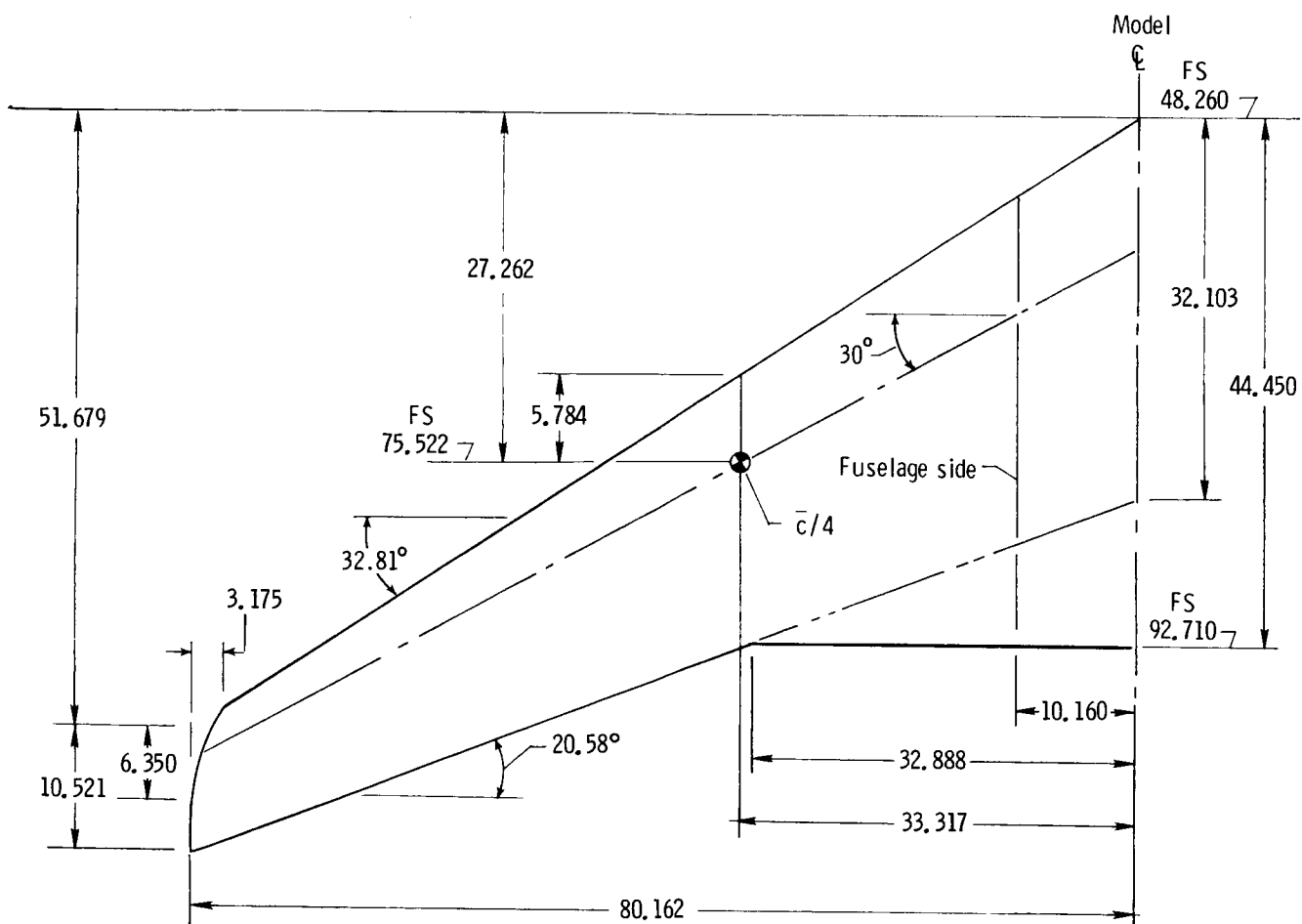
(a) Basic shape.

Figure 3.- Fuselage geometry. Linear dimensions are in centimeters.



(b) Fuselage closure with sting cavity.

Figure 3.- Concluded.



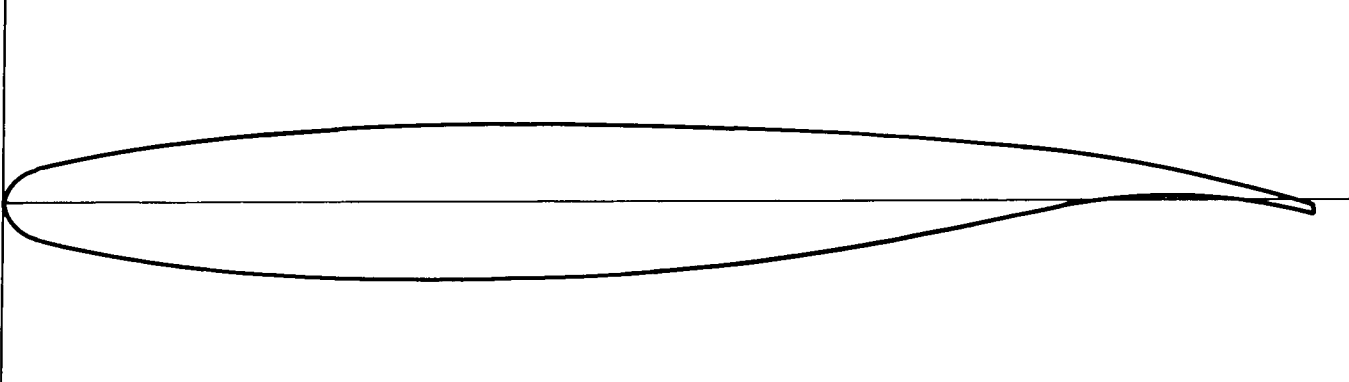
Aspect ratio .....	7.52
Taper ratio .....	0.328
Area (trapezoid), cm <sup>2</sup> ..	3416.66
$\bar{c}$ , cm .....	23.132
$c_{av}$ , cm .....	21.311
Incidence, deg.....	0
Dihedral, deg.....	0

Figure 4.- Details of wing planform. Linear dimensions are in centimeters.

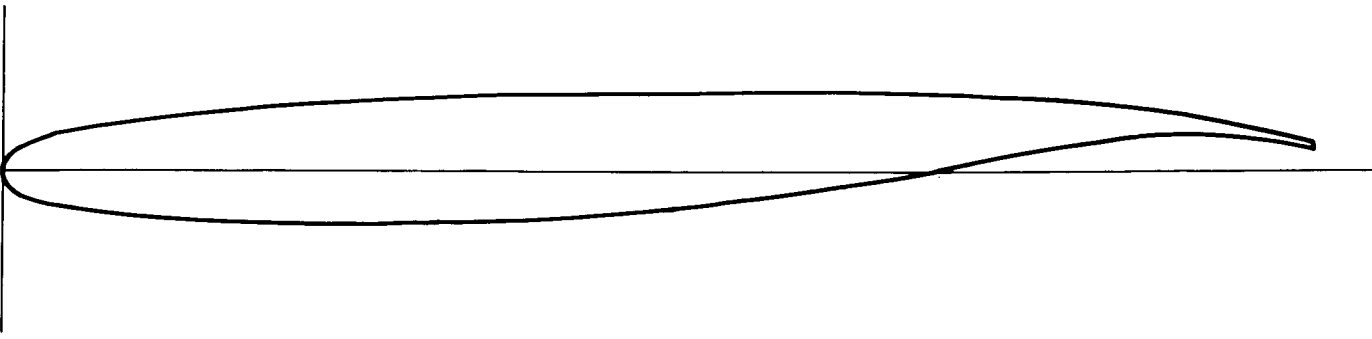


WRP

Fuselage side;  $t/c = 0.144$ , BL 10.160



Planform break;  $t/c = 0.12$ , BL 32.888



Tip;  $t/c = 0.10$ , BL 80.162

Figure 5.- Defining airfoil sections of model wing. All linear dimensions are in centimeters.

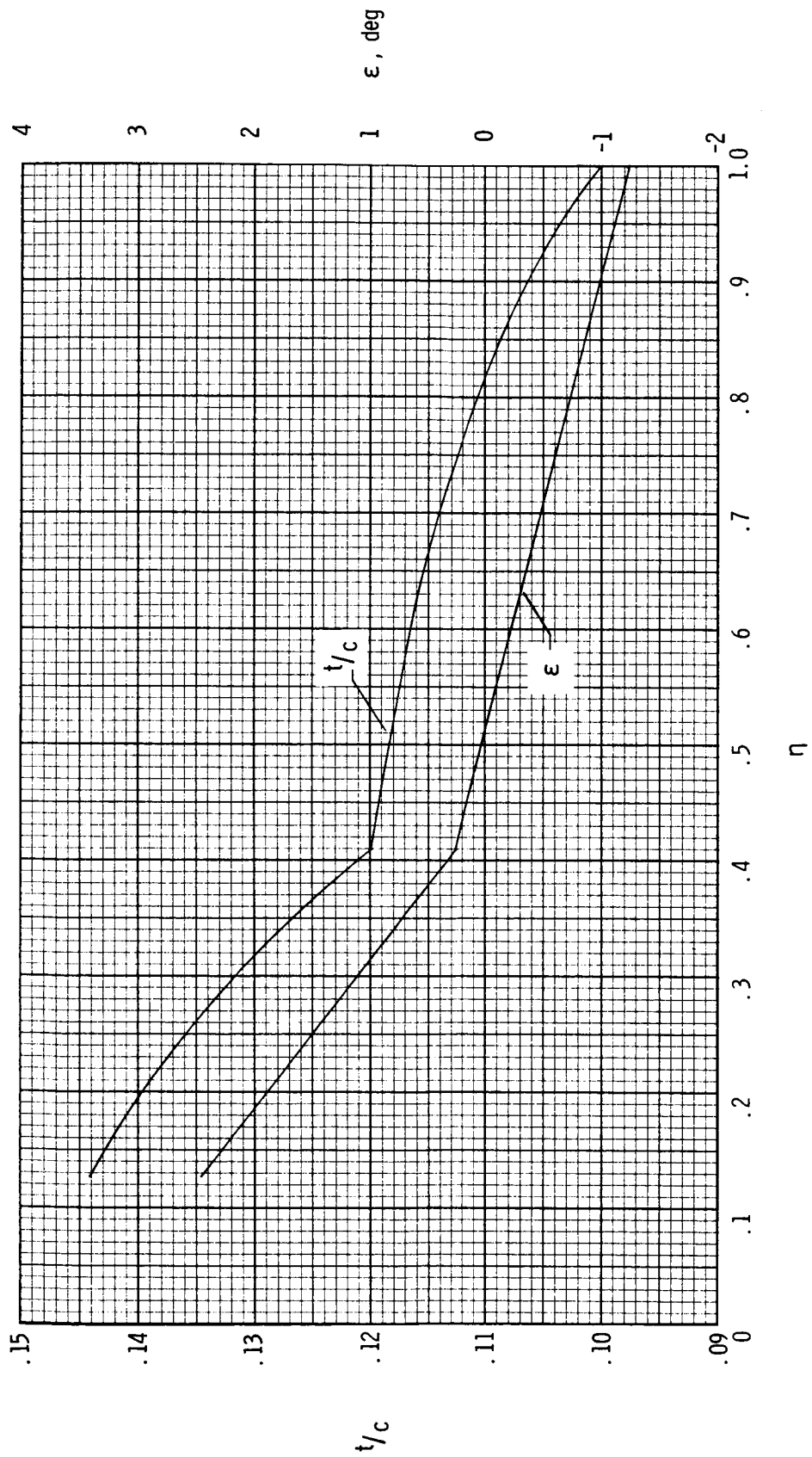
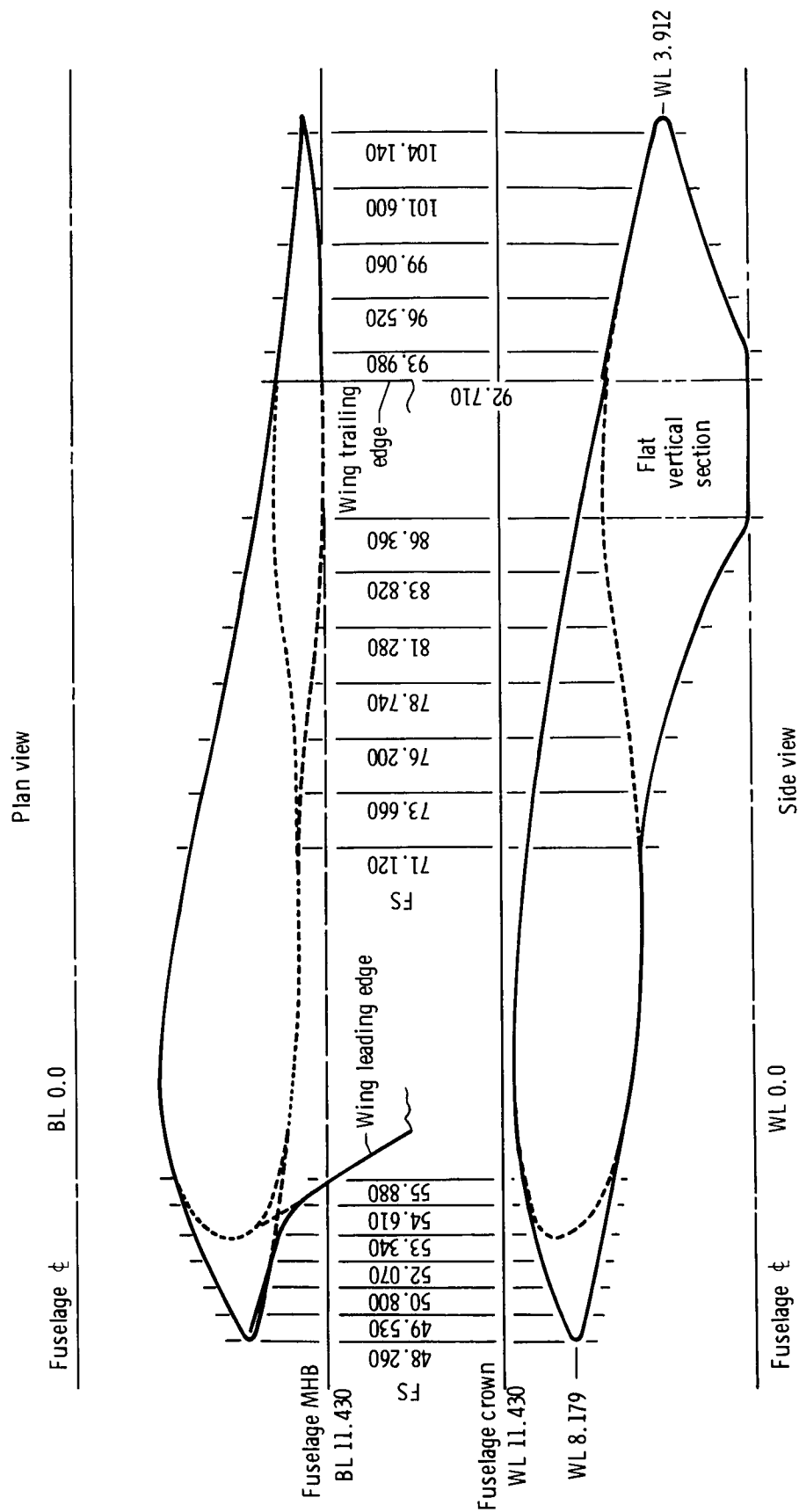


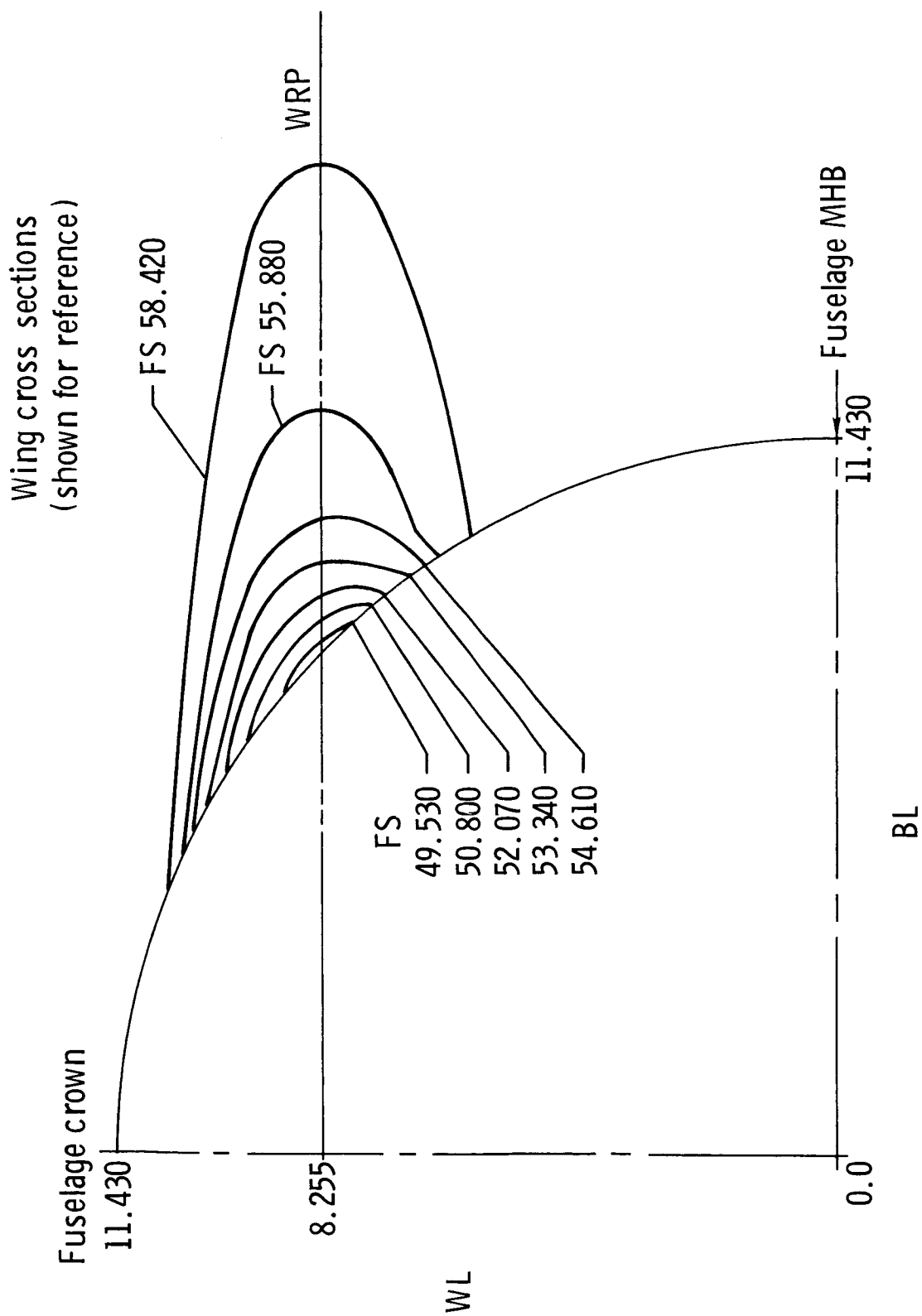
Figure 6.-- Spanwise thickness and twist distributions of wing.





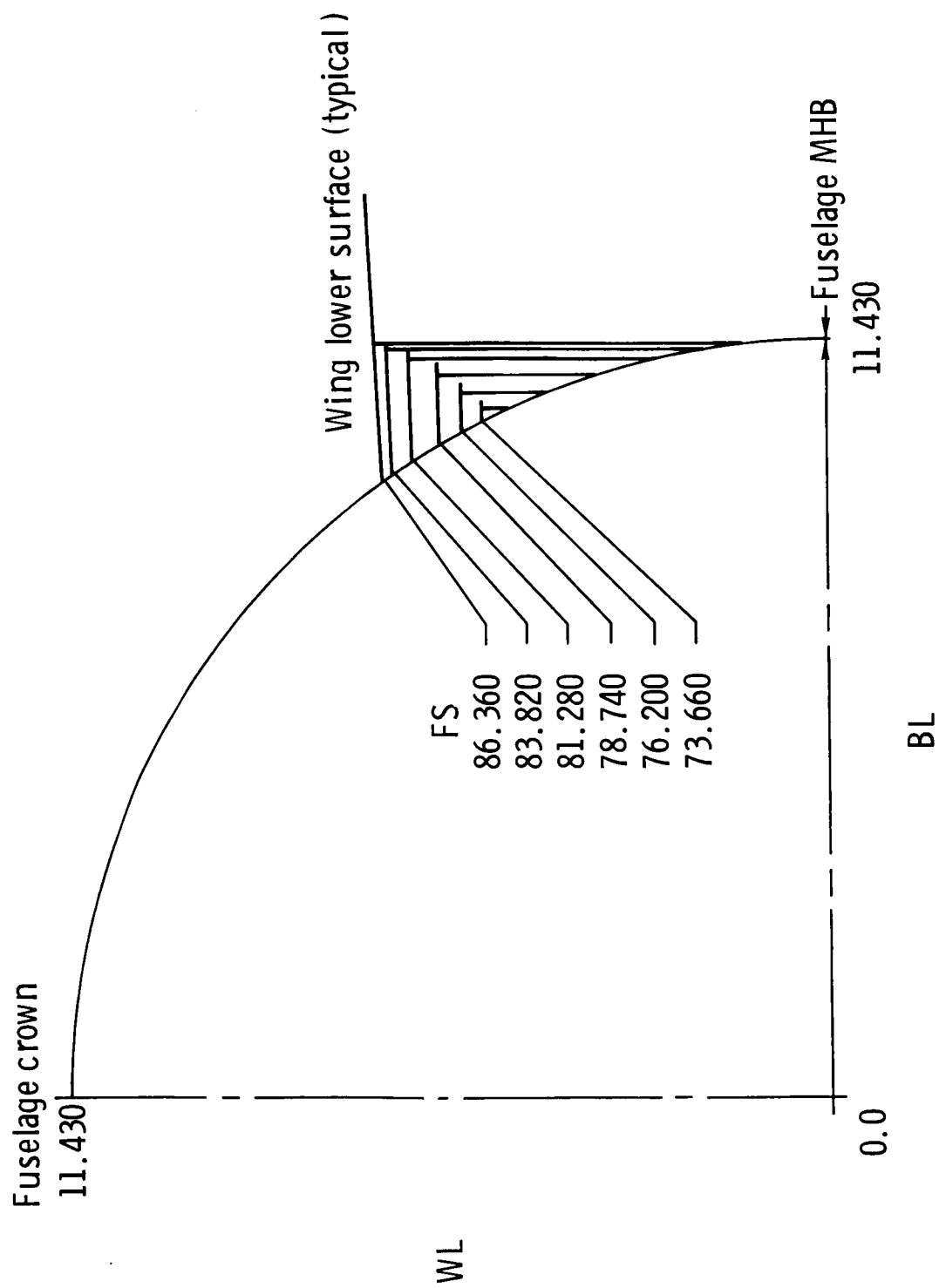
(a) Top and side profiles.

Figure 7.- Wing-fuselage fairing details. All linear dimensions are in centimeters.



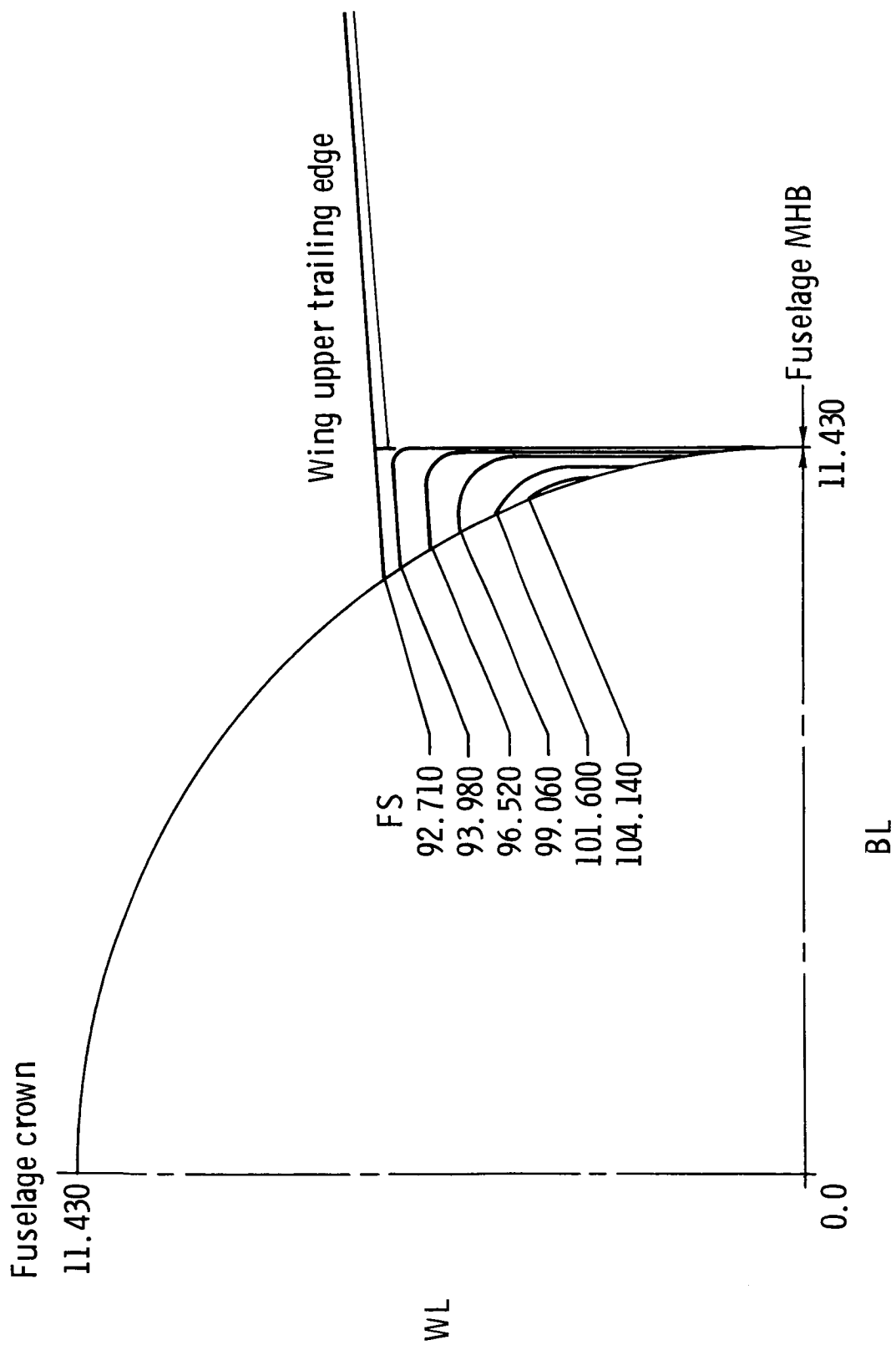
(b) Forward fairing cross sections.

Figure 7.- Continued.



(c) Rear fairing cross sections.

Figure 7.- Continued.



(d) Concluded.

Figure 7.- Concluded.



Streamwise airfoil ordinates	
x/c	± y/c
0	0
.0025	.0066
.0050	.0090
.0075	.0108
.0100	.0122
.0125	.0132
.0250	.0181
.0500	.0248
.0750	.0304
.1000	.0351
.1500	.0423
.2000	.0475
.2500	.0513
.3000	.0540
.3500	.0556
.4000	.0563
.4500	.0563
.5000	.0555
.6000	.0499
.7000	.0394
.7500	.0328
1.0000	.0004

LER/c = 0.0100

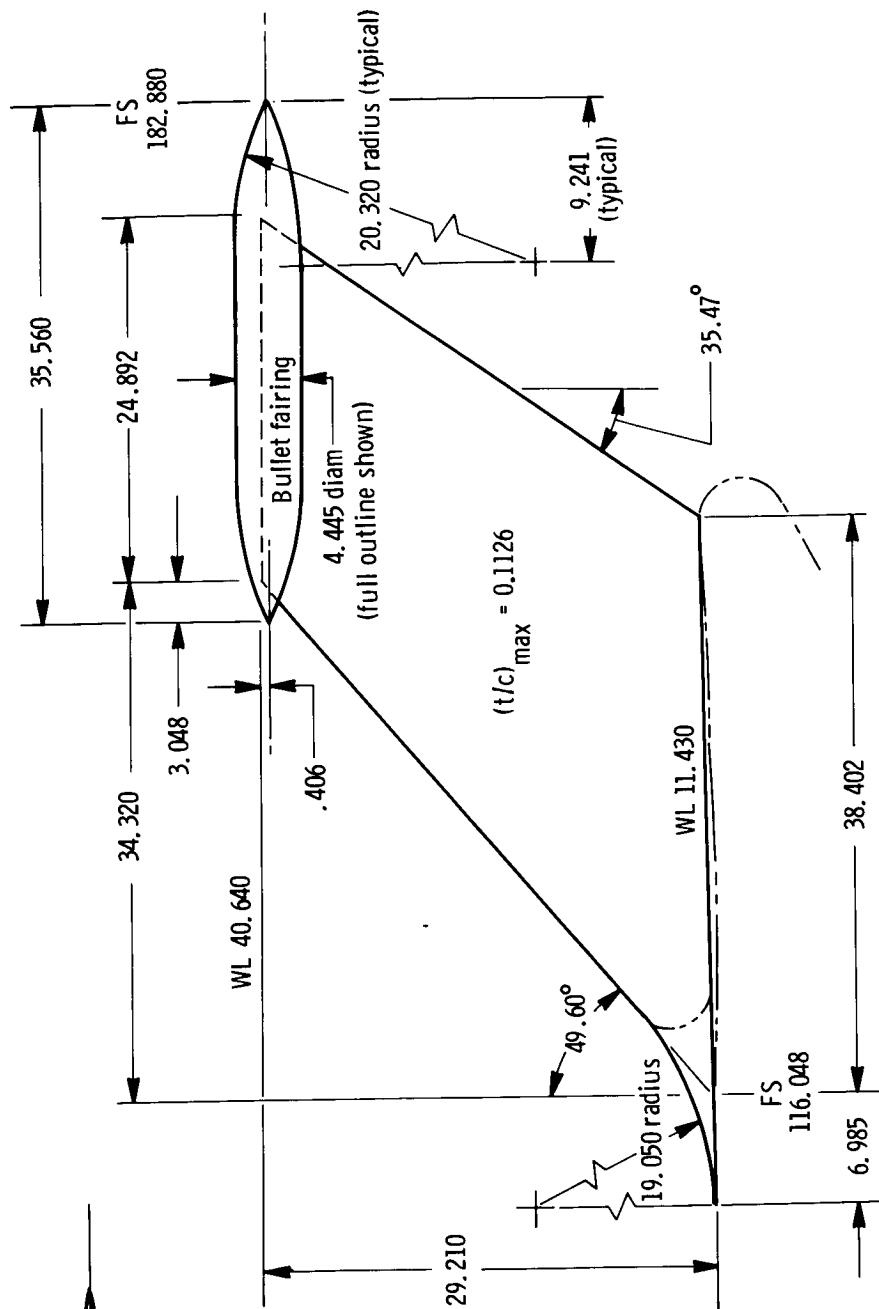


Figure 8.- Vertical tail geometry. All linear dimensions are in centimeters.

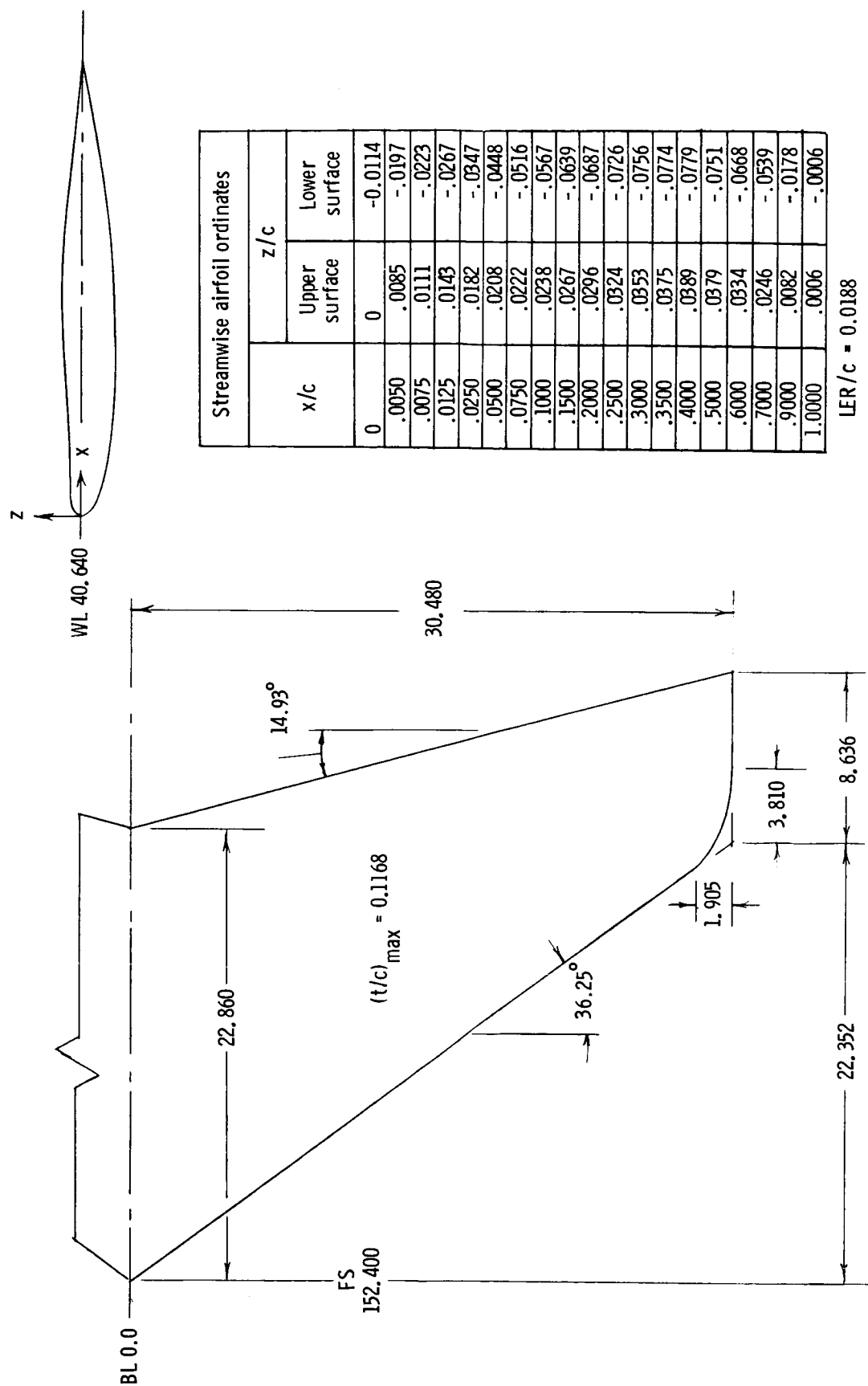
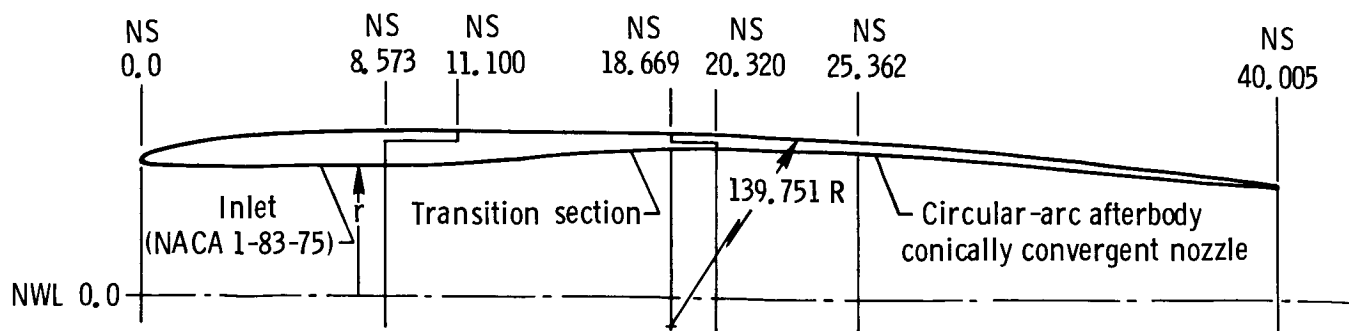


Figure 9.- Horizontal tail geometry. All linear dimensions are in centimeters.

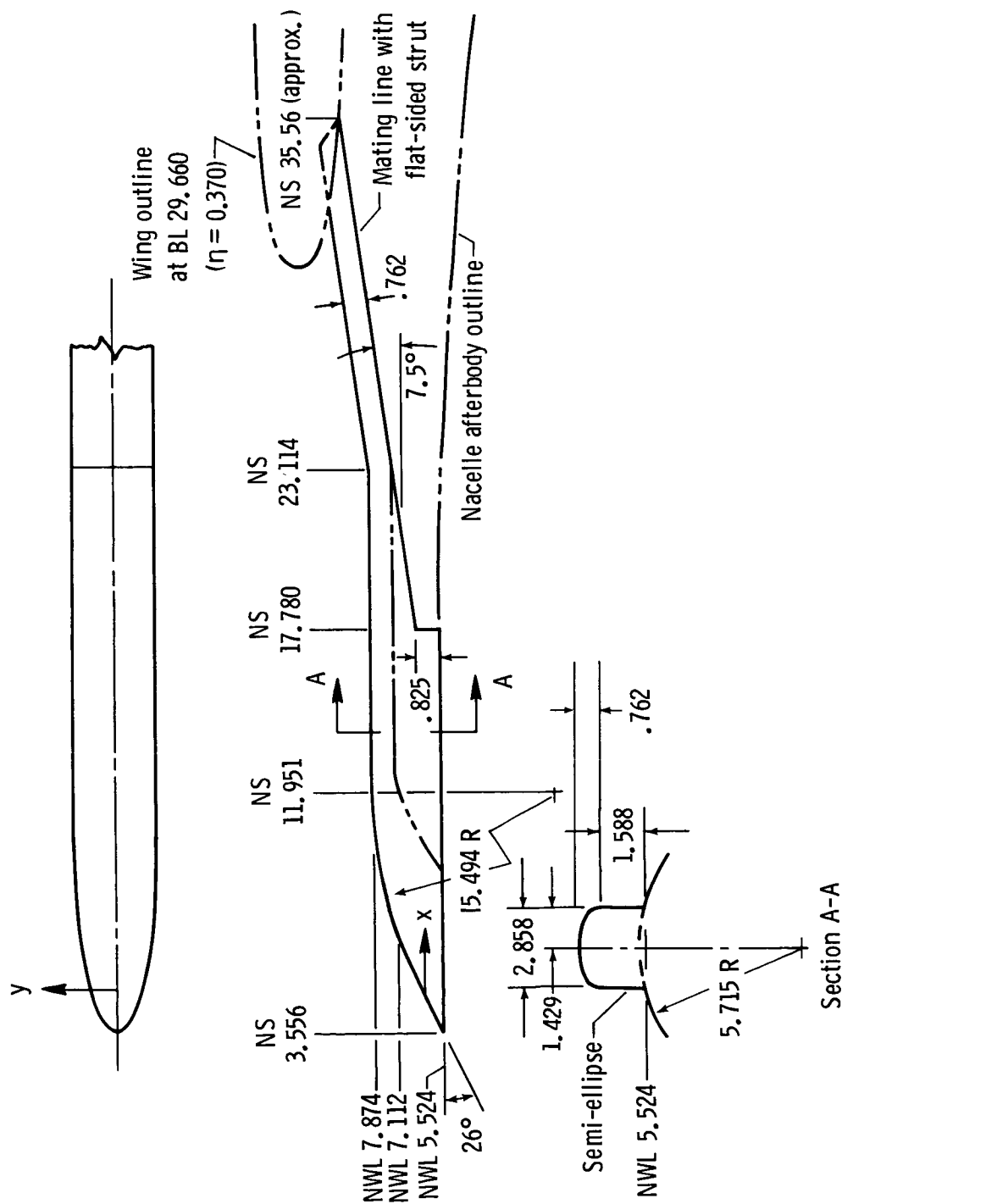


Inlet coordinates			
External		Internal	
NS	r	NS	r
0	4.760	0	4.760
.018	4.806	.018	4.699
.036	4.823	.036	4.676
.051	4.836	.051	4.658
.086	4.859	.086	4.633
.130	4.882	.130	4.608
.173	4.900	.173	4.592
.214	4.917	.214	4.577
.257	4.935	.257	4.569
.343	4.966	.373	4.559
.429	4.994	8.572	4.559
.599	5.042		
.859	5.105		
1.285	5.192		
1.714	5.263		
2.144	5.324		
2.570	5.380		
3.000	5.431		
3.429	5.474		
3.858	5.514		
4.288	5.550		
5.144	5.611		
5.999	5.657		
6.858	5.690		
7.717	5.710		
8.573	5.715		
11.100	5.715		

Transition section and nozzle coordinates	
Internal	
NS	r
8.572	4.559
9.748	4.577
10.922	4.628
12.098	4.699
13.272	4.788
14.448	4.884
15.621	4.978
16.797	5.067
17.970	5.138
19.147	5.189
20.320	5.207
25.362	5.207
Conically convergent	
40.005	4.001

Afterbody coordinates	
External	
NS	r
18.669	5.715
20.574	5.702
22.606	5.659
23.622	5.626
24.638	5.588
26.924	5.471
27.178	5.456
29.210	5.316
30.734	5.194
31.496	5.126
33.782	4.895
34.290	4.839
36.068	4.628
37.592	4.427
38.100	4.359
39.370	4.173
40.005	4.077

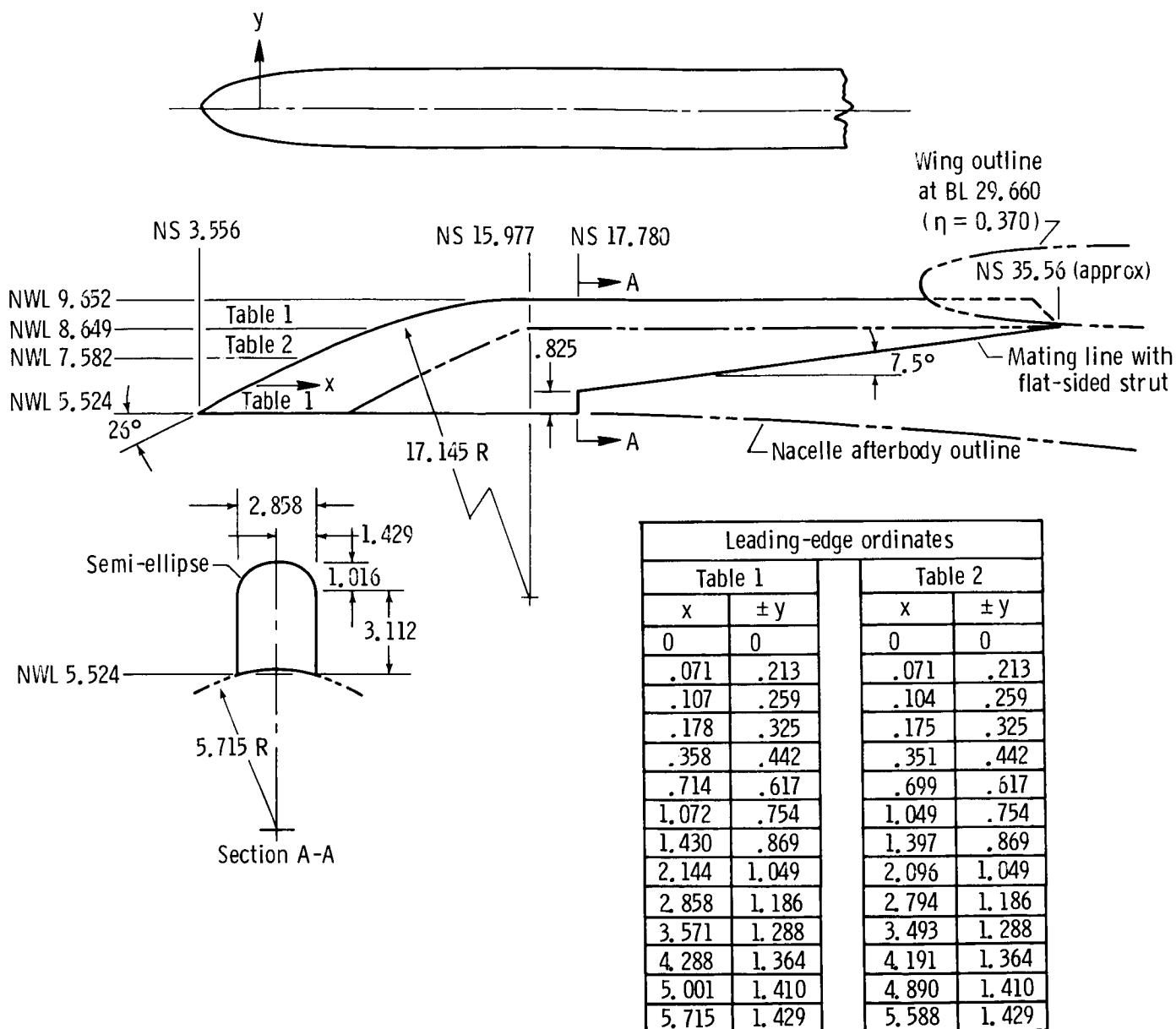
Figure 10.- Geometric details of nacelles. All linear dimensions are in centimeters.



(a) Pylon A leading edge.

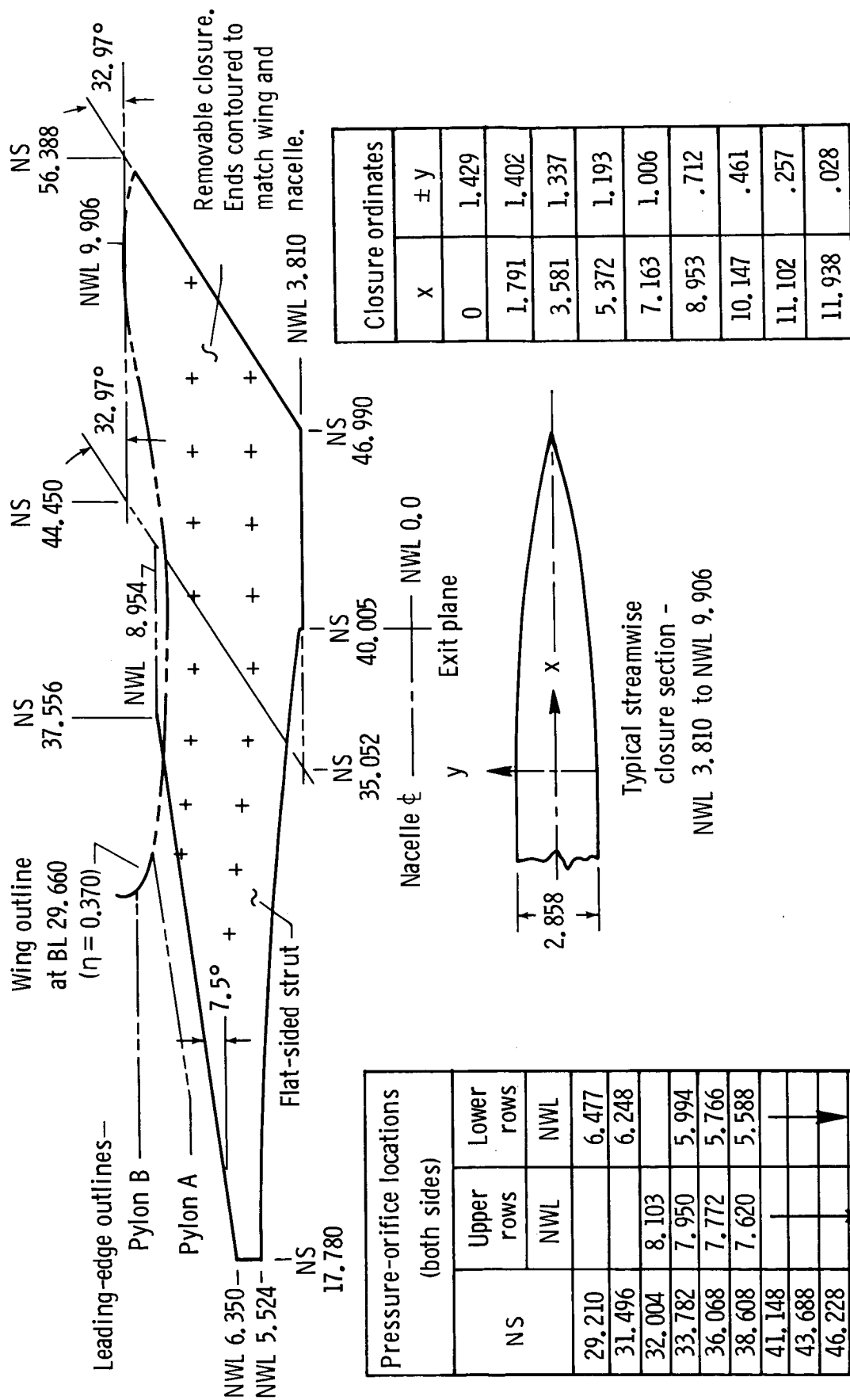
Figure 11.- Pylon details. All linear dimensions are in centimeters.





(b) Pylon B leading edge.

Figure 11.- Continued.



(c) Common strut and trailing edge.

Figure 11.- Concluded.

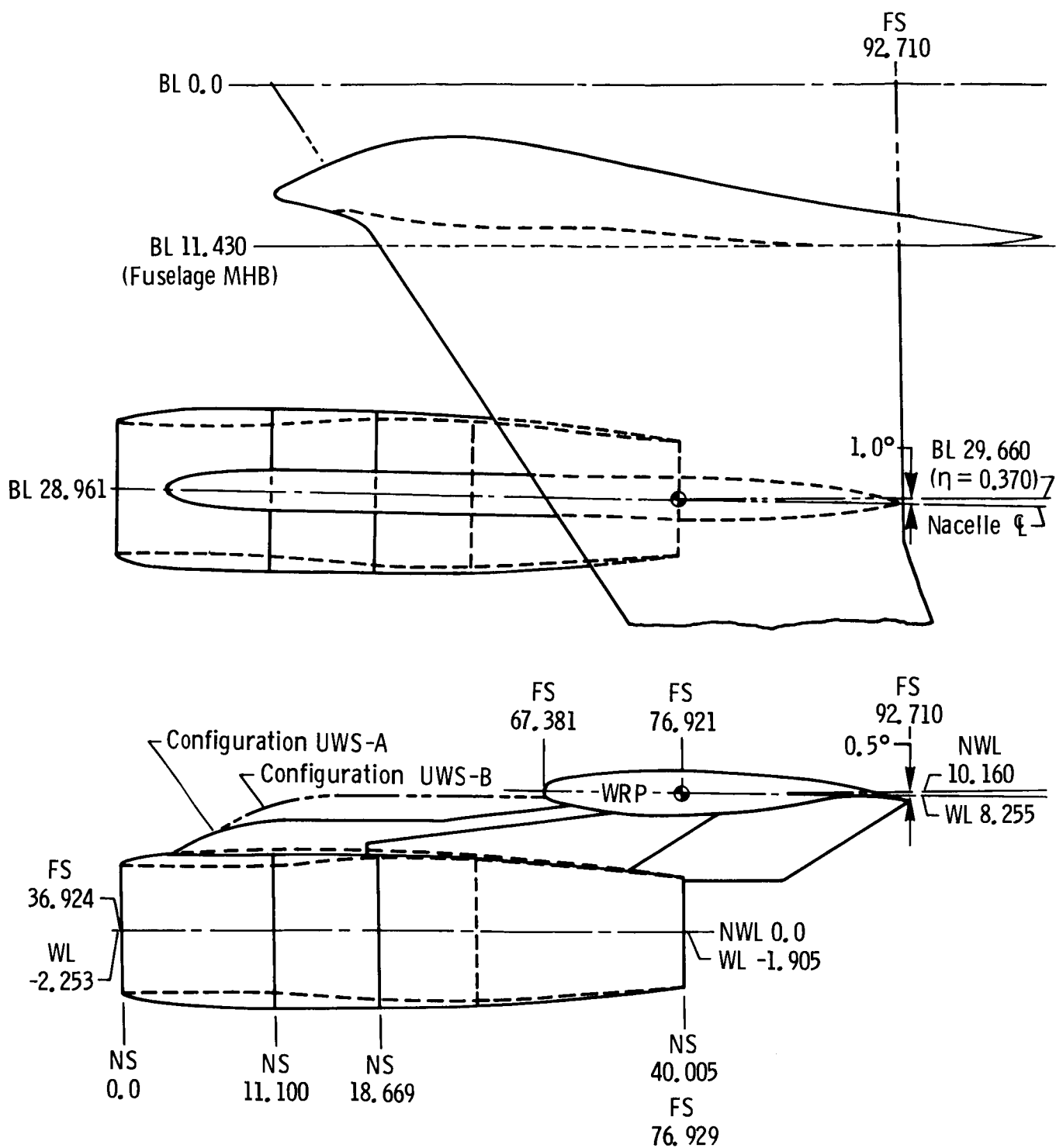
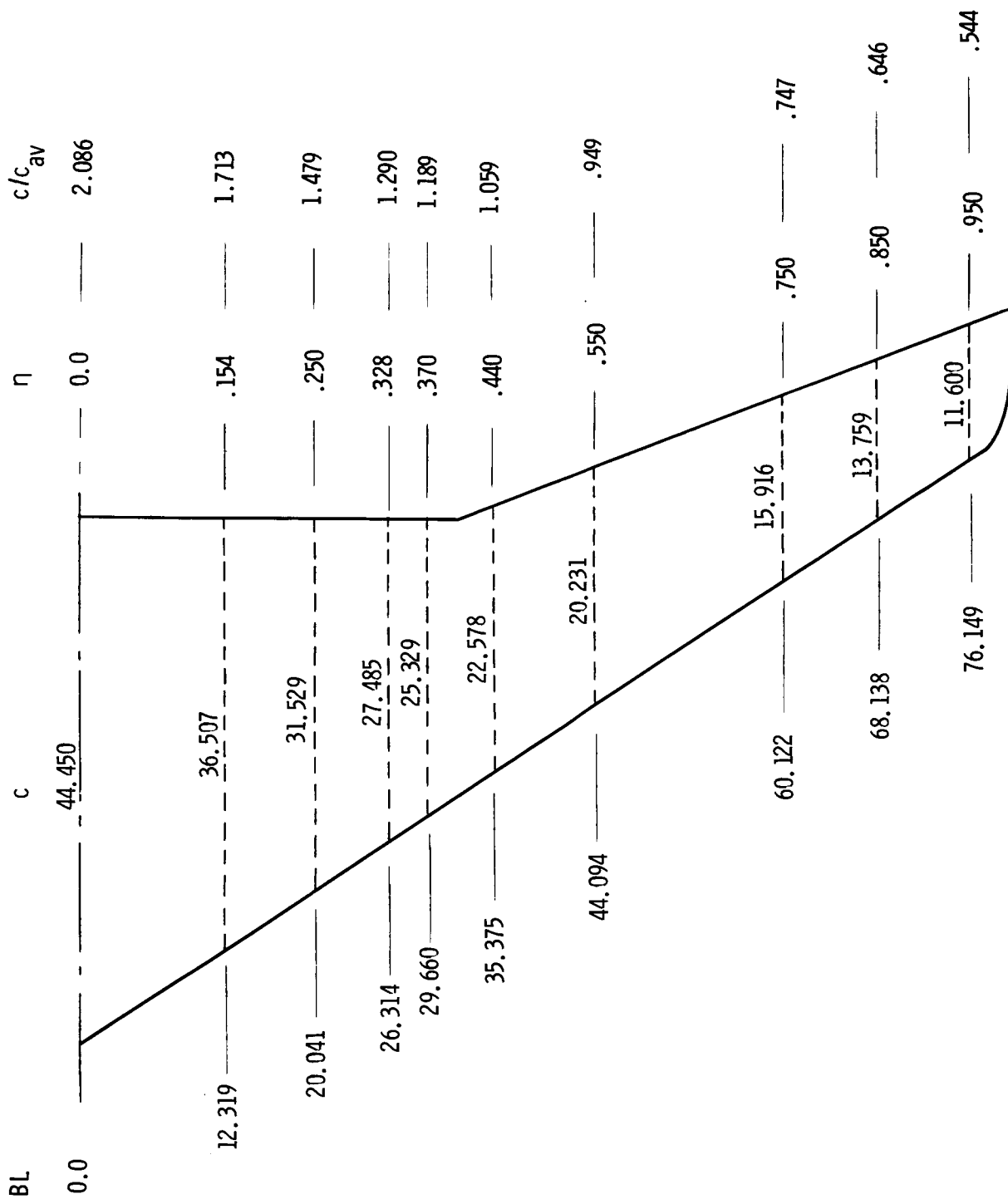


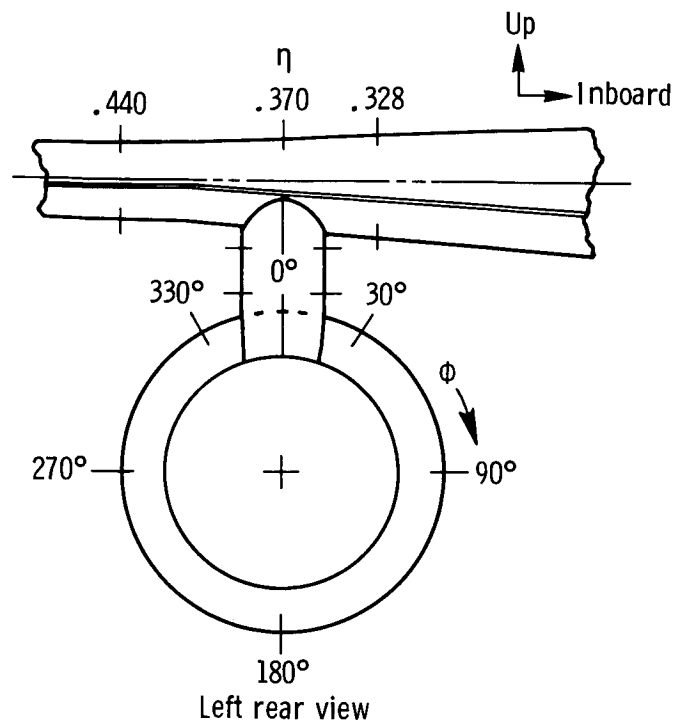
Figure 12.- Pylon-nacelle installation on wing. All linear dimensions are in centimeters.



(a) Spanwise locations of wing pressure orifice rows.

Figure 13.- Surface static-pressure orifice locations on wing and nacelle. All linear dimensions are in centimeters.

Nacelle orifice locations				
NS, cm	$\Phi$ , deg			
	0	30/330	90/270	180
0.51	*		*	*
1.78	*		*	*
3.05	*			
3.81		*	*	*
5.84		*	*	*
7.87		*	*	*
11.43				*
11.68		*	*	
13.72		*	*	
14.99				*
15.75		*	*	
18.03		*	*	*
20.57		*	*	*
22.61		*		
23.62			*	*
24.64		*		
26.92		*		
27.18			*	*
29.21		*		
30.73			*	*
31.50		*		
33.78		*		
34.29			*	*
36.07		*		
37.59			*	*
38.10		*		
39.37		*	*	*



(b) Nacelle pressure orifice locations with adjacent pylon and wing instrumentation shown for reference.

Figure 13.- Concluded.

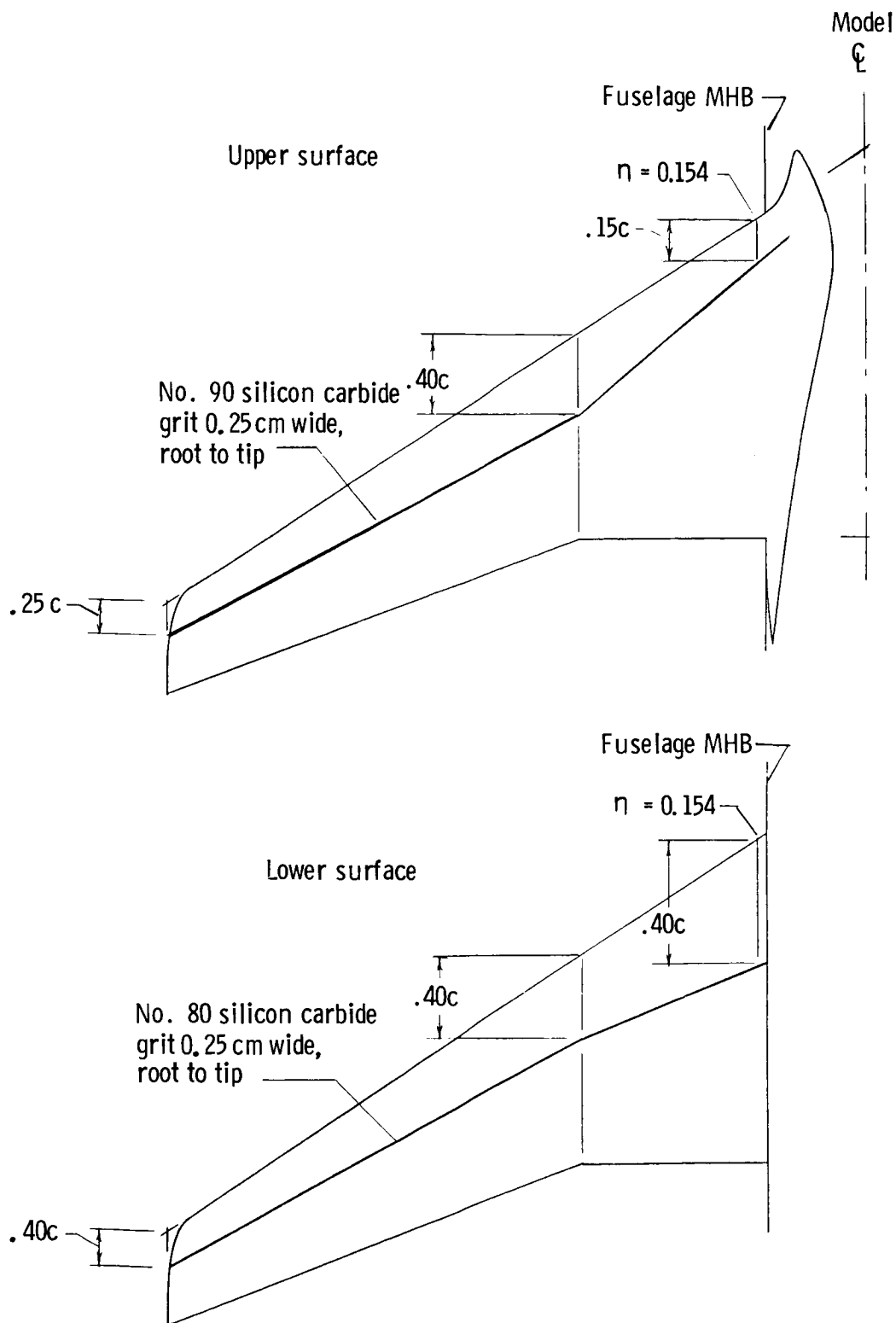


Figure 14.- Locations of boundary-layer transition strips on wing.

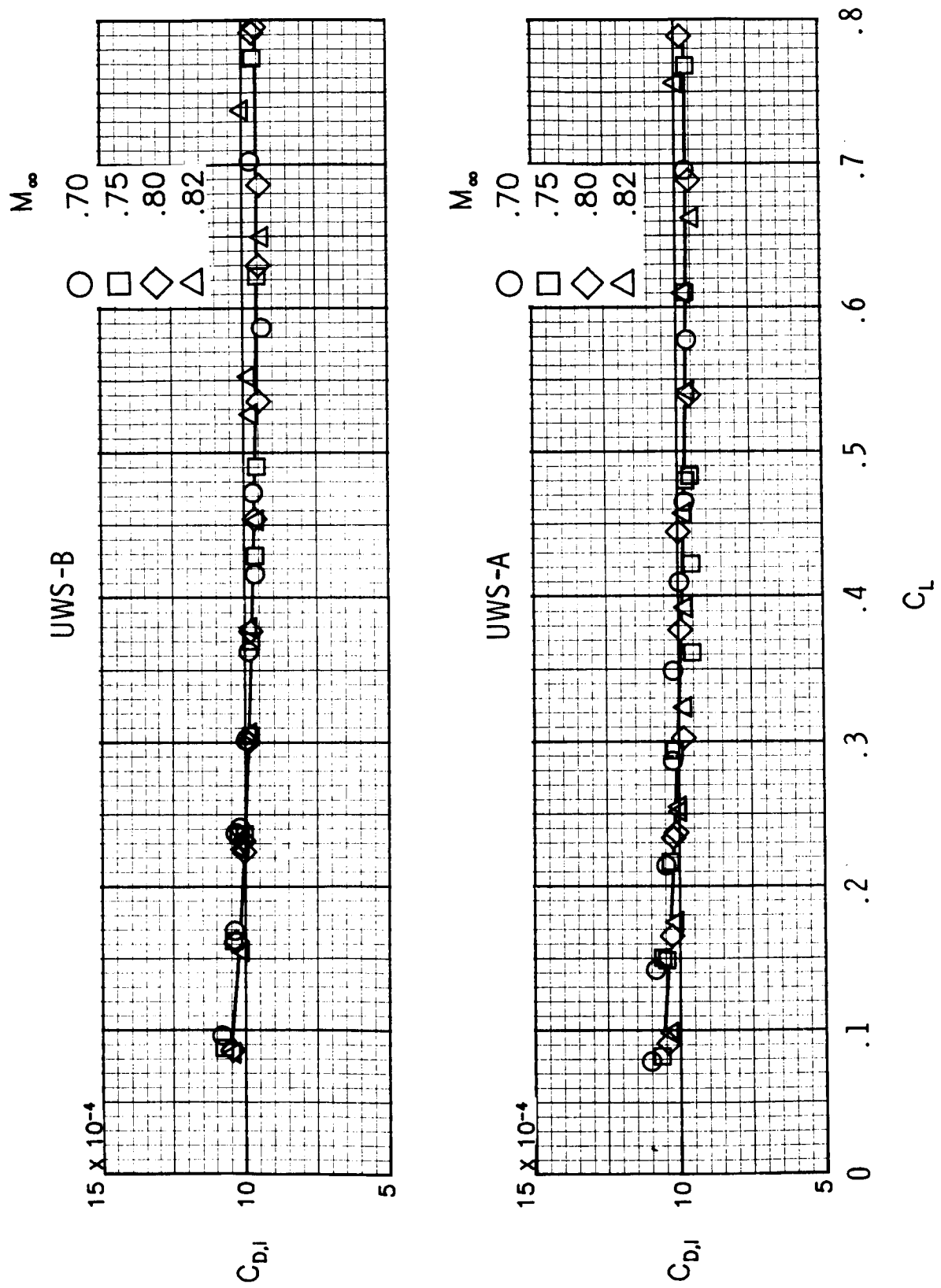
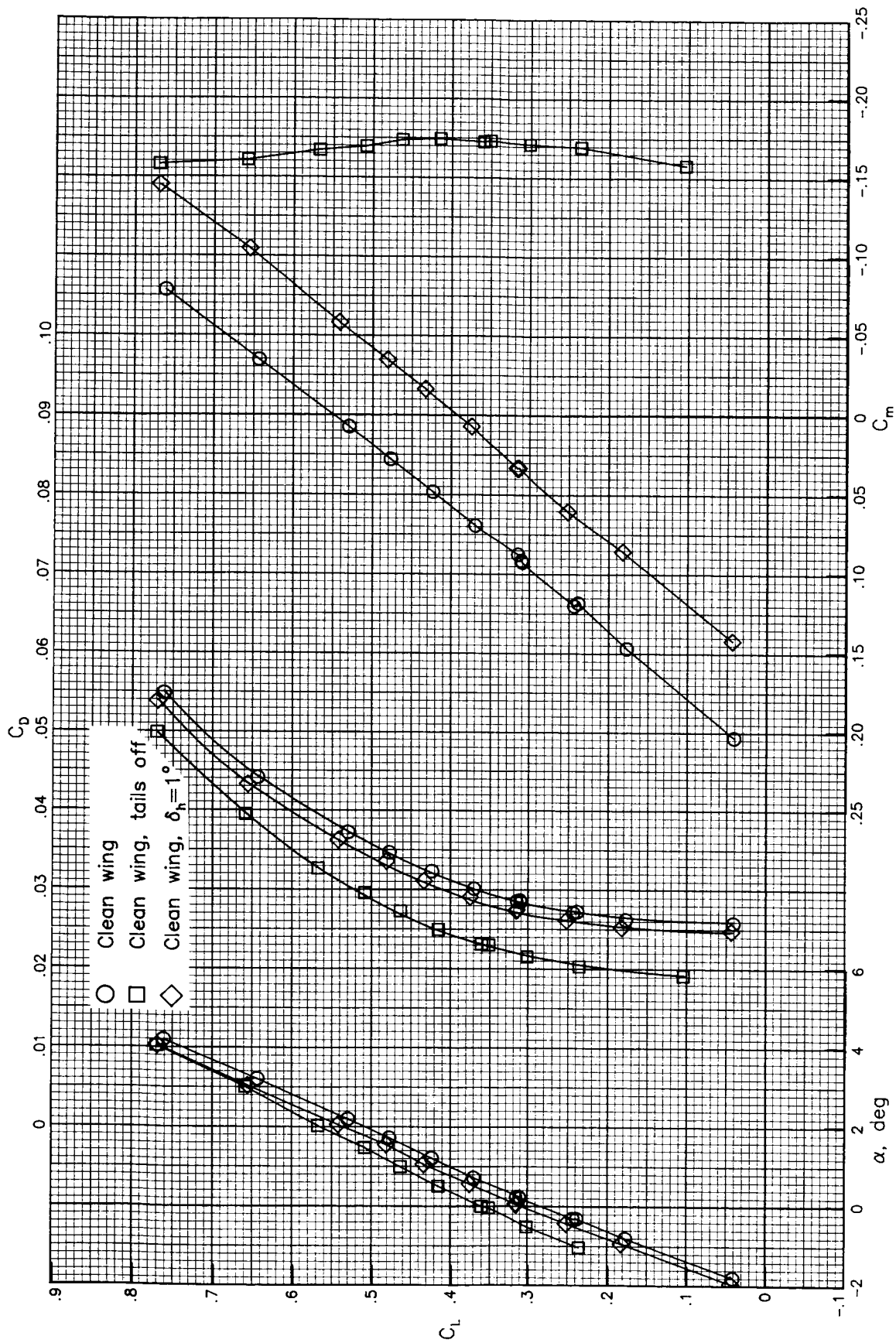


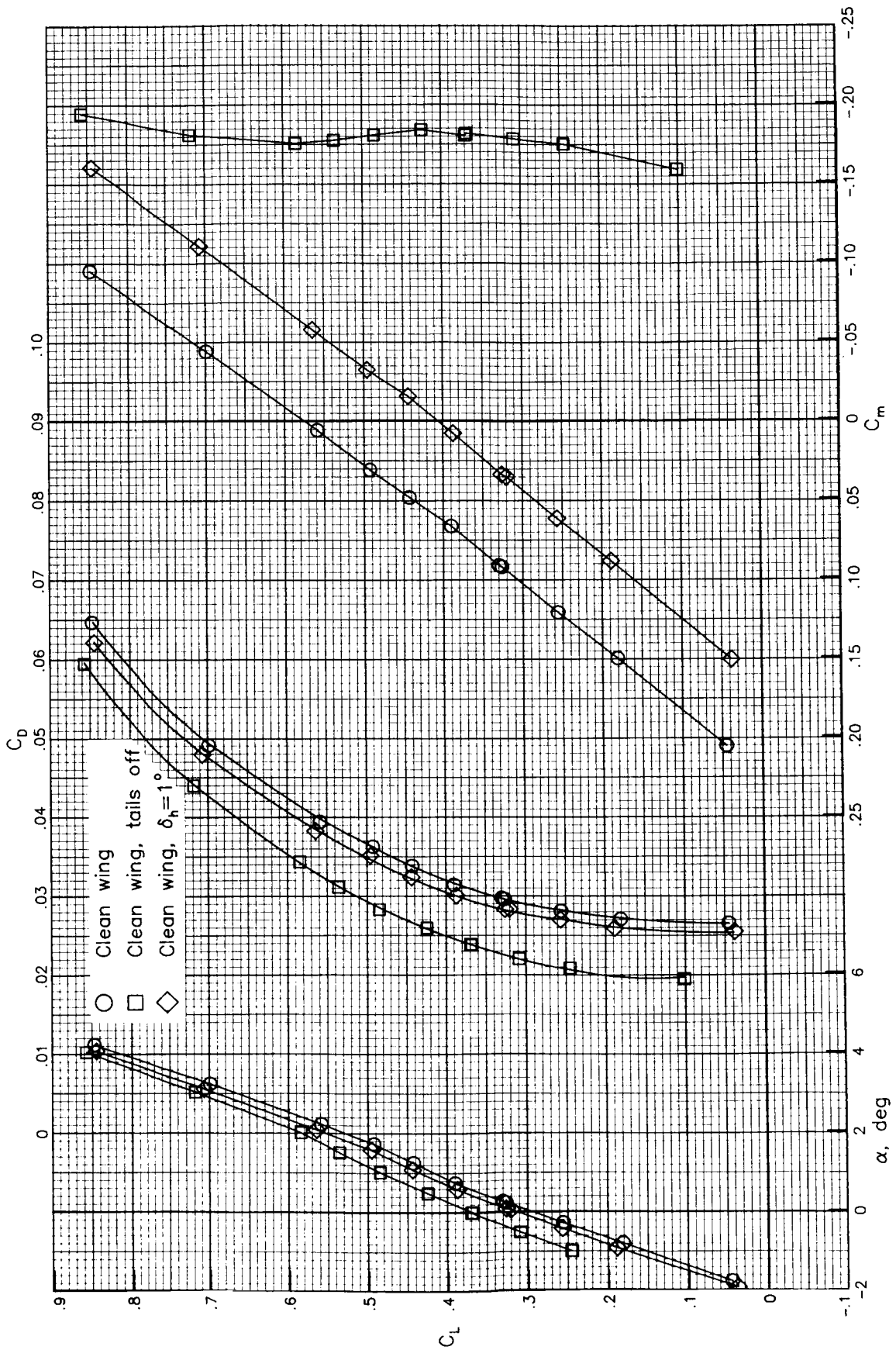
Figure 15.- Variation of total internal drag coefficient with lift coefficient and Mach number for two nacelles.



(a)  $M_\infty = 0.70$ .

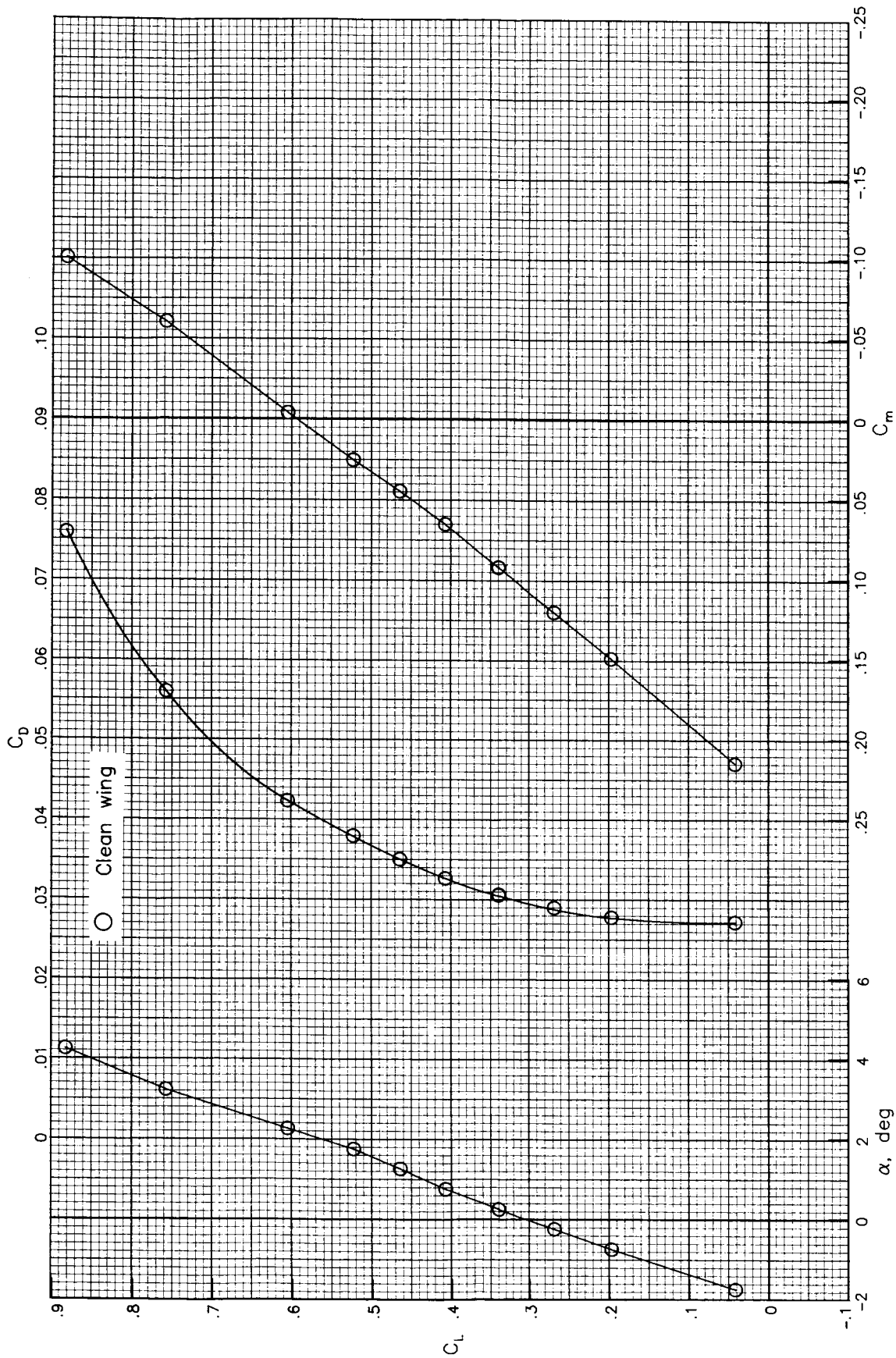
Figure 16.- Aerodynamic force data for transport model with clean wing.





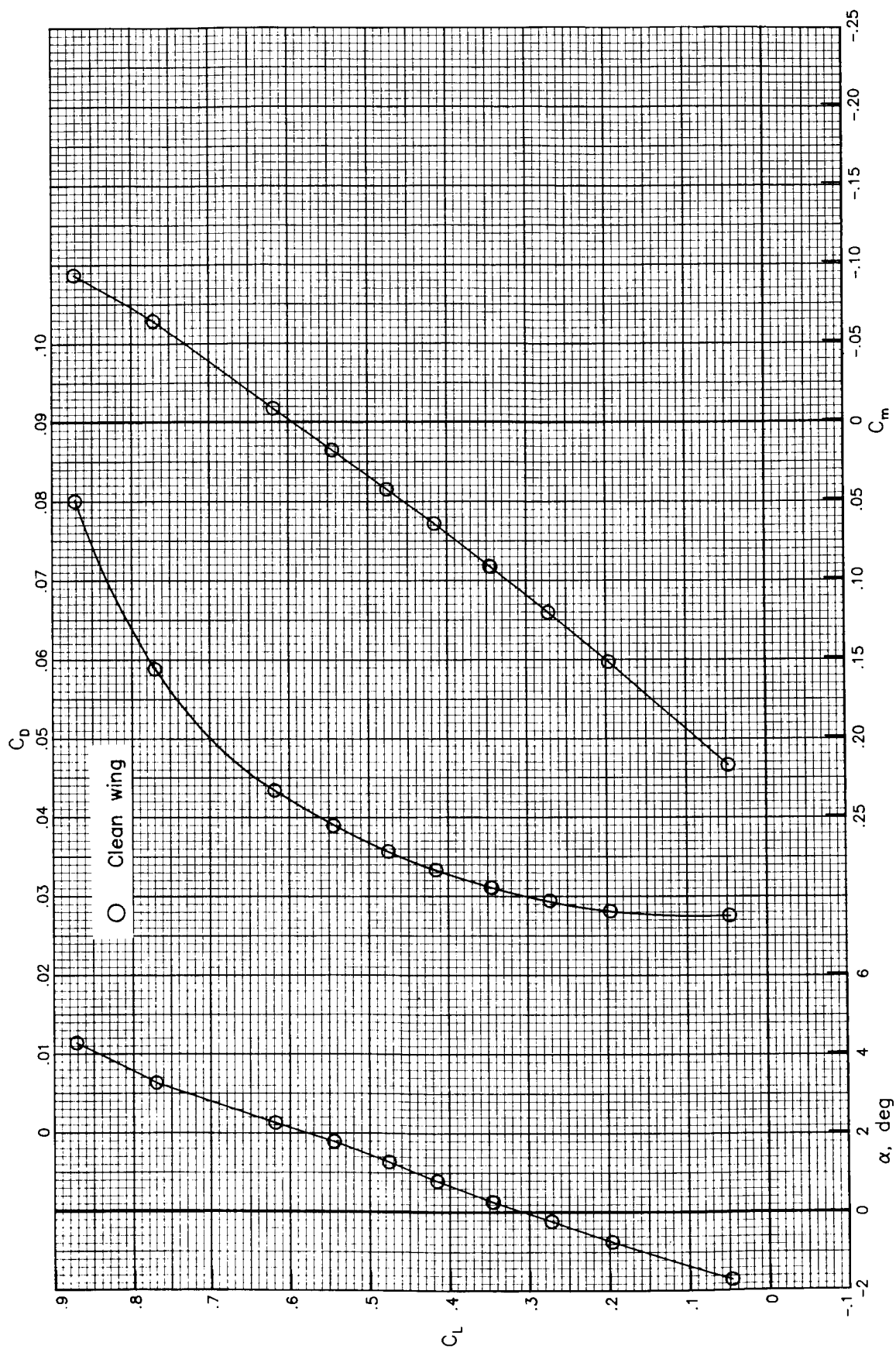
(b)  $M_\infty = 0.75$ .

Figure 16.- Continued.



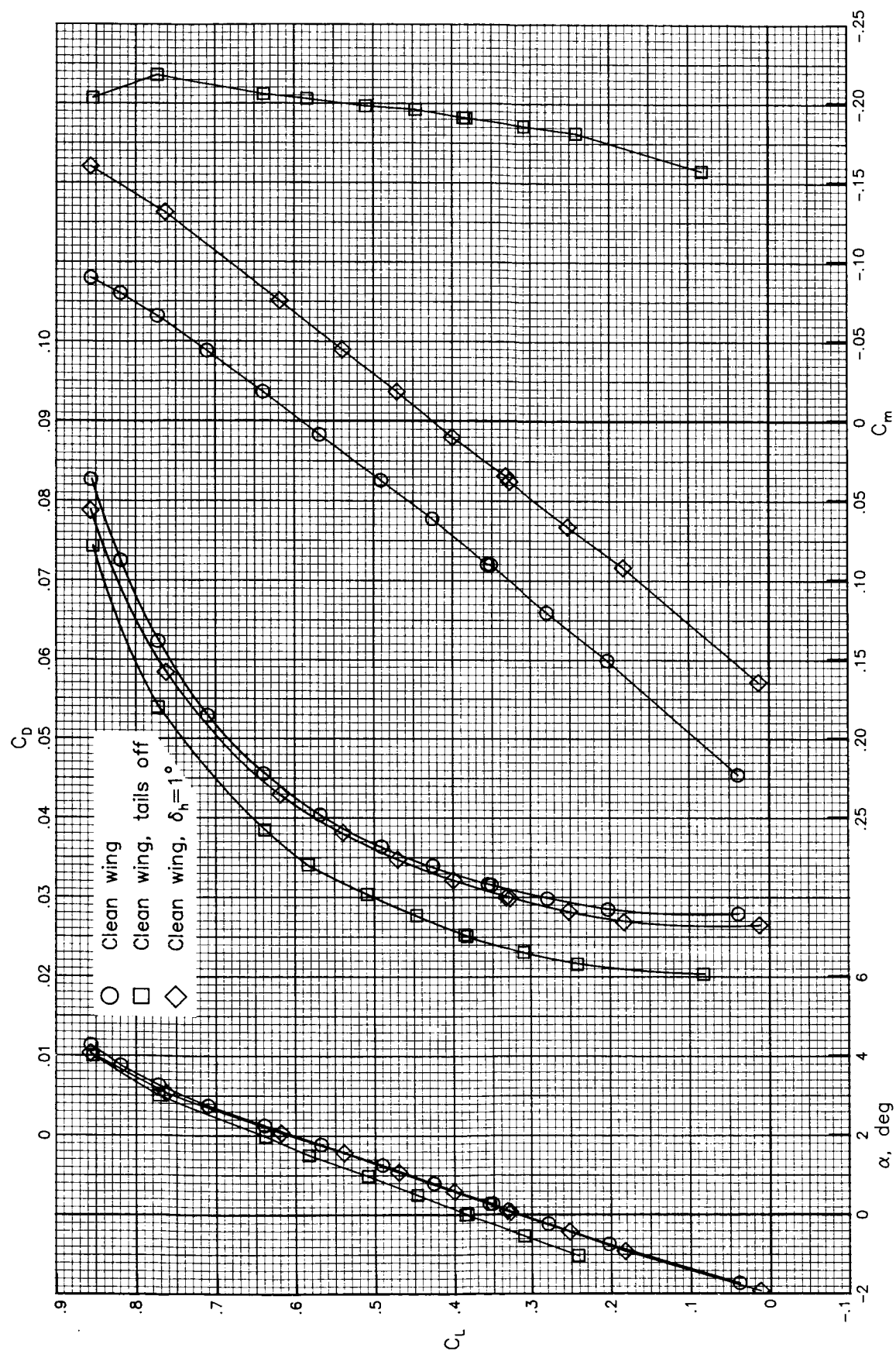
(c)  $M_{\infty} = 0.78$ .

Figure 16.- Continued.



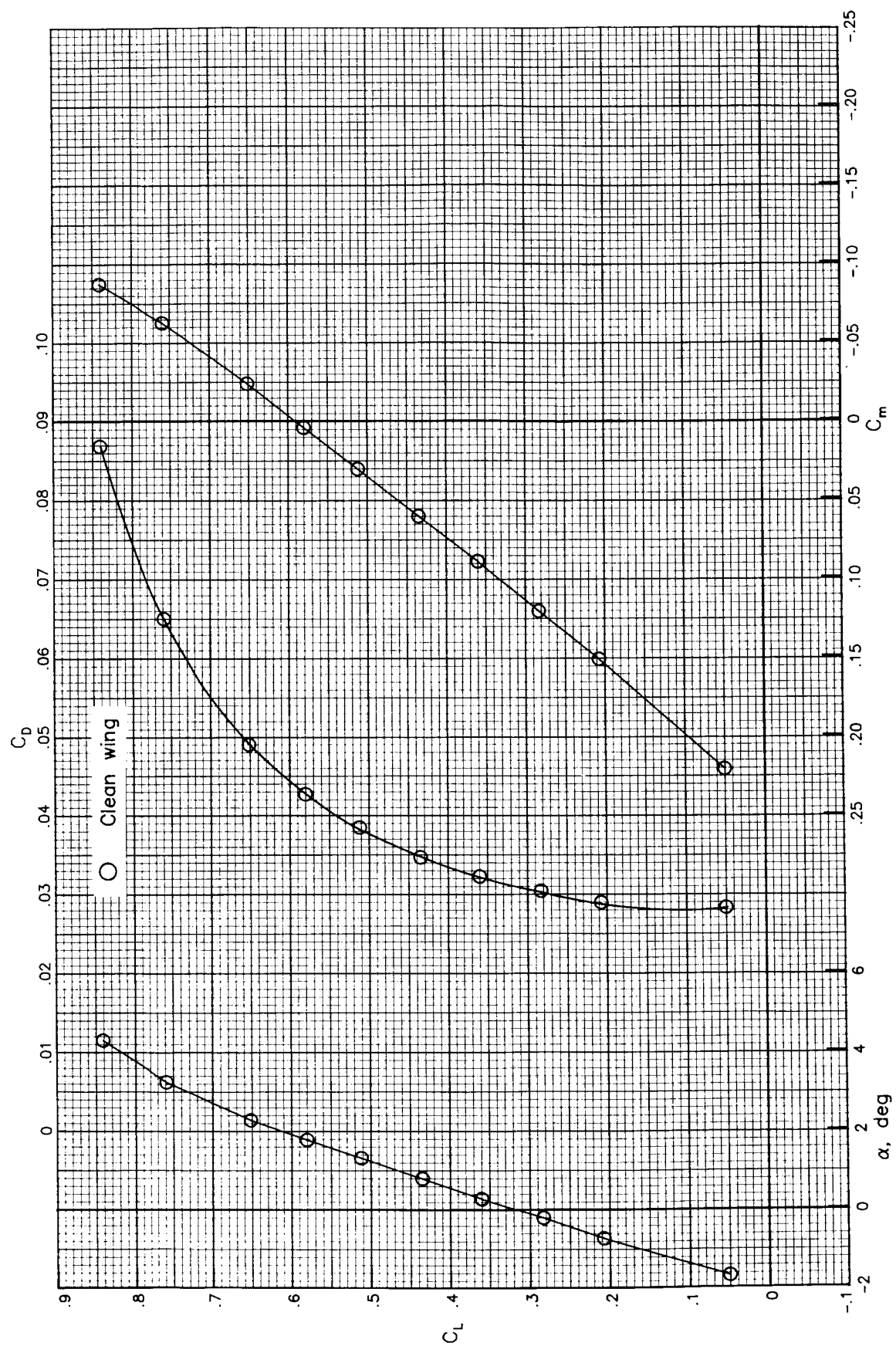
(d)  $M_\infty = 0.79$ .

Figure 16.- Continued.



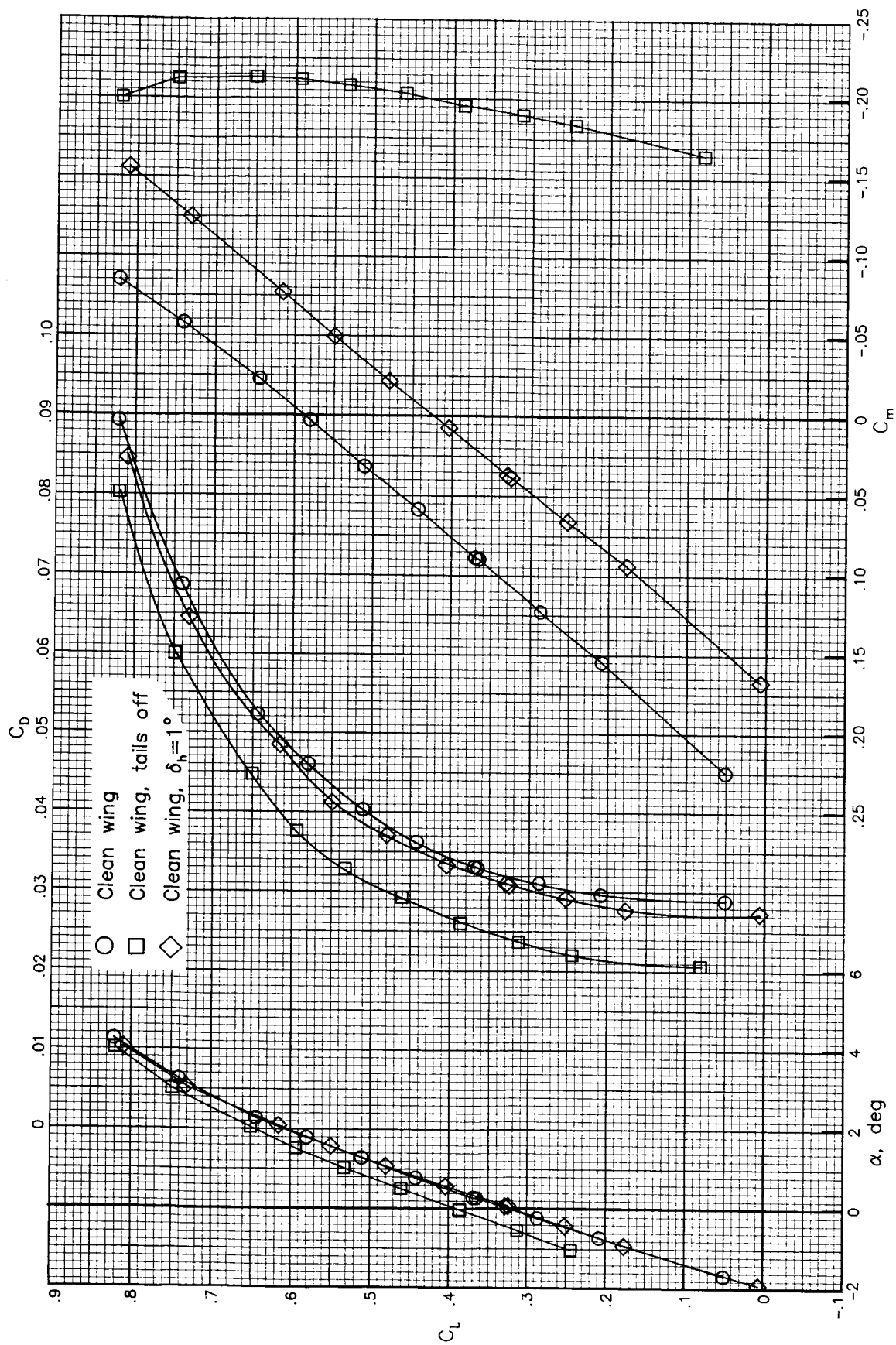
(e)  $M_\infty = 0.80$ .

Figure 16.- Continued.



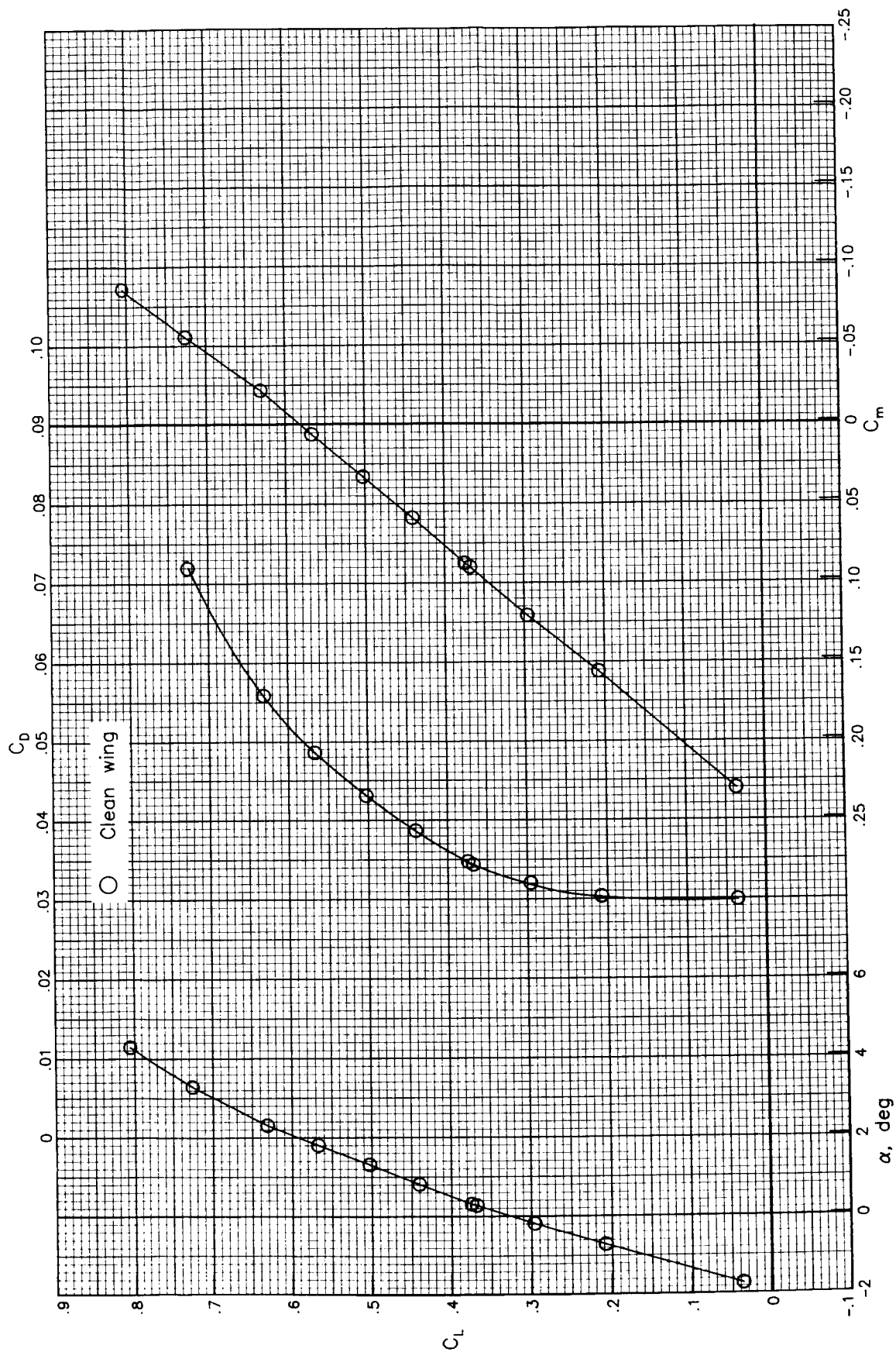
(f)  $M_\infty = 0.81$ .

Figure 16.- Continued.



(g)  $M_\infty = 0.82$ .

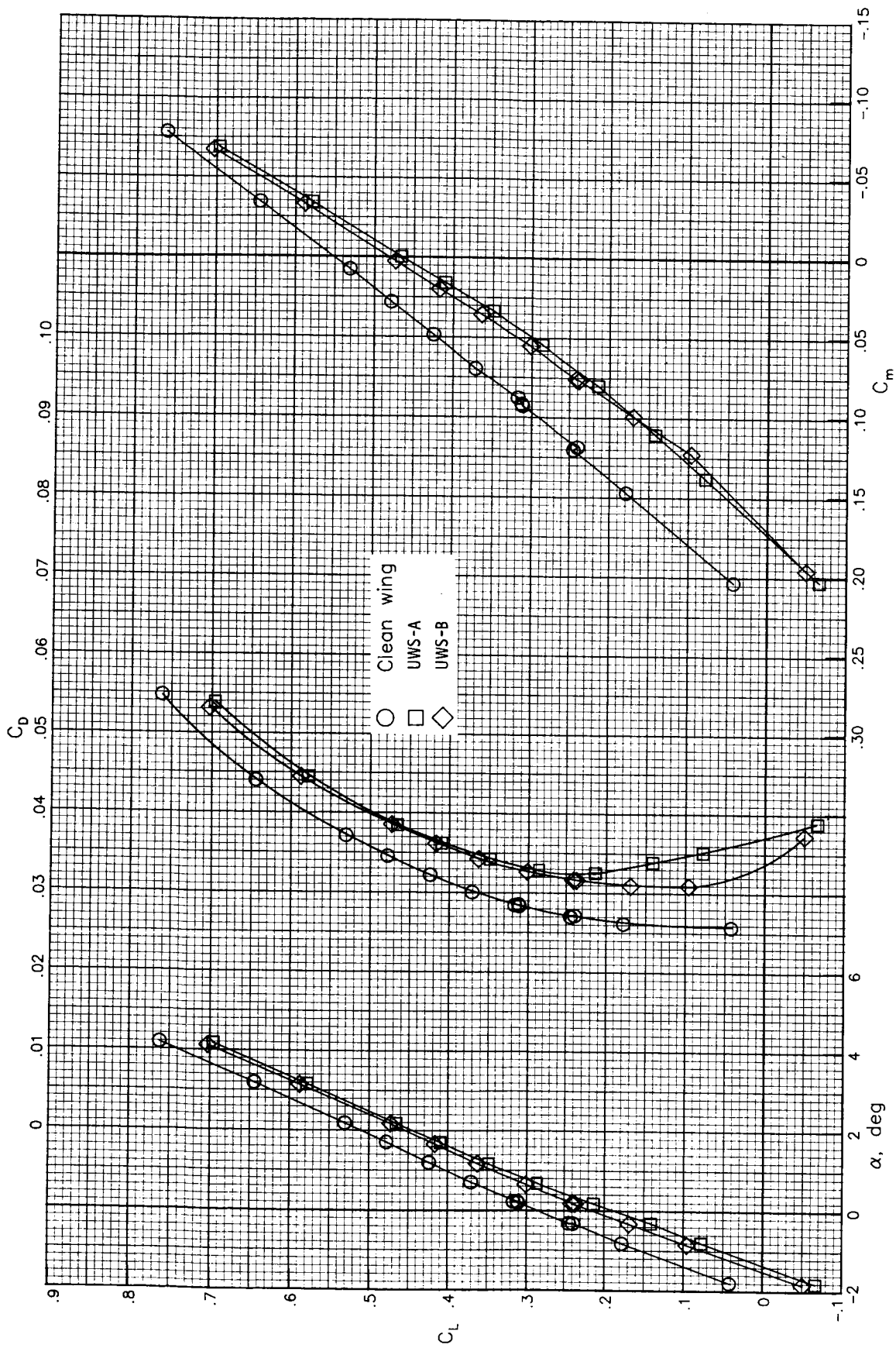
Figure 16.- Continued.



(h)  $M_\infty = 0.83$ .

Figure 16.- Concluded.

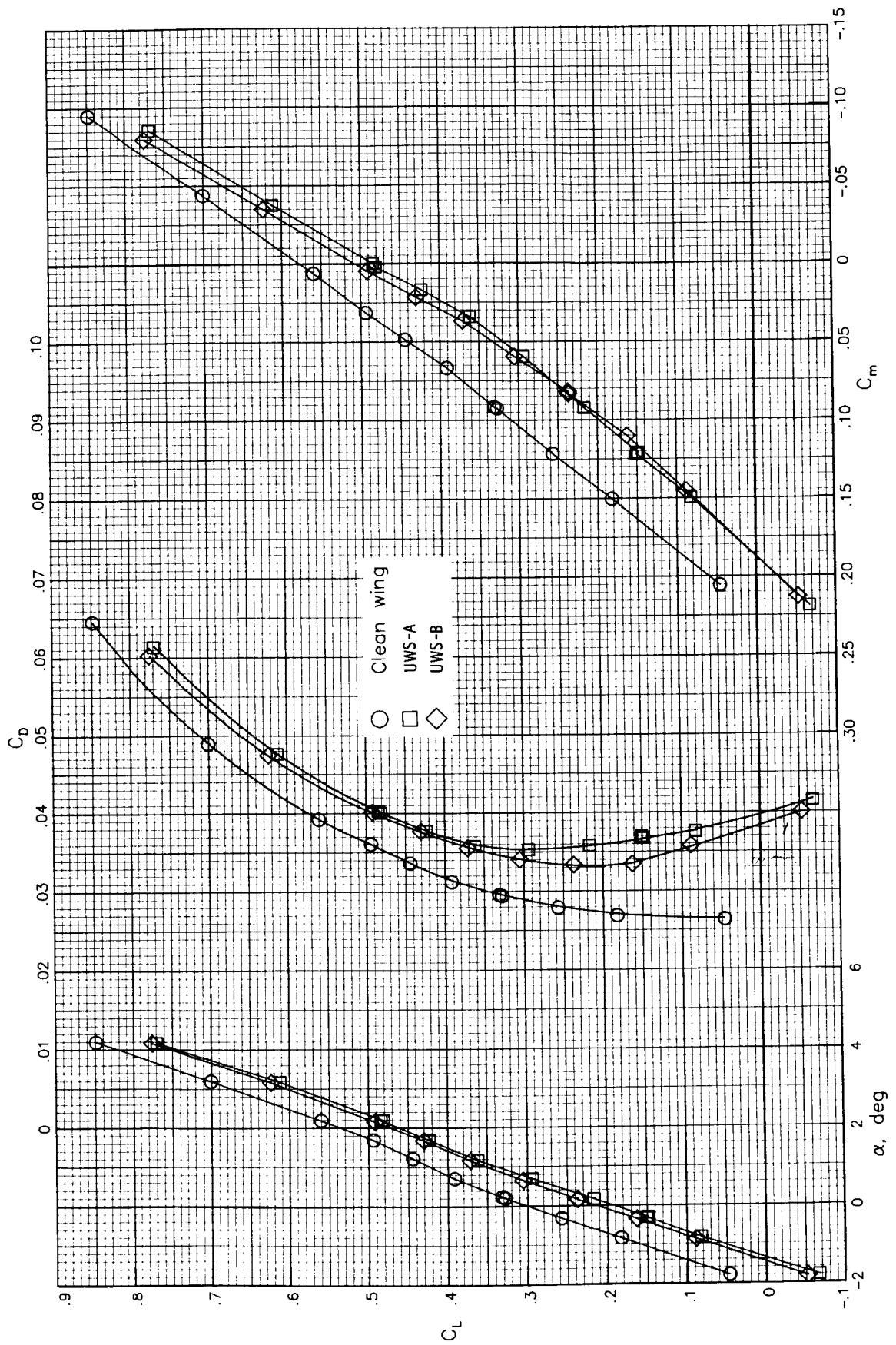




(a)  $M_\infty = 0.70$ .

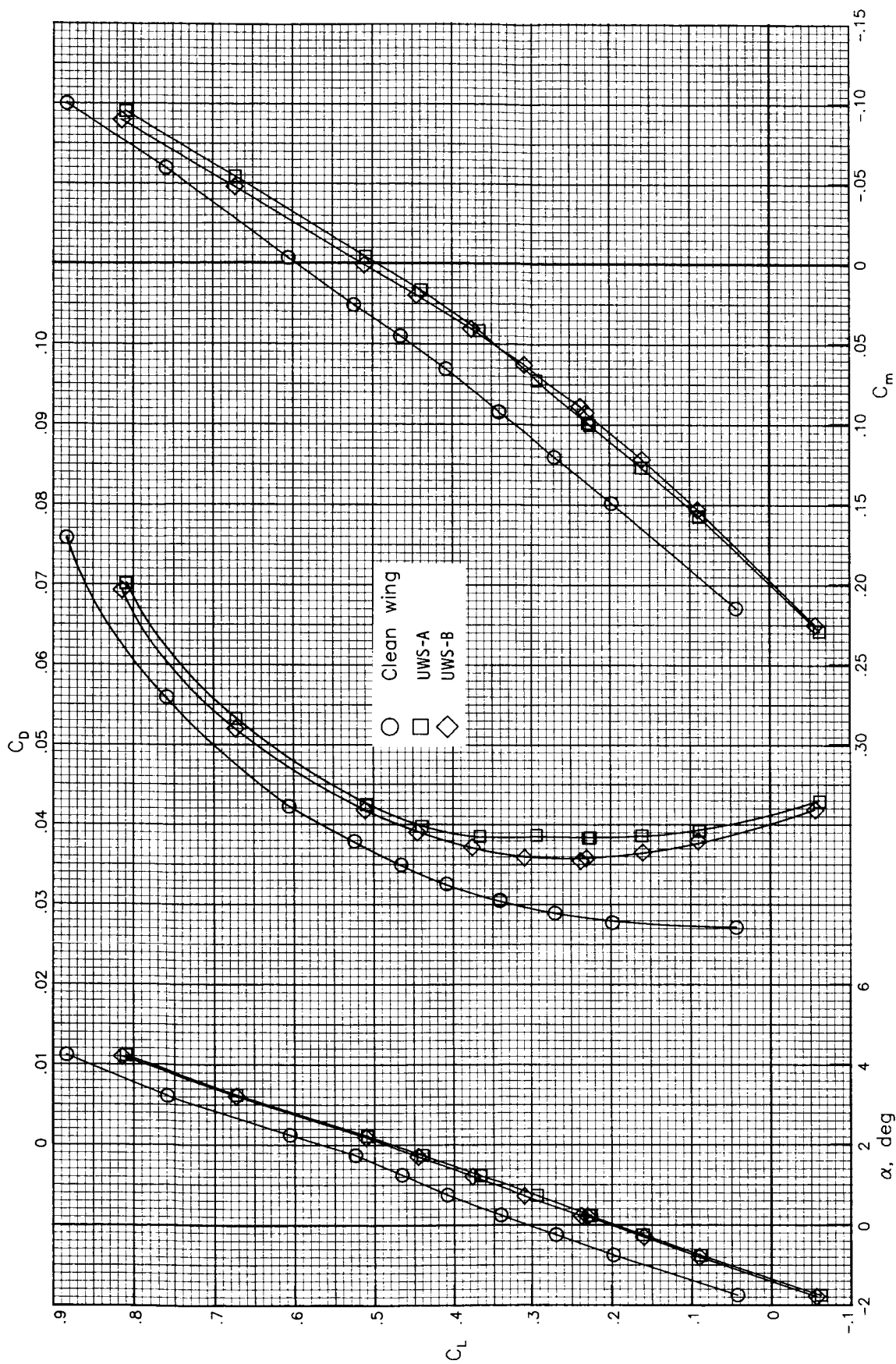
Figure 17.- Comparison of aerodynamic force data for the transport model with pylon-mounted nacelles, and the clean-wing configuration.





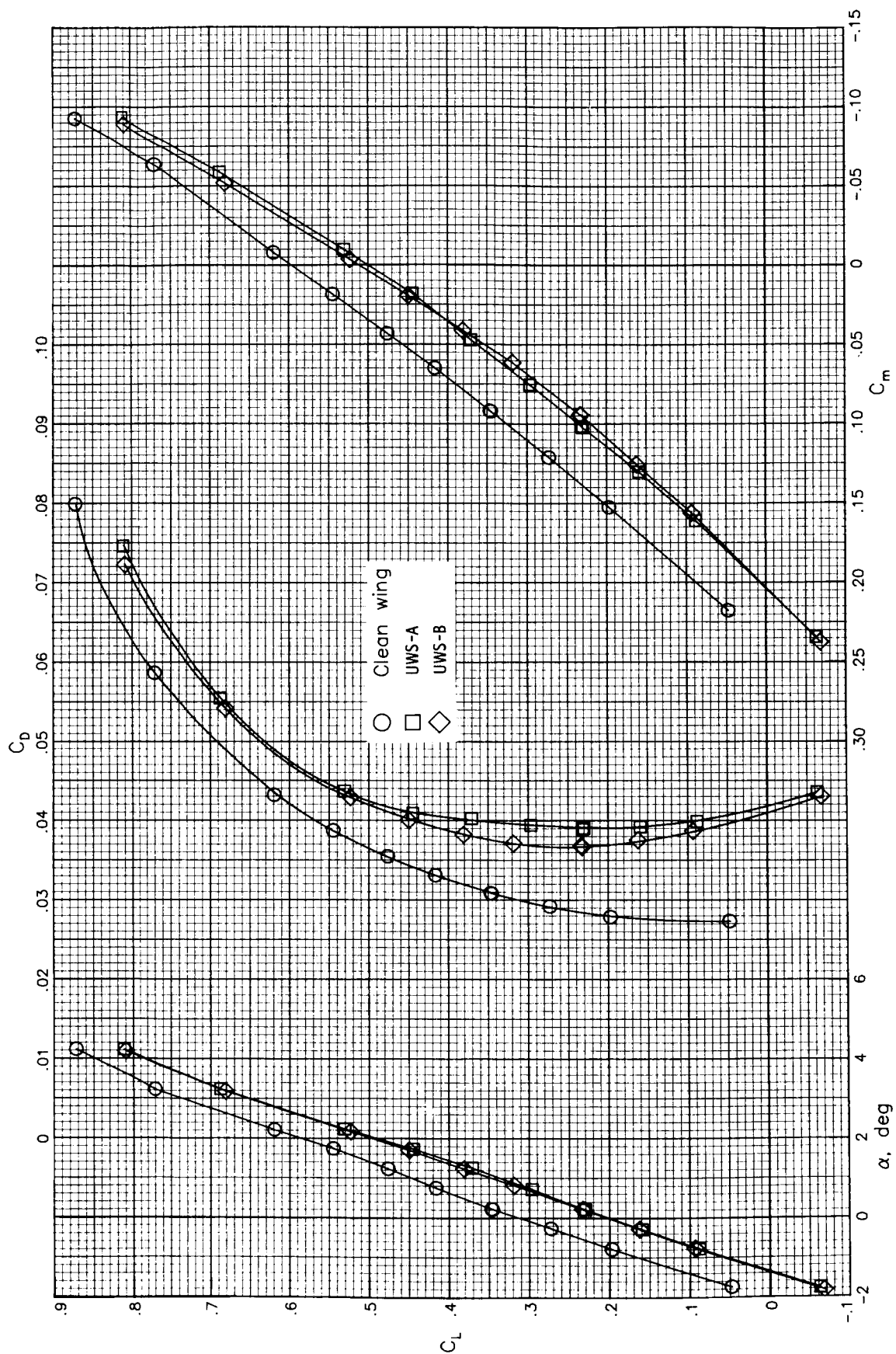
(b)  $M_\infty = 0.75$ .

Figure 17.- Continued.



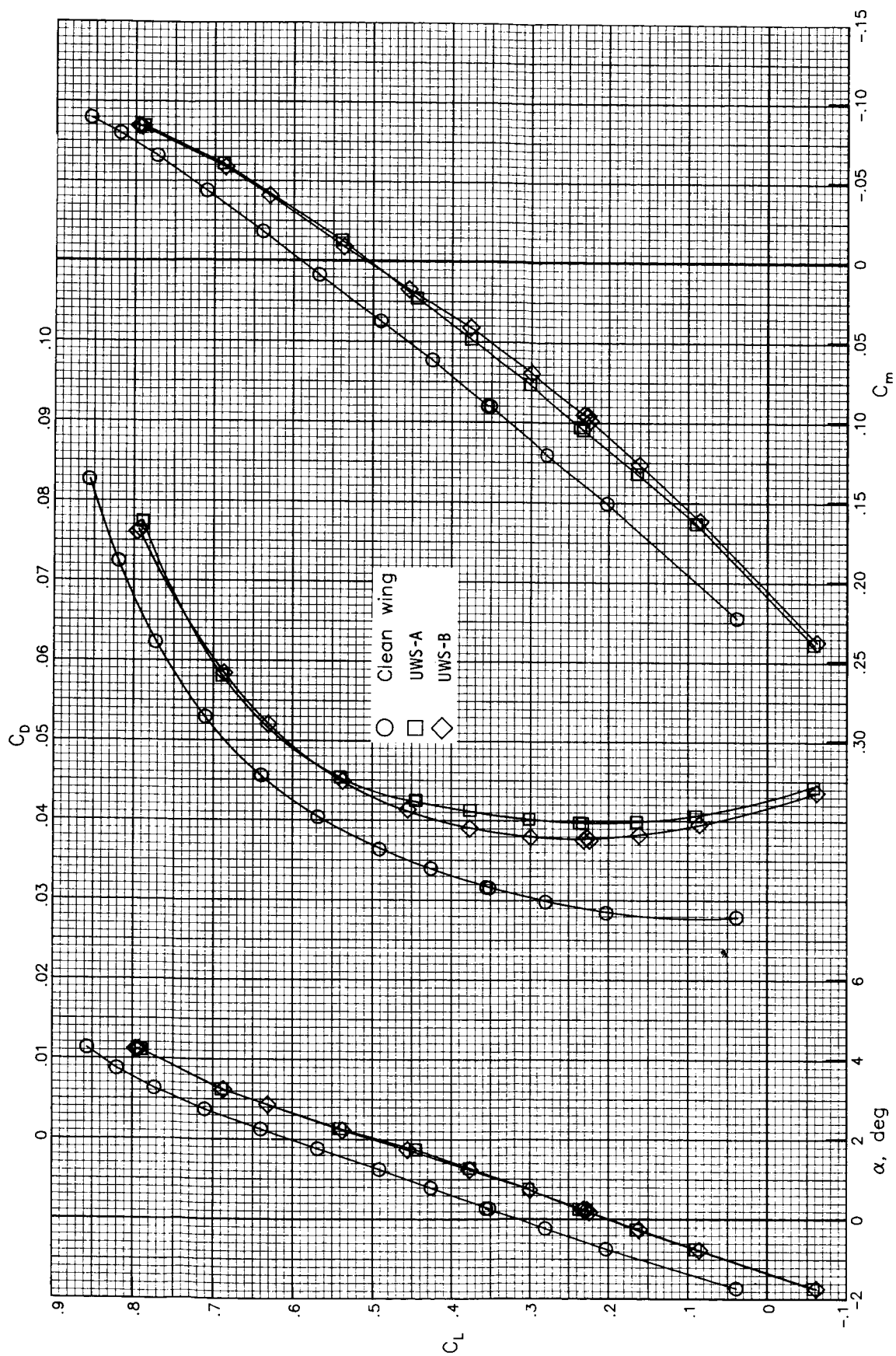
(c)  $M_\infty = 0.78$ .

Figure 17.- Continued.



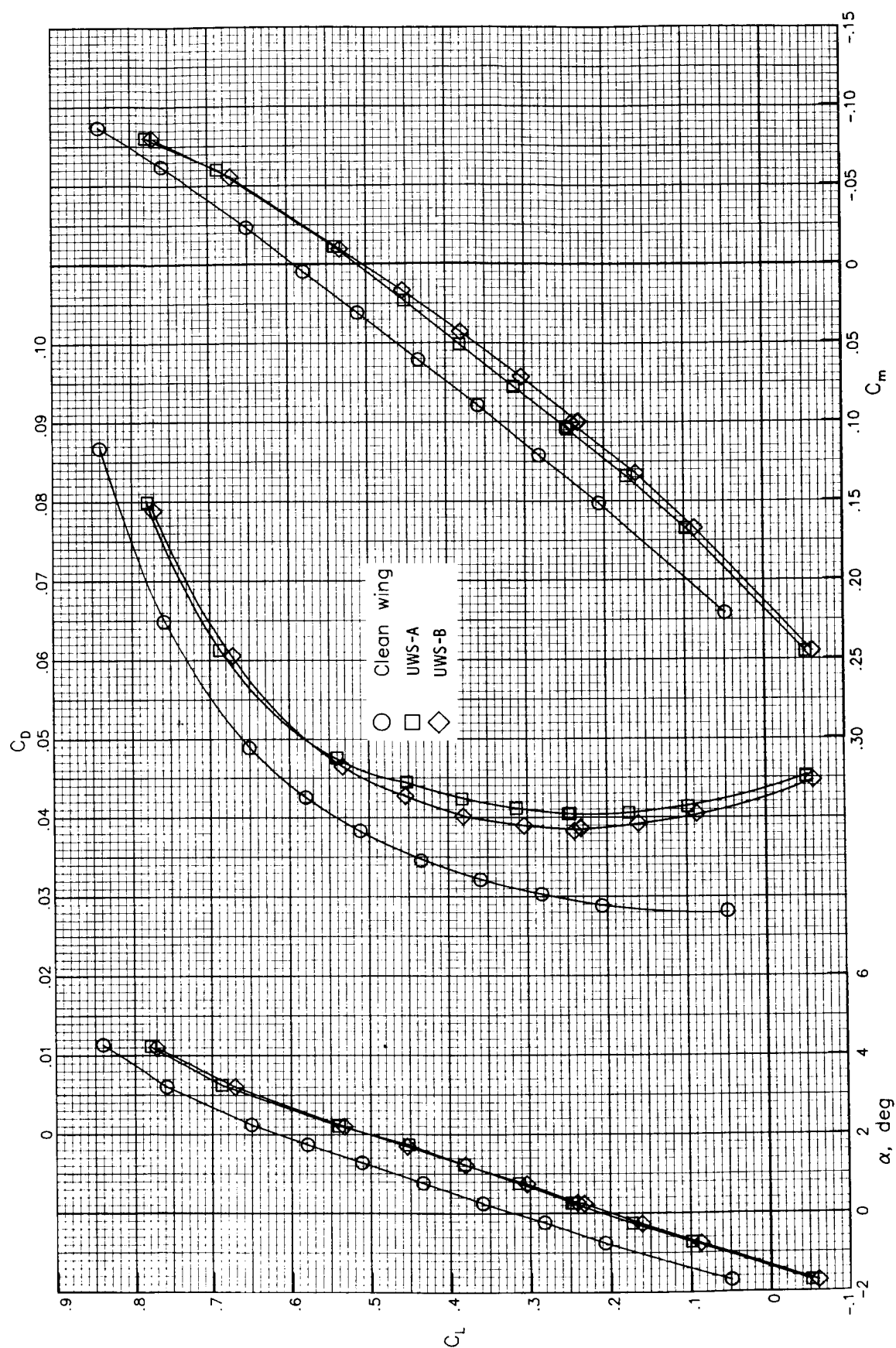
(d)  $M_\infty = 0.79$ .

Figure 17.- Continued.



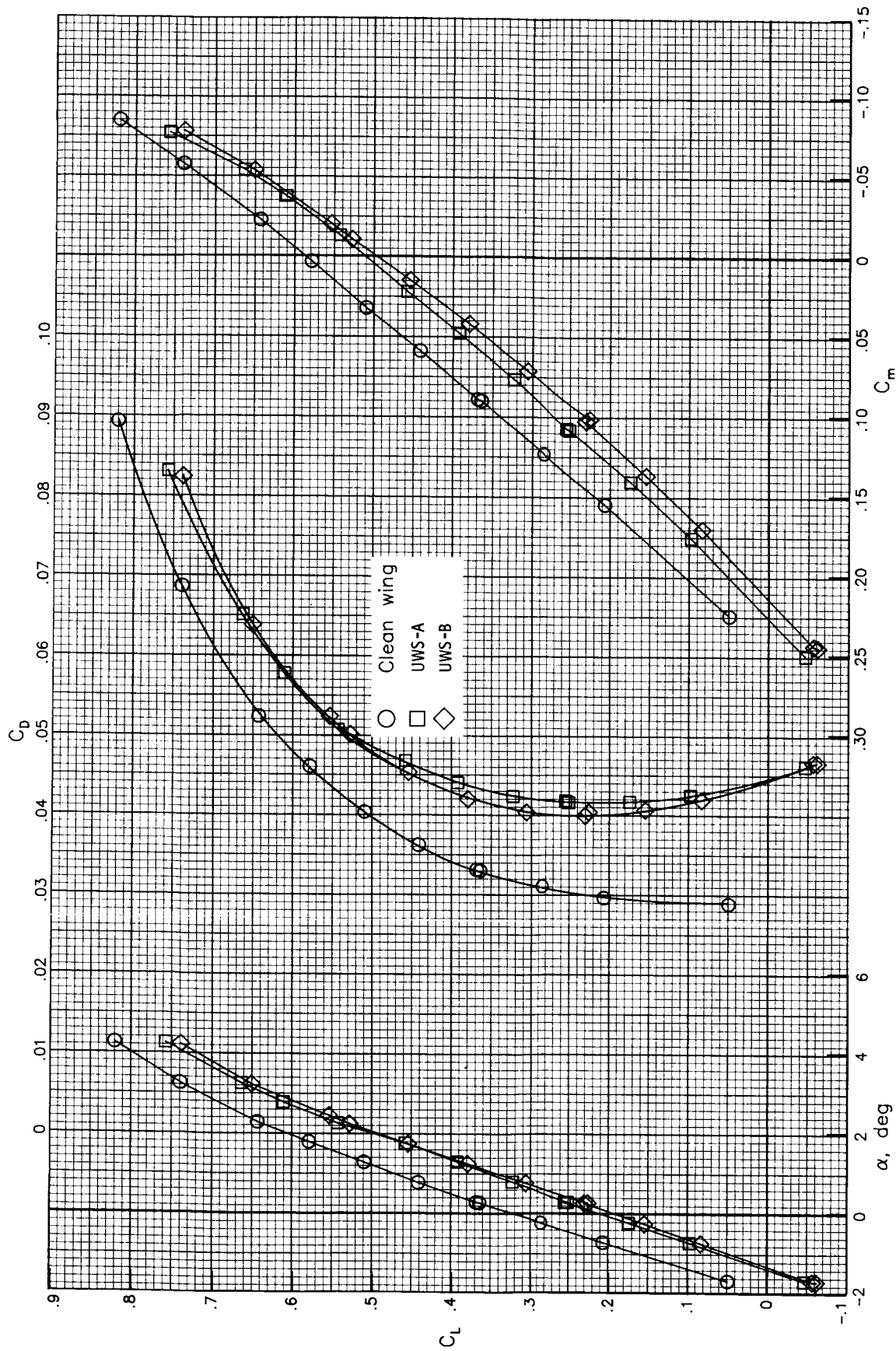
(e)  $M_\infty = 0.80$ .

Figure 17.- Continued.



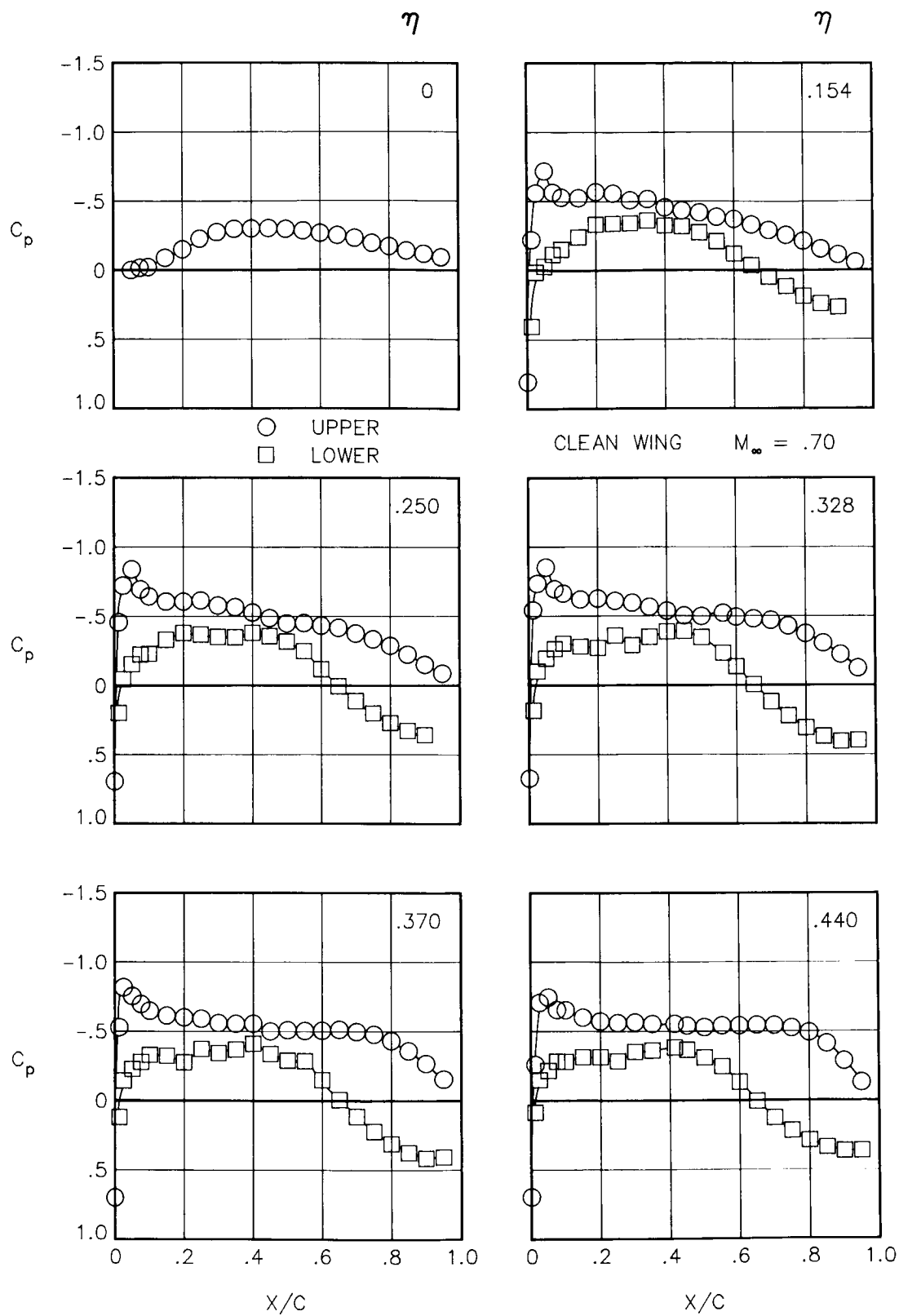
(f)  $M_\infty = 0.81$ .

Figure 17.- Continued.



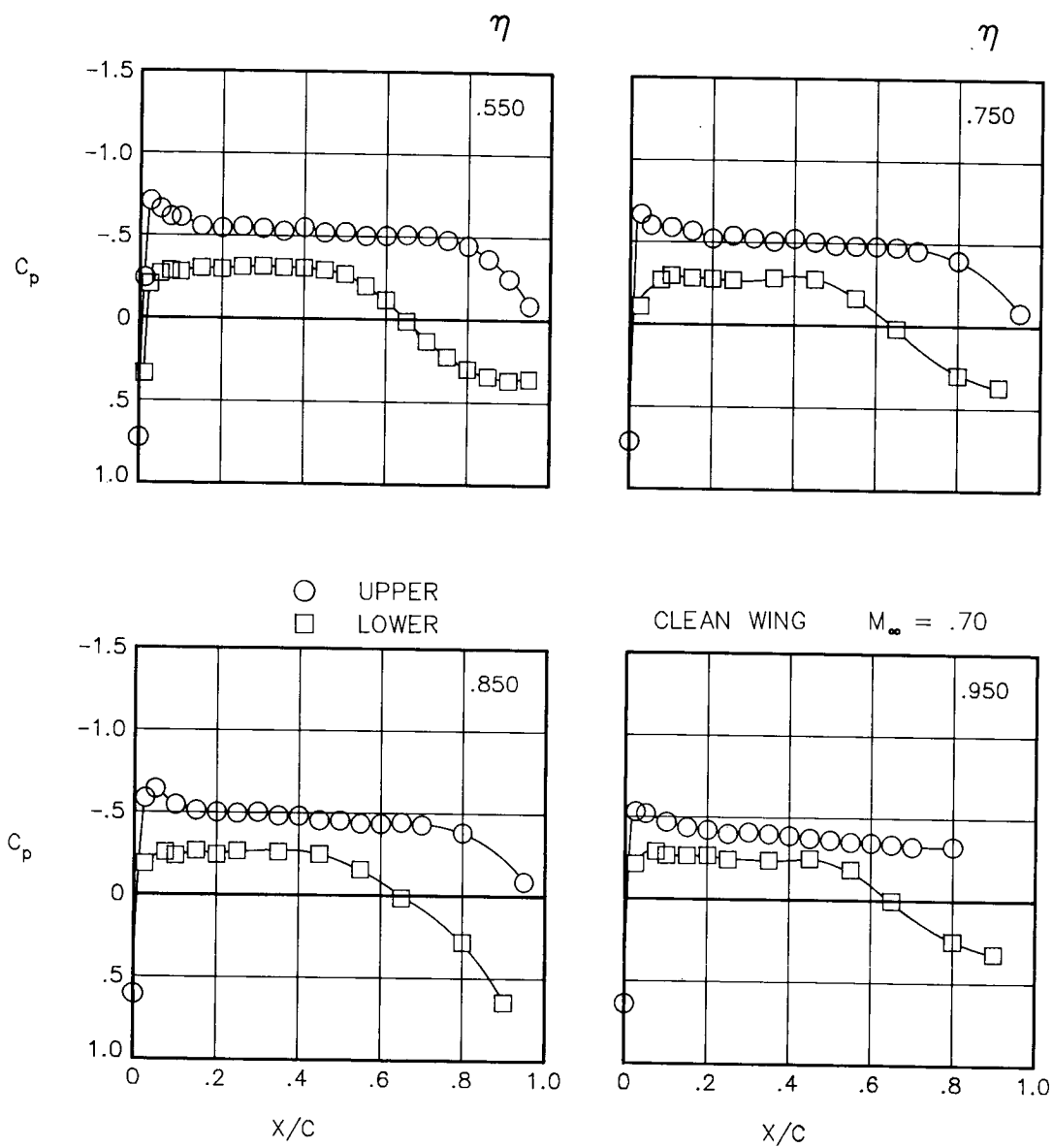
(g)  $M_\infty = 0.82$ .

Figure 17.- Concluded.



(a)  $\alpha = 0.19^\circ$ ;  $C_L = 0.31$ .

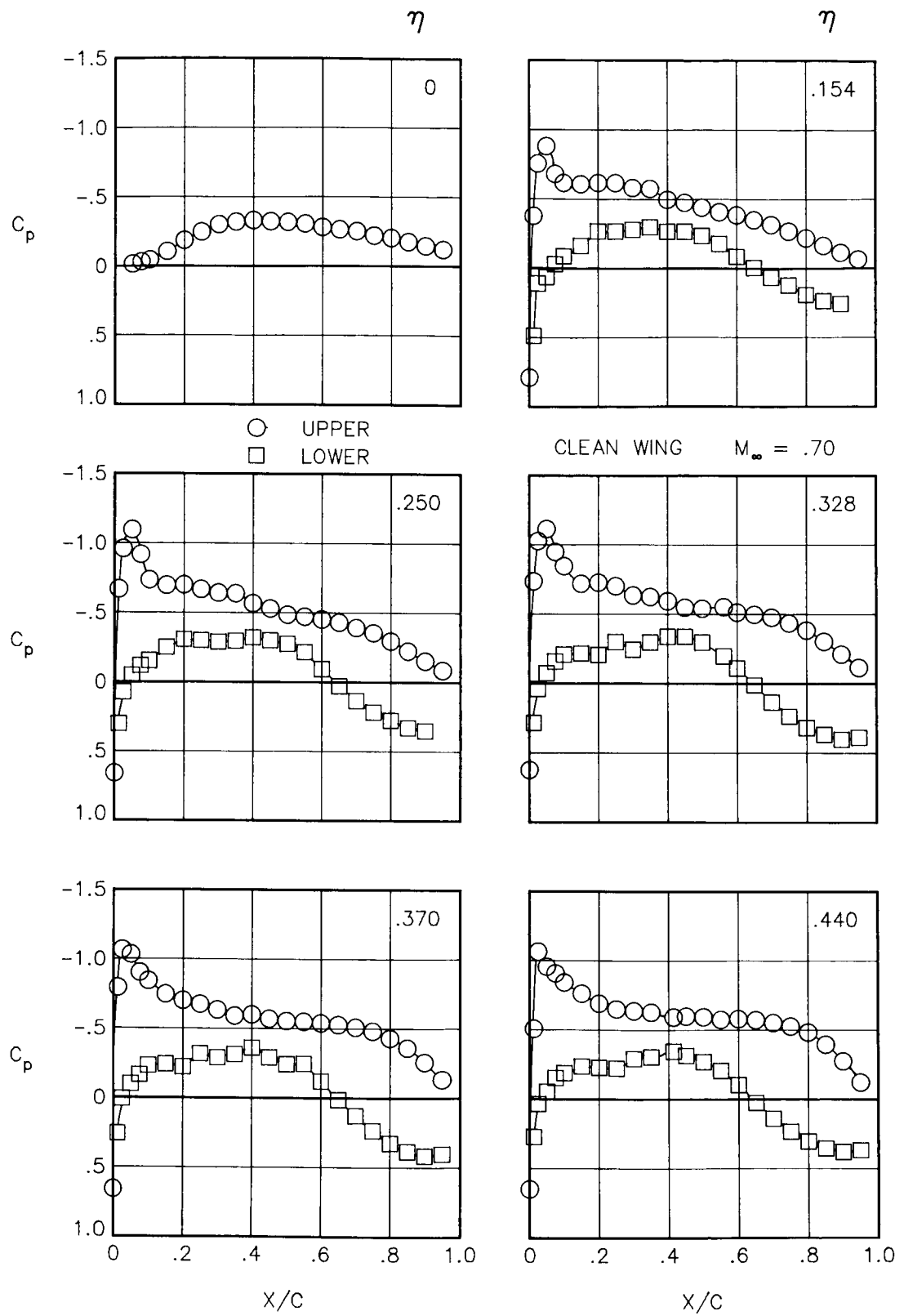
Figure 18.- Chordwise pressure coefficient distributions on clean-wing configuration at various angles of attack and  $M_\infty = 0.70$ .



(a) Concluded.

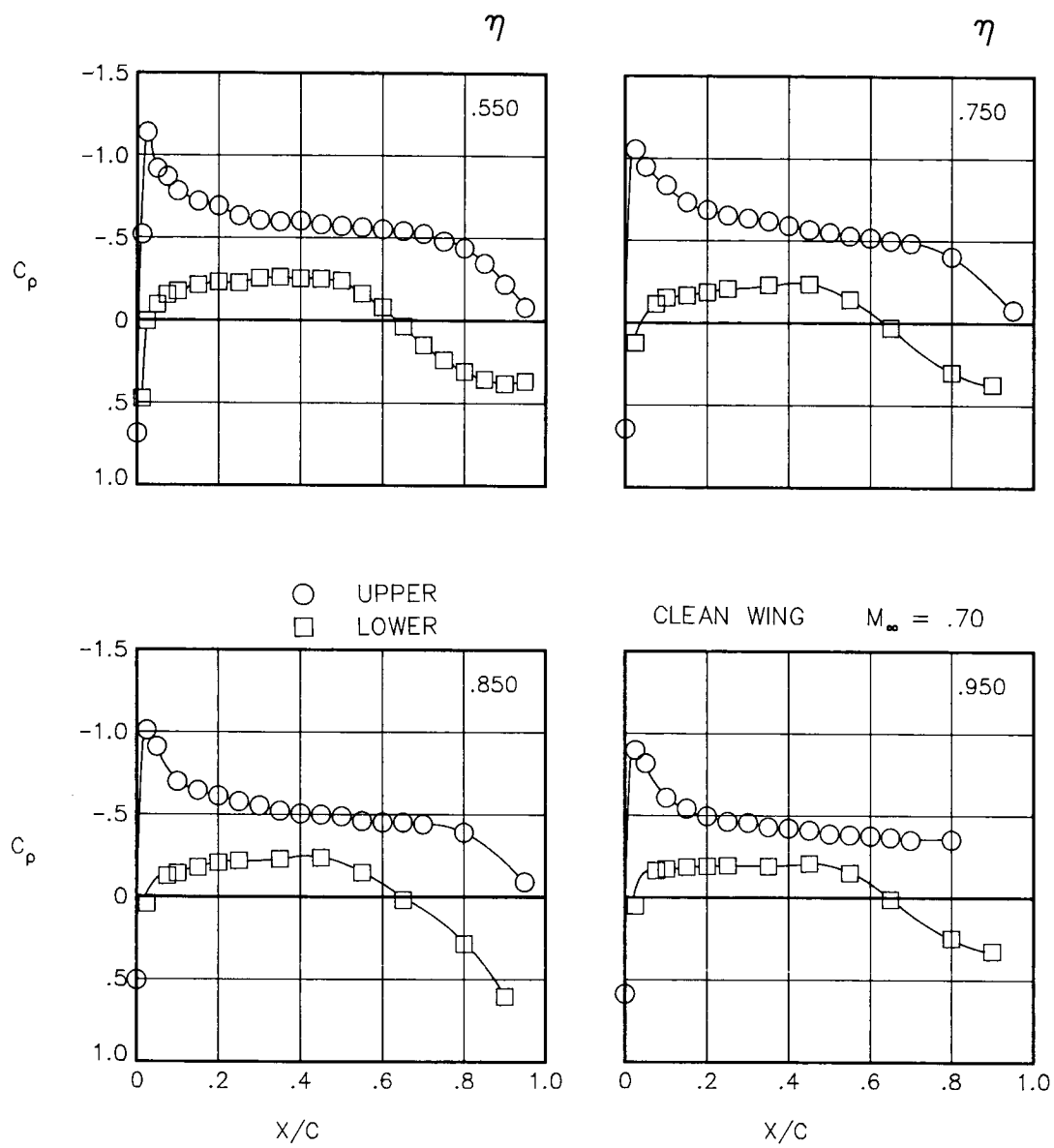
Figure 18.- Continued.





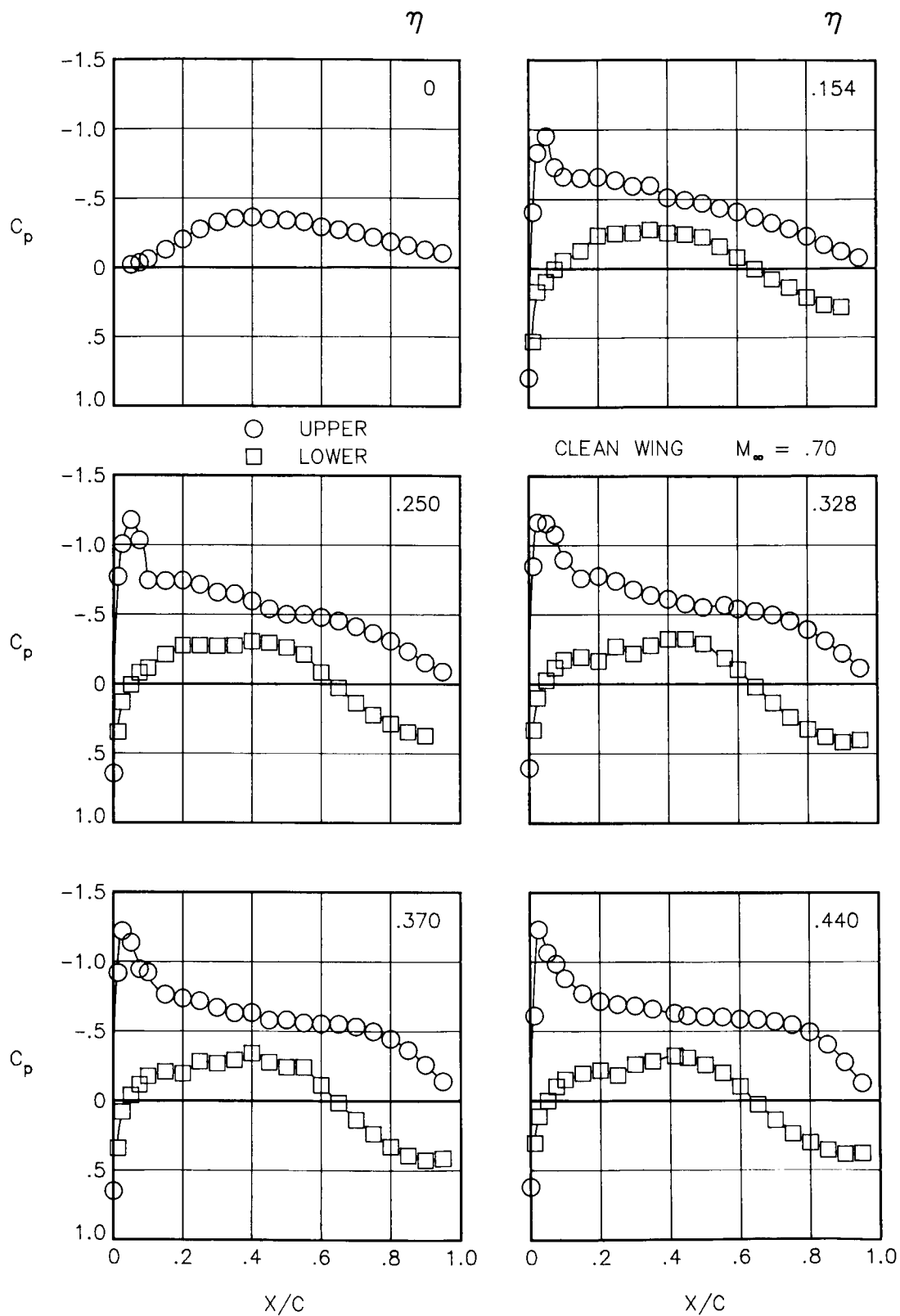
(b)  $\alpha = 1.20^\circ$ ;  $C_L = 0.43$ .

Figure 18.- Continued.



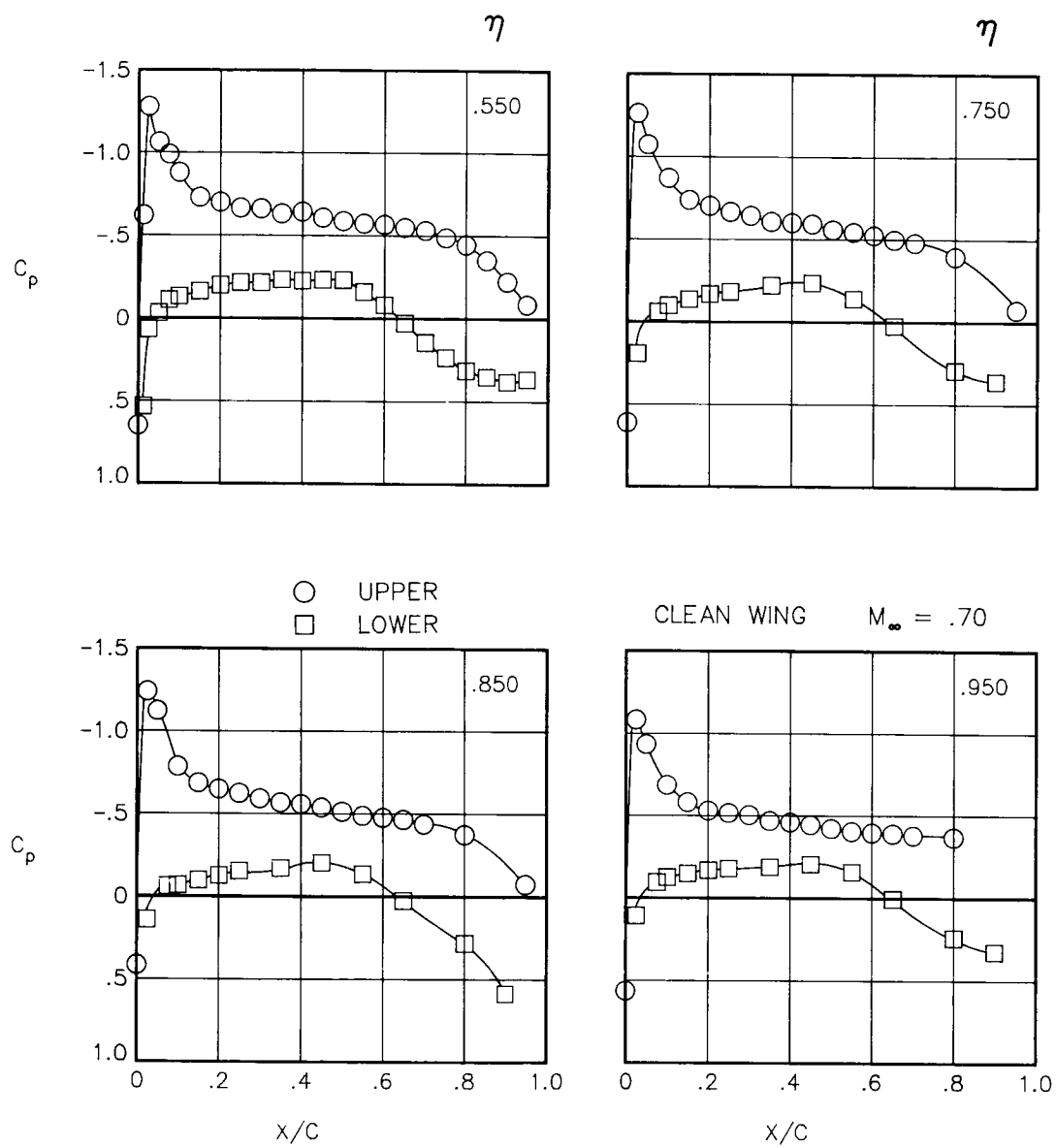
(b) Concluded.

Figure 18.- Continued.



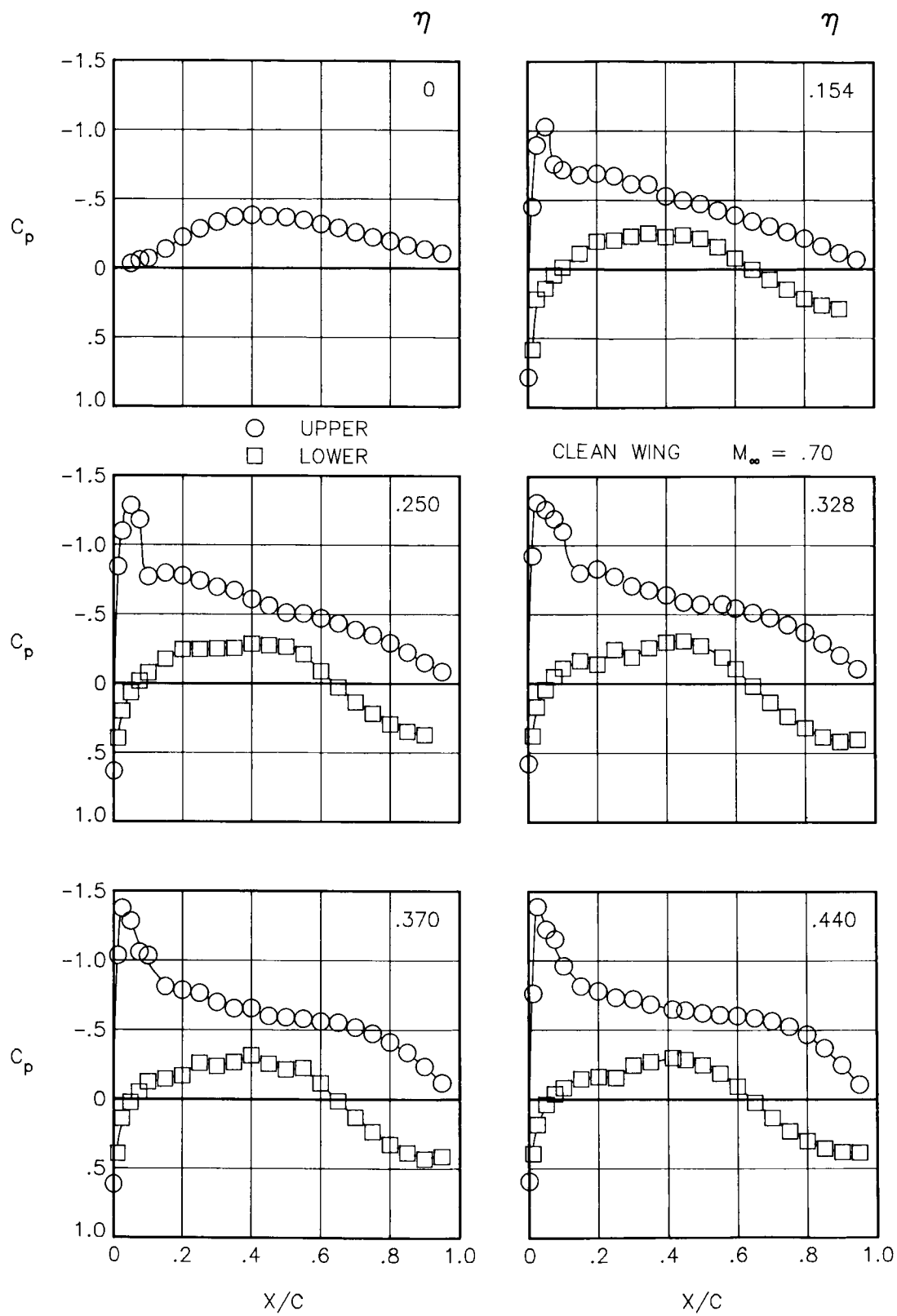
(c)  $\alpha = 1.71^\circ$ ;  $C_L = 0.48$ .

Figure 18.- Continued.



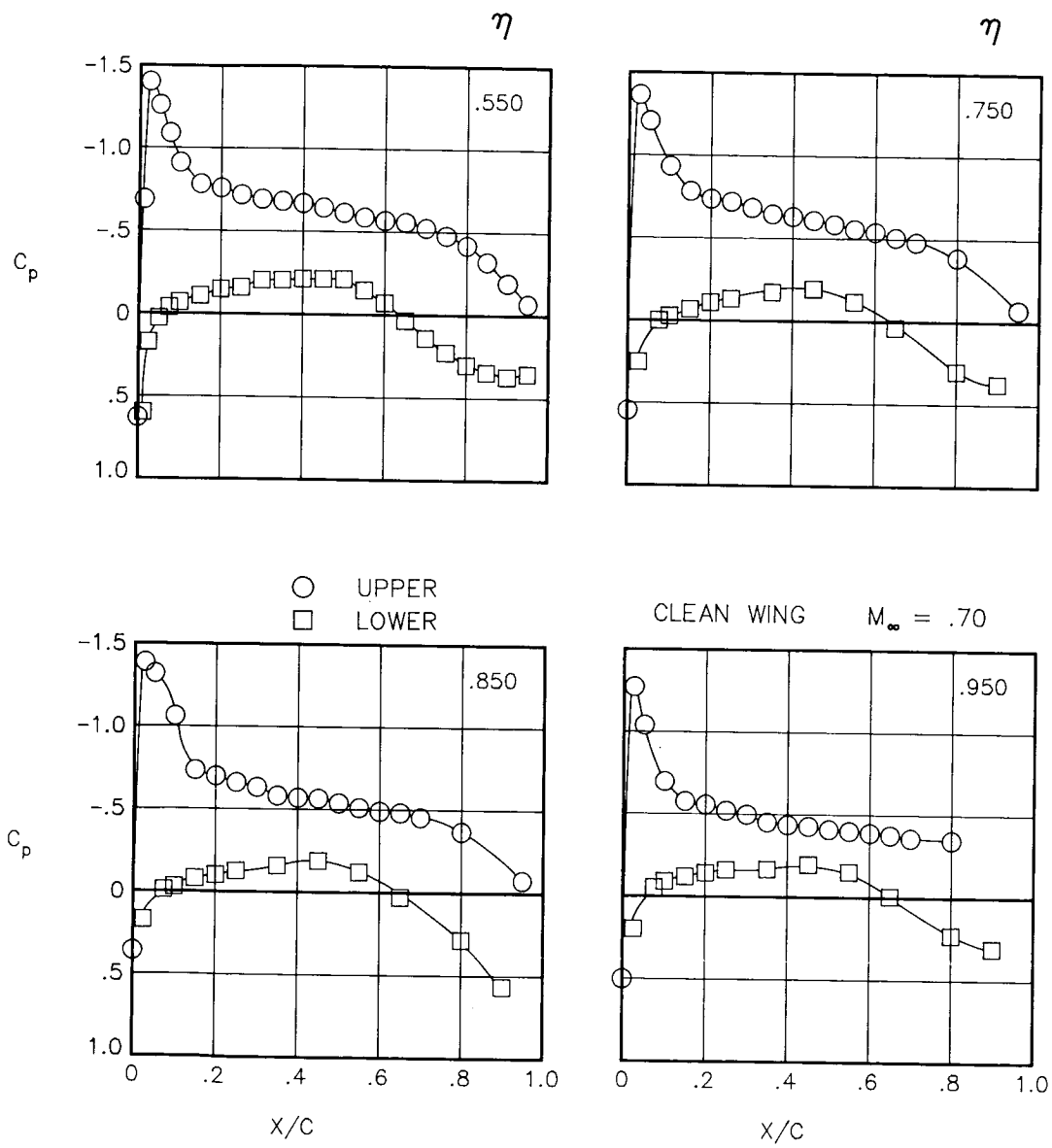
(c) Concluded.

Figure 18.- Continued.



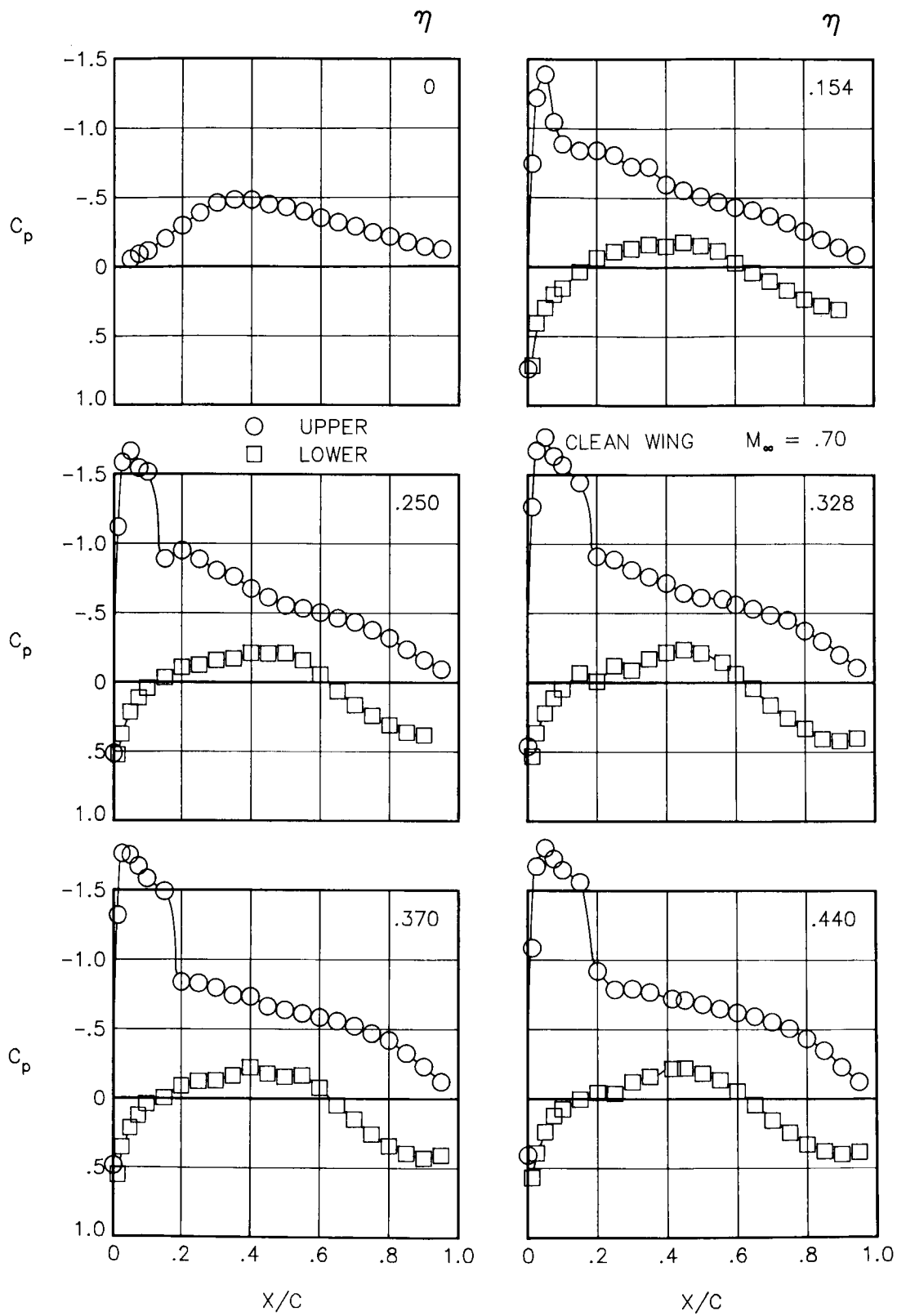
(d)  $\alpha = 2.18^\circ$ ;  $C_L = 0.53$ .

Figure 18.- Continued.



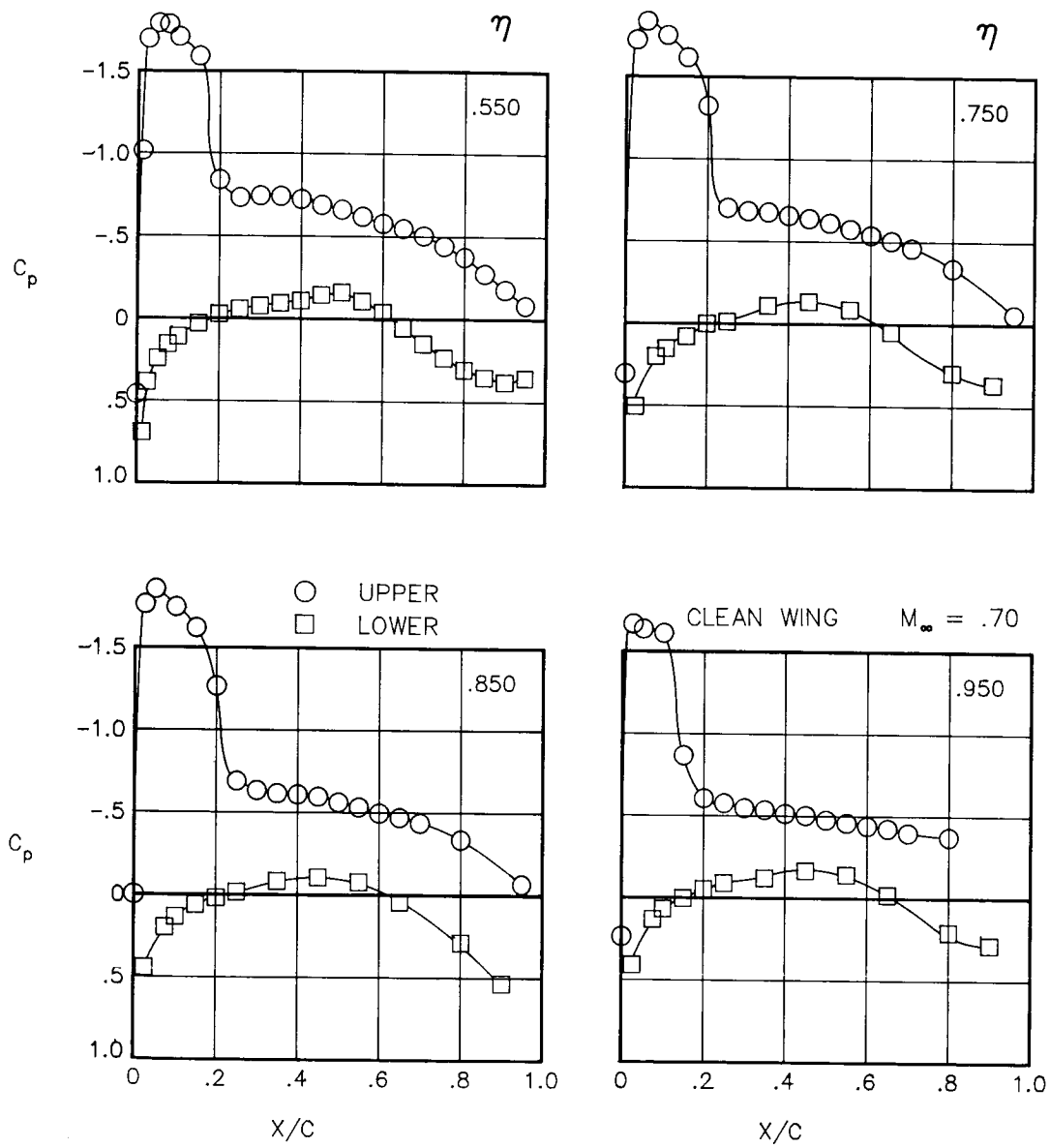
(d) Concluded.

Figure 18.- Continued.



(e)  $\alpha = 4.19^\circ$ ;  $C_L = 0.76$ .

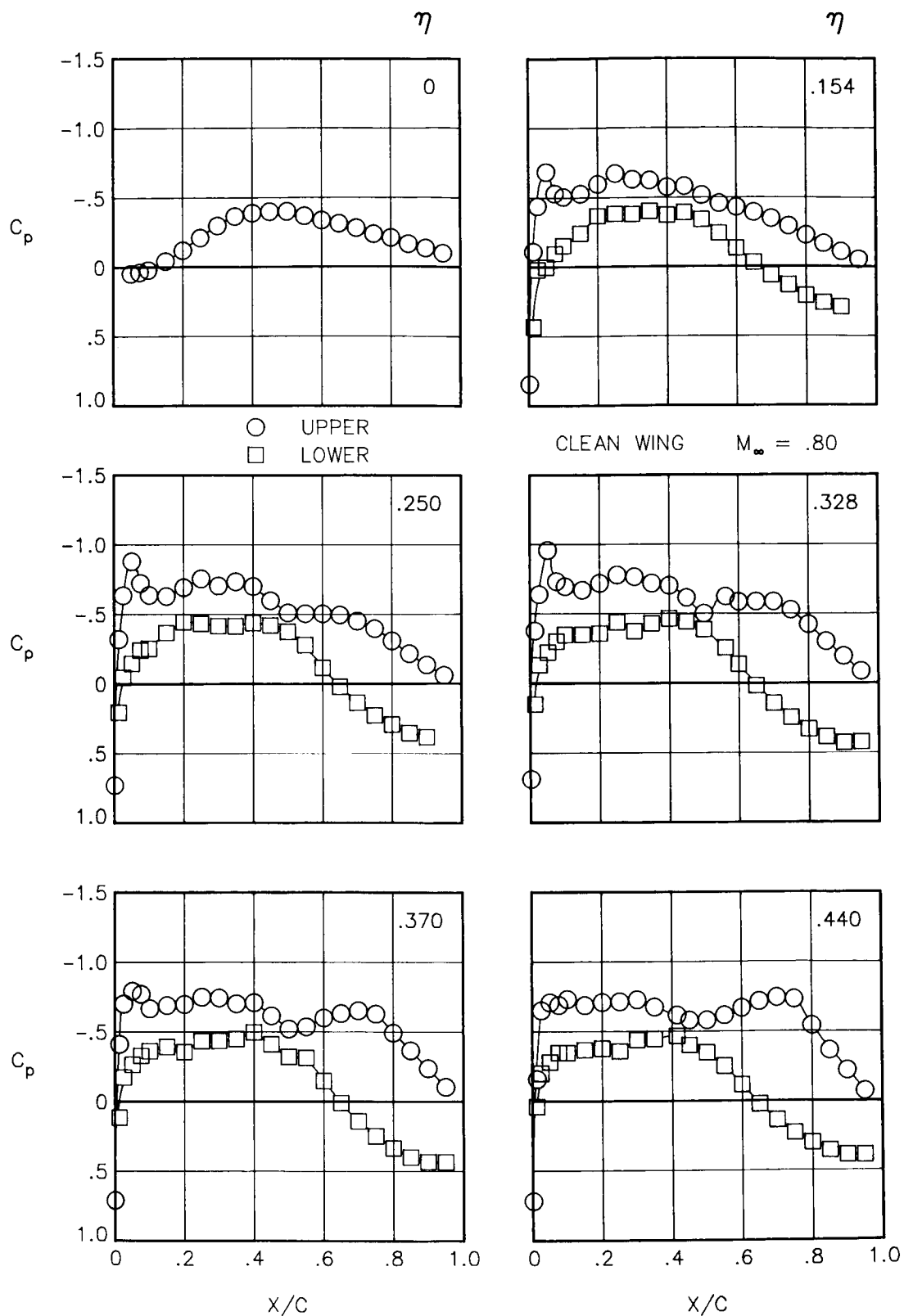
Figure 18.- Continued.



(e) Concluded.

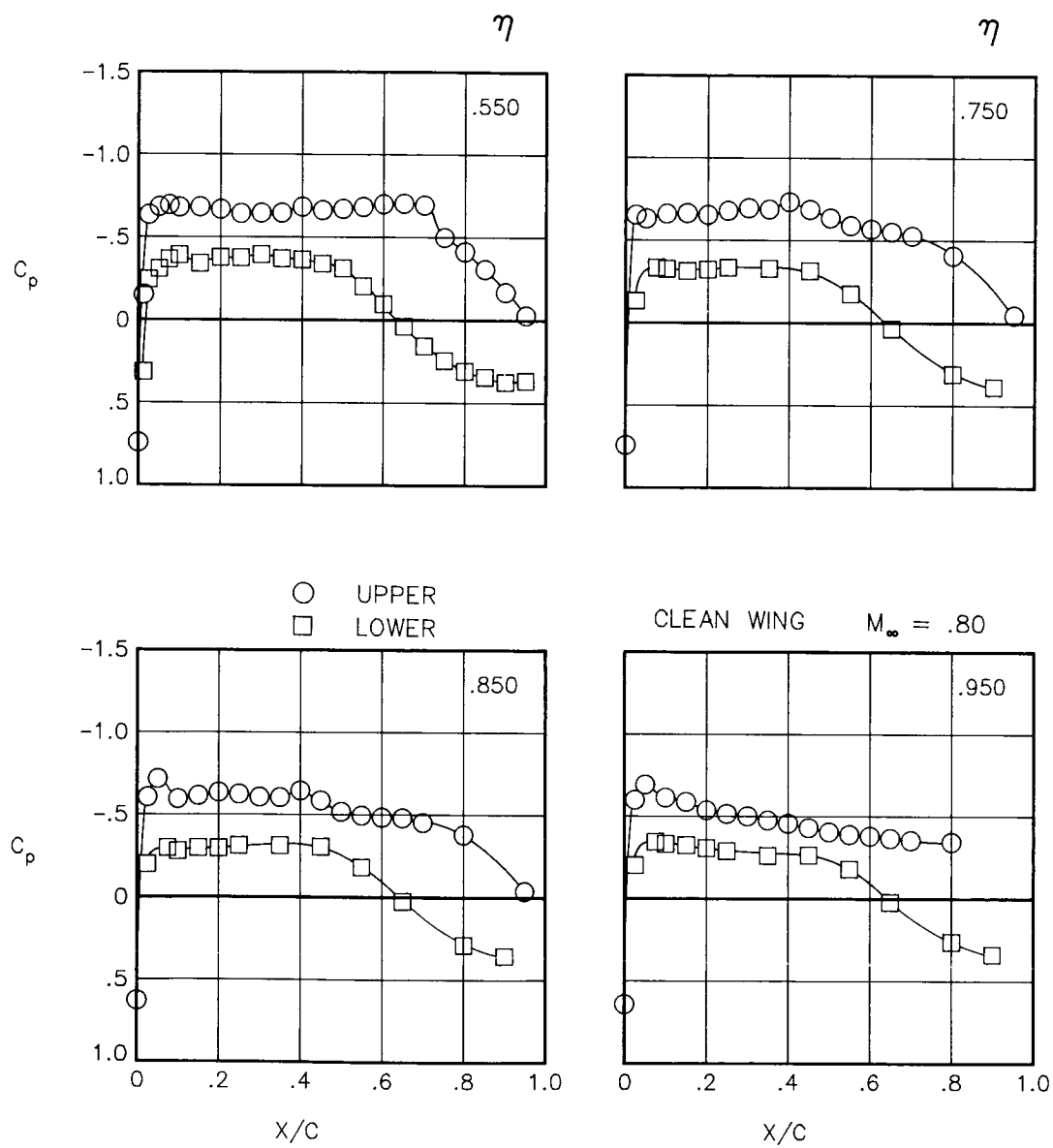
Figure 18.- Concluded.





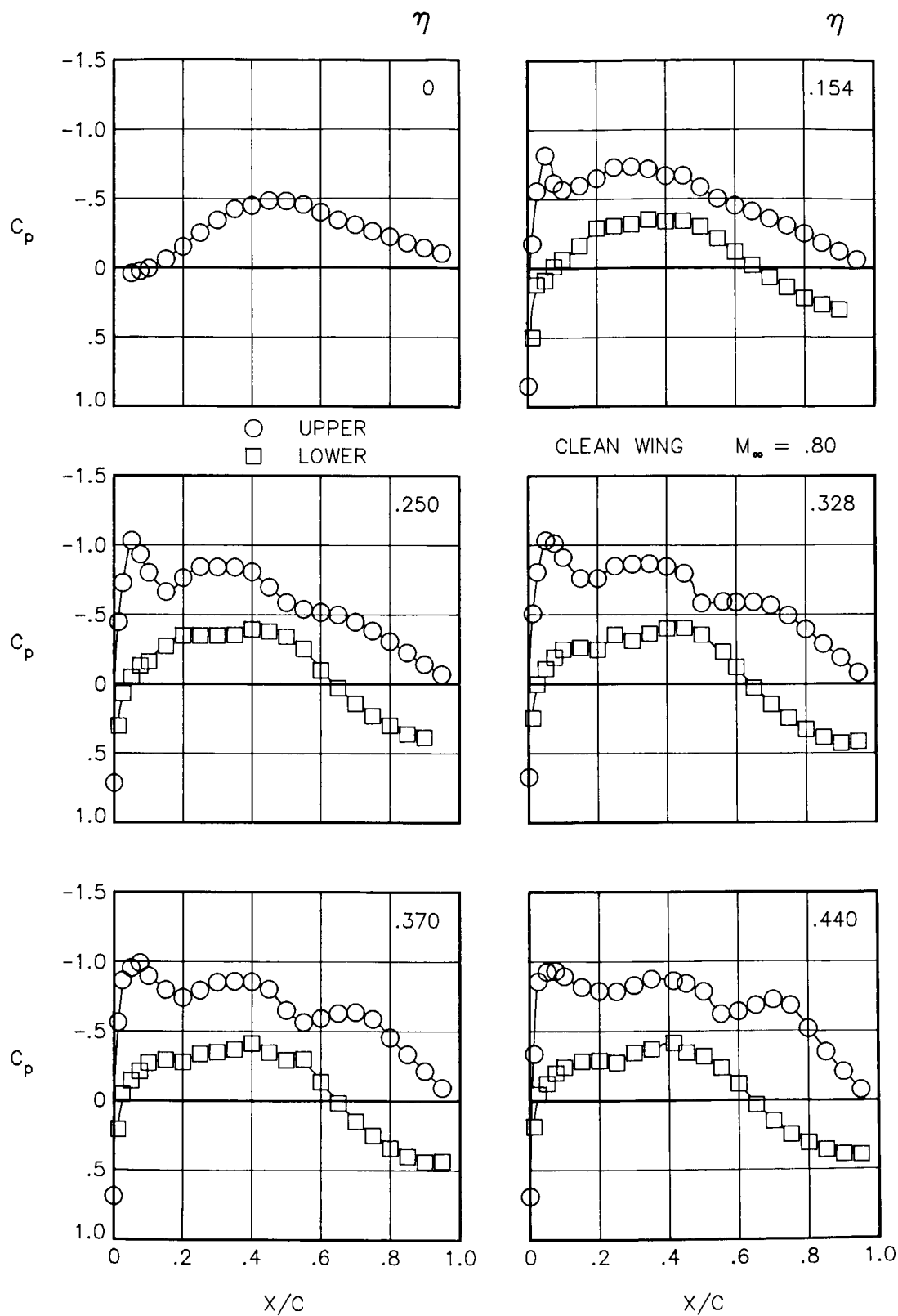
(a)  $\alpha = 0.26^\circ$ ;  $C_L = 0.35$ .

Figure 19.- Chordwise pressure coefficient distributions on clean-wing configuration at various angles of attack and  $M_\infty = 0.80$ .



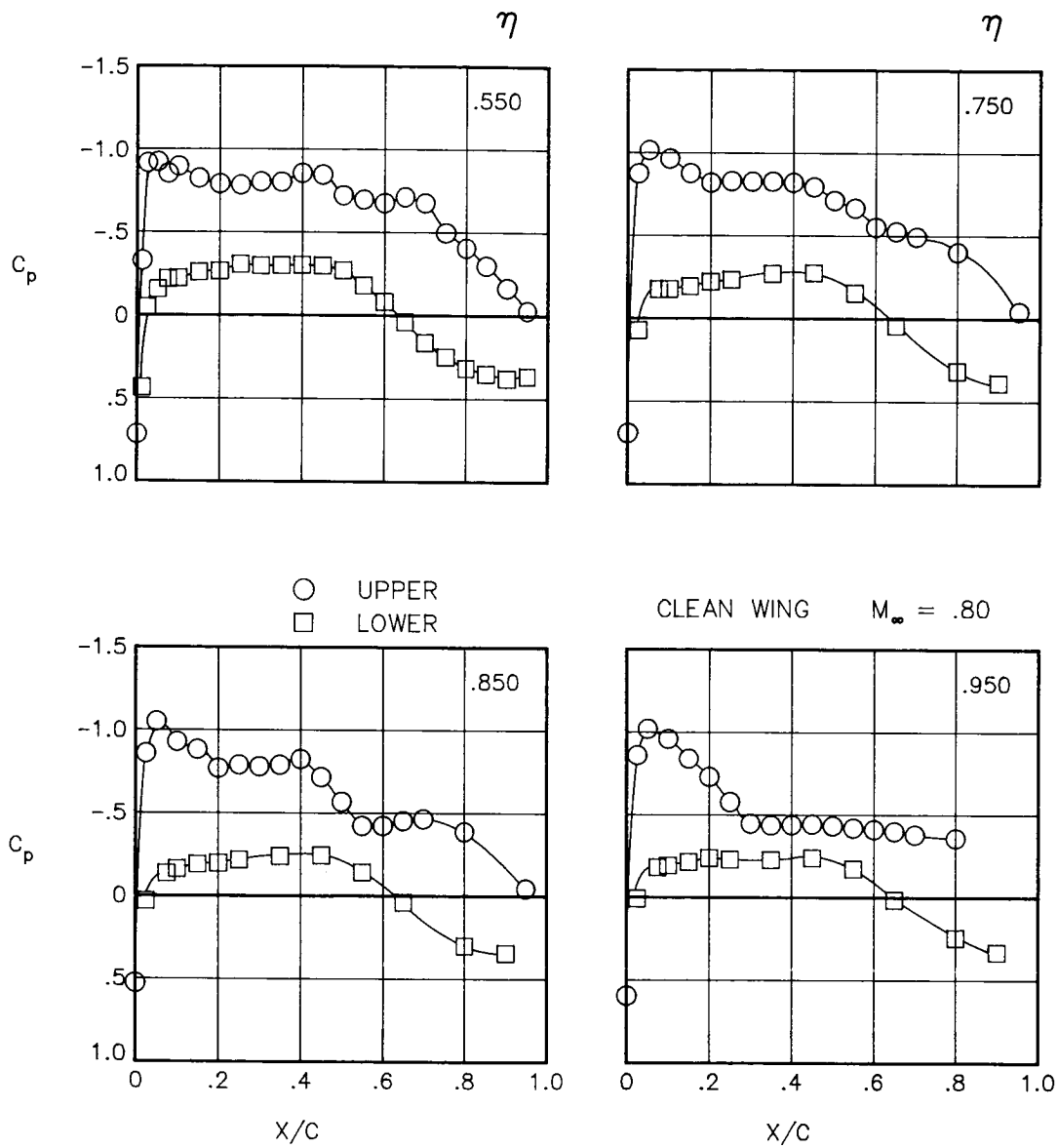
(a) Concluded.

Figure 19.- Continued.



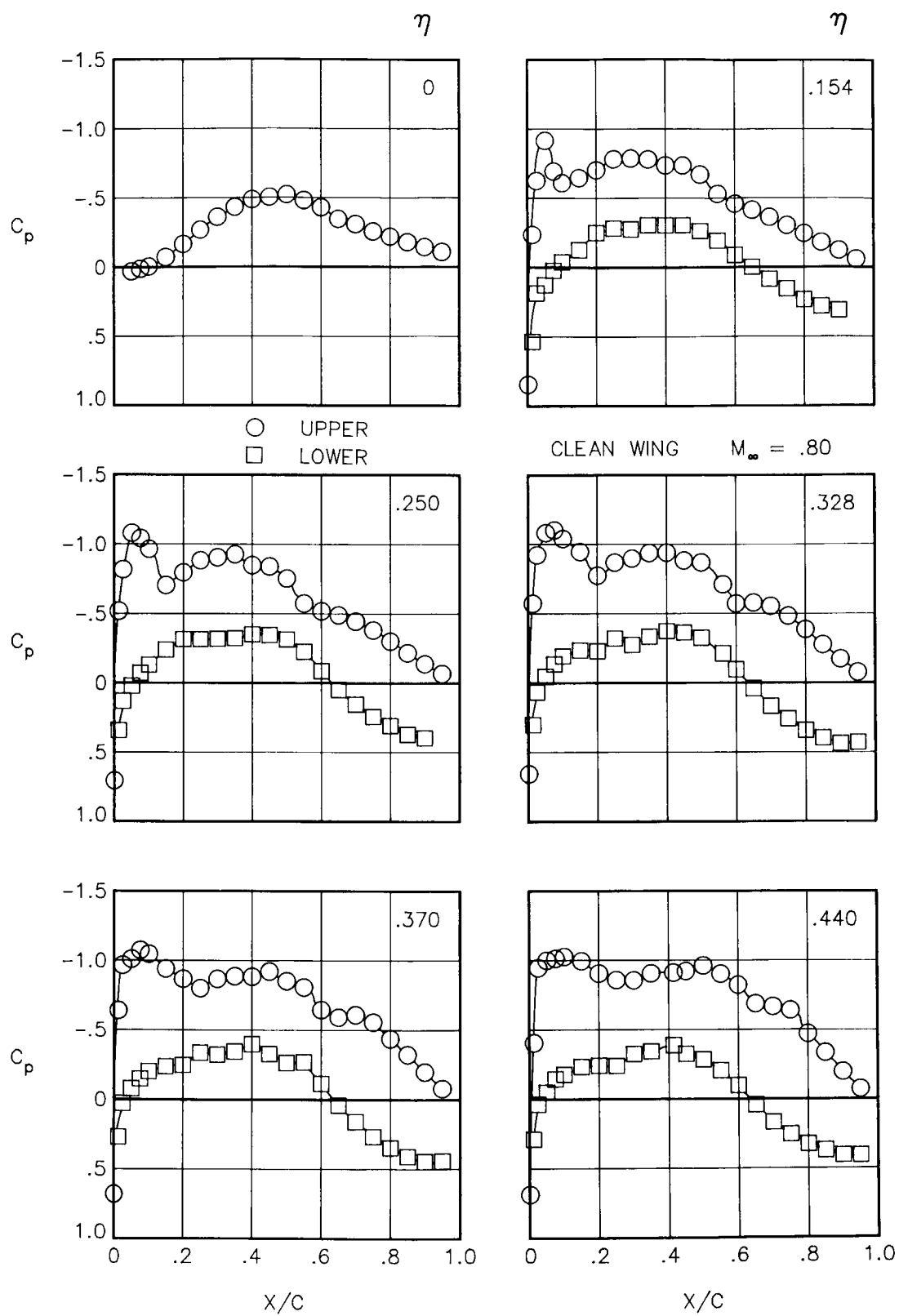
(b)  $\alpha = 1.24^\circ$ ;  $C_L = 0.49$ .

Figure 19.- Continued.



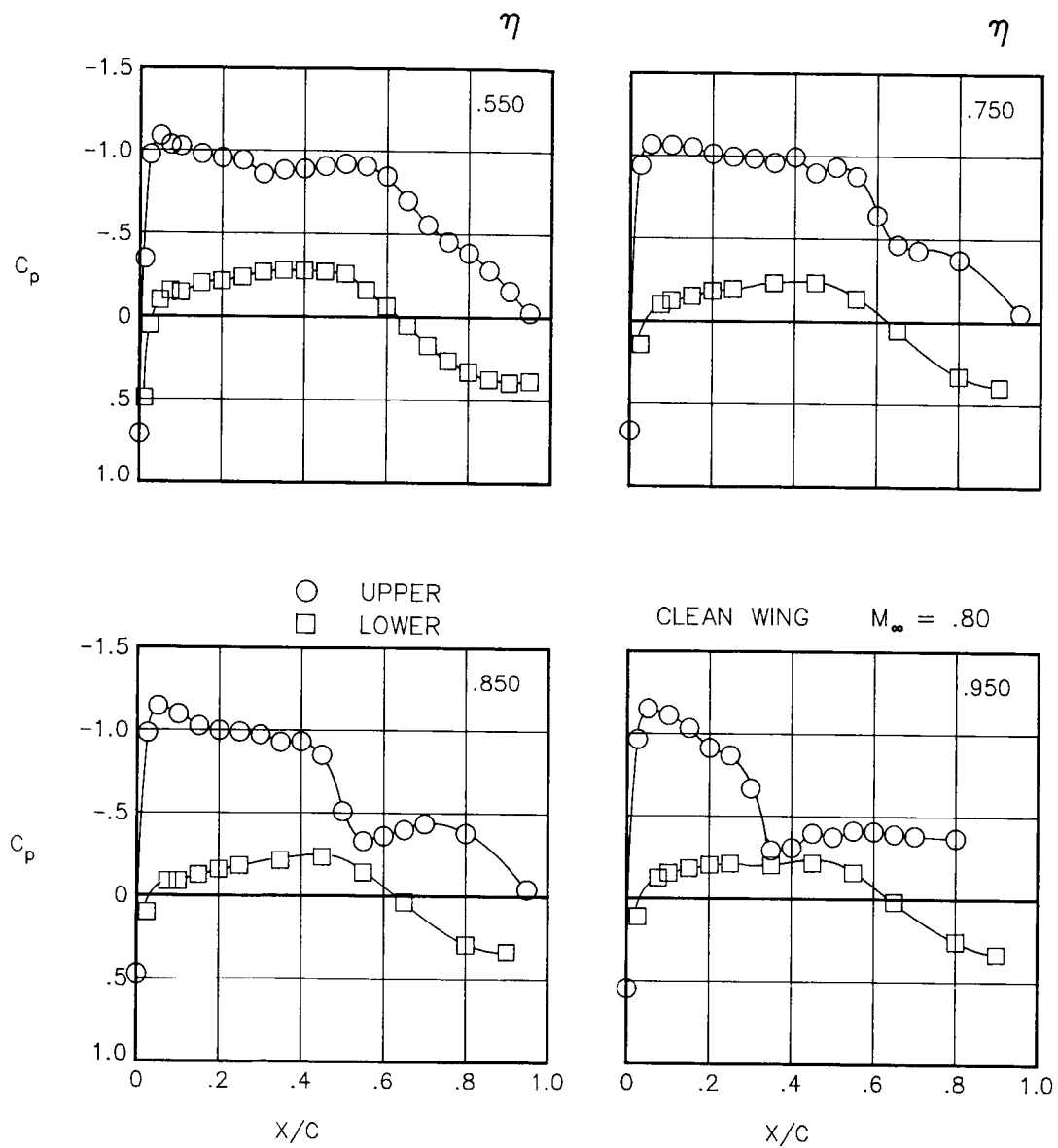
(b) Concluded.

Figure 19.- Continued.



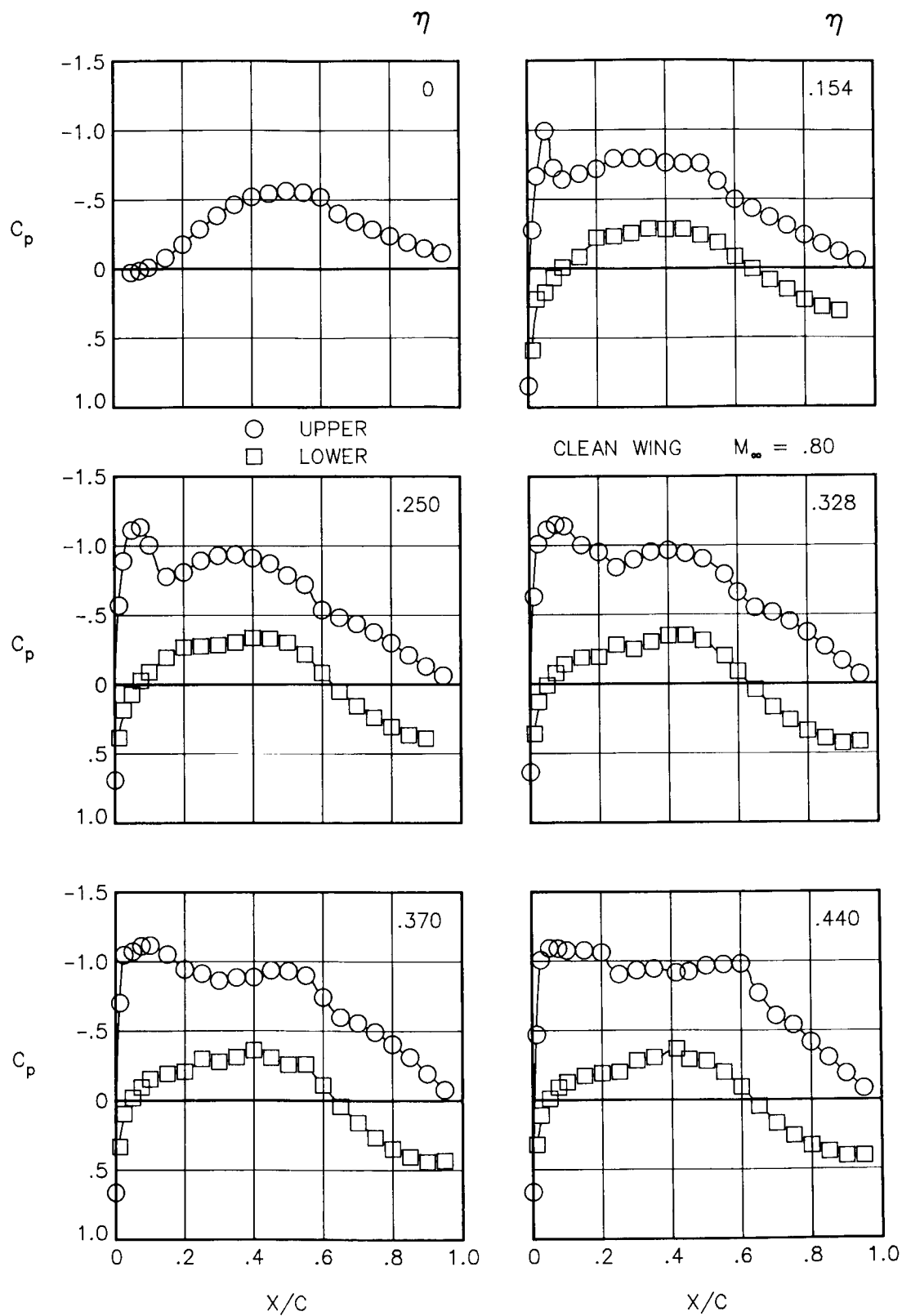
(c)  $\alpha = 1.75^\circ$ ;  $C_L = 0.57$ .

Figure 19.- Continued.



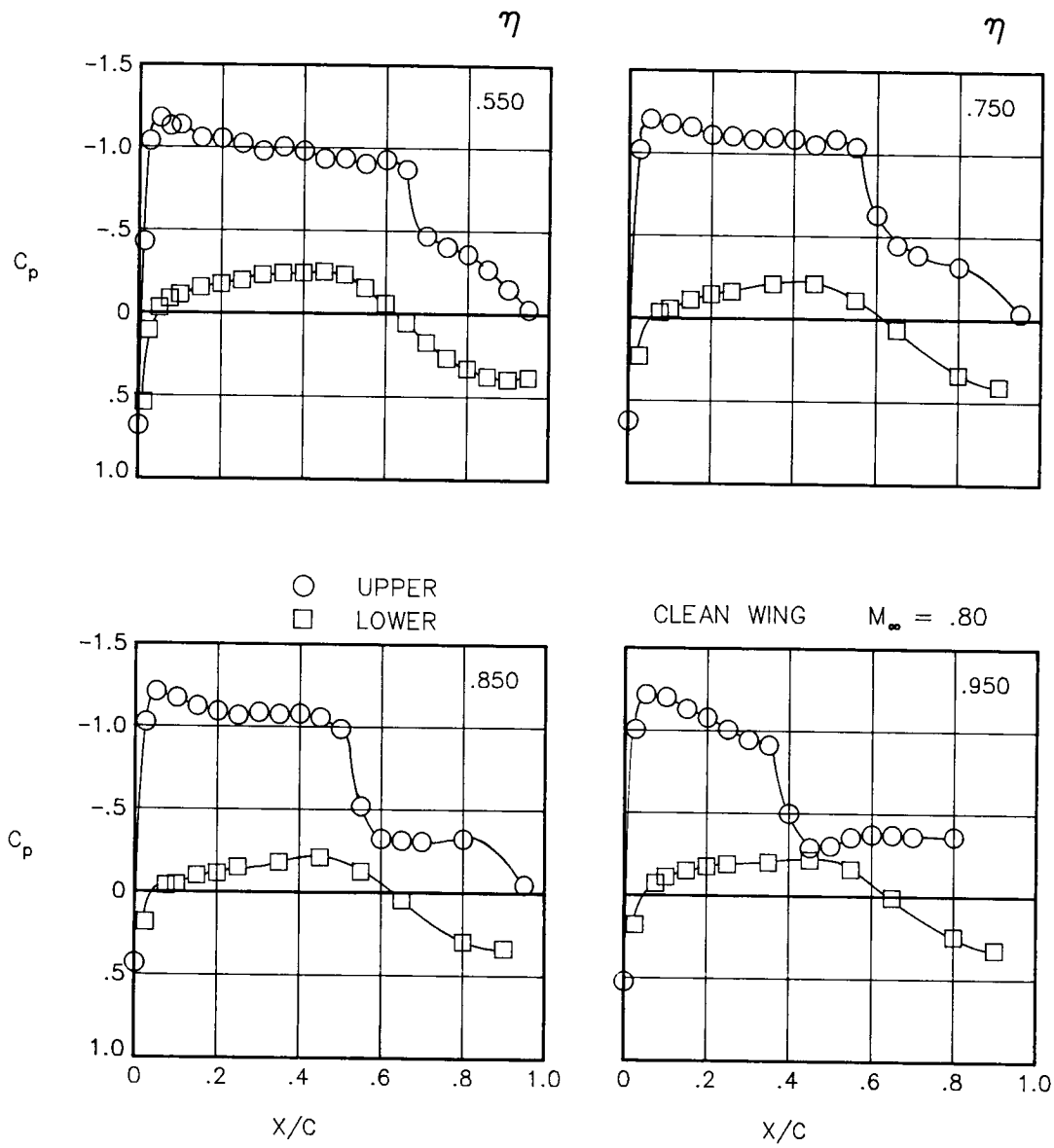
(c) Concluded.

Figure 19.- Continued.



(d)  $\alpha = 2.23^\circ$ ;  $C_L = 0.64$ .

Figure 19.- Continued.

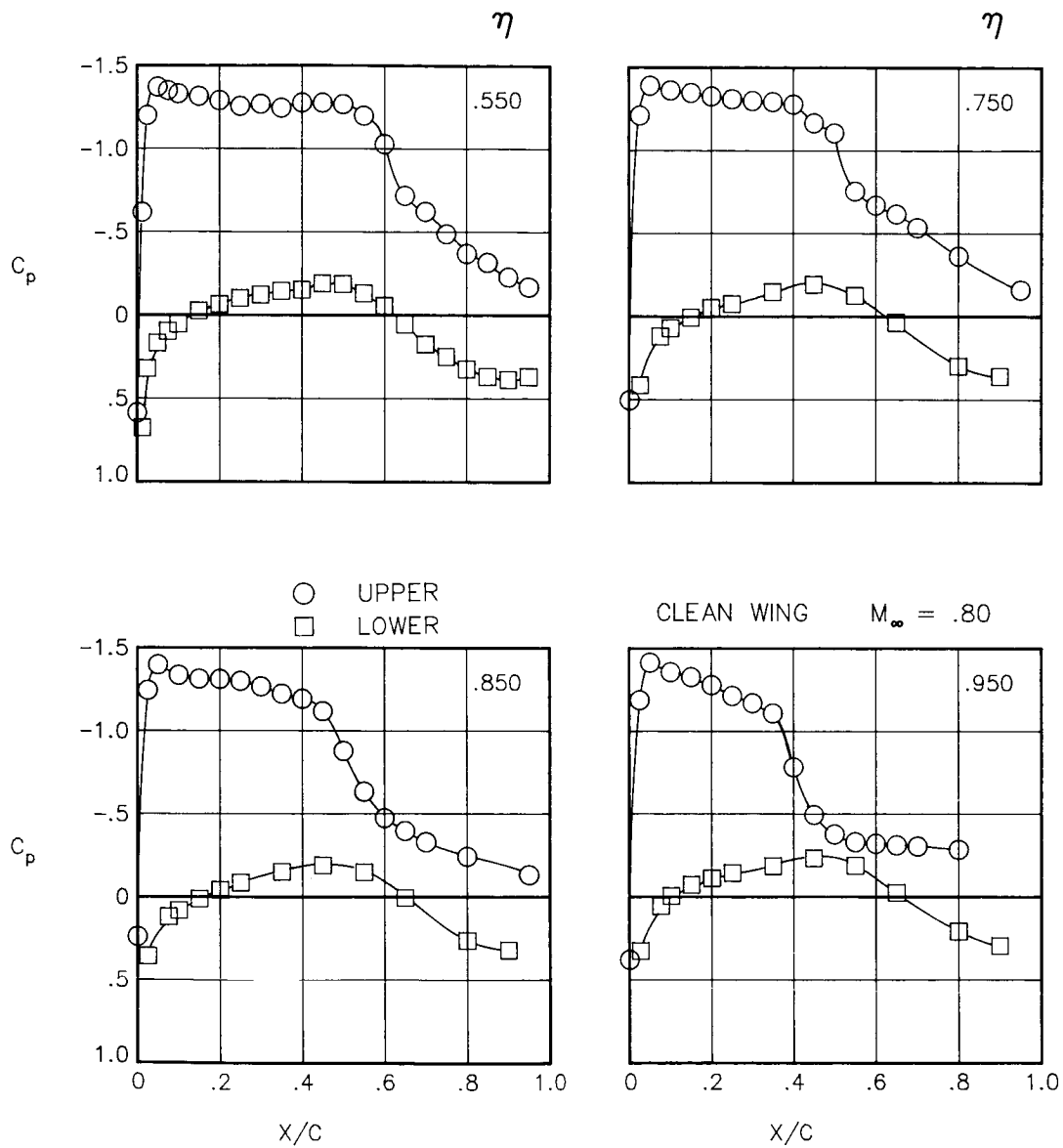


(d) Concluded.

Figure 19.- Continued.







(e) Concluded.

Figure 19.- Concluded.

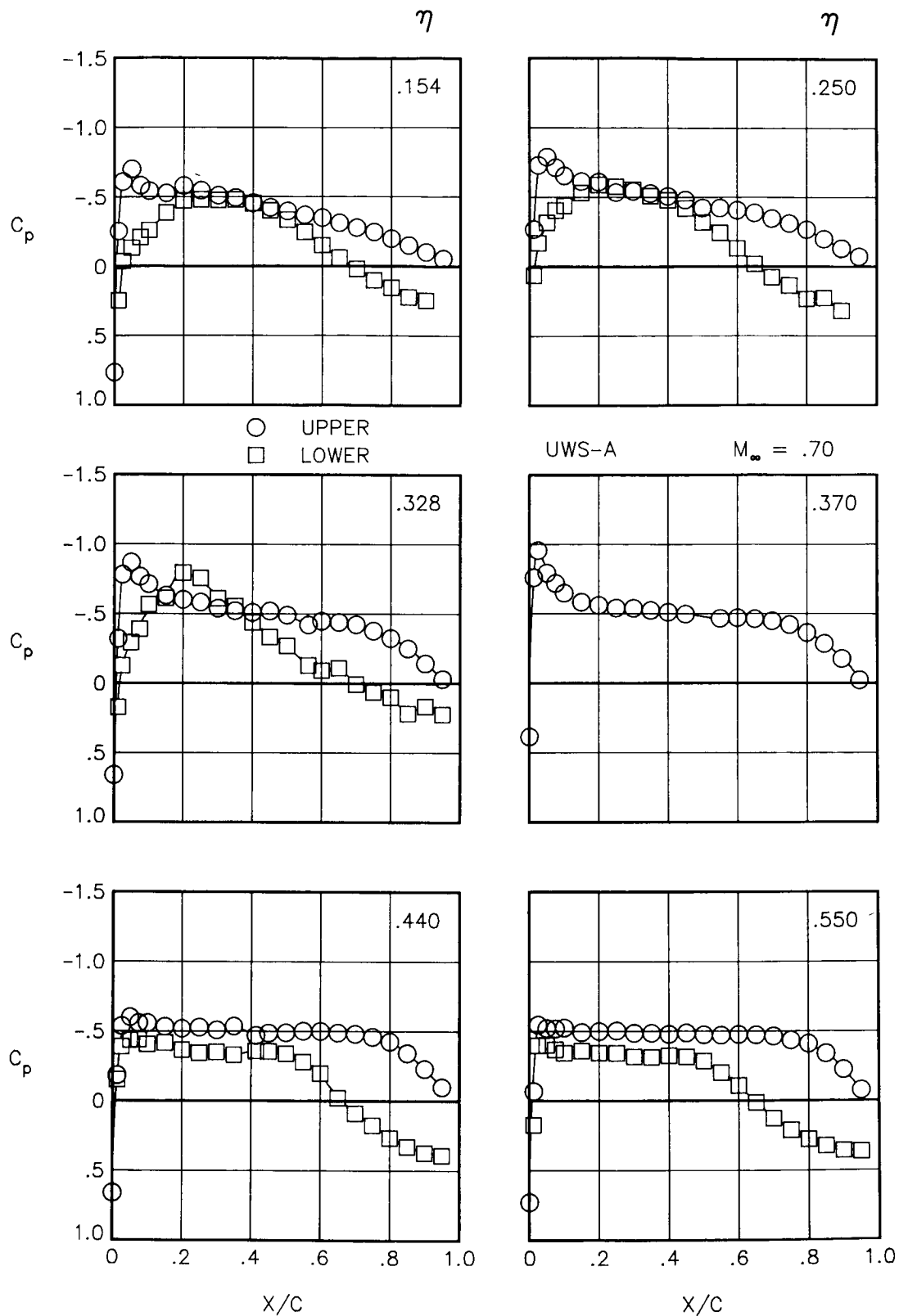
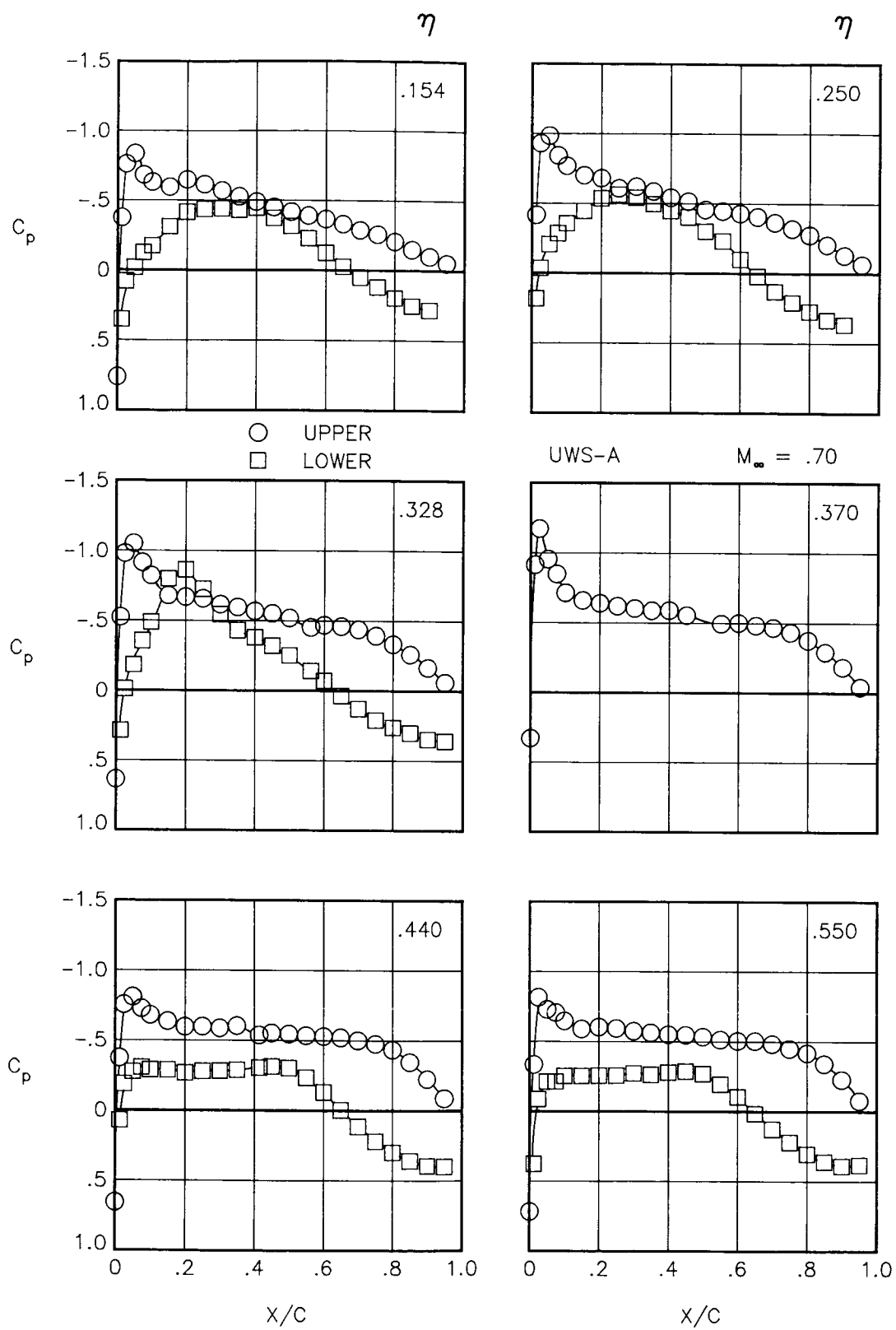
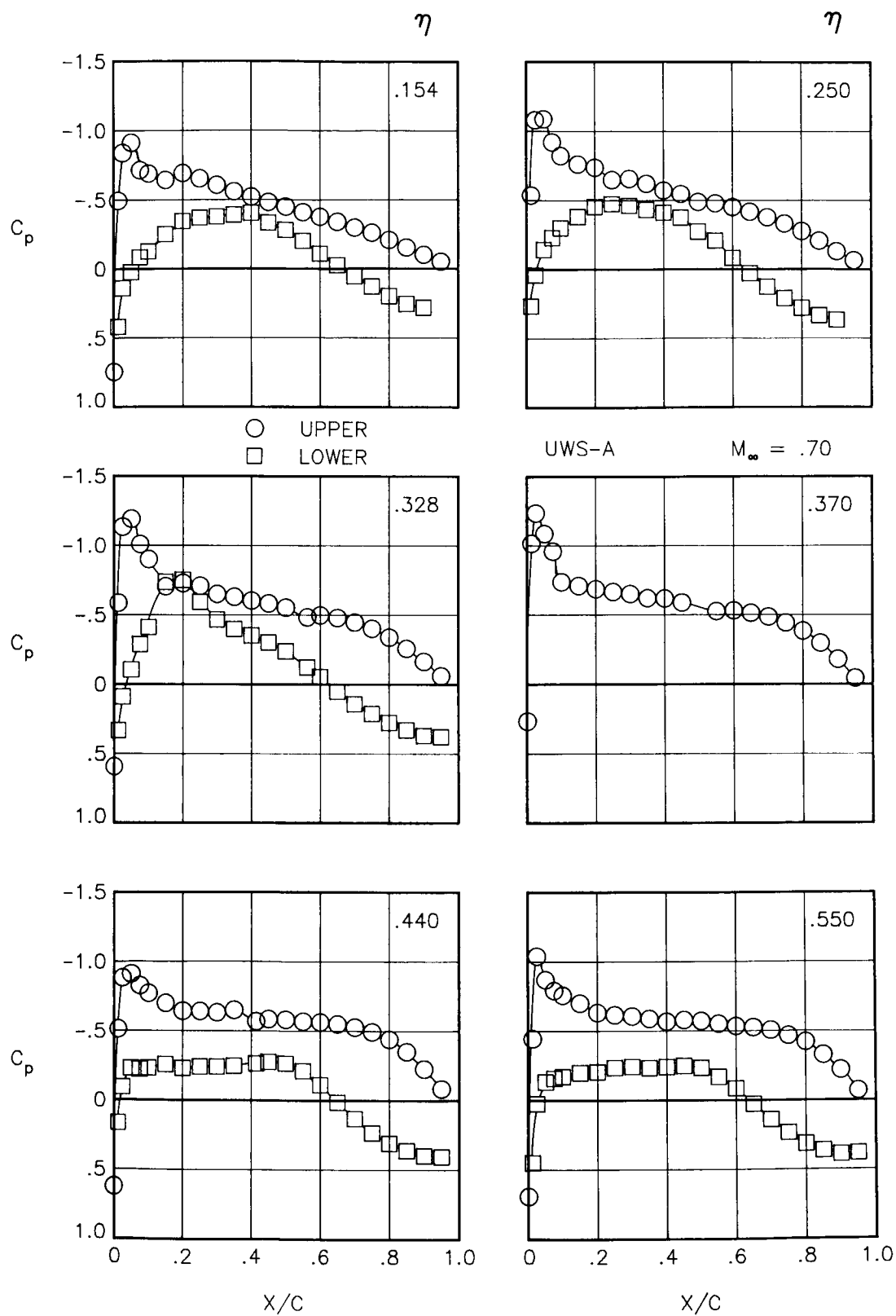


Figure 20.- Chordwise pressure coefficient distributions for configuration UWS-A at various angles of attack and  $M_\infty = 0.70$ .



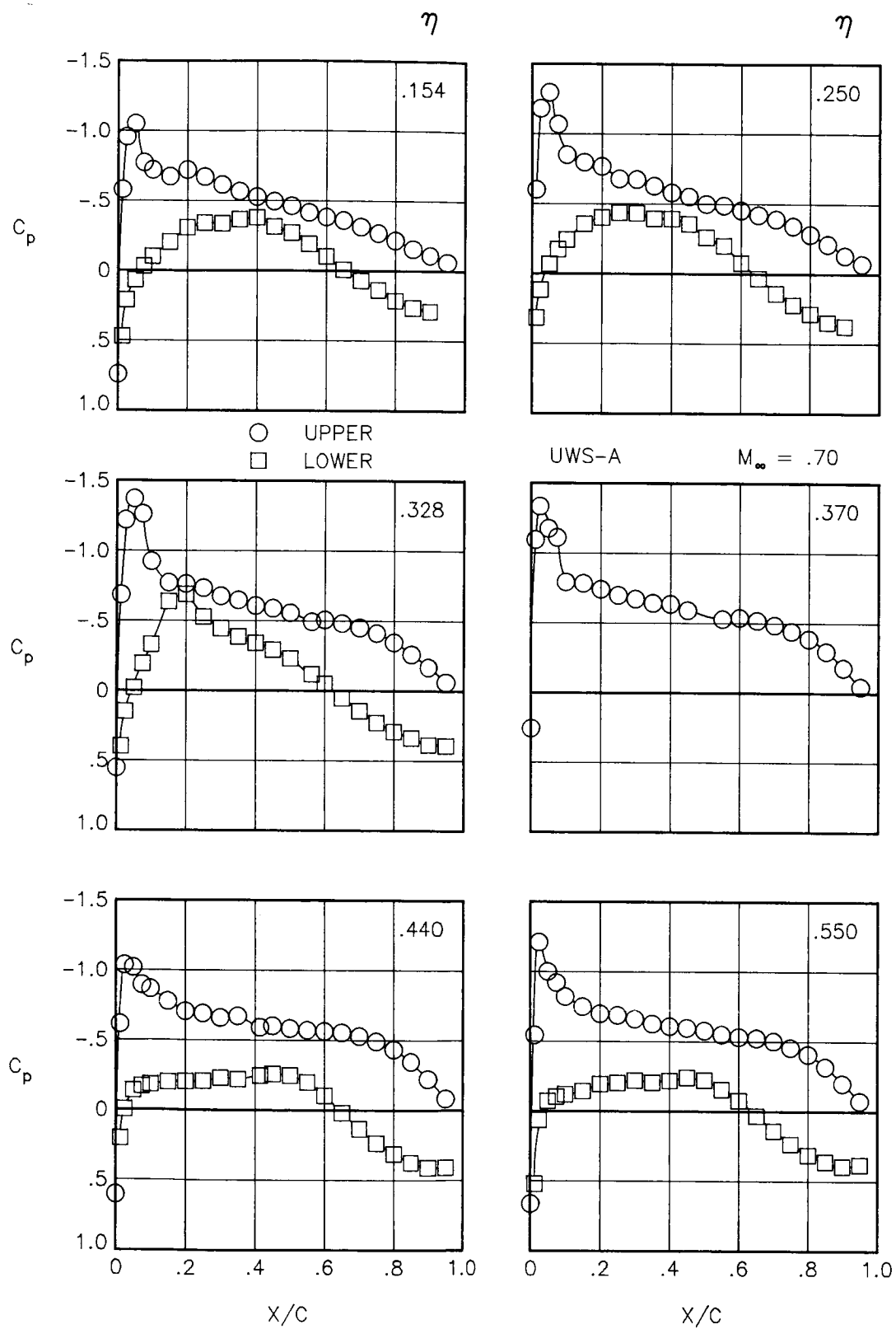
(b)  $\alpha = 1.17^\circ$ ;  $C_L = 0.35$ .

Figure 20.- Continued.



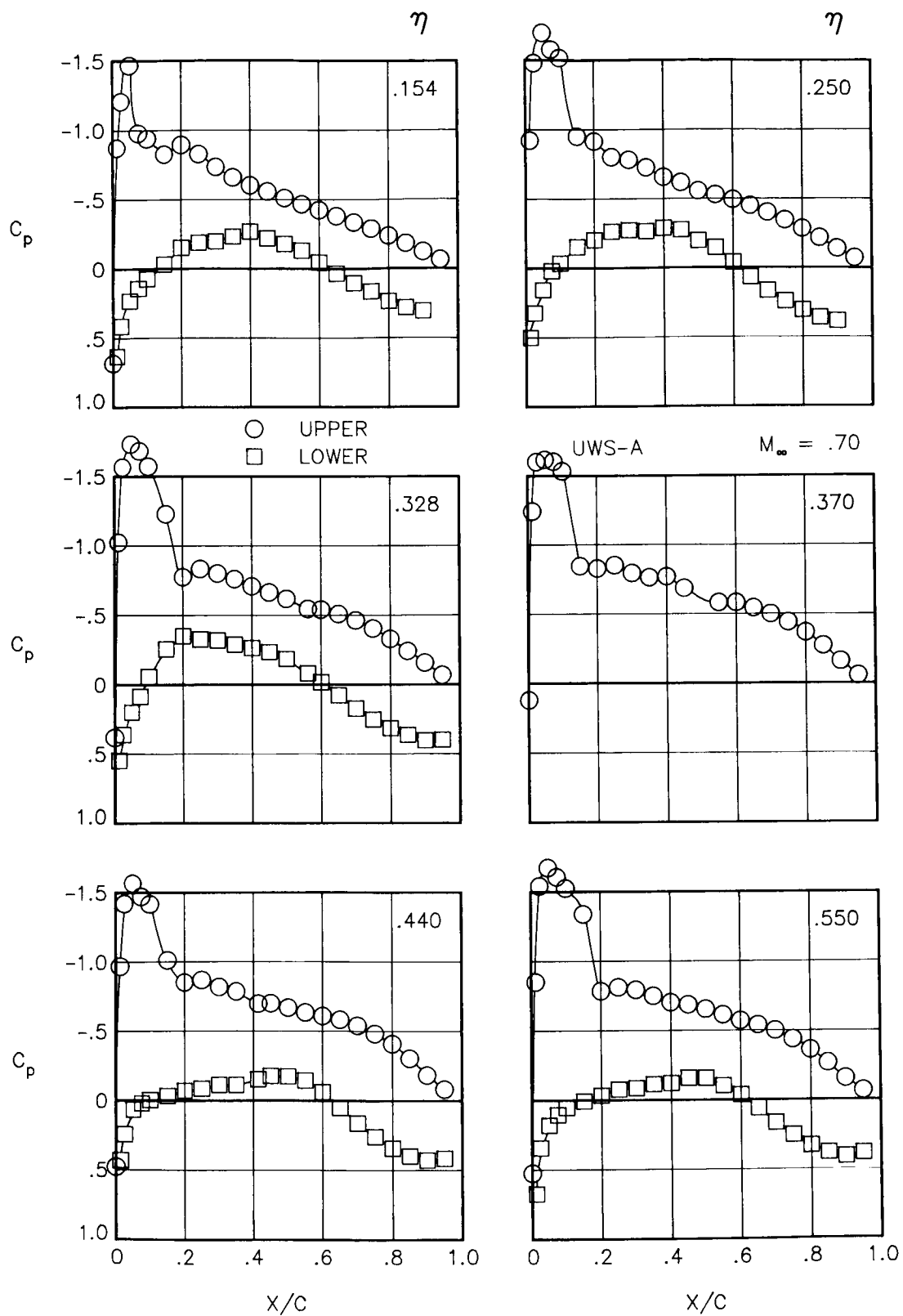
(c)  $\alpha = 1.70^\circ$ ;  $C_L = 0.41$ .

Figure 20.- Continued.



(d)  $\alpha = 2.18^\circ$ ;  $C_L = 0.47$ .

Figure 20.- Continued.

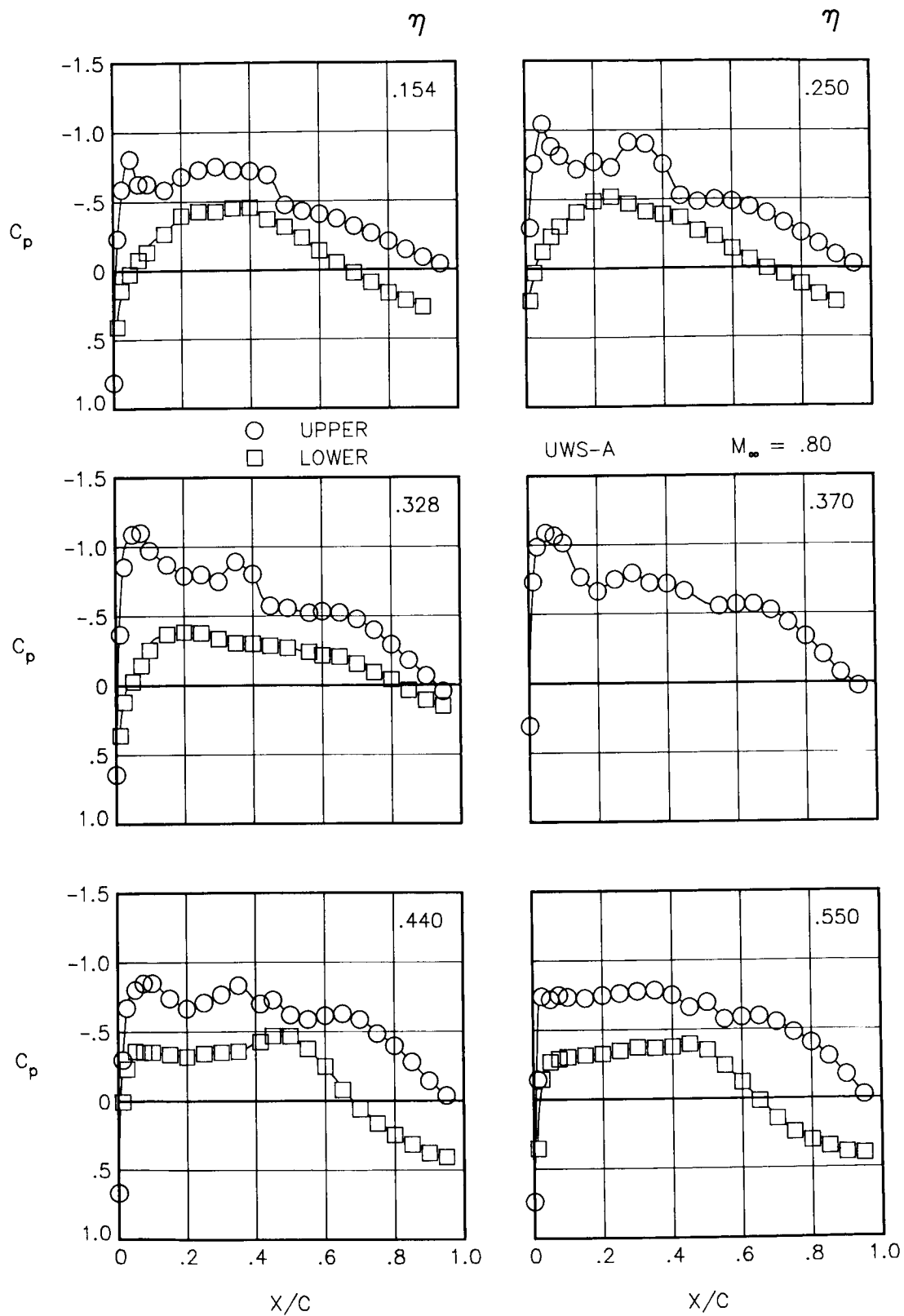


(e)  $\alpha = 4.18^\circ$ ;  $C_L = 0.70$ .

Figure 20.- Concluded.

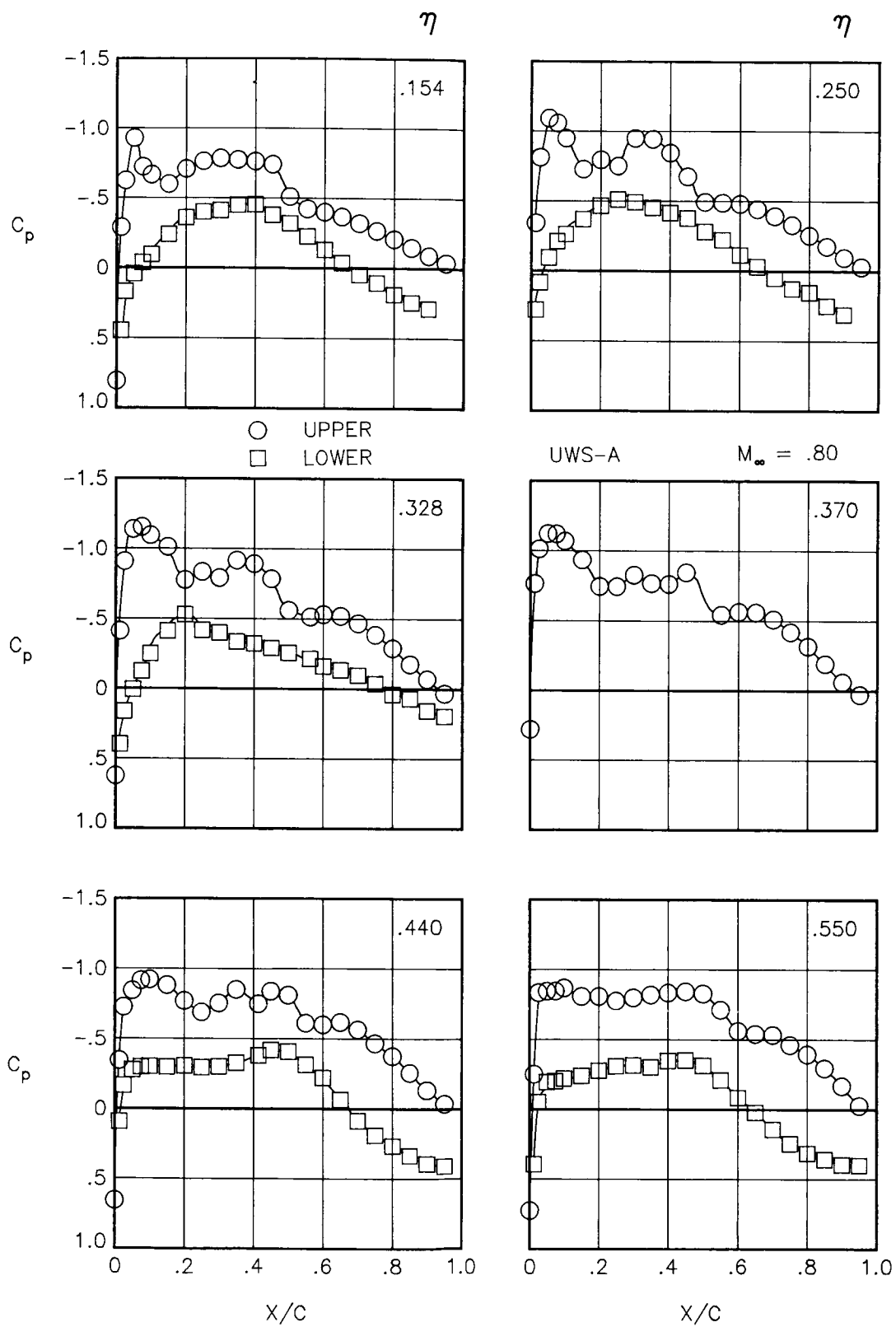






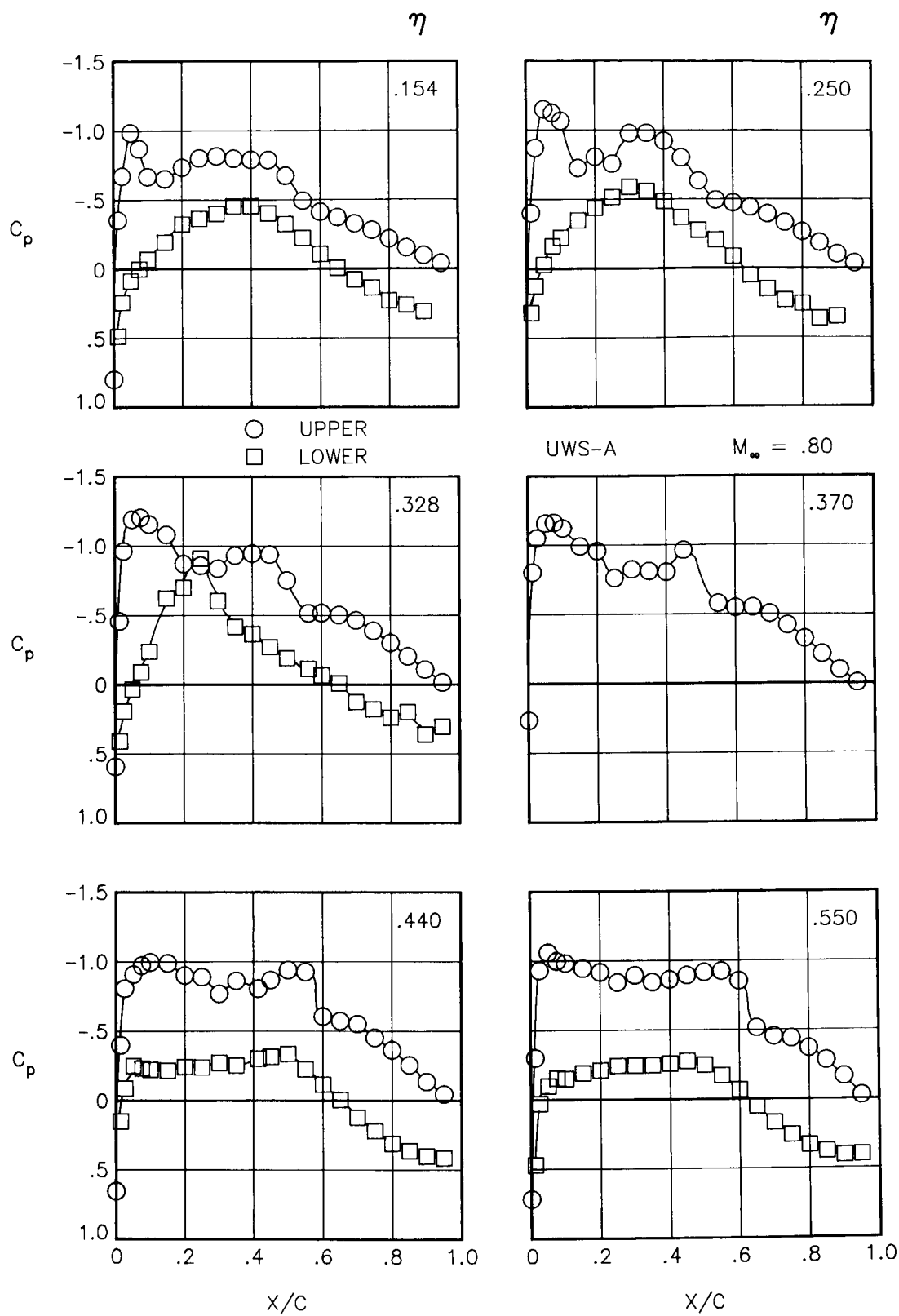
(b)  $\alpha = 1.27^\circ$ ;  $C_L = 0.38$ .

Figure 21.- Continued.



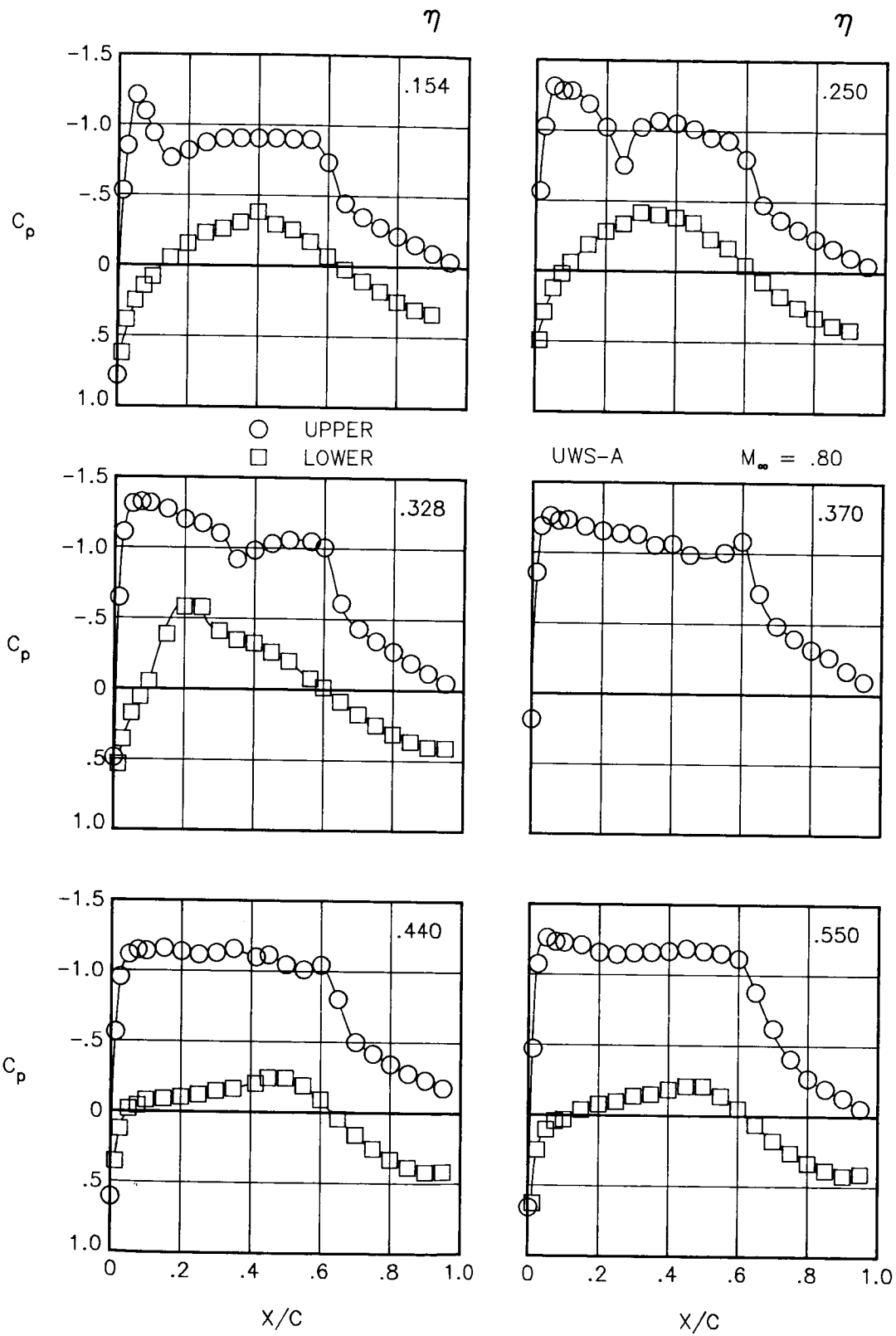
(c)  $\alpha = 1.73^\circ$ ;  $C_L = 0.45$ .

Figure 21.- Continued.



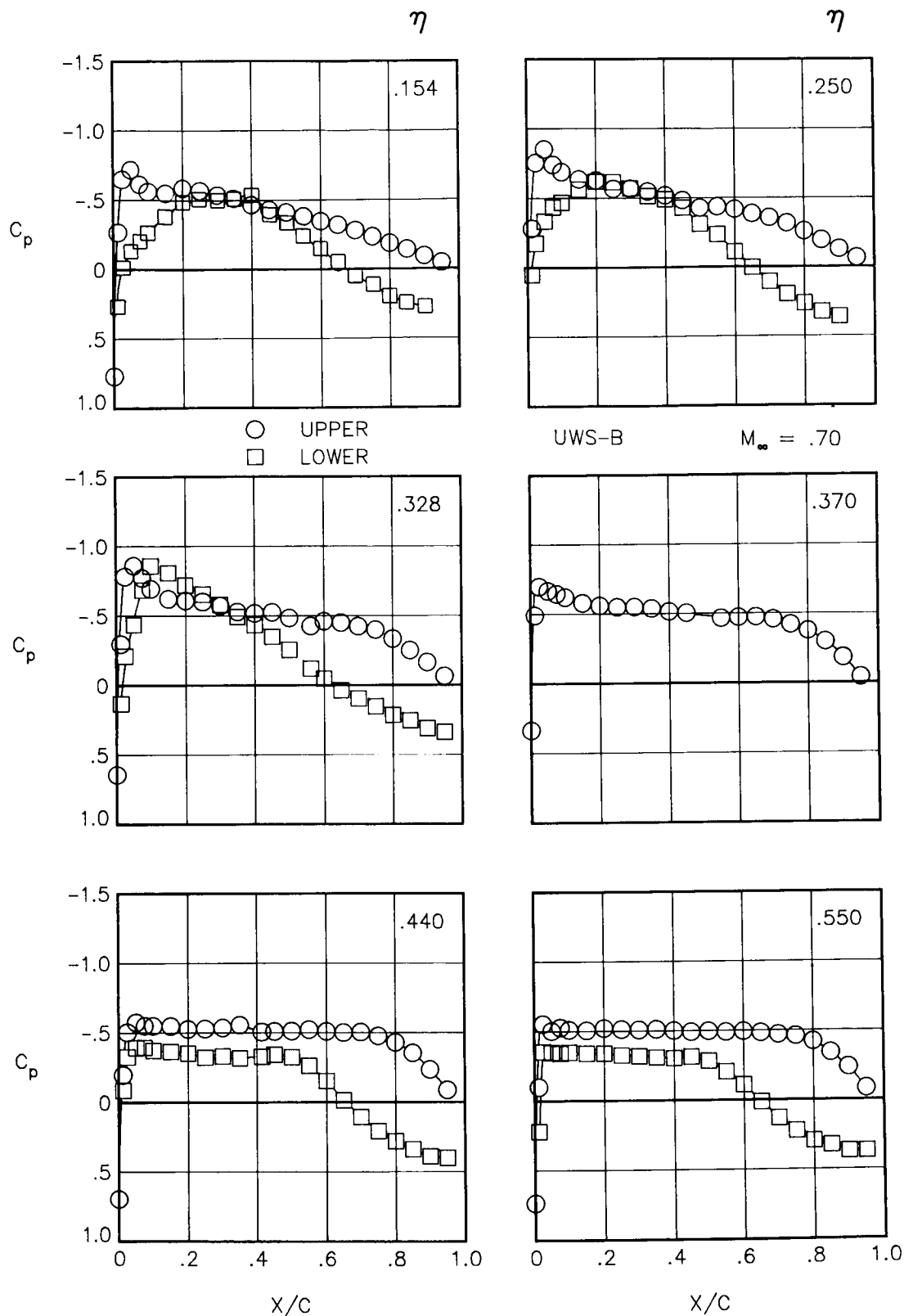
(d)  $\alpha = 2.25^\circ$ ;  $C_L = 0.54$ .

Figure 21.- Continued.



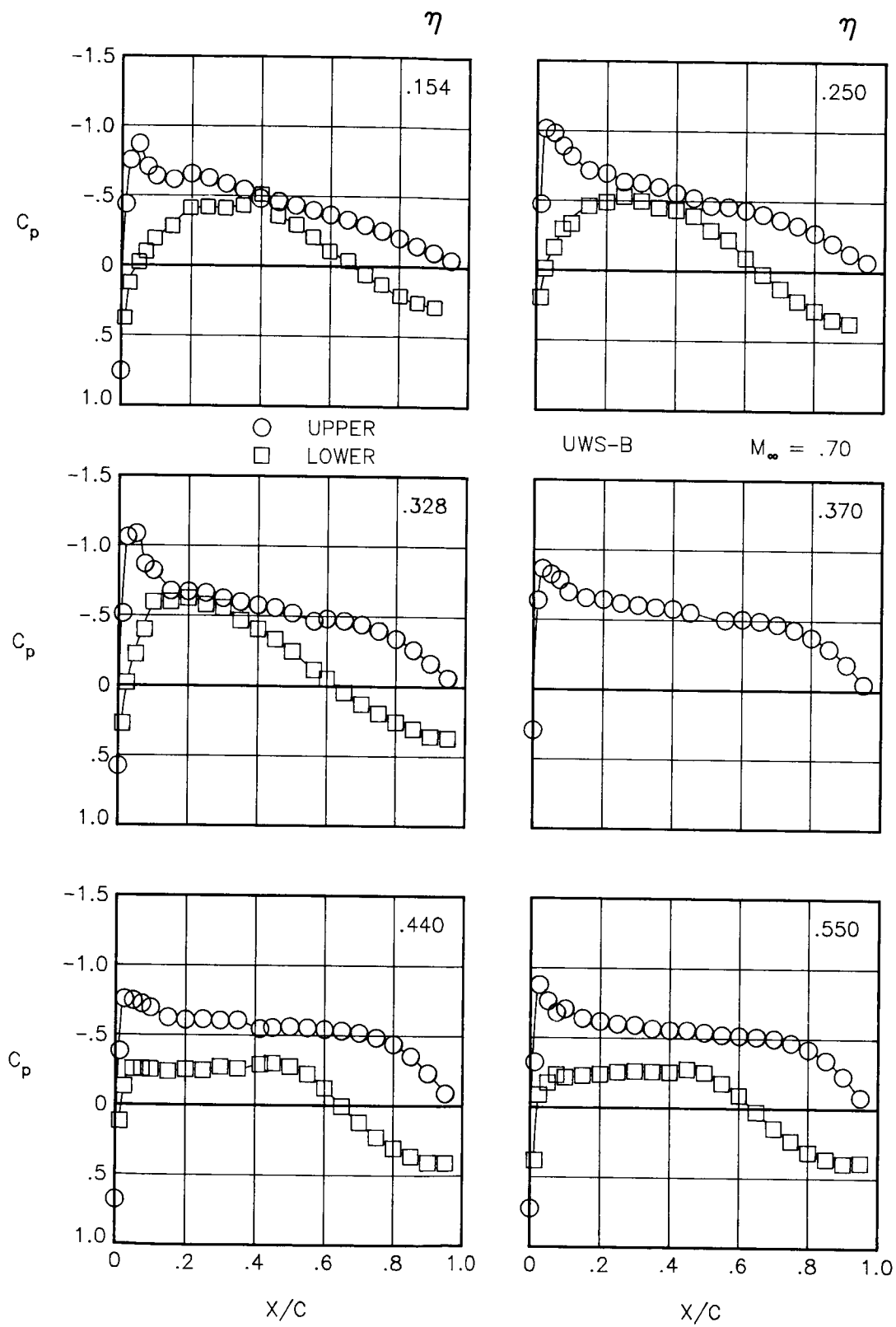
(e)  $\alpha = 4.19^\circ$ ;  $C_L = 0.79$ .

Figure 21.- Concluded.



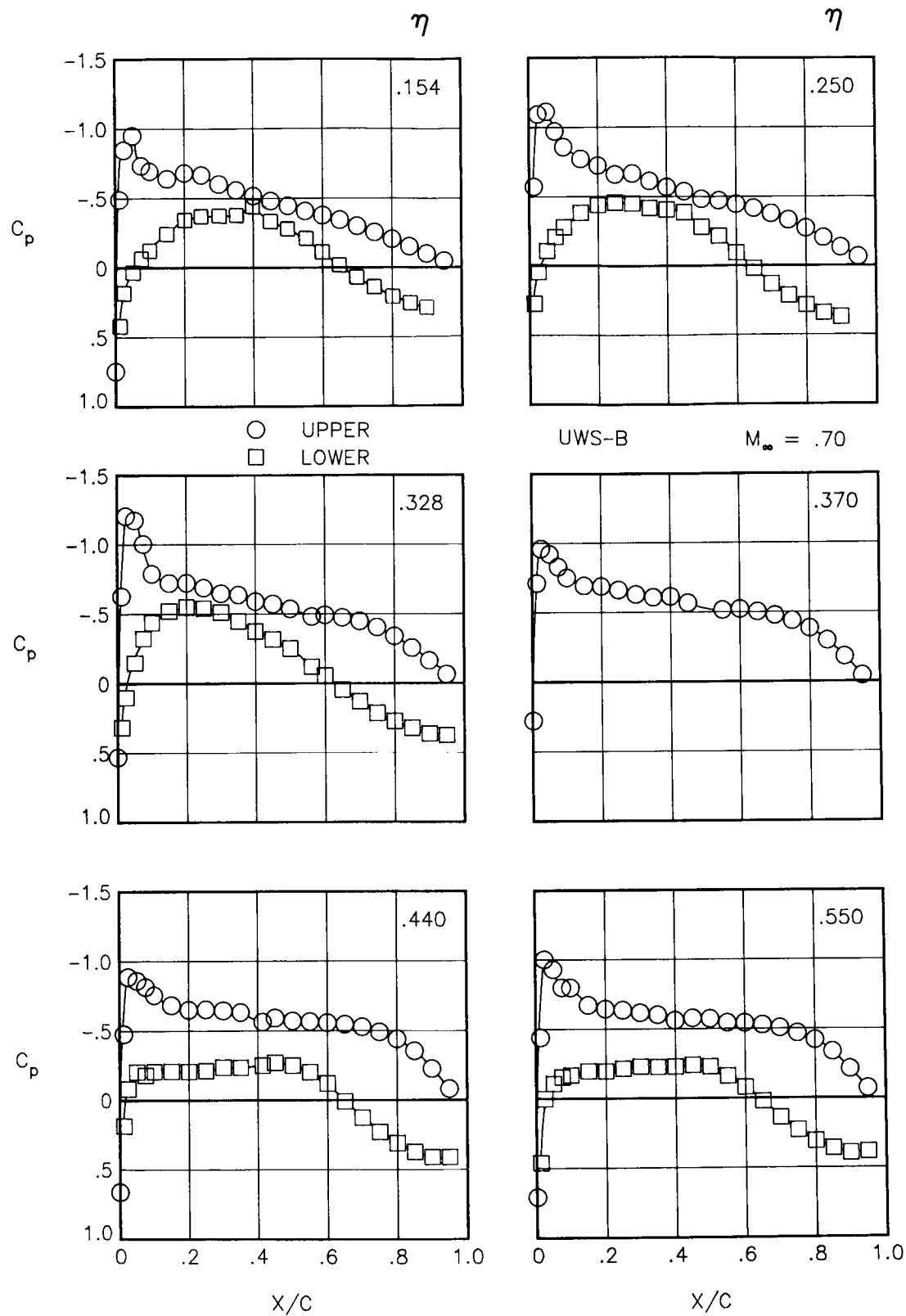
(a)  $\alpha = 0.17^\circ$ ;  $C_L = 0.24$ .

Figure 22.- Chordwise pressure coefficient distributions for configuration UWS-B at various angles of attack and  $M_\infty = 0.70$ .



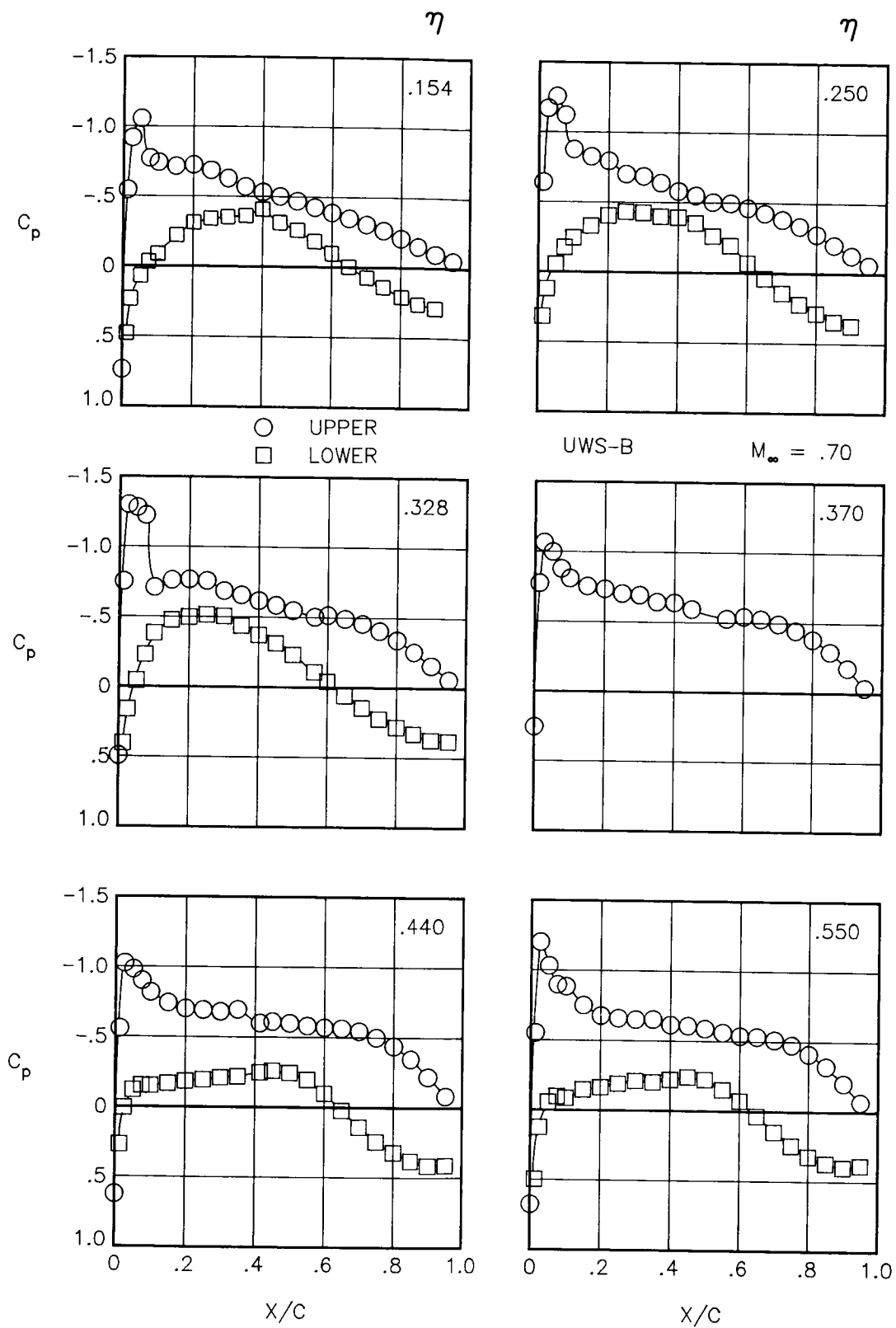
(b)  $\alpha = 1.18^\circ$ ;  $C_L = 0.36$ .

Figure 22.- Continued.



(c)  $\alpha = 1.66^\circ$ ;  $C_L = 0.42$ .

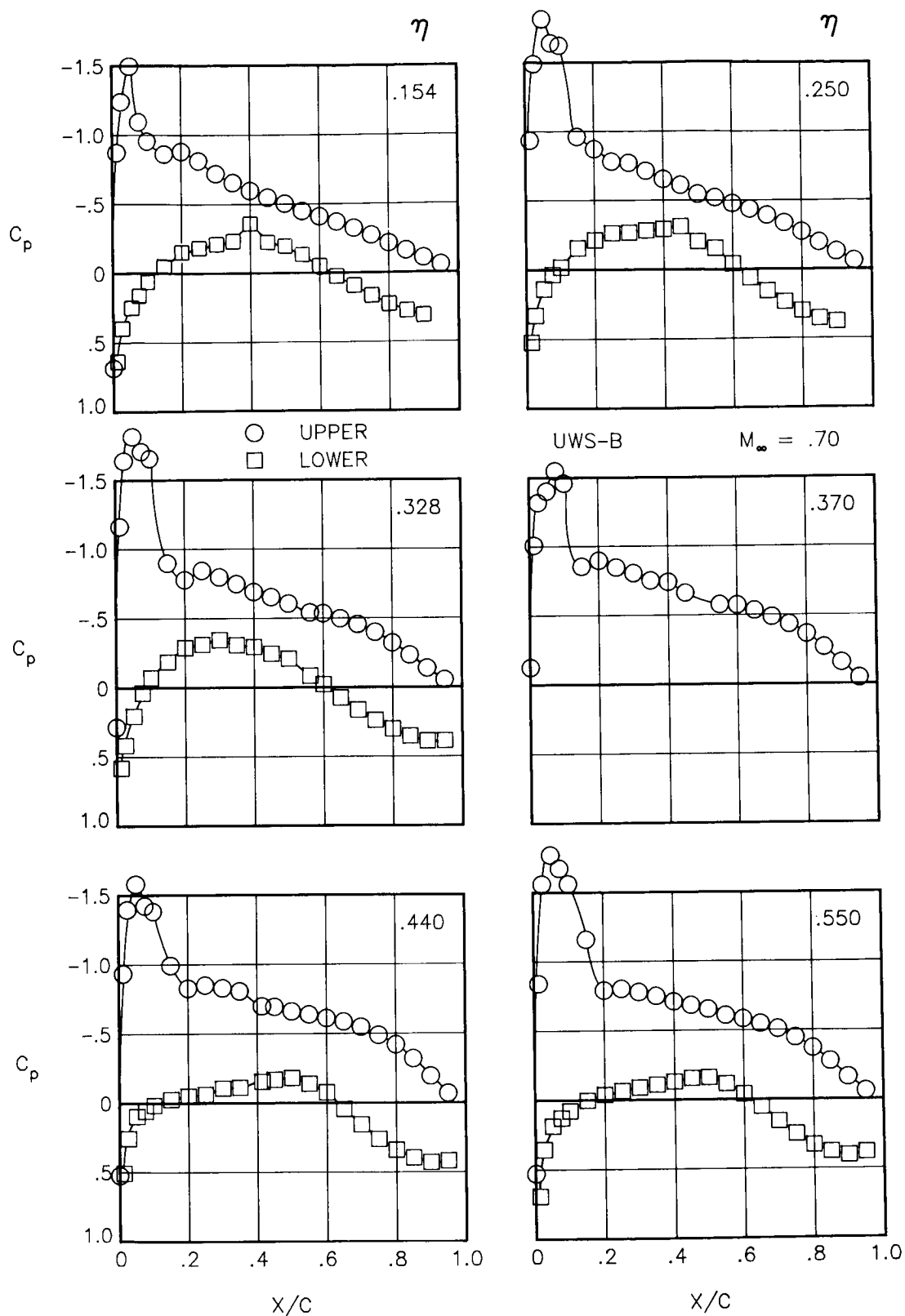
Figure 22.- Continued.



(d)  $\alpha = 2.17^\circ$ ;  $C_L = 0.47$ .

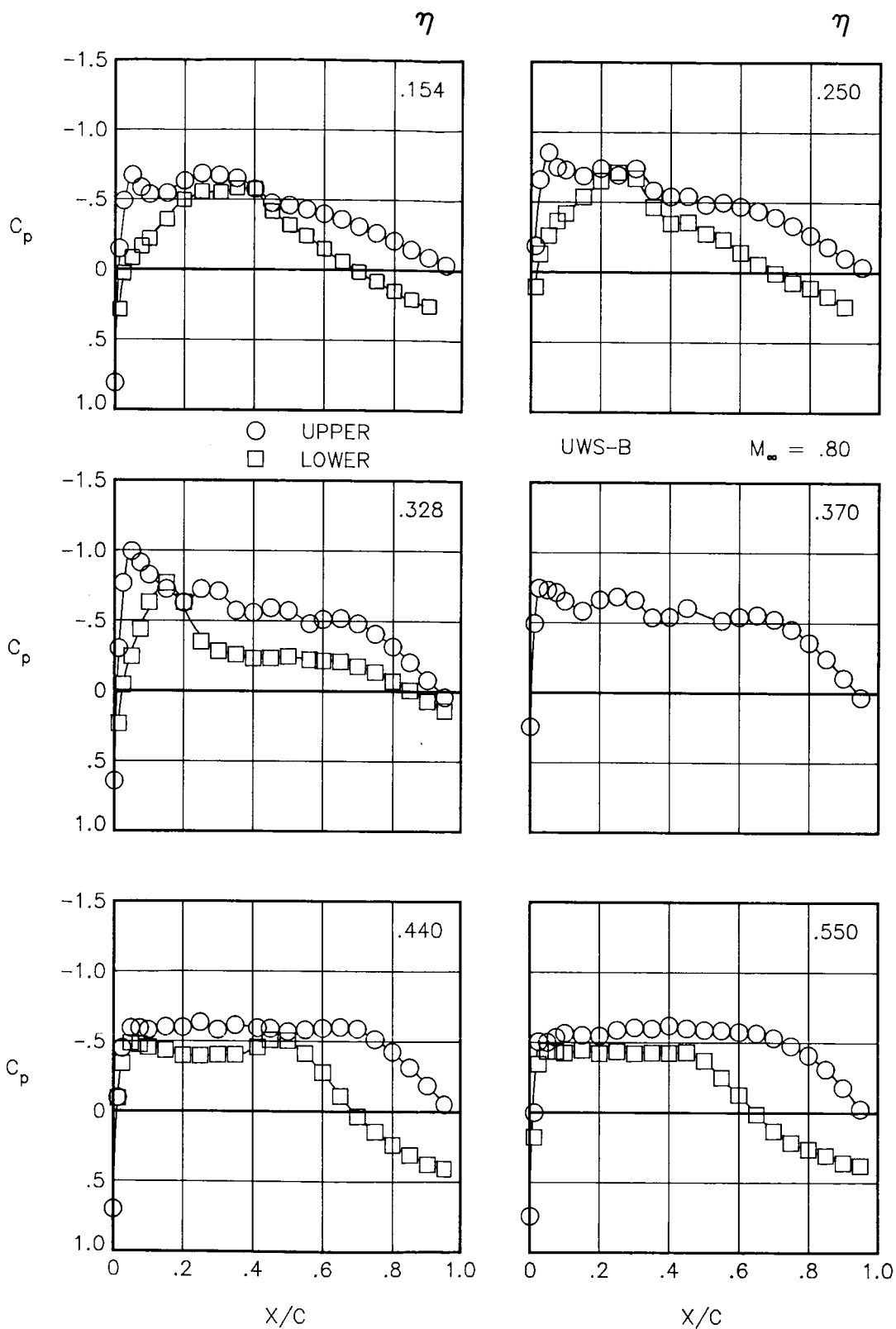
Figure 22.- Continued.





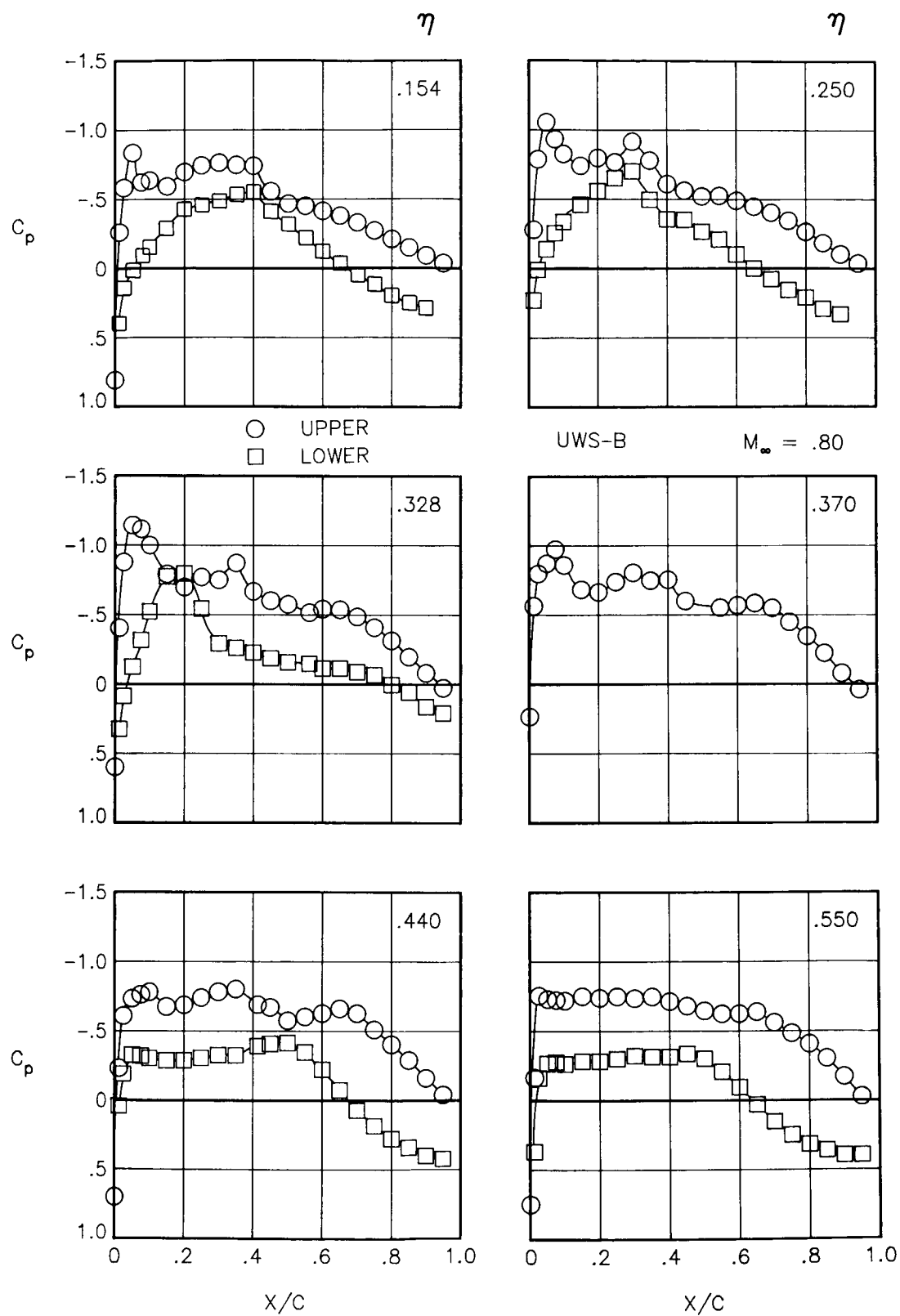
(e)  $\alpha = 4.12^\circ$ ;  $C_L = 0.70$ .

Figure 22.- Concluded.



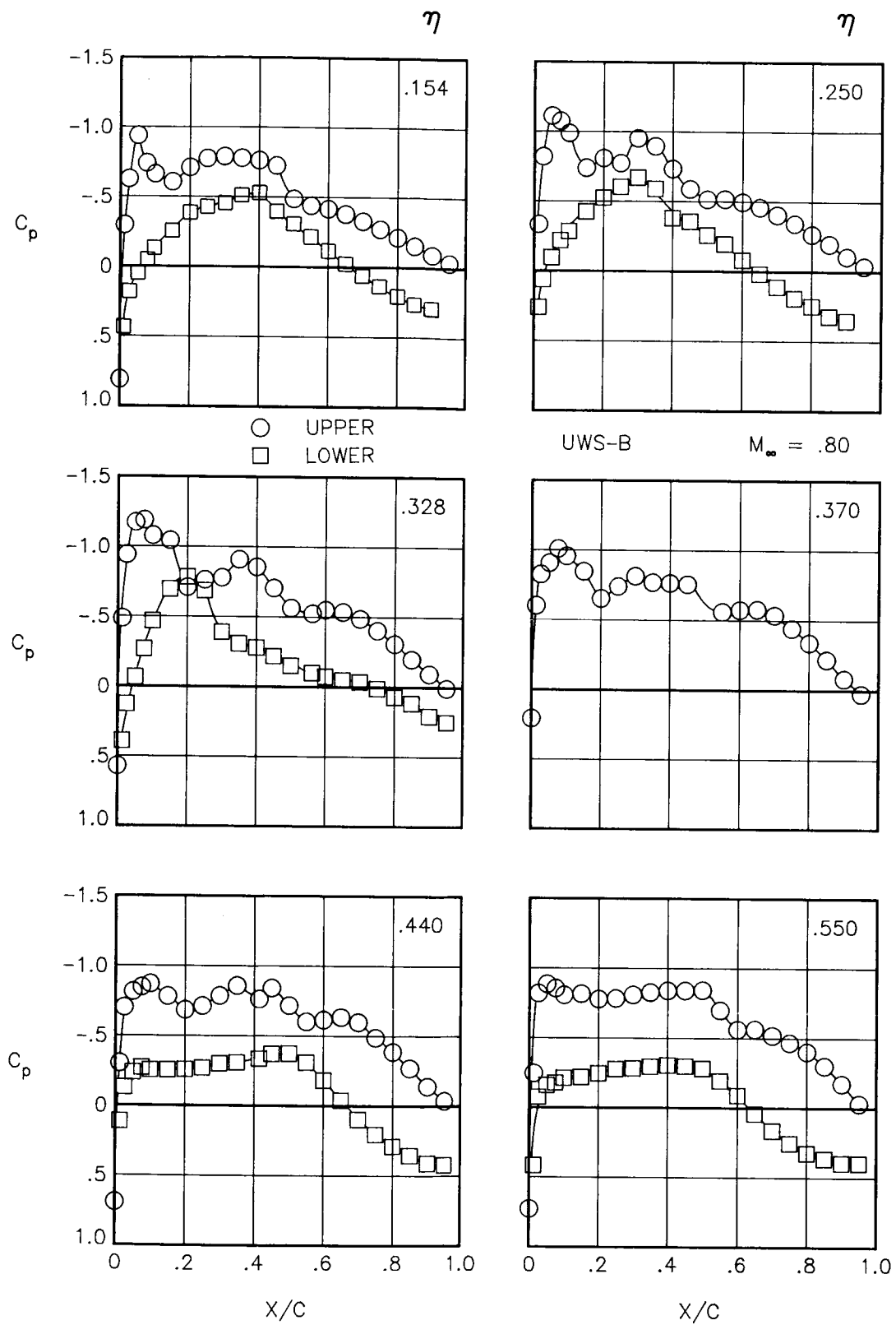
(a)  $\alpha = 0.23^\circ$ ;  $C_L = 0.23$ .

Figure 23.- Chordwise pressure coefficient distributions for configuration UWS-B at various angles of attack and  $M_\infty = 0.80$ .



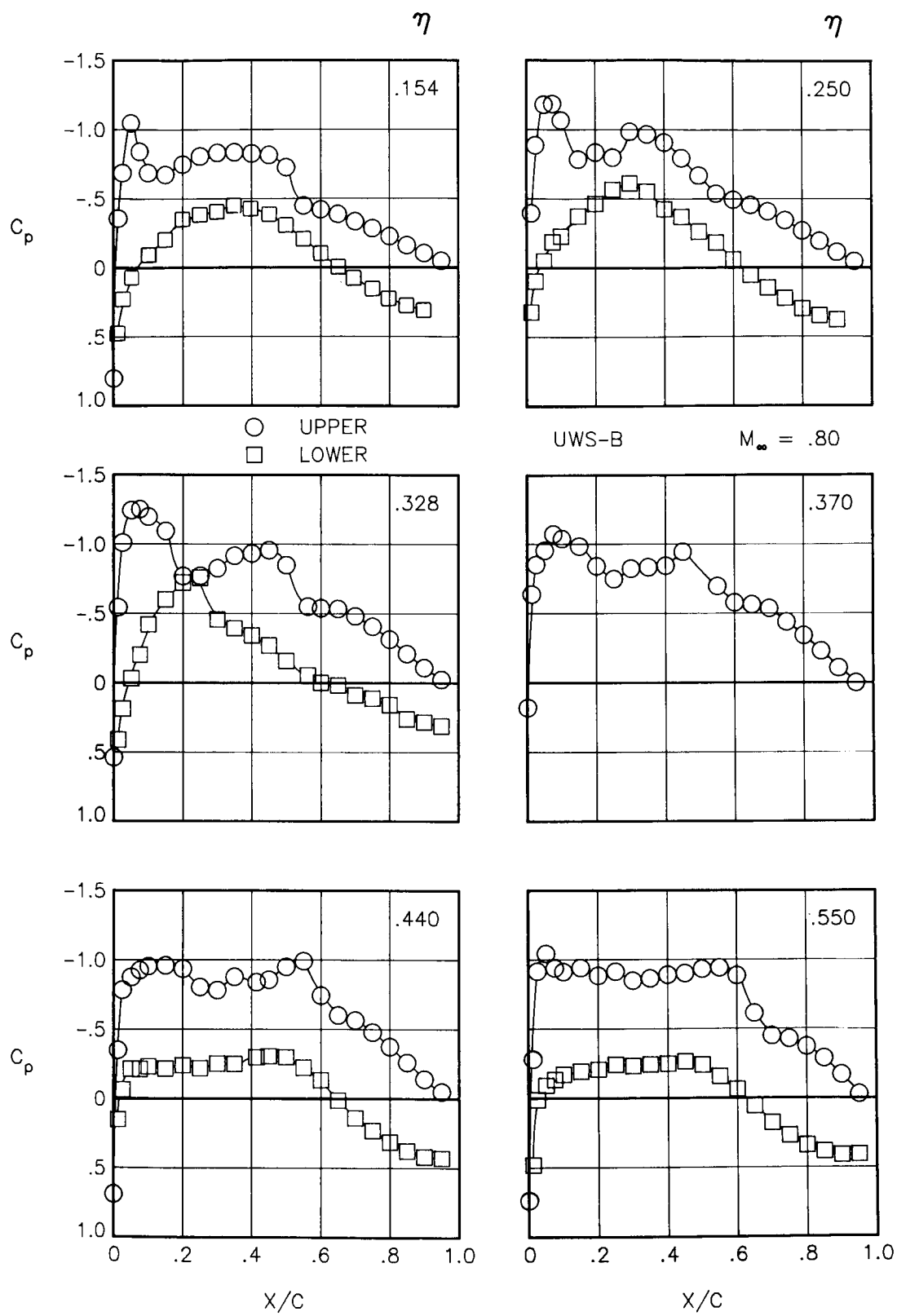
(b)  $\alpha = 1.23^\circ$ ;  $C_L = 0.38$ .

Figure 23.- Continued.



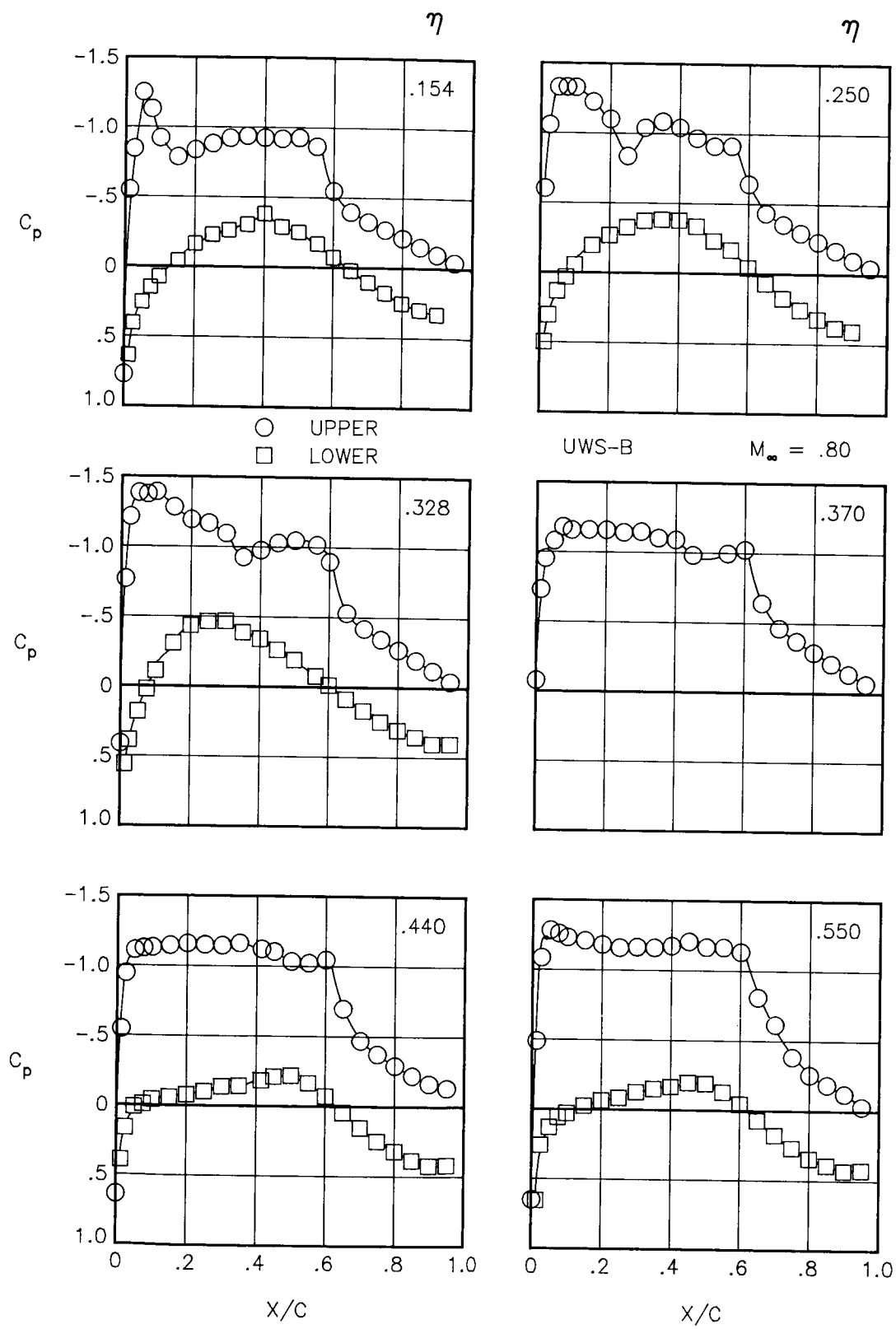
(c)  $\alpha = 1.73^\circ$ ;  $C_L = 0.46$ .

Figure 23.- Continued.



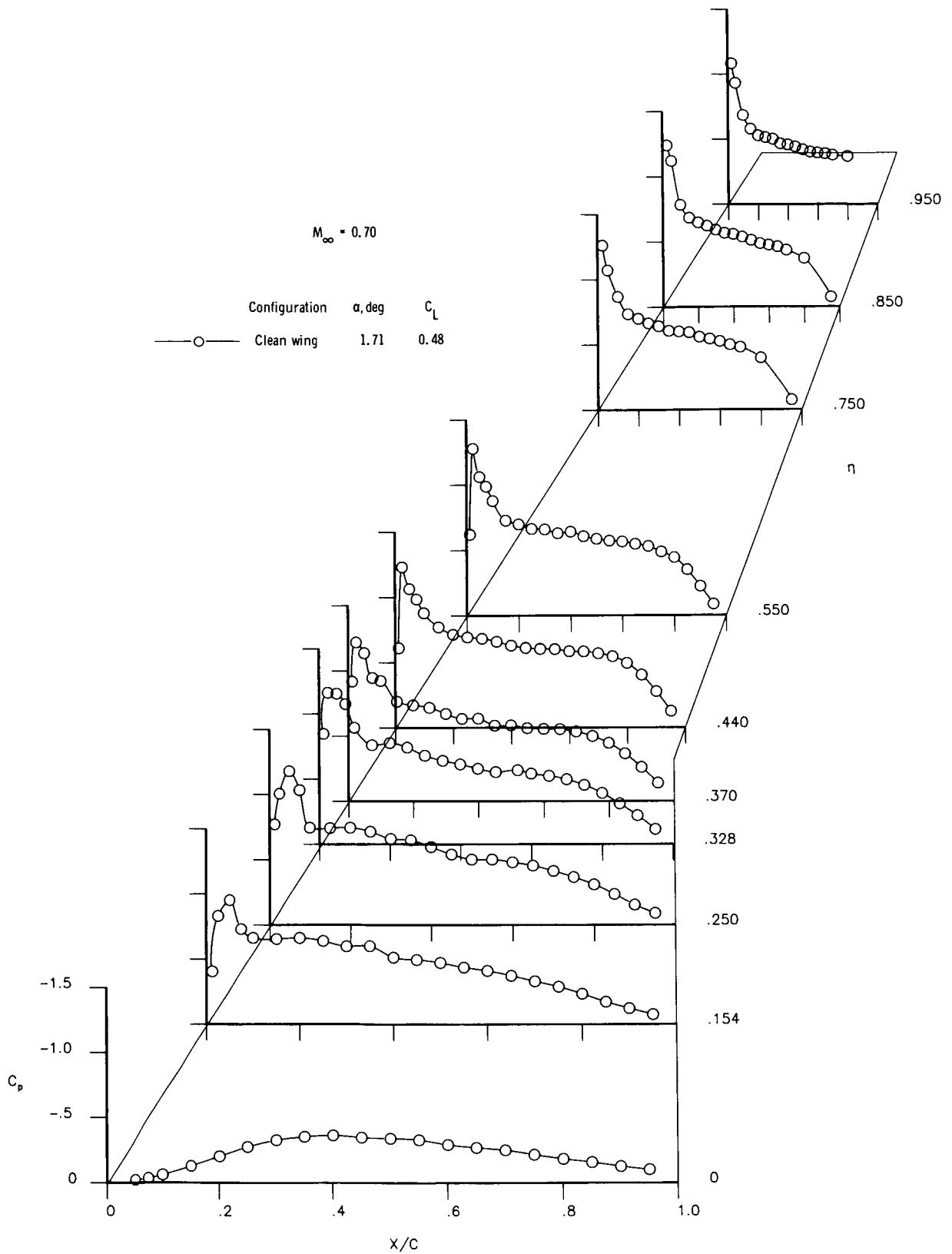
(d)  $\alpha = 2.21^\circ$ ;  $C_L = 0.54$ .

Figure 23.- Continued.



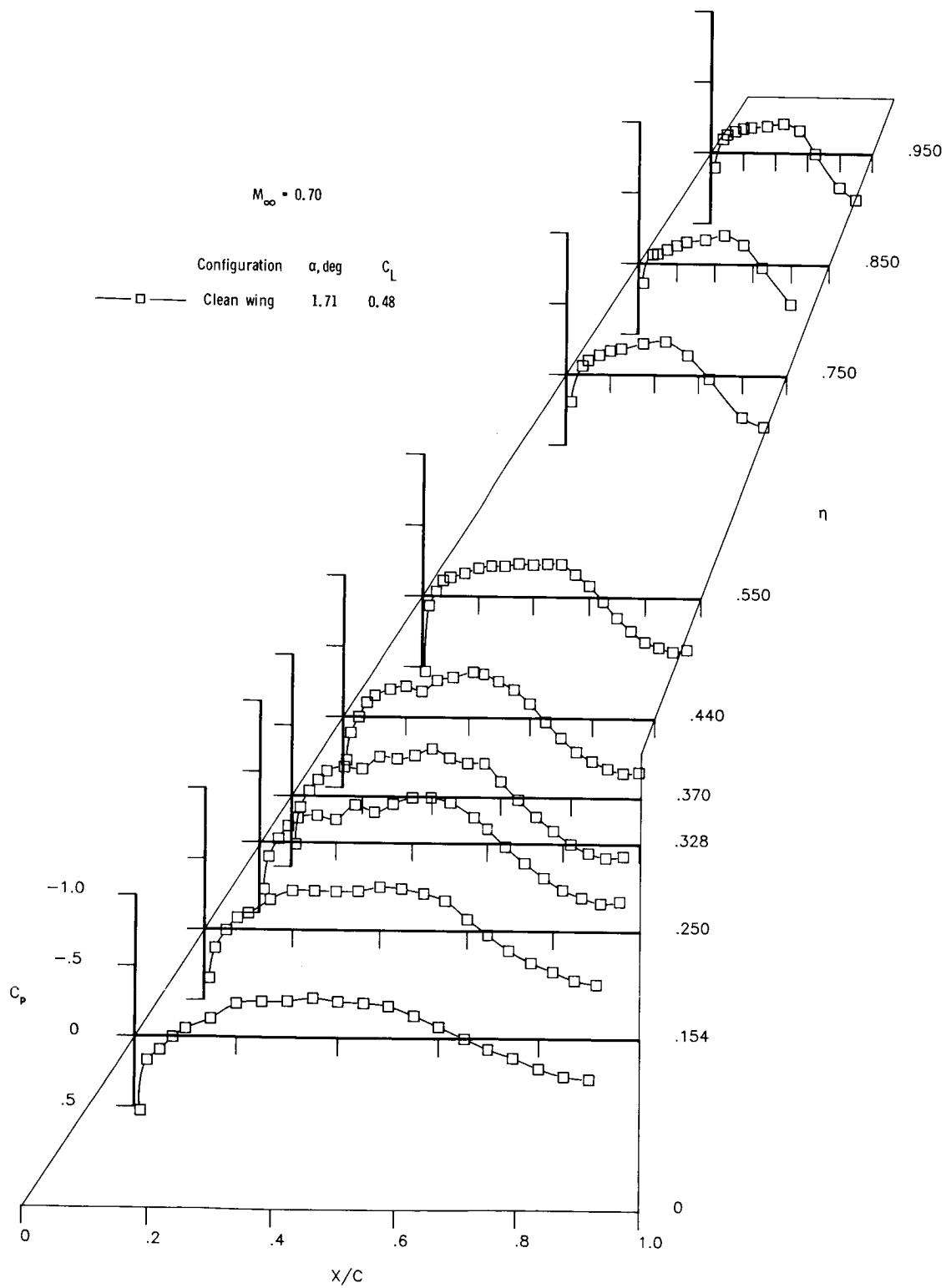
(e)  $\alpha = 4.21^\circ$ ;  $C_L = 0.80$ .

Figure 23.- Concluded.



(a) Upper surface.

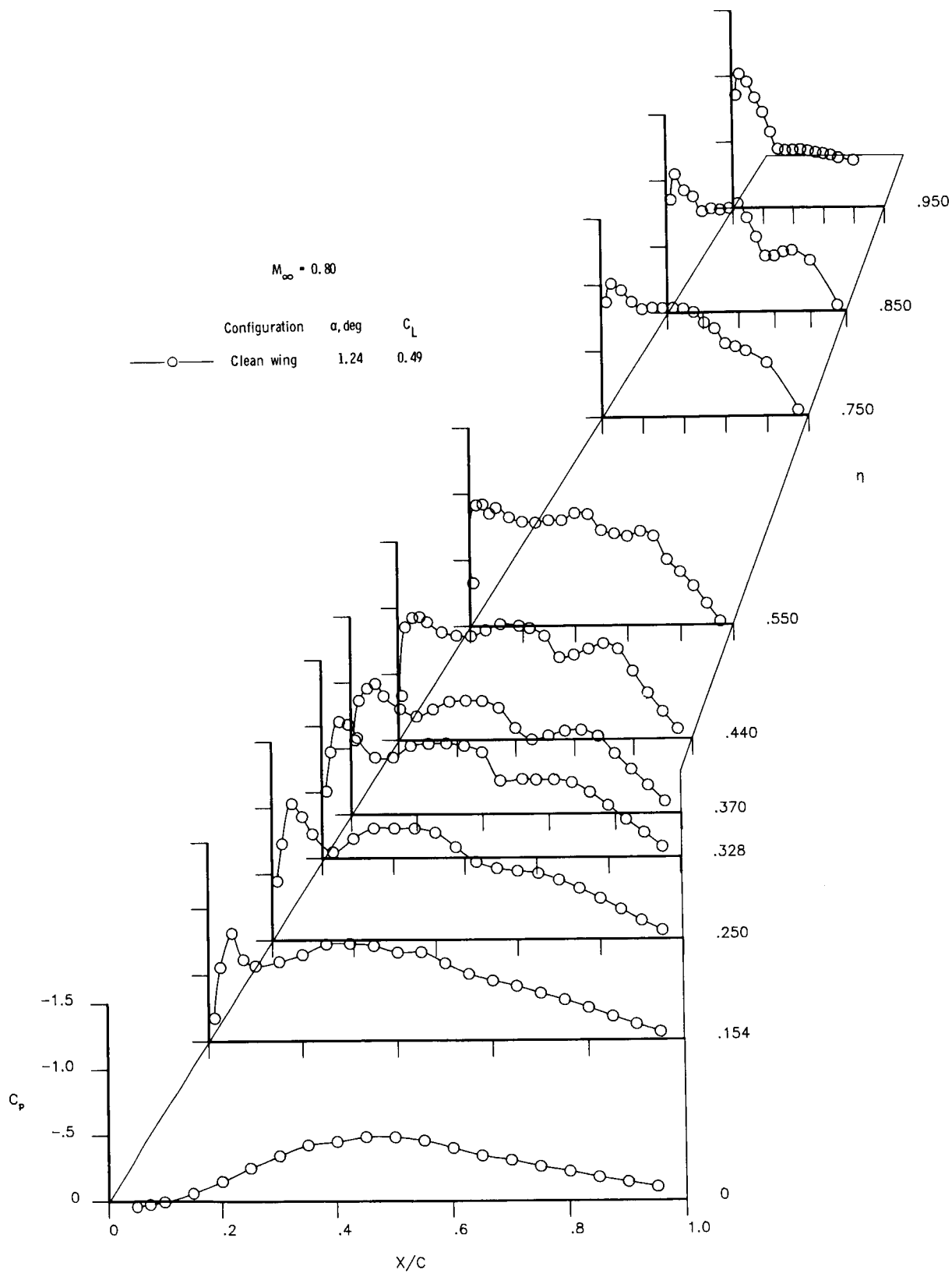
Figure 24.- Pressure coefficient characteristics of clean-wing configuration at near-cruise lift coefficient and  $M_\infty = 0.70$ .



(b) Lower surface.

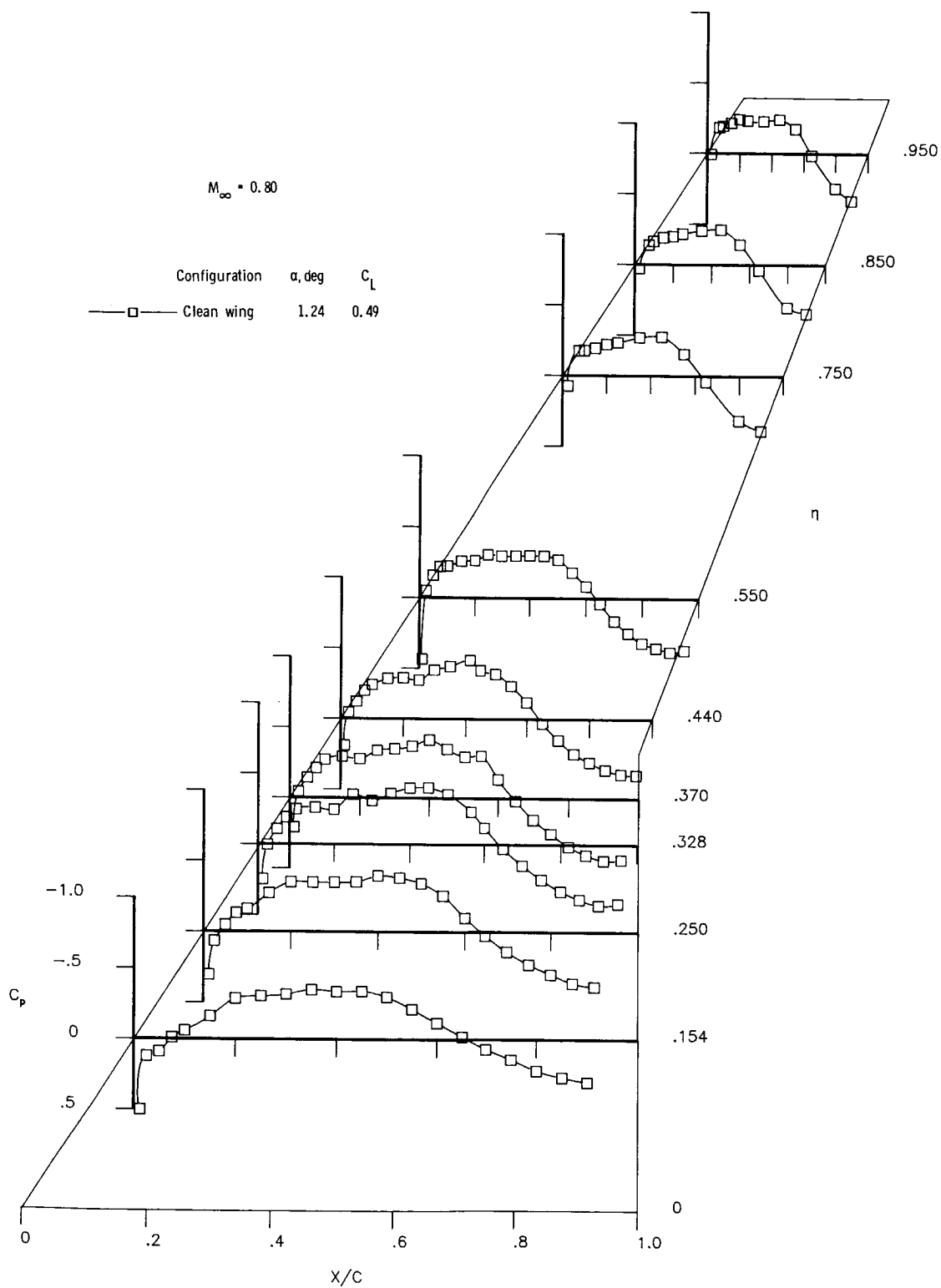
Figure 24.- Concluded.





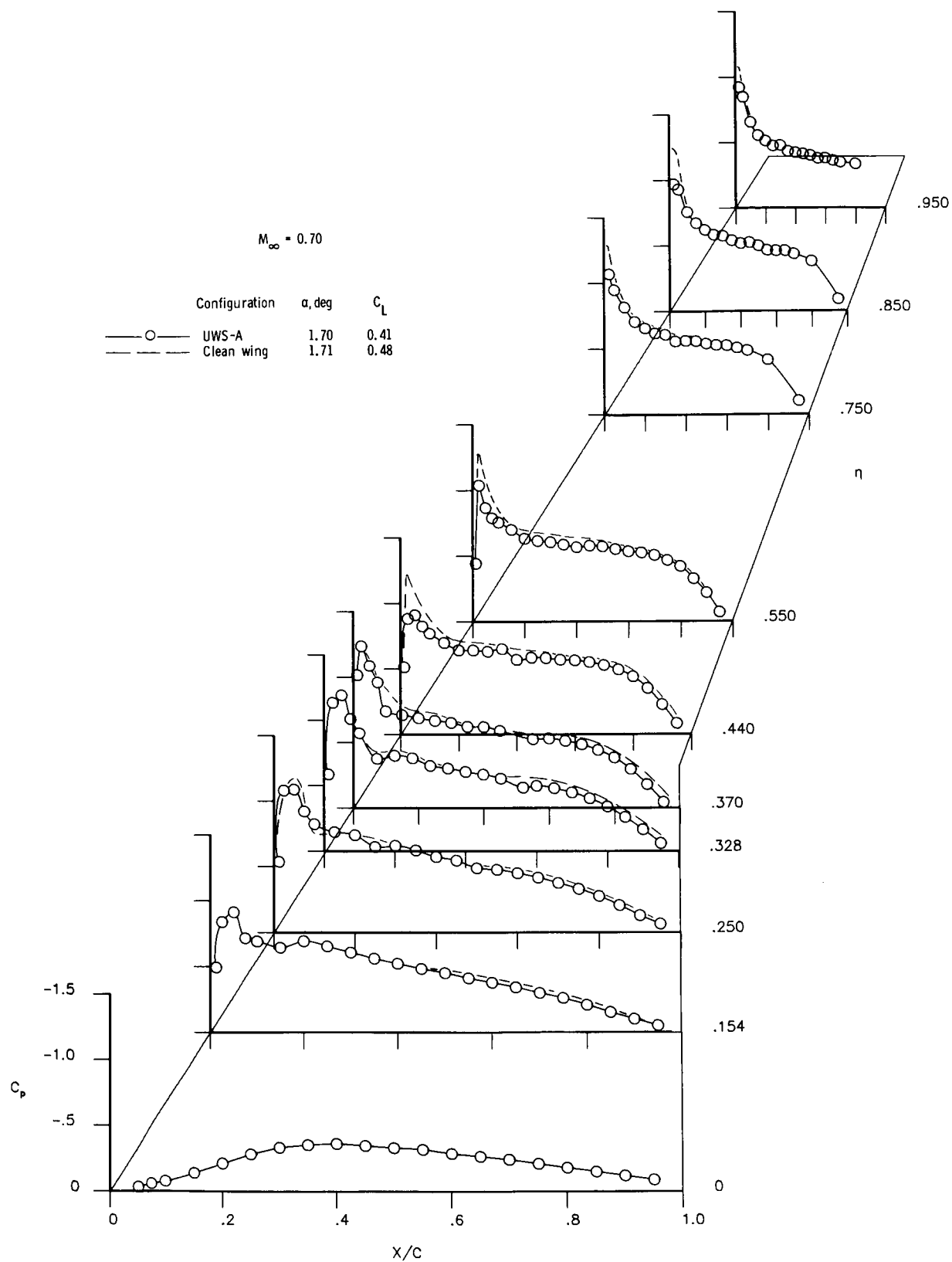
(a) Upper surface.

Figure 25.- Pressure coefficient characteristics of clean-wing configuration at near-cruise lift coefficient and  $M_\infty = 0.80$ .



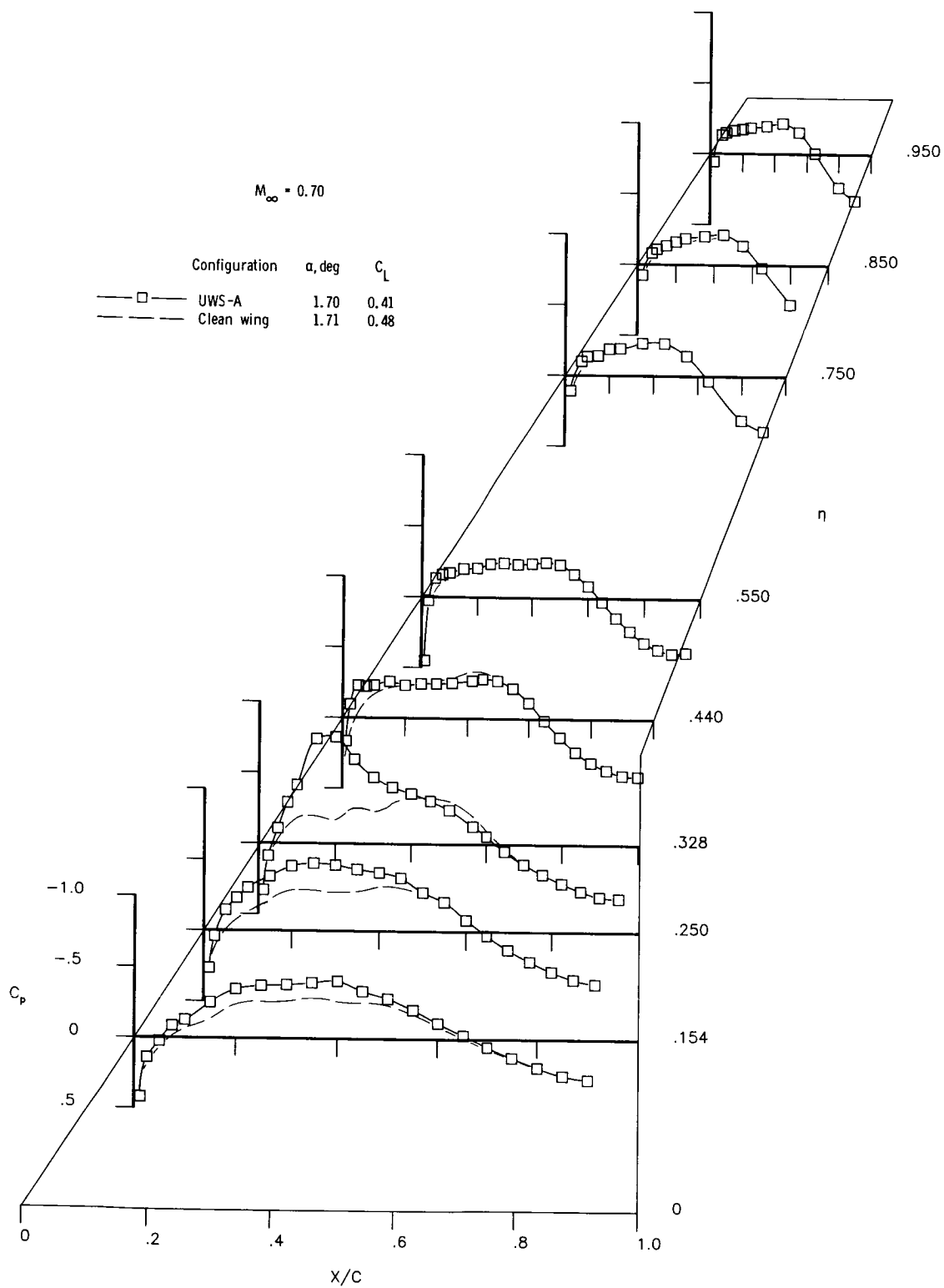
(b) Lower surface.

Figure 25.- Concluded.



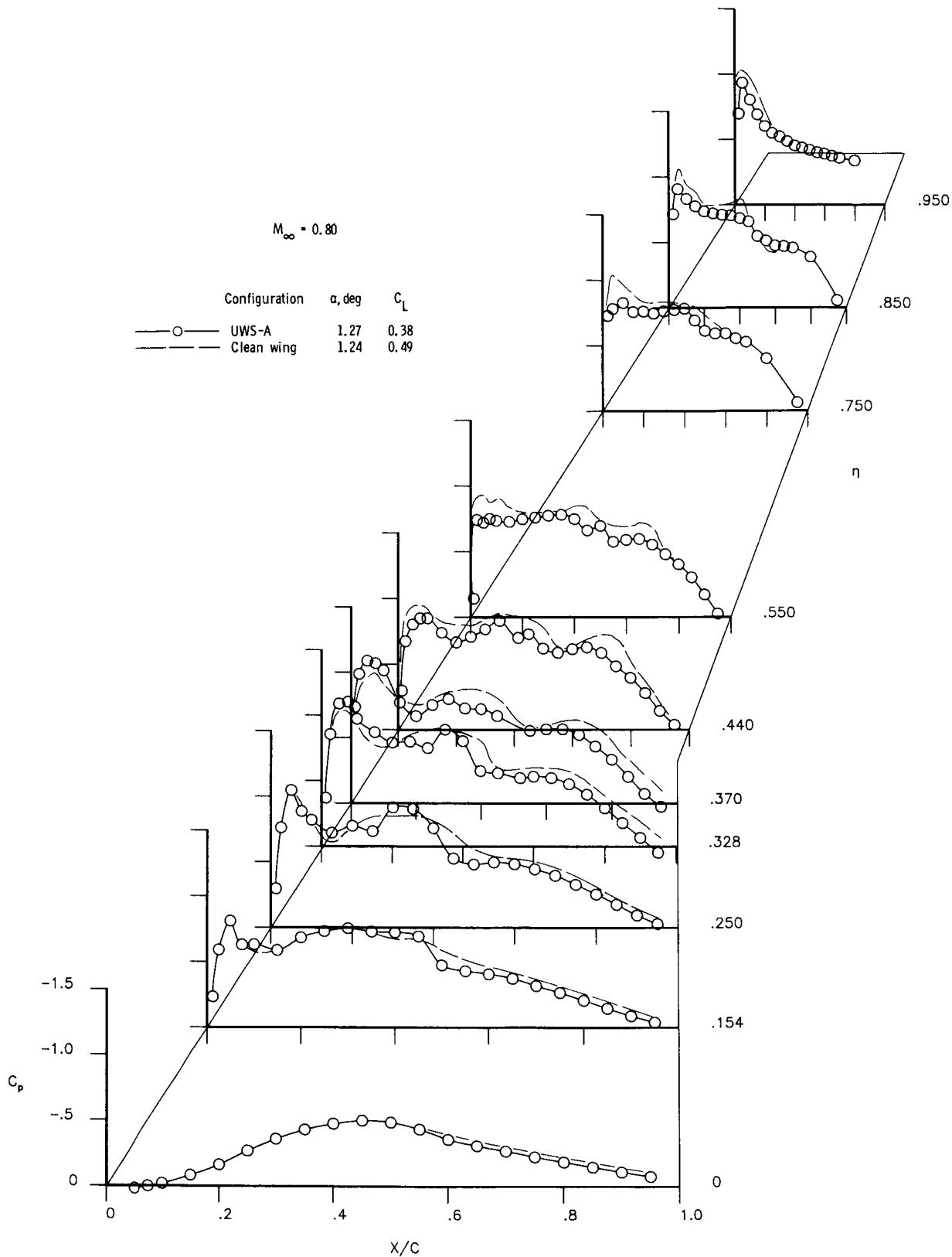
(a) Upper surface.

Figure 26.- Influence of configuration UWS-A nacelle on wing pressure coefficients at near-cruise lift coefficient and  $M_\infty = 0.70$ .



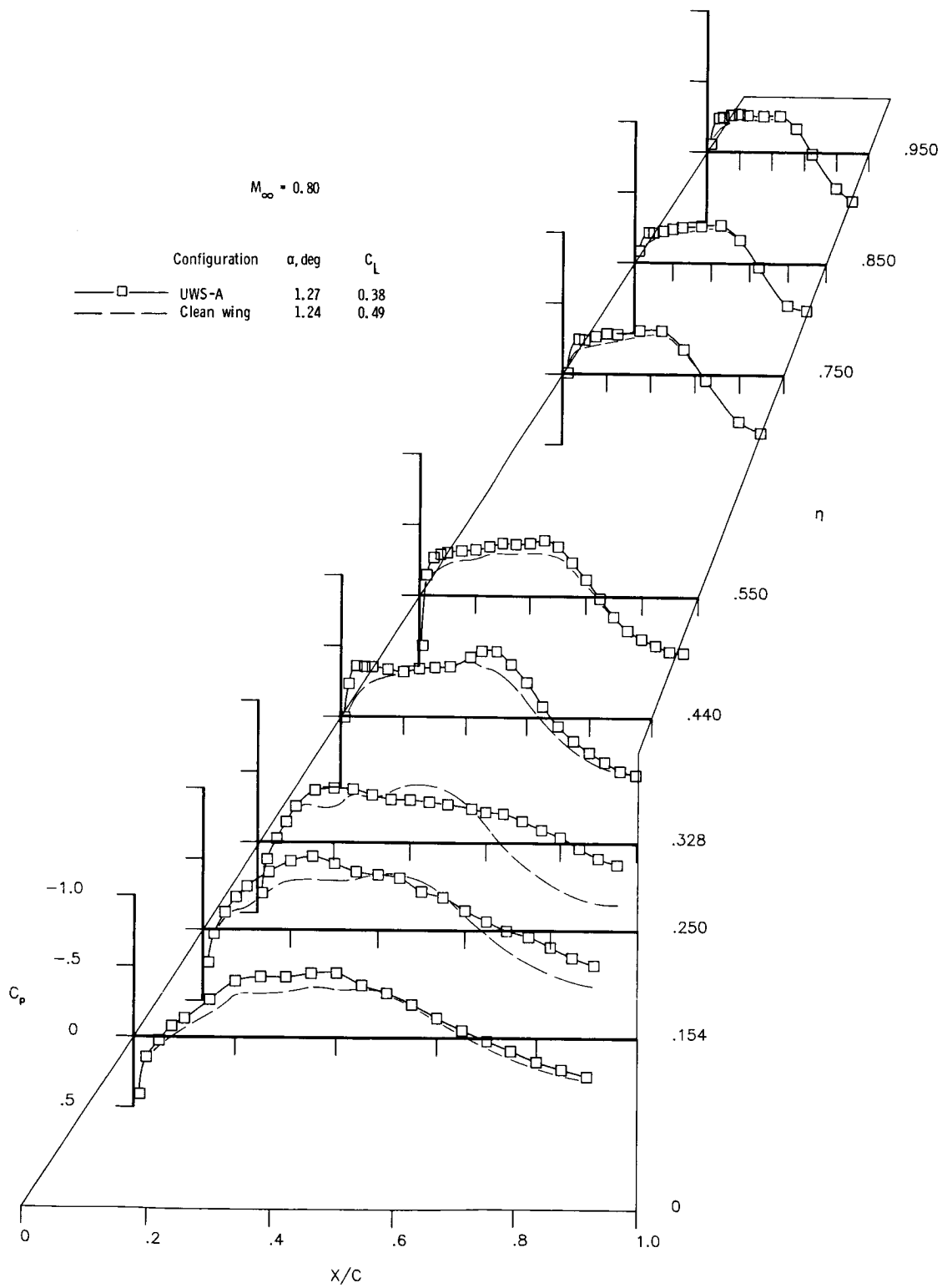
(b) Lower surface.

Figure 26.- Concluded.



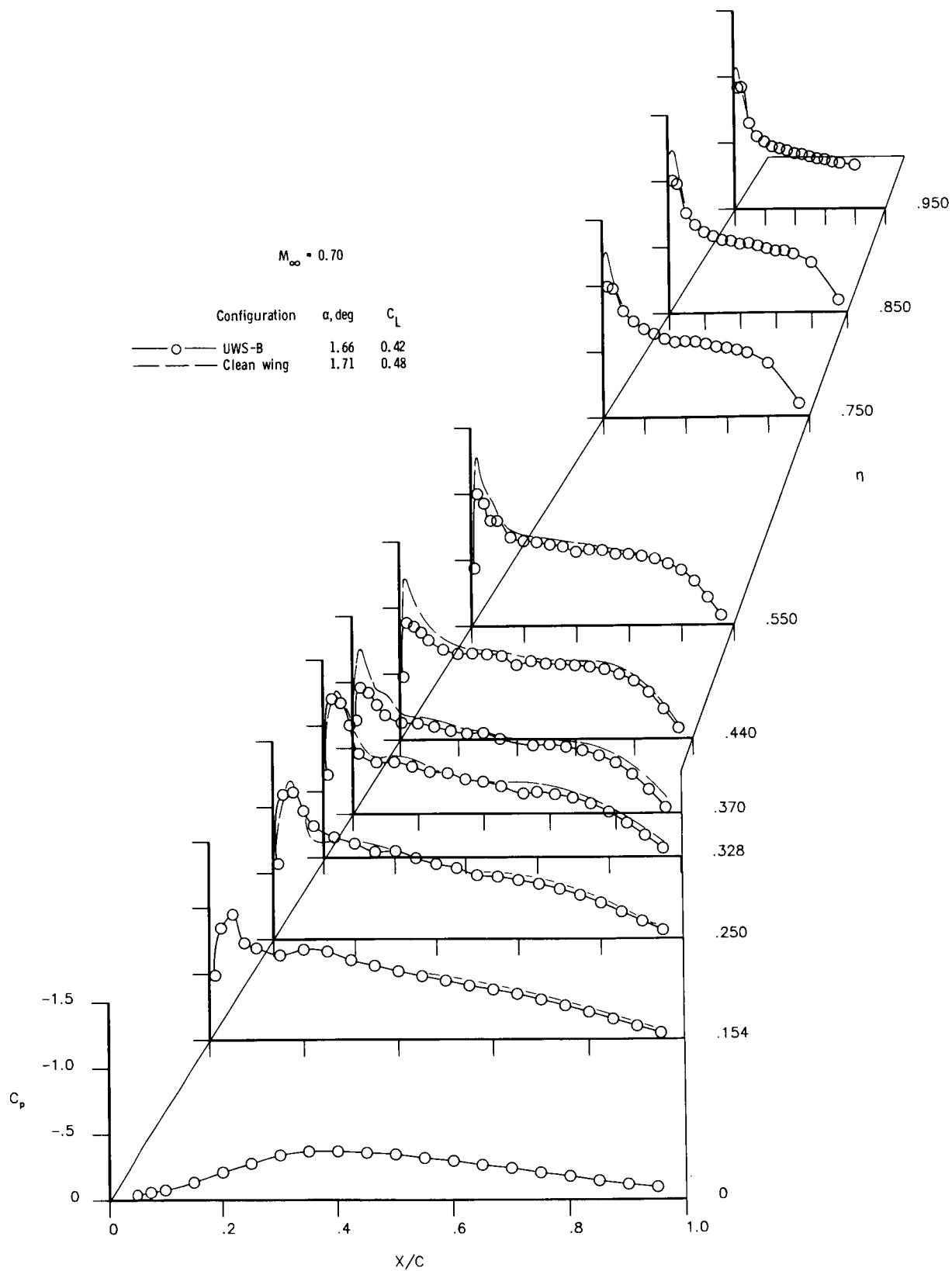
(a) Upper surface.

Figure 27.- Influence of configuration UWS-A nacelle on wing pressure coefficients at near-cruise lift coefficient and  $M_\infty = 0.80$ .



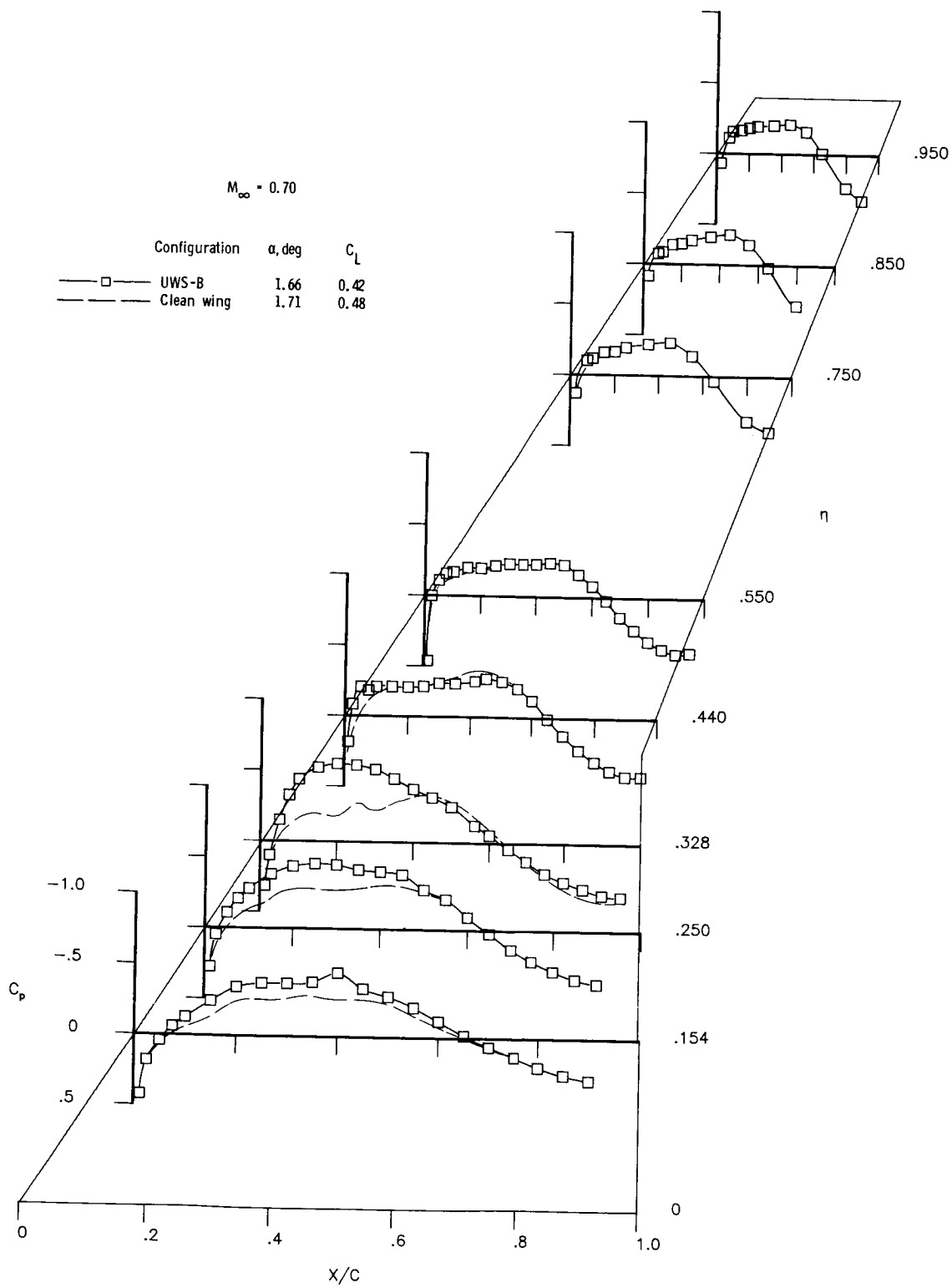
(b) Lower surface.

Figure 27.- Concluded.



(a) Upper surface.

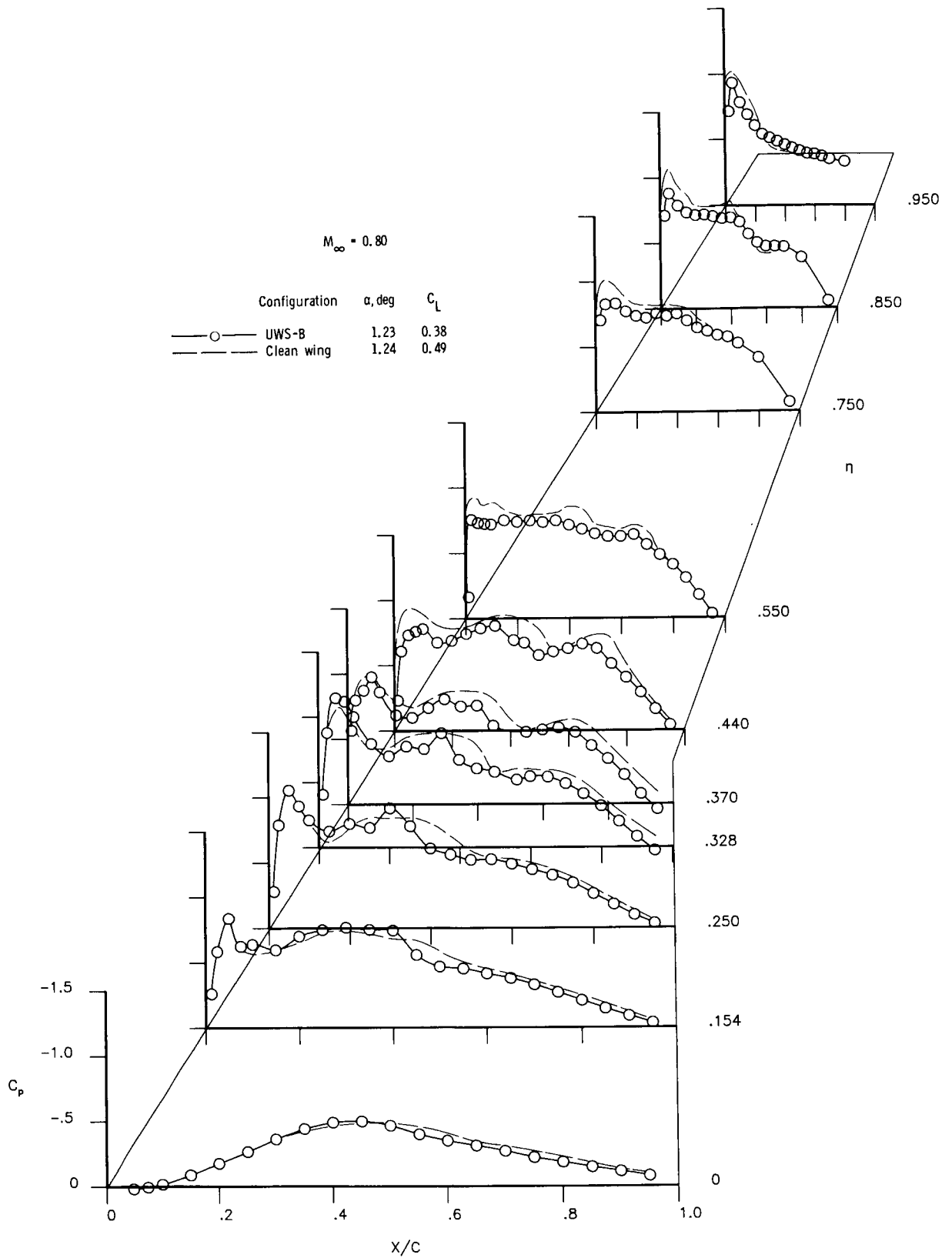
Figure 28.- Influence of configuration UWS-B nacelle on wing pressure coefficients at near-cruise lift coefficient and  $M_\infty = 0.70$ .



(b) Lower surface.

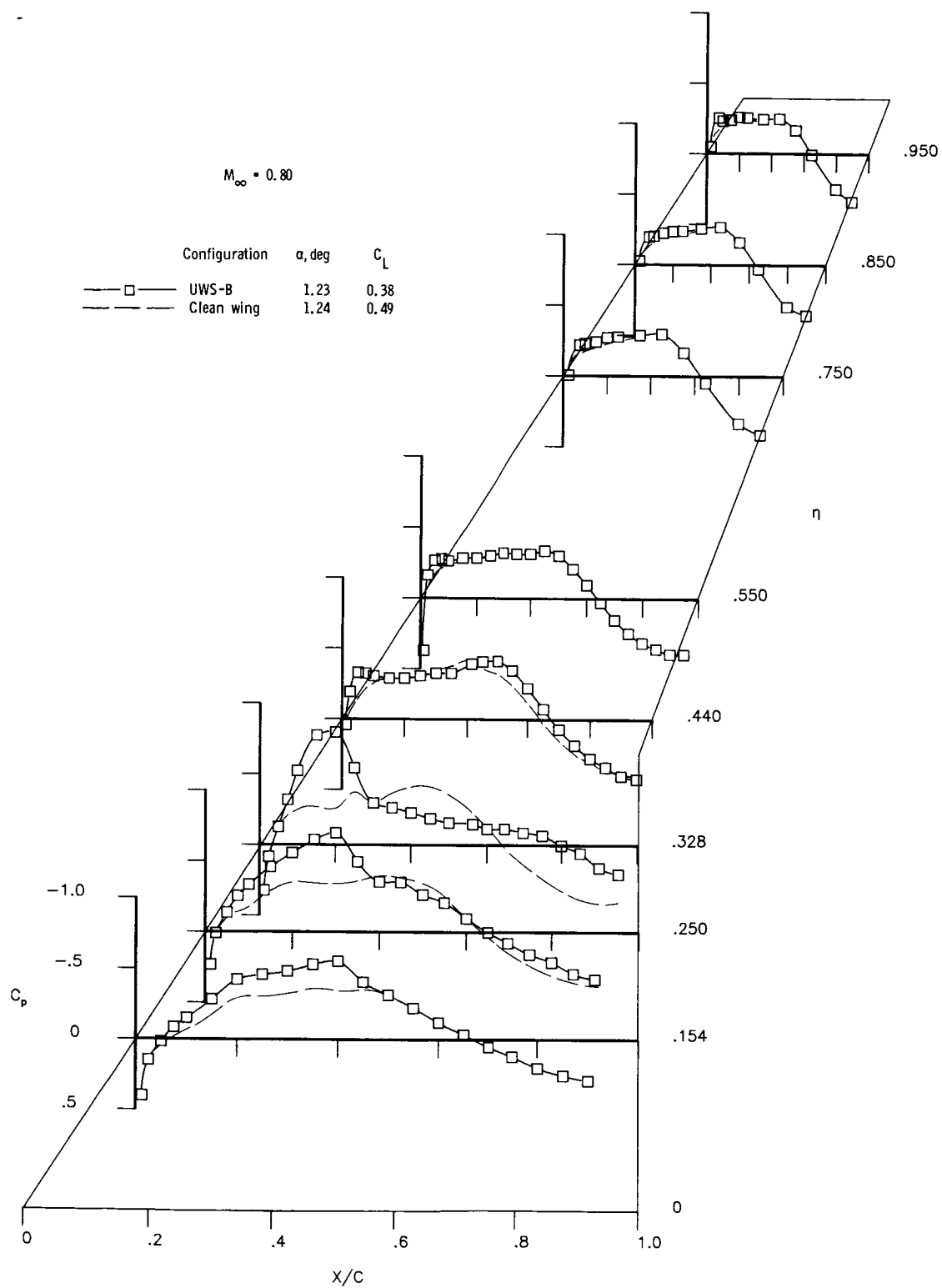
Figure 28.- Concluded.





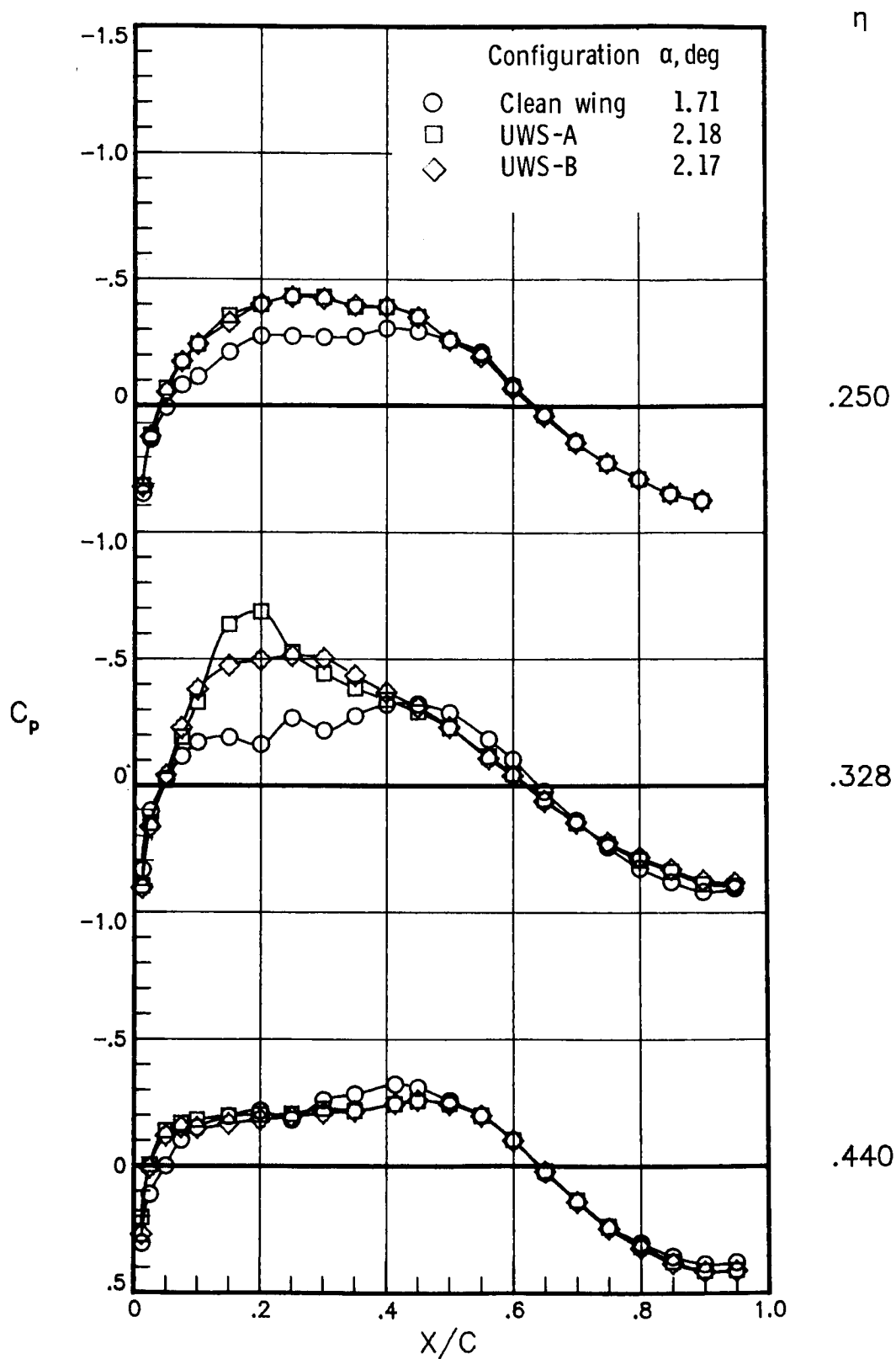
(a) Upper surface.

Figure 29.- Influence of configuration UWS-B nacelle on wing pressure coefficients at near-cruise lift coefficient and  $M_\infty = 0.80$ .



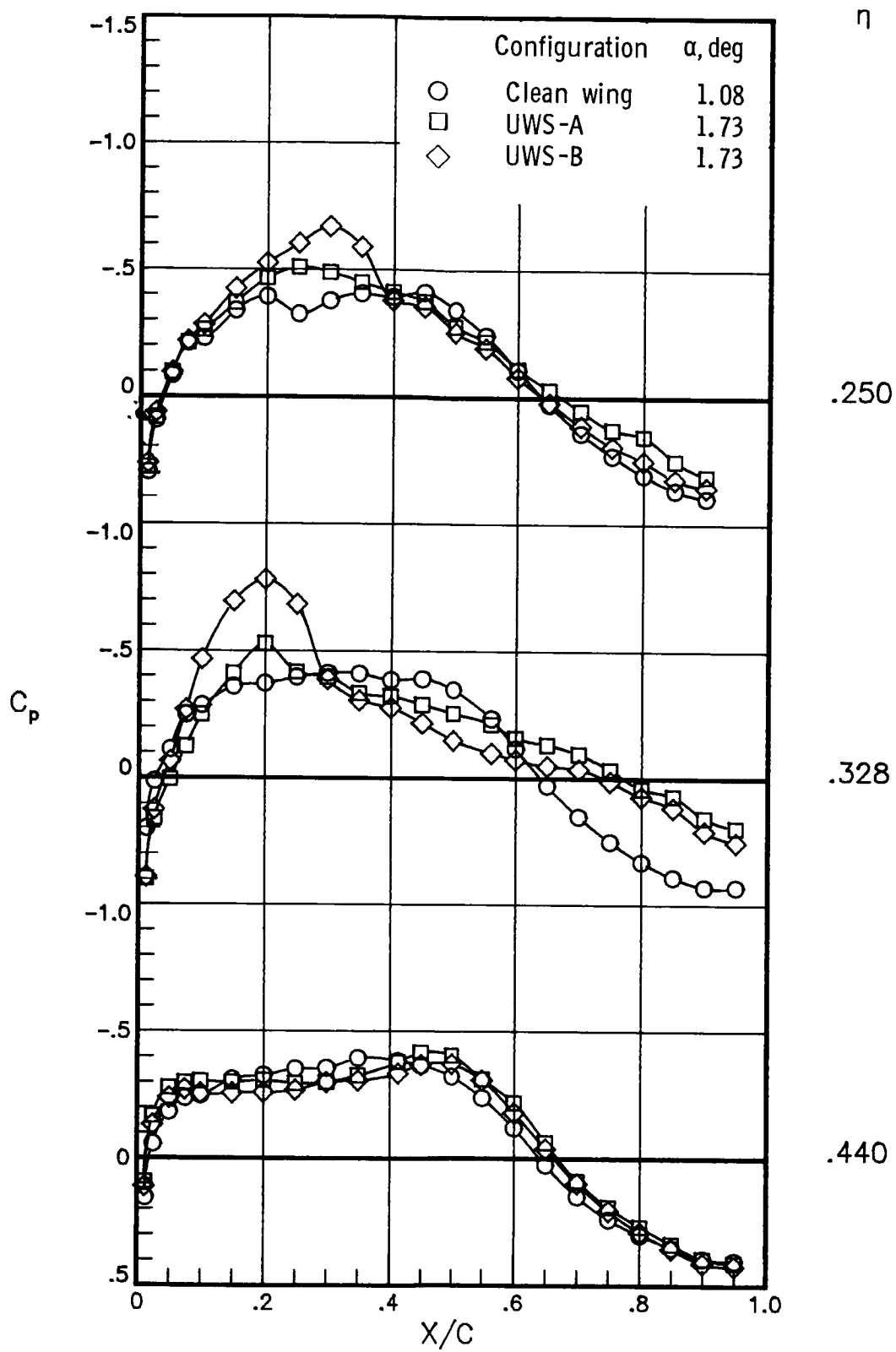
(b) Lower surface.

Figure 29.- Concluded.



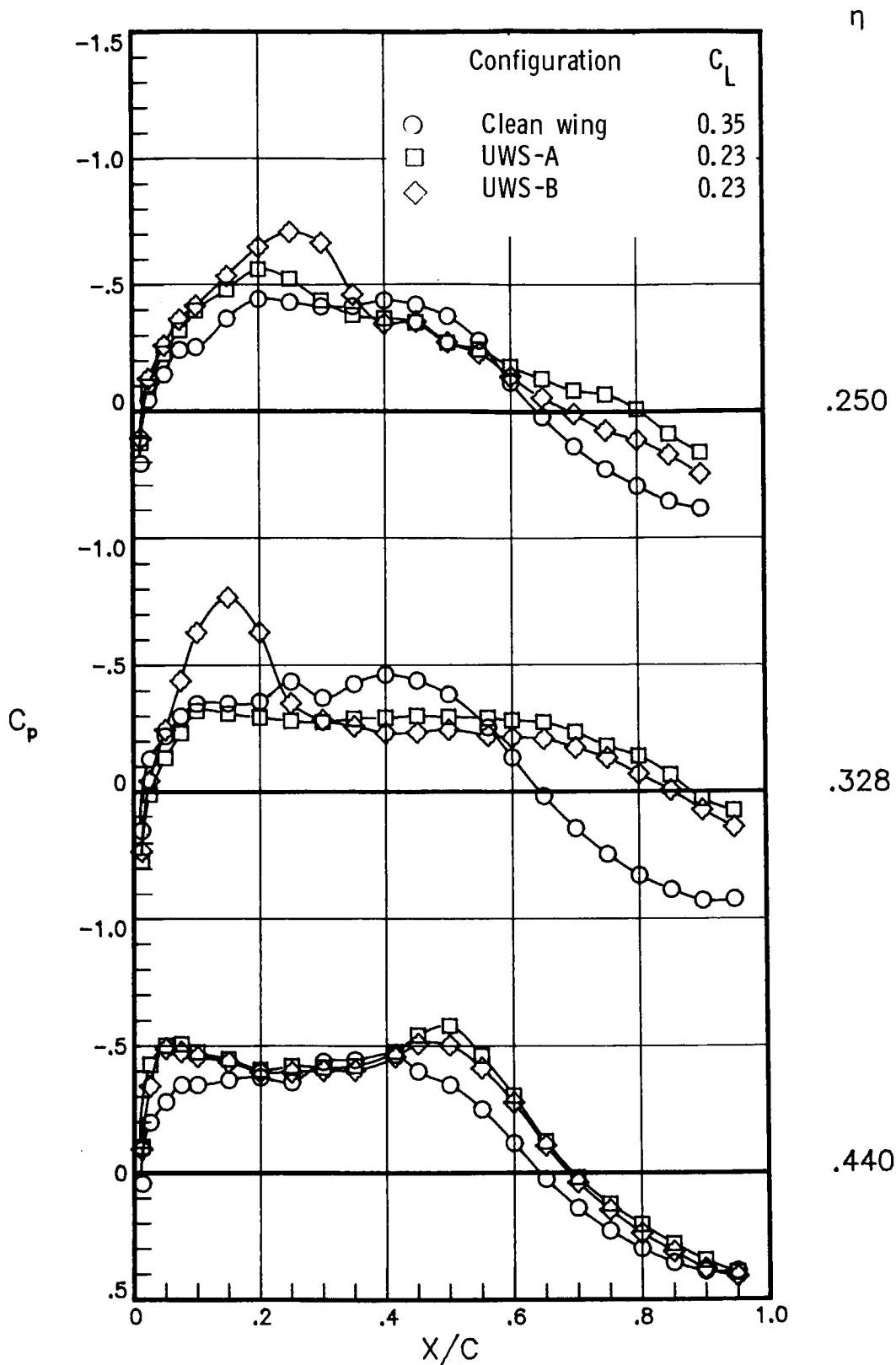
(a)  $M_\infty = 0.70$ ;  $C_L = 0.47$ .

Figure 30.- Local effects of nacelle installations on wing lower surface pressure coefficients at constant lift coefficient.



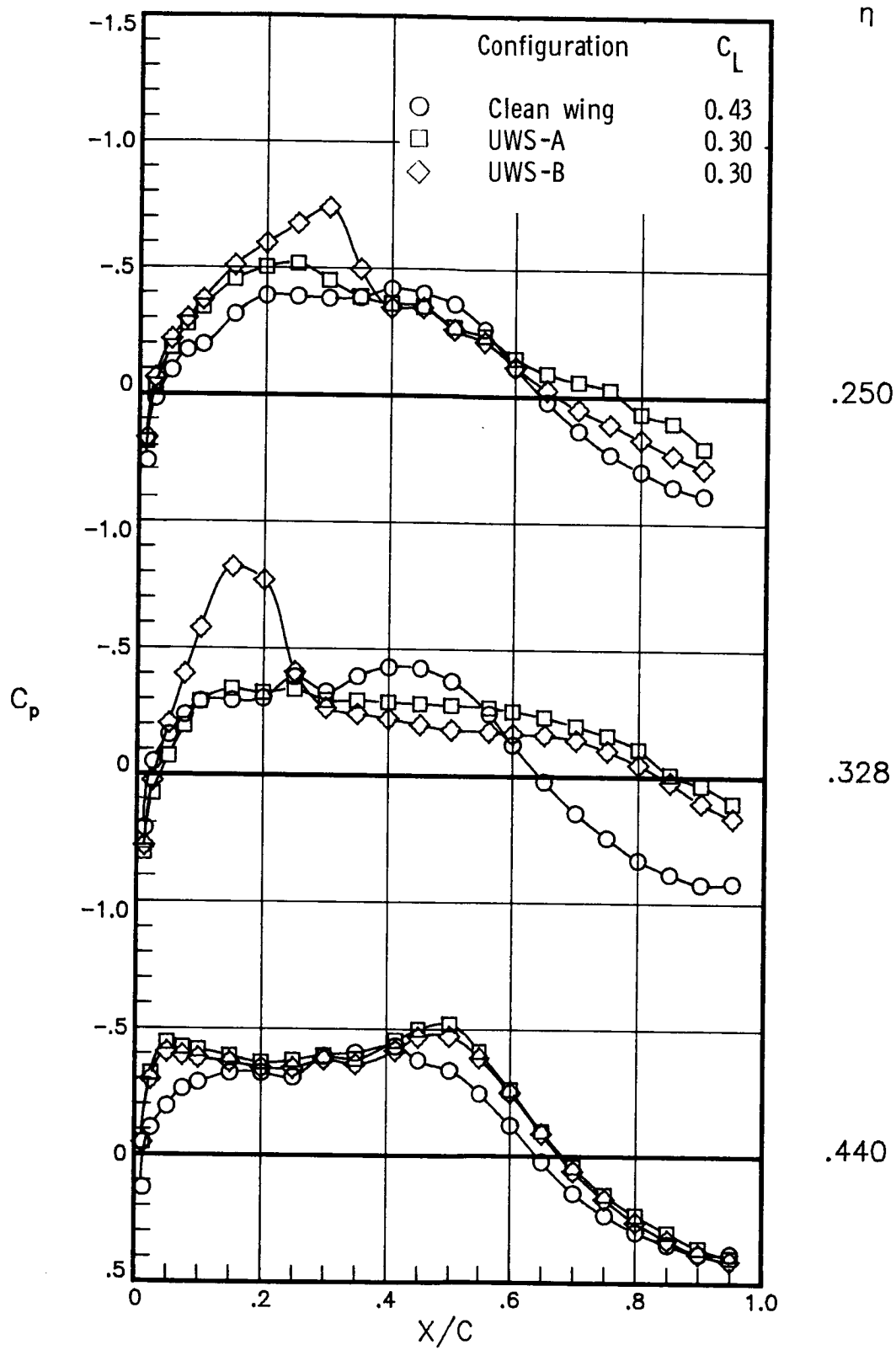
(b)  $M_\infty = 0.80$ ;  $C_{L} = 0.45$ .

Figure 30.- Concluded.



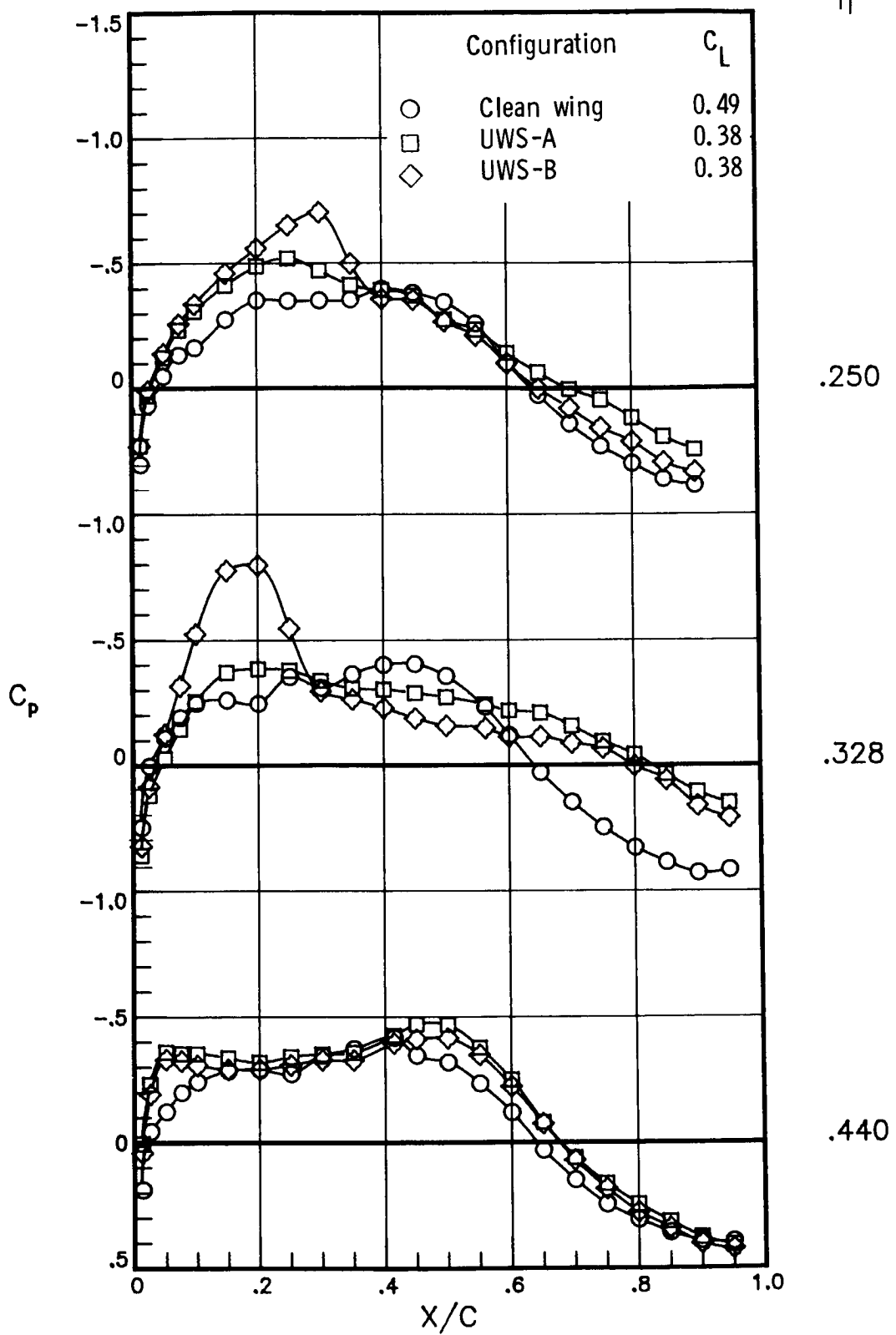
(a)  $\alpha = 0.25^\circ$ ;  $M_\infty = 0.80$ .

Figure 31.- Local effects of nacelle installations on wing lower surface pressure coefficients for various angles of attack at cruise Mach number.



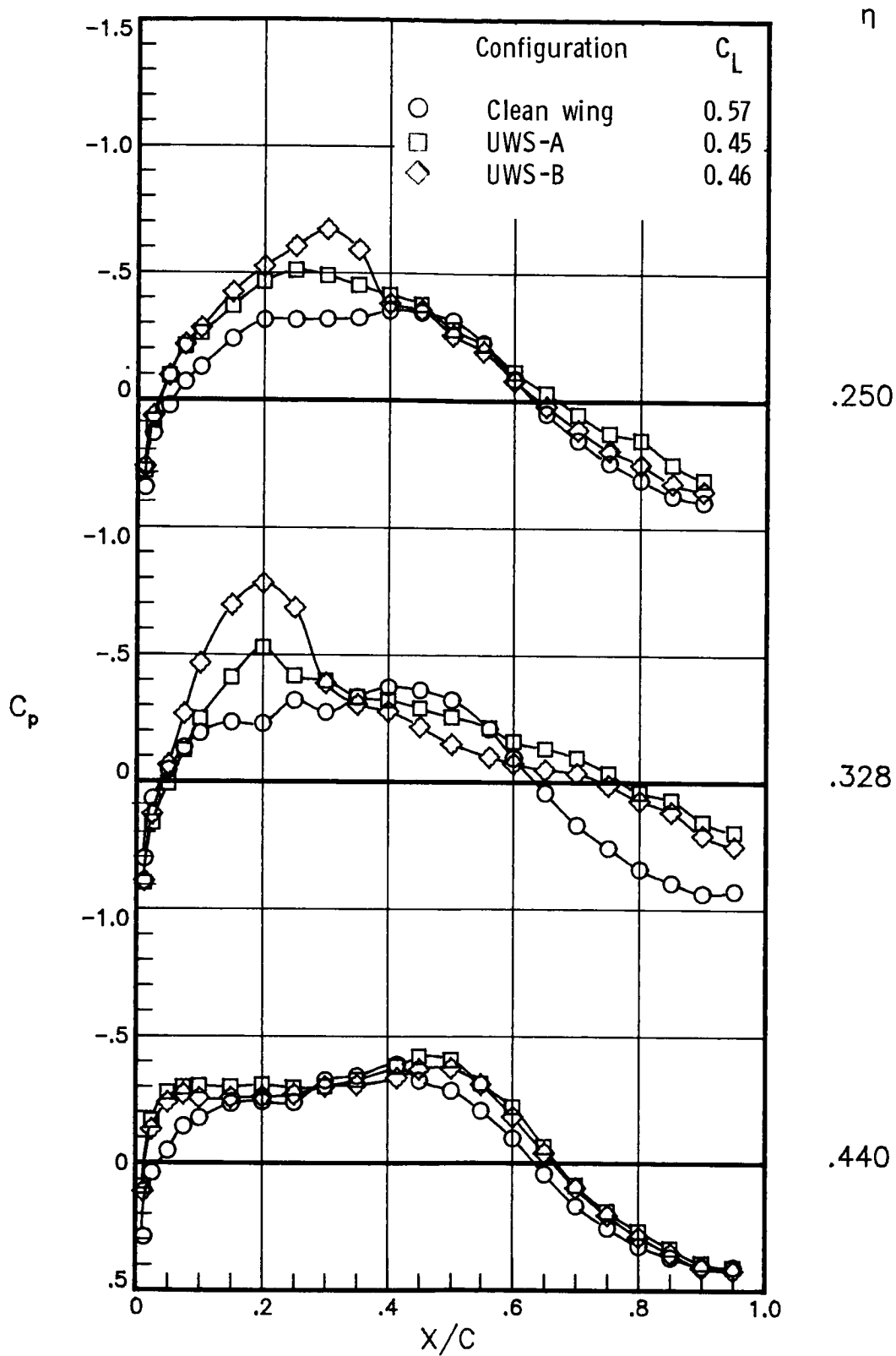
(b)  $\alpha = 0.74^\circ$ ;  $M_\infty = 0.80$ .

Figure 31.- Continued.



(c)  $\alpha = 1.25^\circ$ ;  $M_\infty = 0.80$ .

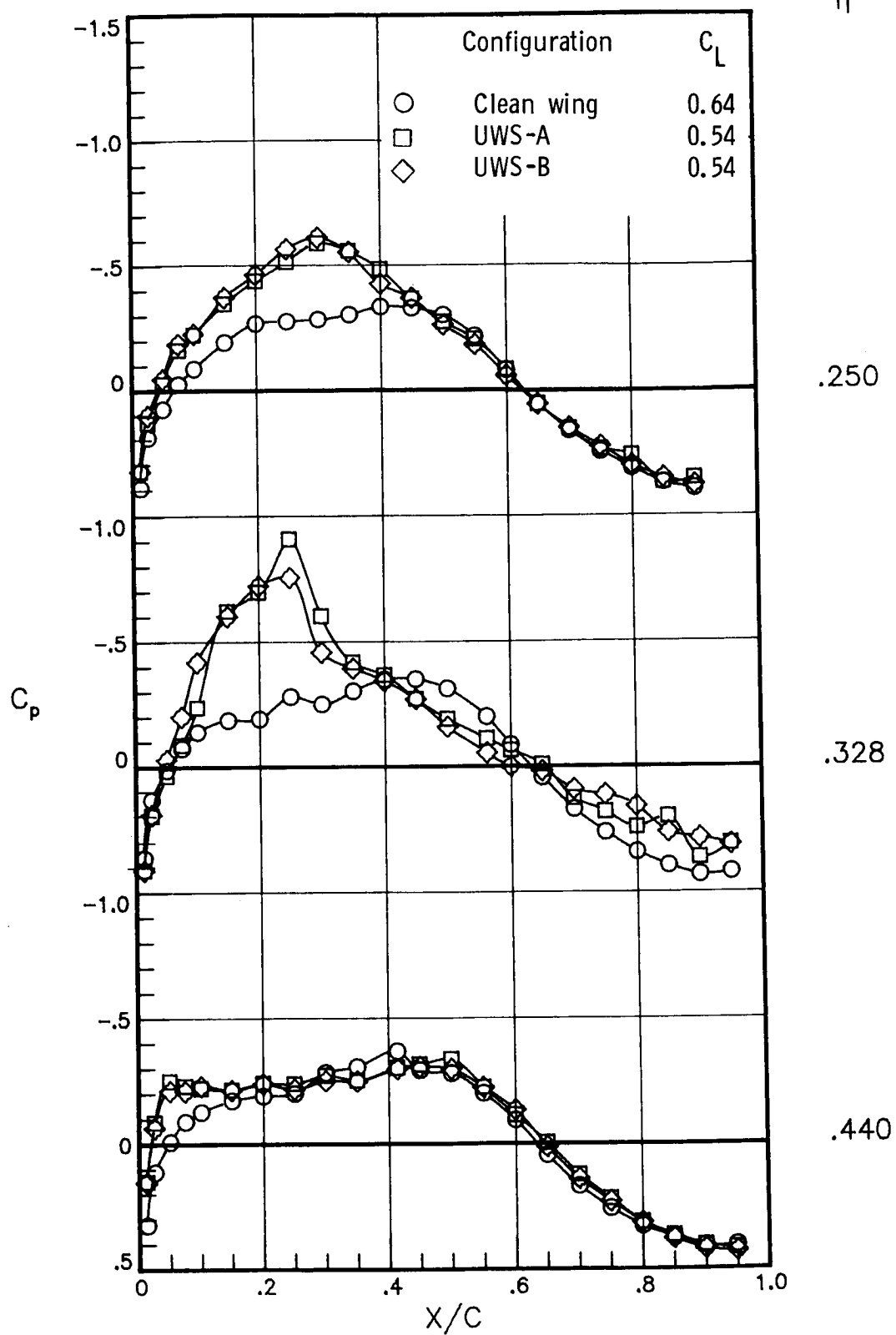
Figure 31.- Continued.



(d)  $\alpha = 1.74^\circ$ ;  $M_\infty = 0.80$ .

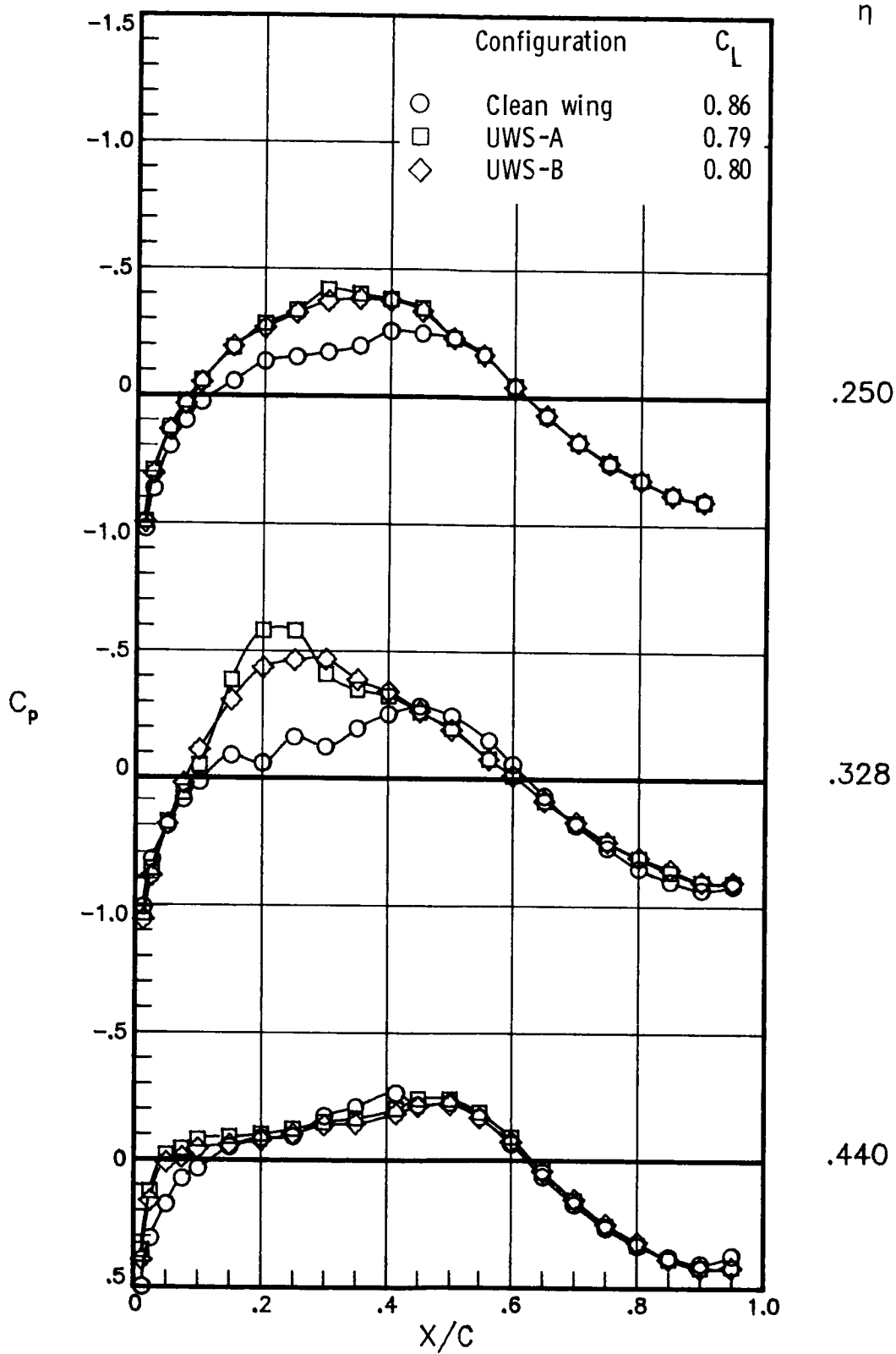
Figure 31.- Continued.





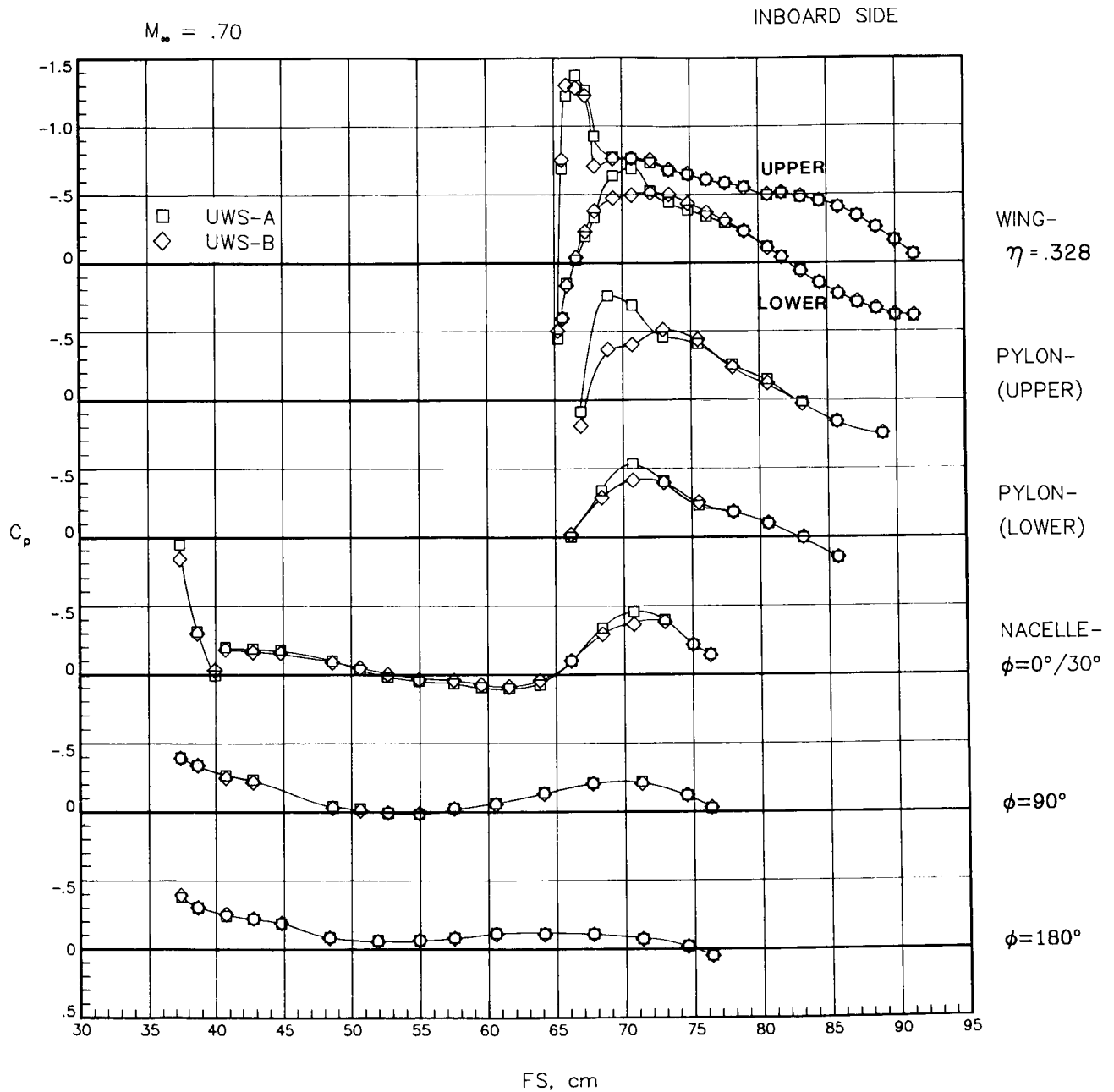
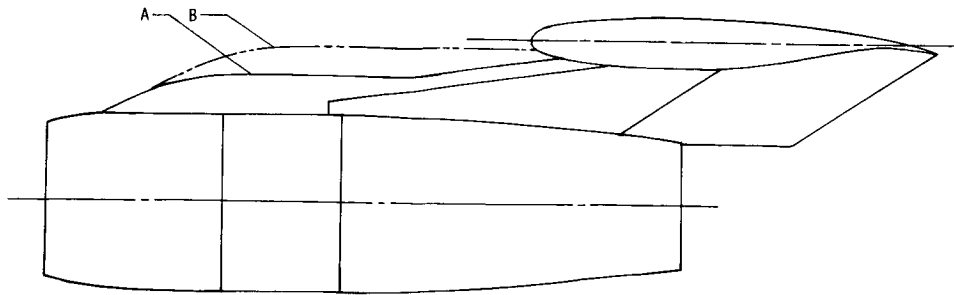
(e)  $\alpha = 2.23^\circ$ ;  $M_\infty = 0.80$ .

Figure 31.- Continued.



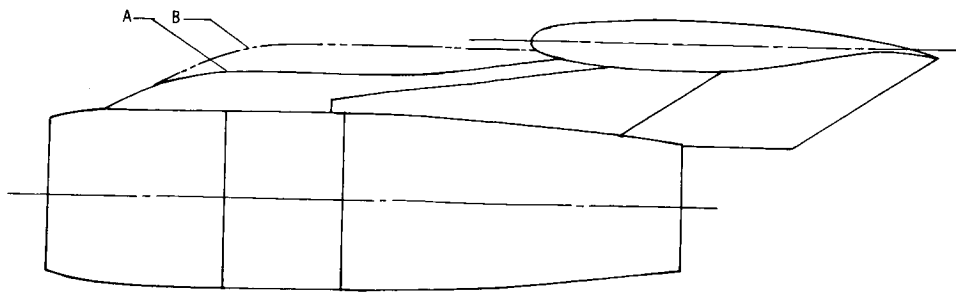
(f)  $\alpha = 4.22^\circ$ ;  $M_\infty = 0.80$ .

Figure 31.- Concluded.



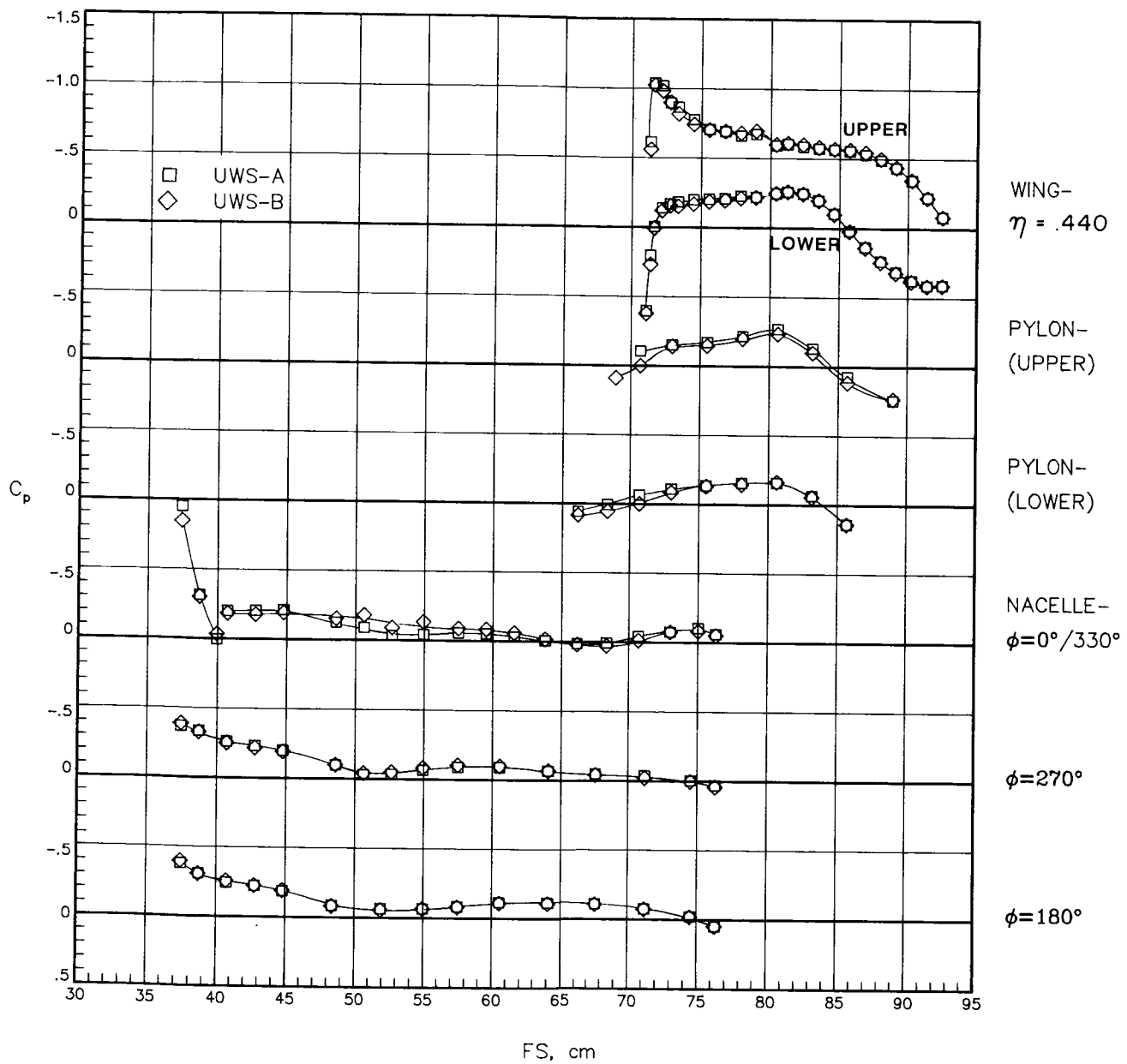
(a) Inboard side.

Figure 32.- Pressure coefficient distributions on nacelle and adjacent wing surfaces at  $M_\infty = 0.70$ ,  $\alpha = 2.18^\circ$ , and  $C_L = 0.47$ .



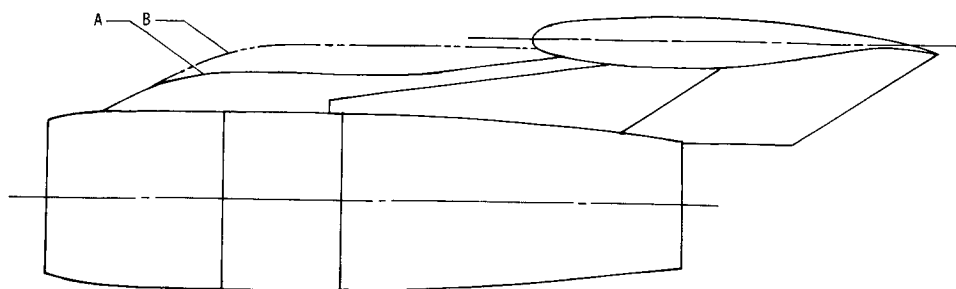
$M_\infty = .70$

OUTBOARD SIDE



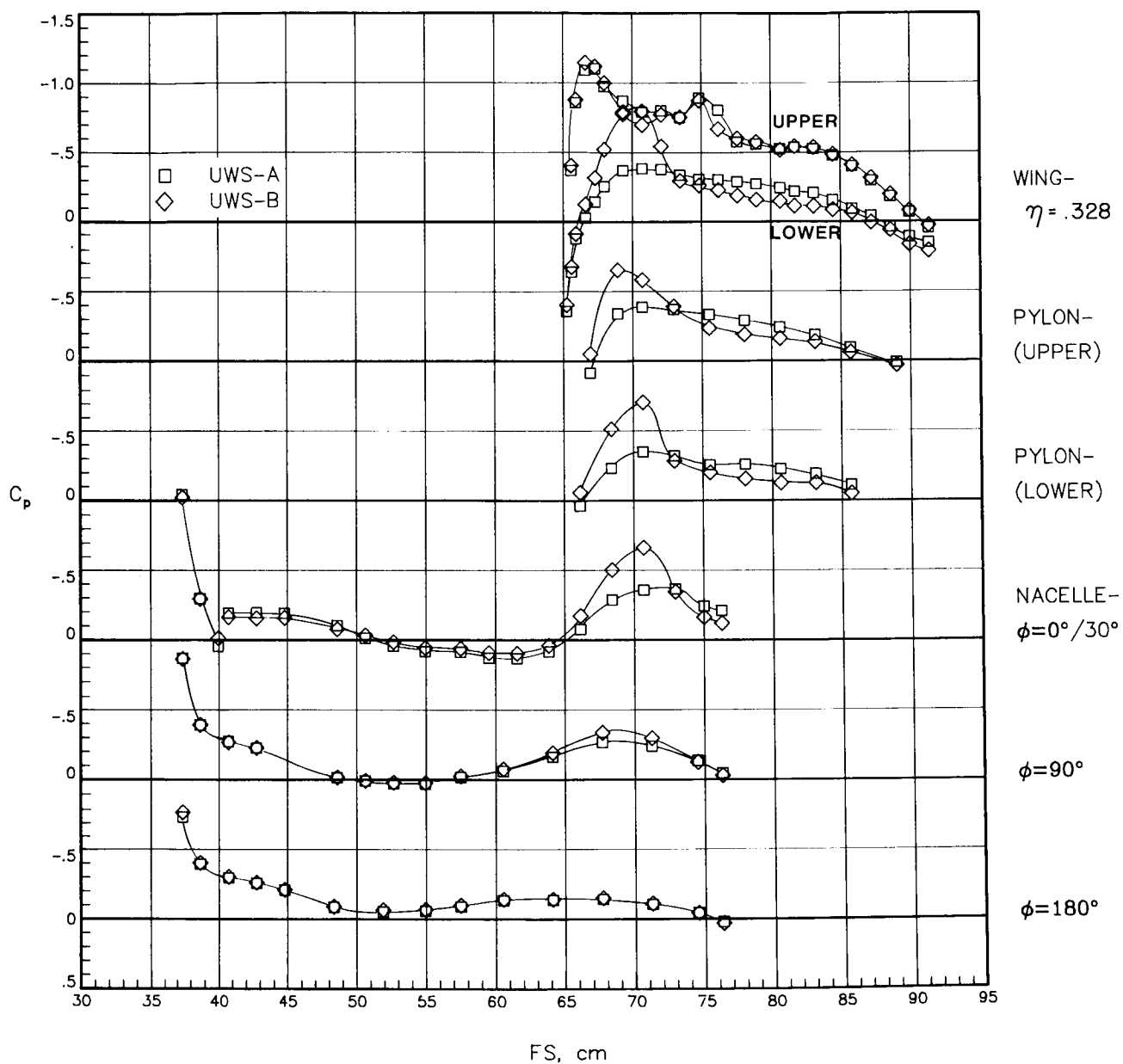
(b) Outboard side.

Figure 32.- Concluded.



$M_\infty = .80$

INBOARD SIDE



(a)  $\alpha = 1.25^\circ$ ;  $C_L = 0.38$ .

Figure 33.- Pressure coefficient distributions on nacelle and adjacent wing surfaces for various angles of attack at cruise Mach number.

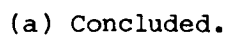
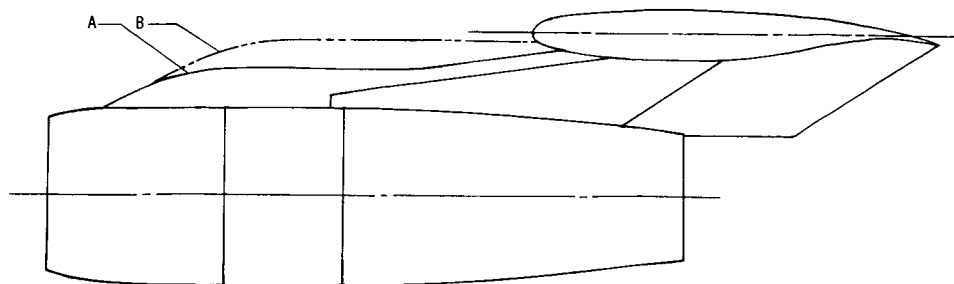
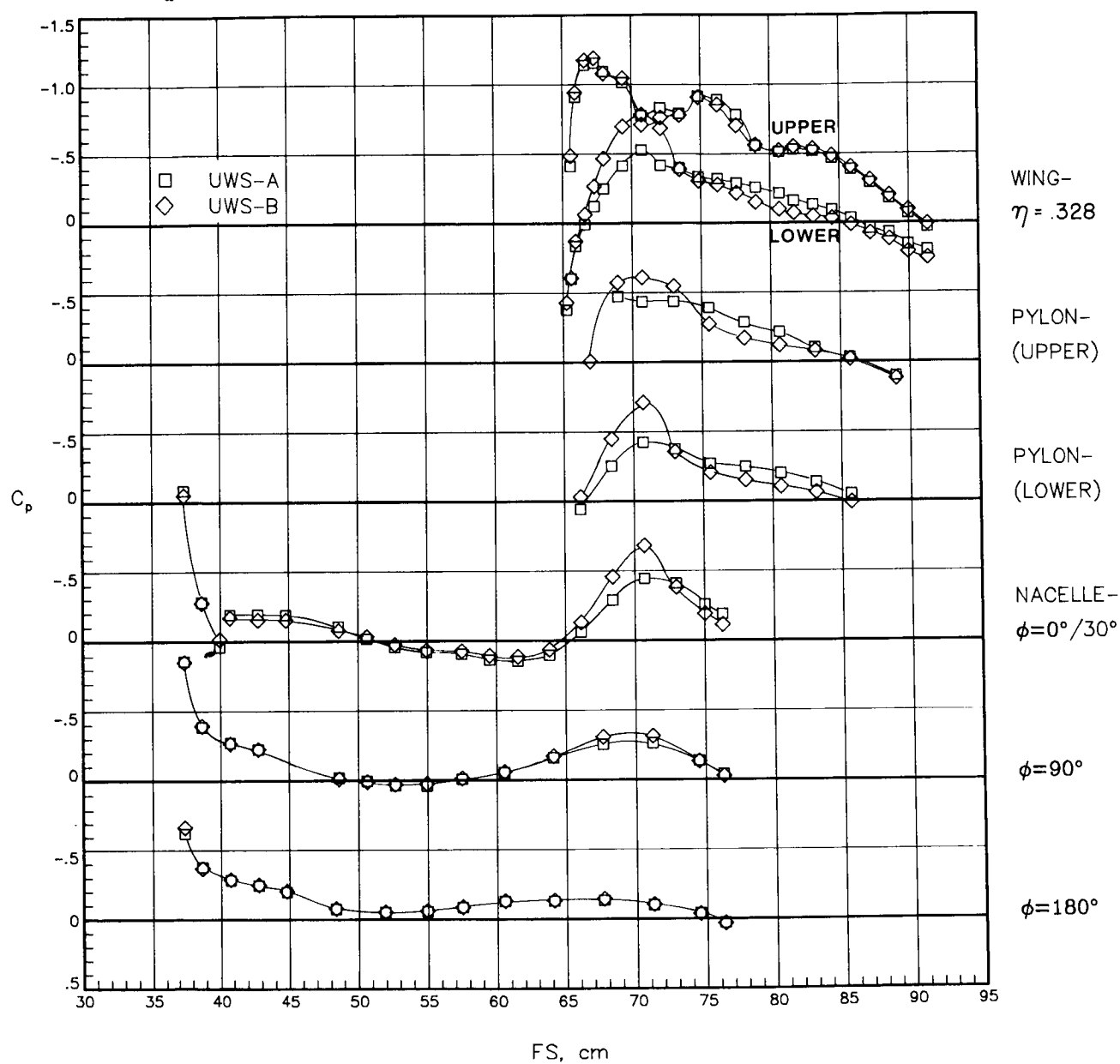


Figure 33.- Continued.



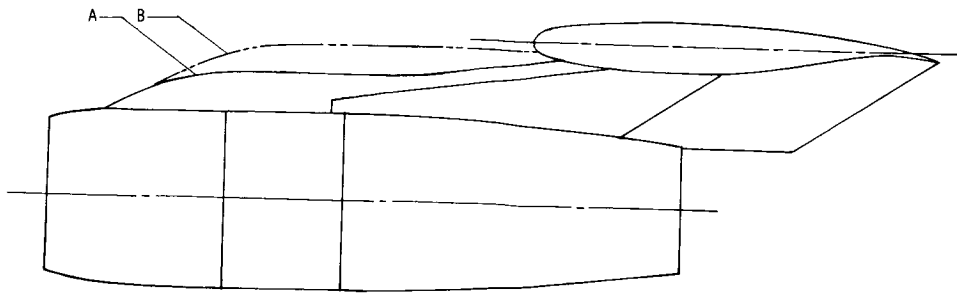
$M_\infty = .80$

INBOARD SIDE



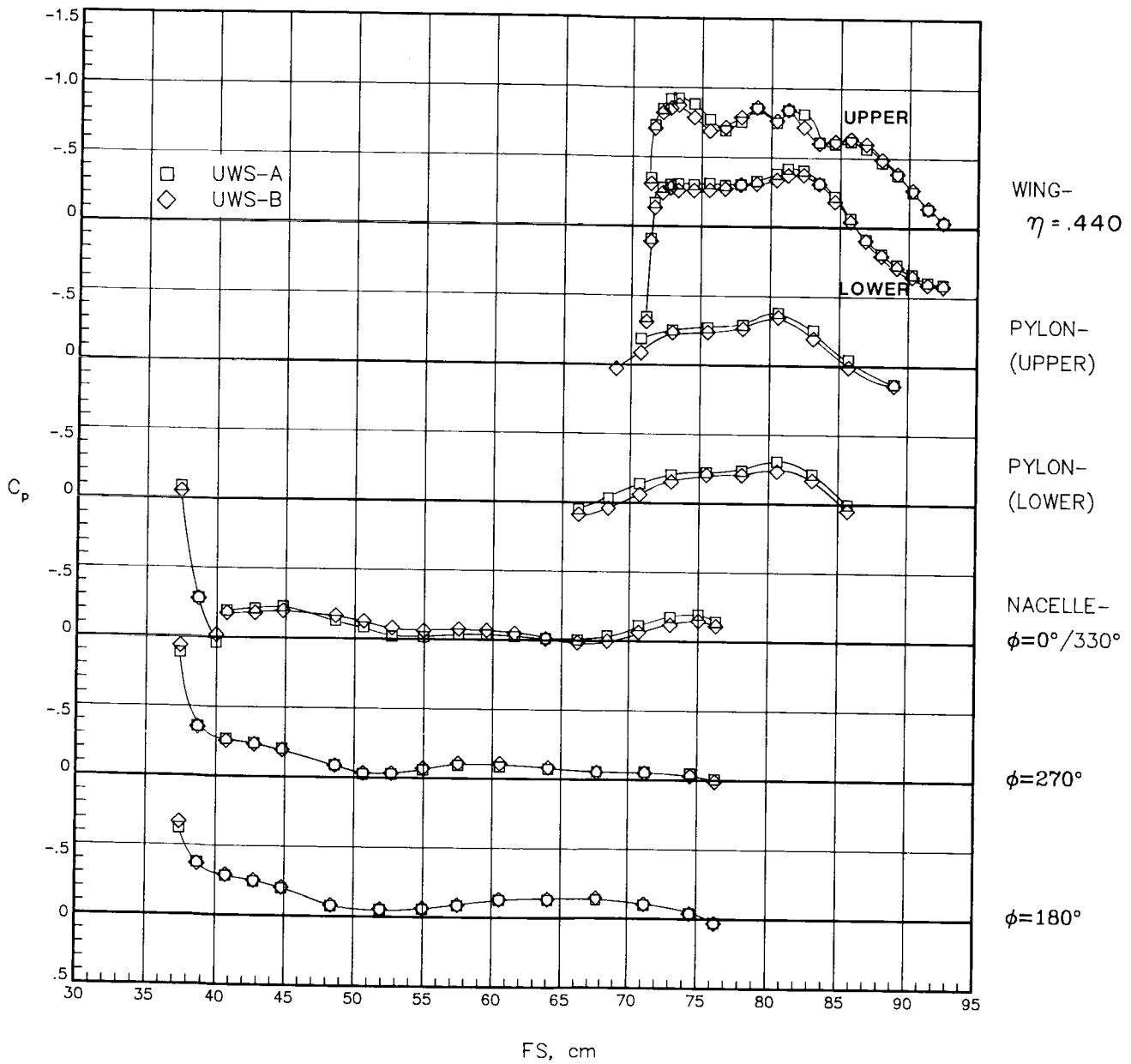
(b)  $\alpha = 1.73^\circ$ ;  $C_L = 0.45$ .

Figure 33.- Continued.



$M_\infty = .80$

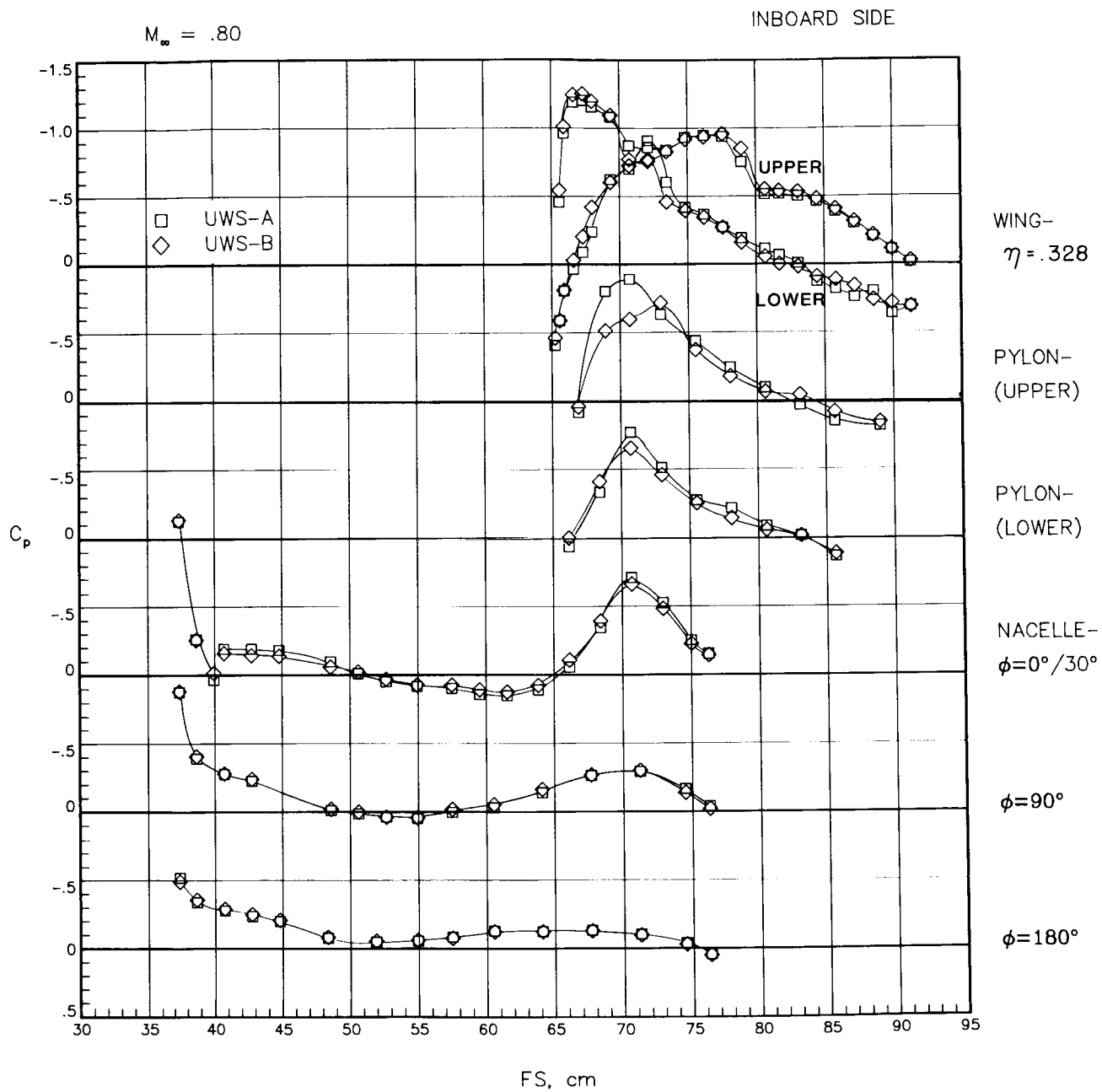
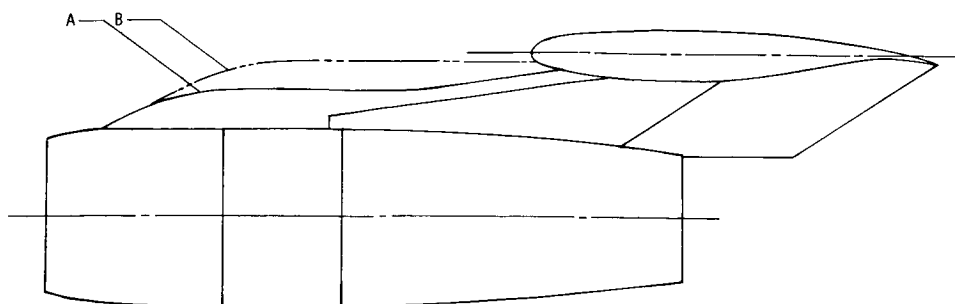
OUTBOARD SIDE



(b) Concluded.

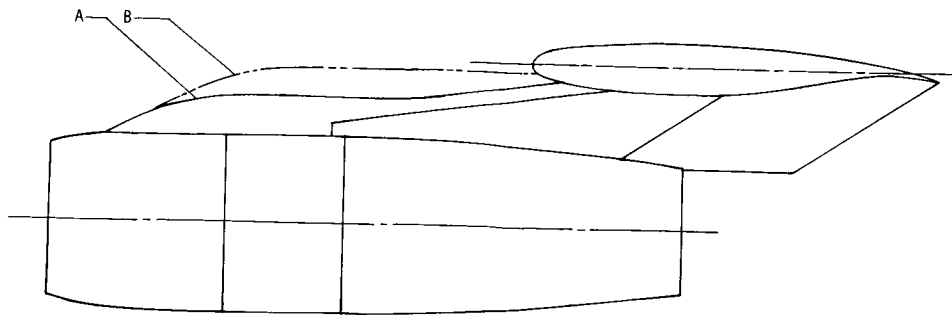
Figure 33.- Continued.





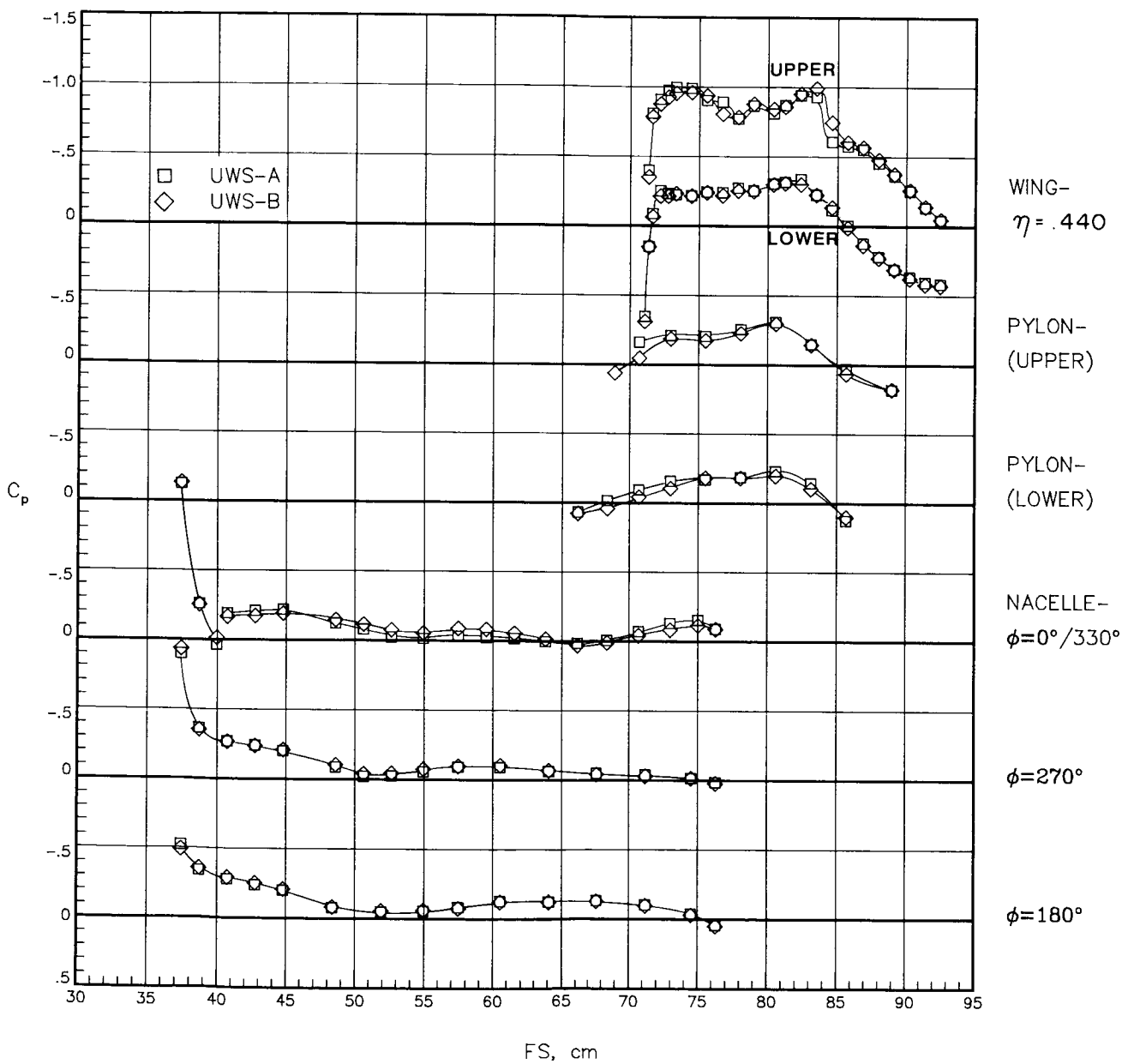
(c)  $\alpha = 2.23^\circ$ ;  $C_L = 0.54$ .

Figure 33.- Continued.



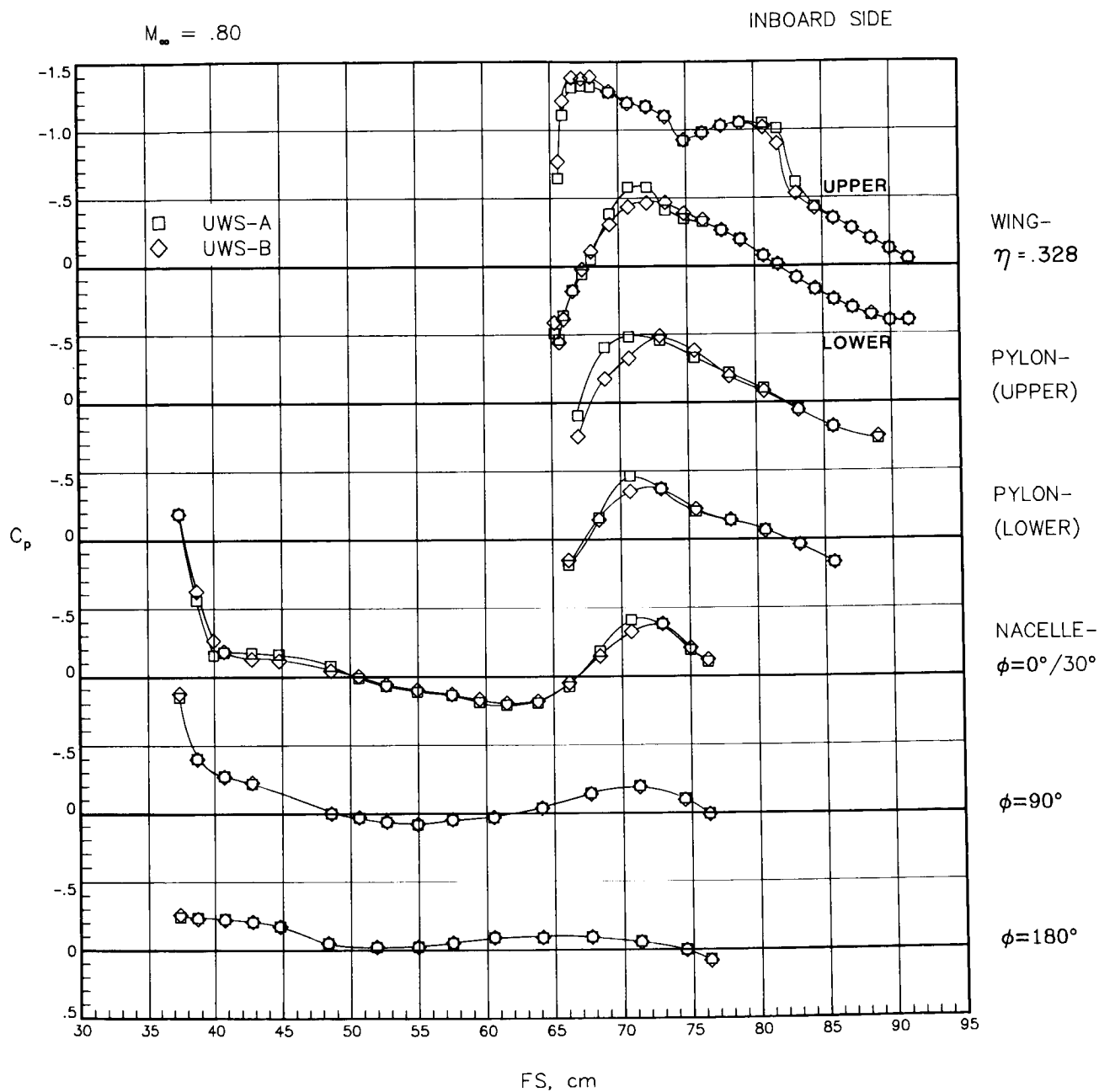
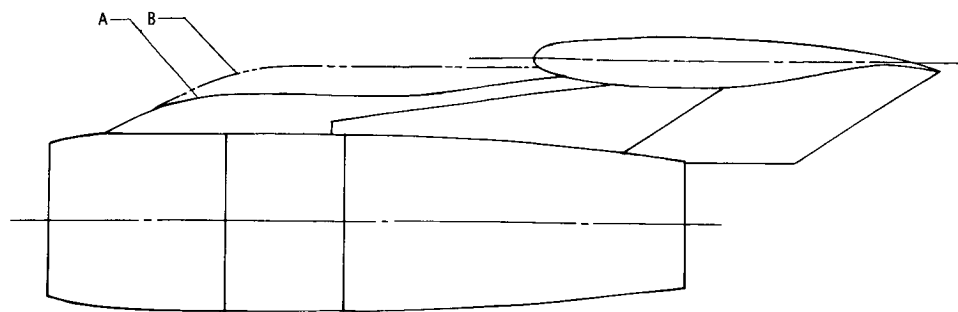
$M_\infty = .80$

OUTBOARD SIDE



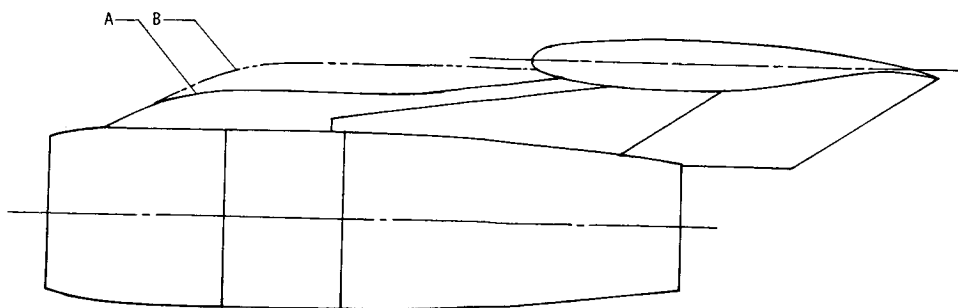
(c) Concluded.

Figure 33.- Continued.



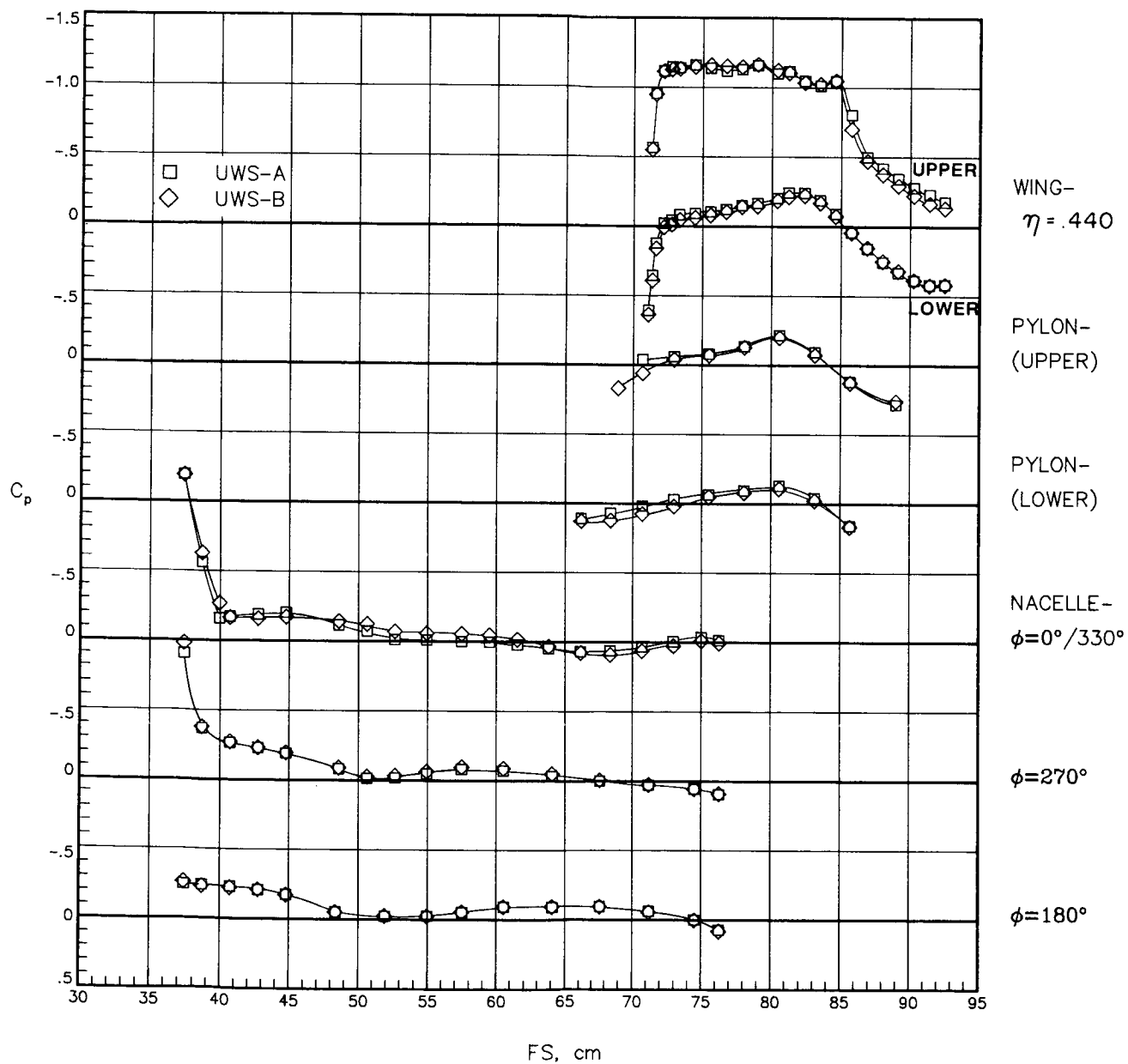
(d)  $\alpha = 4.20^\circ$ ;  $C_L = 0.79$ .

Figure 33.- Continued.



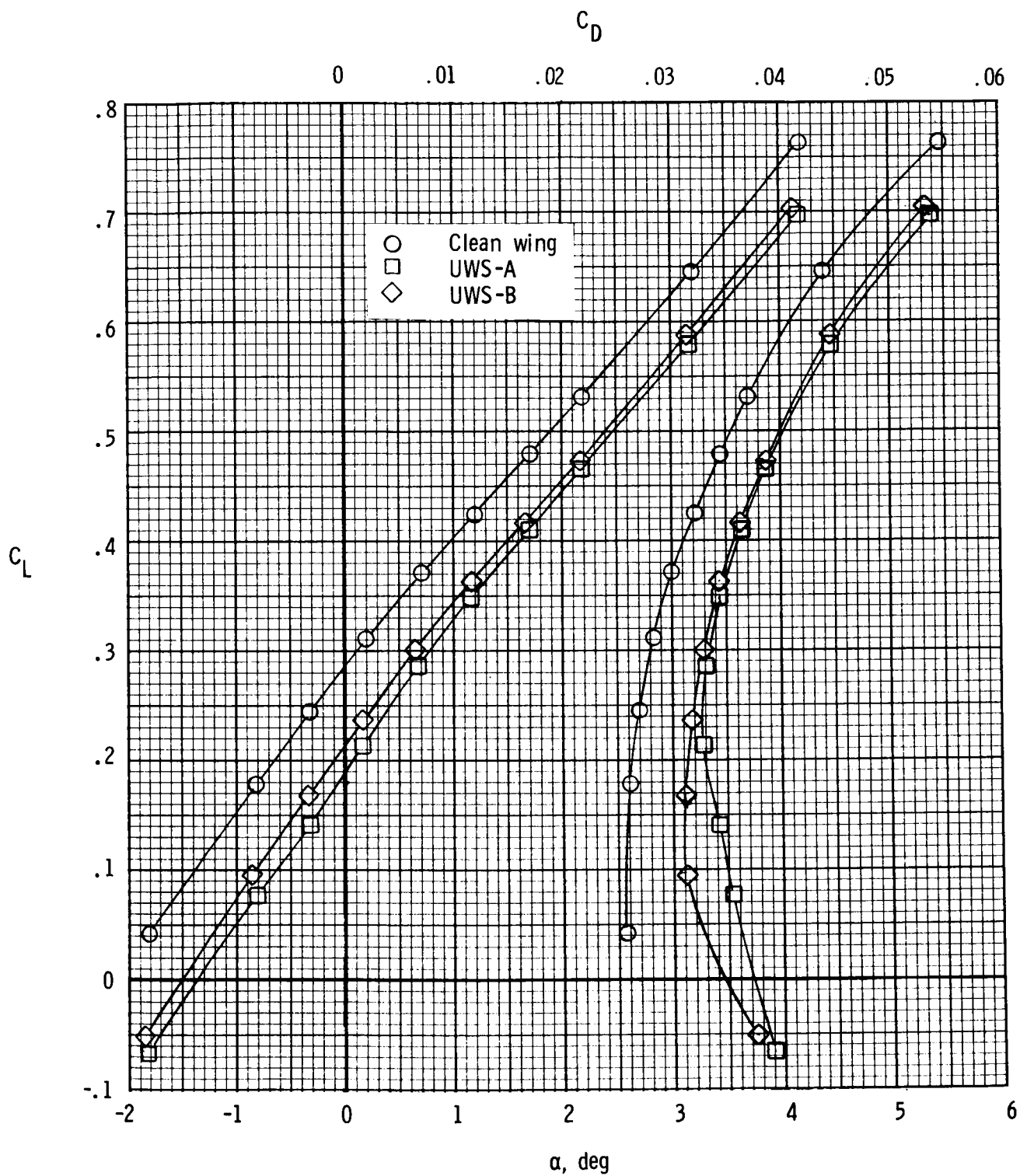
$M_{\infty} = .80$

OUTBOARD SIDE



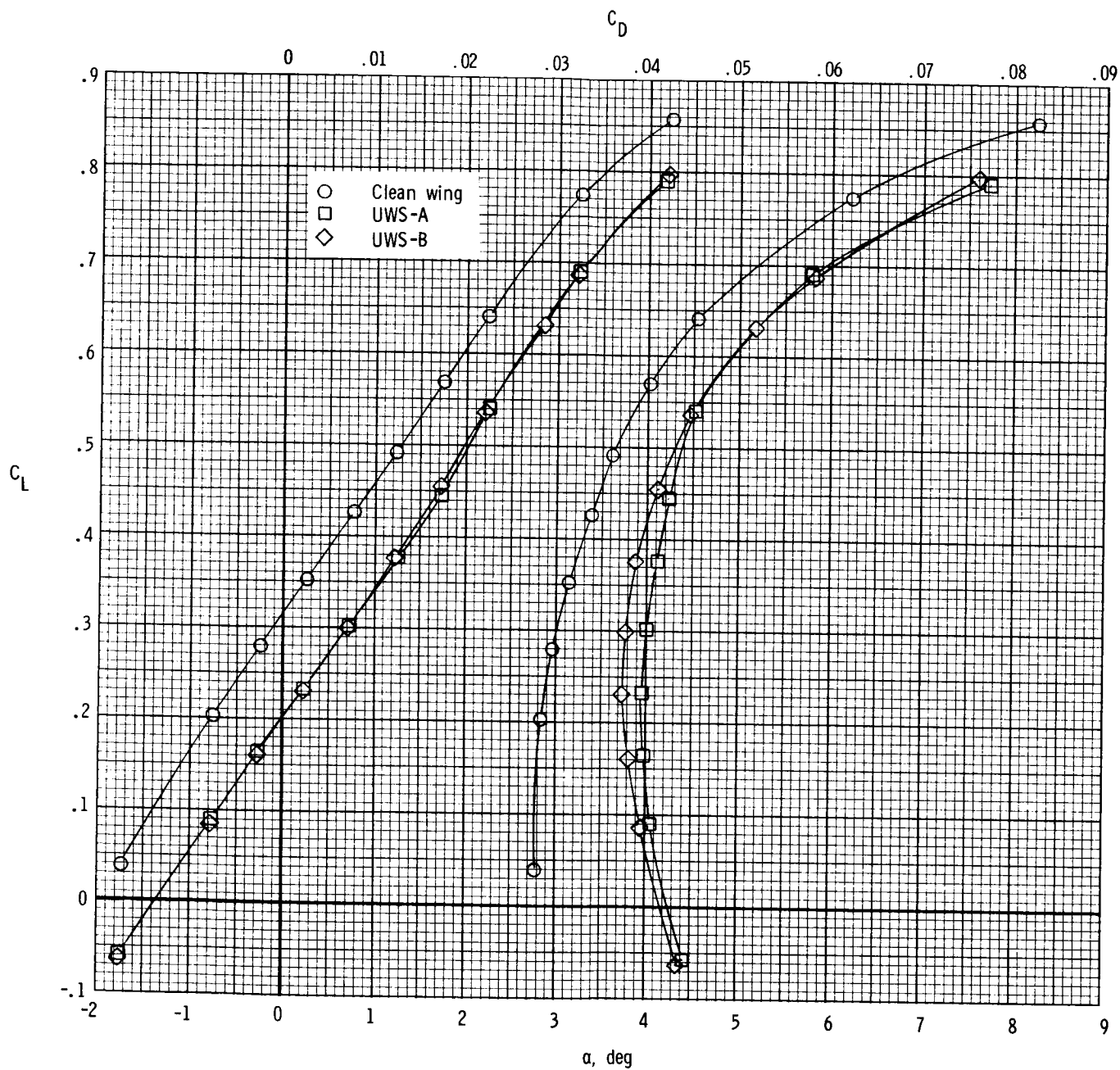
(d) Concluded.

Figure 33.- Concluded.



(a)  $M_\infty = 0.70$ .

Figure 34.- Effects of nacelle installations on total lift and drag coefficients.



(b)  $M_\infty = 0.80$ .

Figure 34.- Concluded.

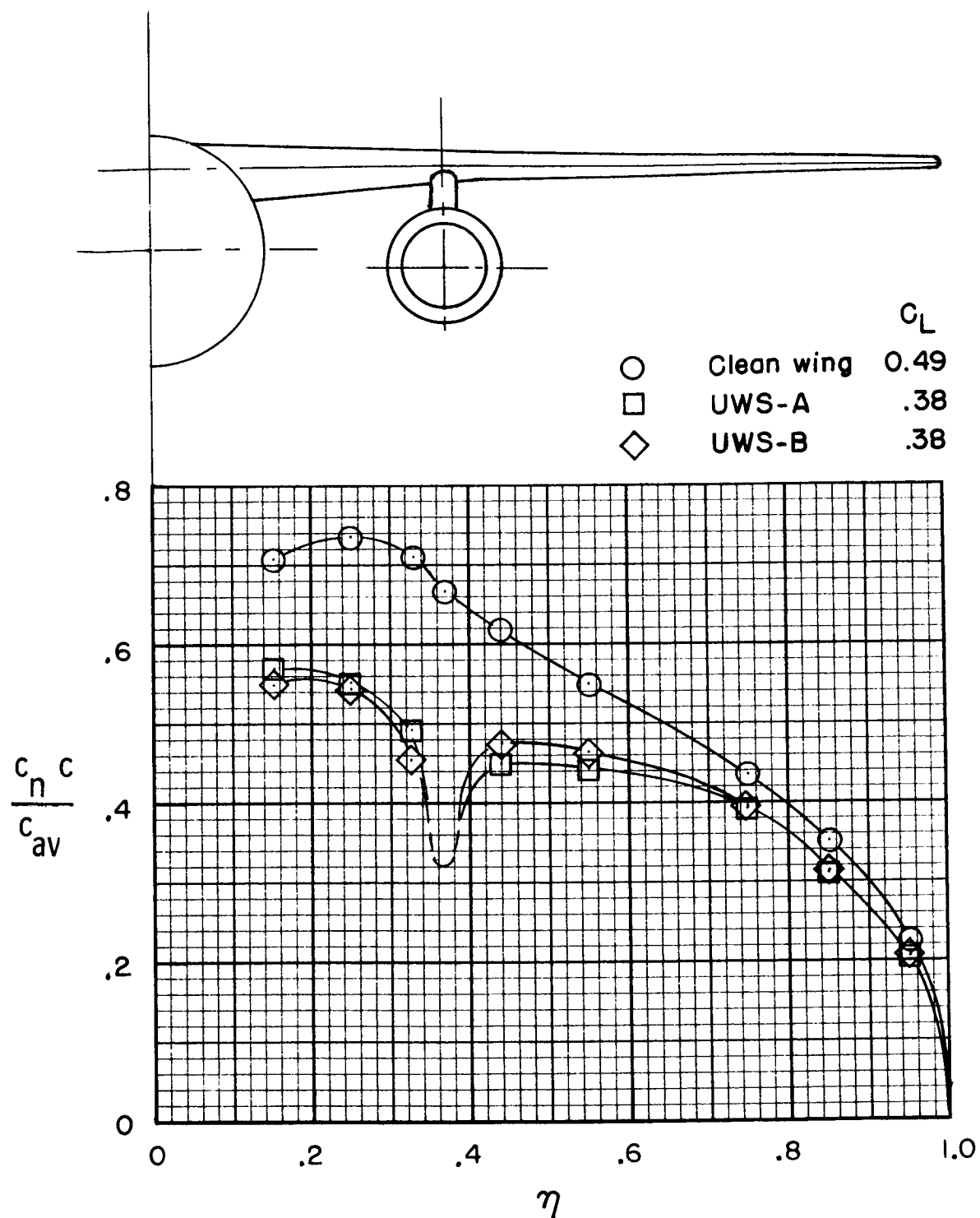


Figure 35.- Influence of pylon-nacelle installations on spanwise load distribution of wing.  $M_\infty = 0.80$  and  $\alpha \approx 1.25^\circ$ .

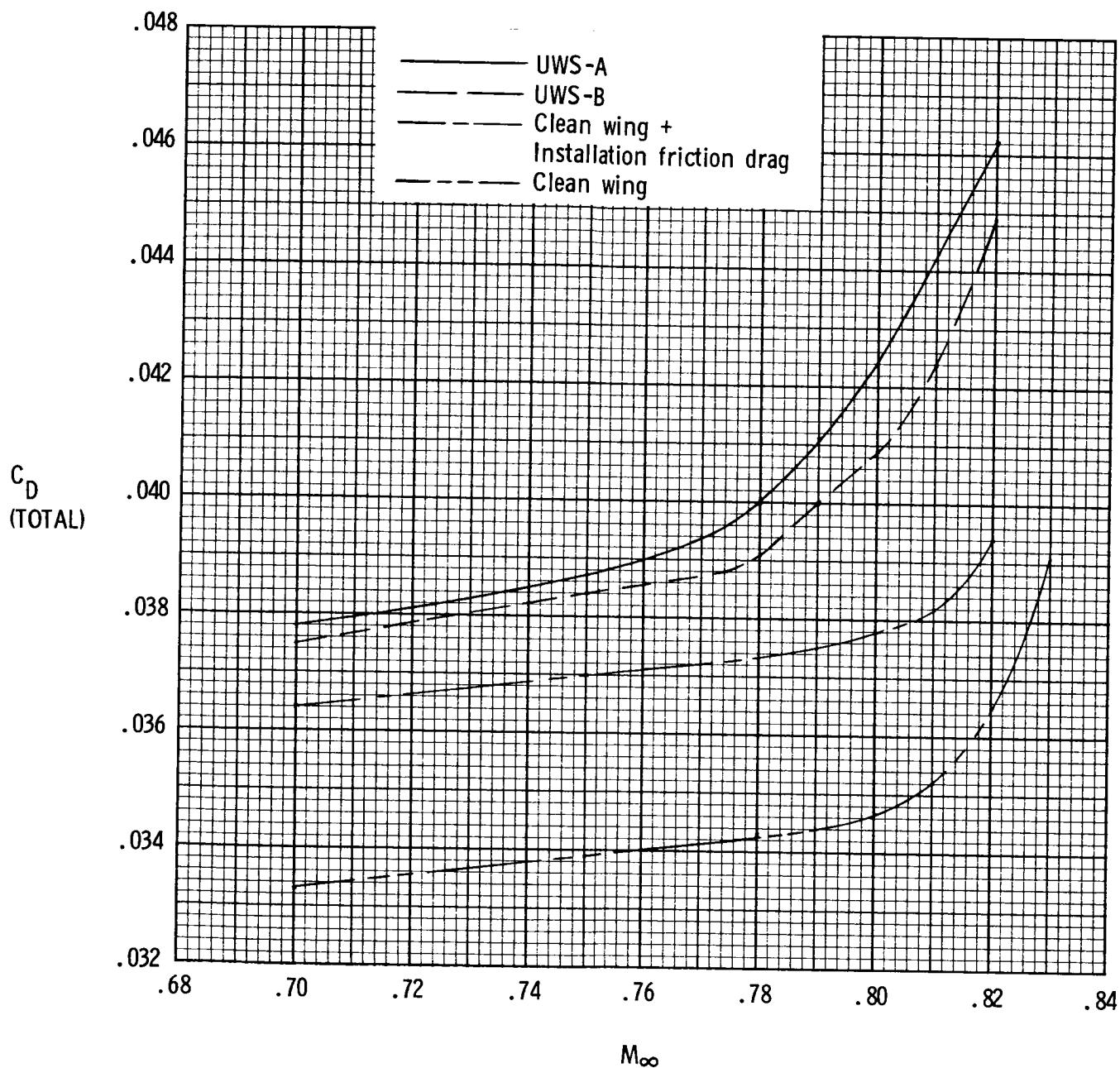


Figure 36.- Variation of total drag coefficient with Mach number at constant lift coefficient ( $C_L = 0.45$ ), with and without nacelles.



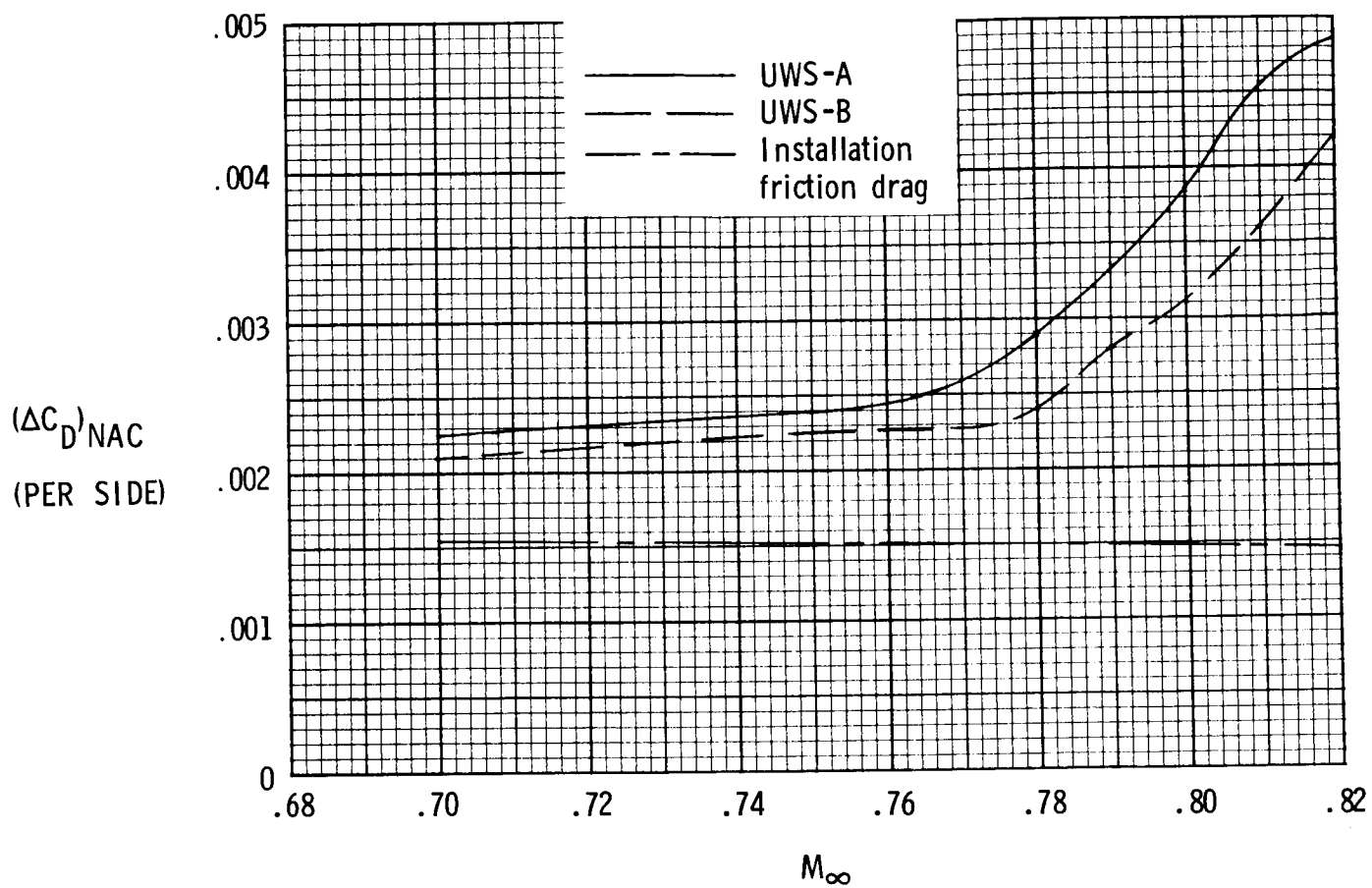
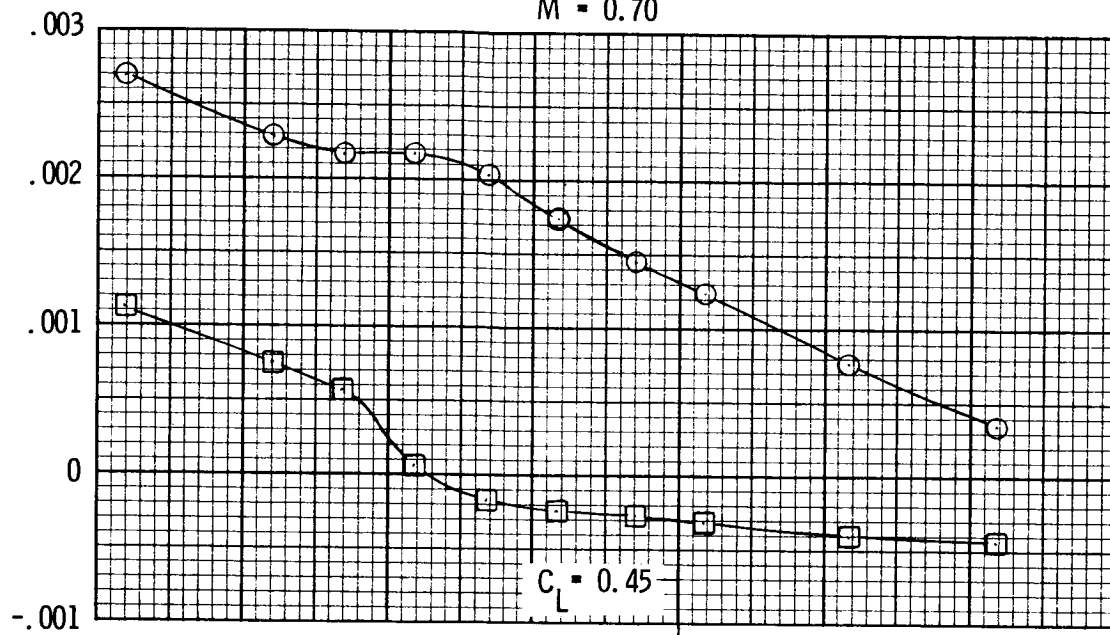


Figure 37.- Variation of drag coefficient of a single pylon-nacelle installation with Mach number at constant lift coefficient ( $C_L = 0.45$ ).

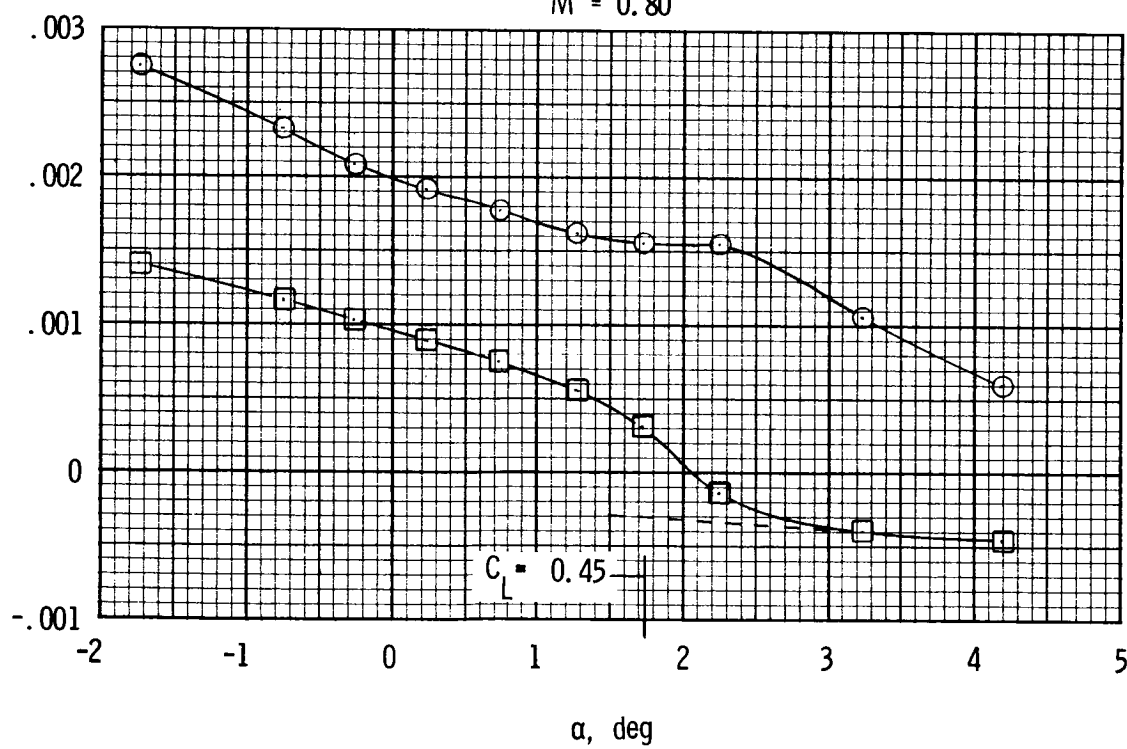
- Nacelle boattail
- Pylon trailing edge
- - - Estimated attached flow

$M = 0.70$

$C_D$   
(PER SIDE)



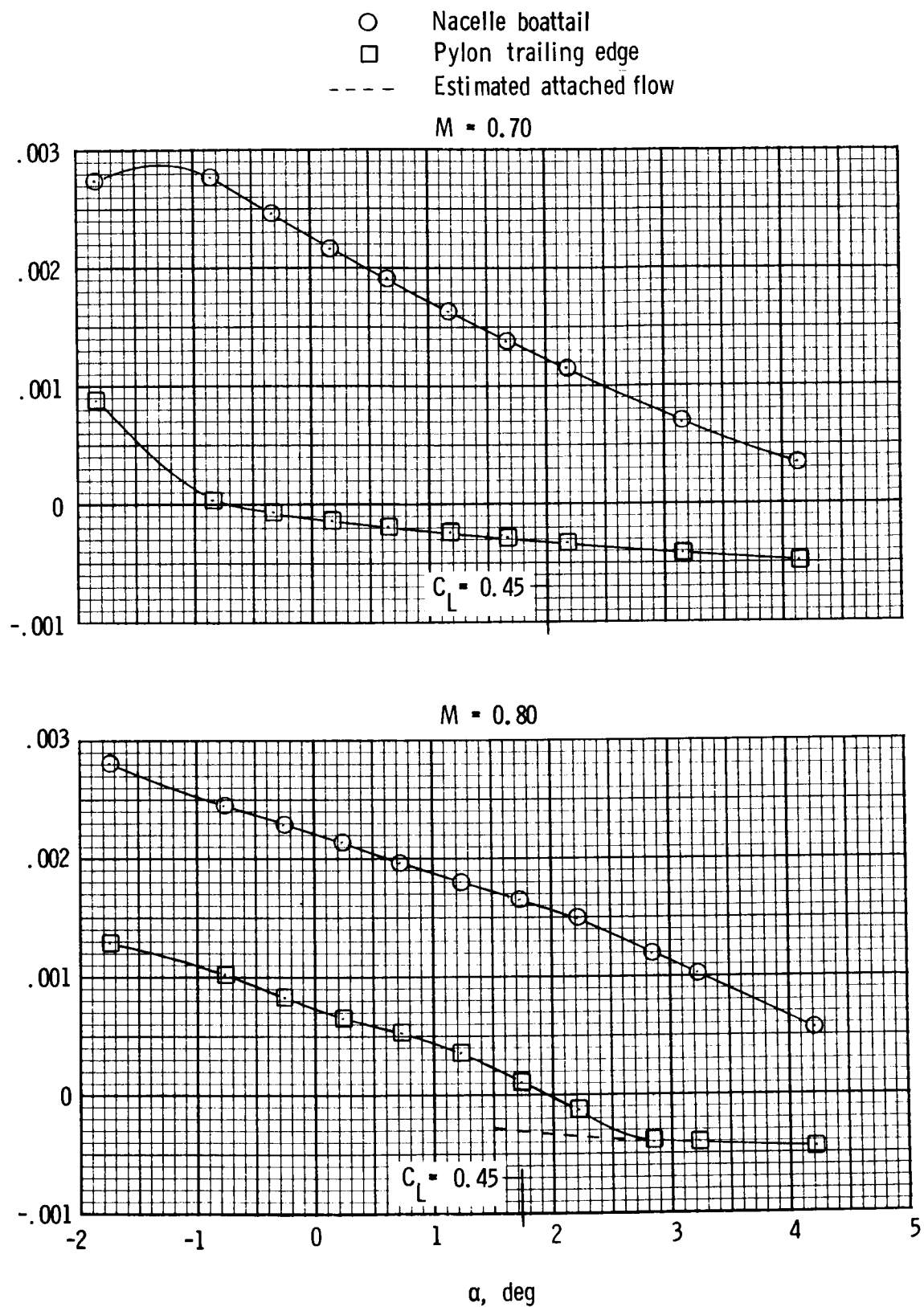
$M = 0.80$



(a) Configuration UWS-A.

Figure 38.- Integrated pressure drag coefficient on the closures on one pylon and nacelle.

$C_D$   
(PER SIDE)



(b) Configuration UWS-B.

Figure 38.- Concluded.

1. Report No. NASA TP-2457		2. Government Accession No.		3. Recipient's Catalog No.	
4. Title and Subtitle Installation Effects of Long-Duct Pylon-Mounted Nacelles on a Twin-Jet Transport Model With Swept Supercritical Wing				5. Report Date December 1985	
				6. Performing Organization Code 505-40-90-01	
7. Author(s) Edwin E. Lee, Jr., and Odis C. Pendergraft, Jr.				8. Performing Organization Report No. L-15932	
				10. Work Unit No.	
9. Performing Organization Name and Address NASA Langley Research Center Hampton, VA 23665-5225				11. Contract or Grant No.	
				13. Type of Report and Period Covered Technical Paper	
12. Sponsoring Agency Name and Address National Aeronautics and Space Administration Washington, DC 20546-0001				14. Sponsoring Agency Code	
15. Supplementary Notes					
16. Abstract  The installation interference effects of an underwing-mounted, long-duct, turbofan nacelle have been evaluated in the Langley 16-Foot Transonic Tunnel with two different pylon shapes installed on a twin-engine transport model having a supercritical wing swept 30°. Wing, pylon, and nacelle pressures and overall model force data were obtained at Mach numbers from 0.70 to 0.83 and nominal angles of attack from -2° to 4° at an average unit Reynolds number of $11.9 \times 10^6$ per meter. The results show that adding the long-duct nacelles to the supercritical wing, in the near-sonic flow field, changed the magnitude and direction of flow velocities over the entire span, significantly reduced cruise lift, and caused large interference drag on the nacelle afterbody.					
17. Key Words (Suggested by Author(s)) Twin long-duct nacelles High-wing transport model Swept supercritical wing Installation interference Underwing nacelles Propulsion integration			18. Distribution Statement Unclassified - Unlimited  Subject Category 02		
19. Security Classif. (of this report) Unclassified	20. Security Classif. (of this page) Unclassified	21. No. of Pages 143	22. Price A07		

**National Aeronautics and  
Space Administration  
Code NIT-4**

**Washington, D.C.  
20546-0001**

**Official Business  
Penalty for Private Use, \$300**

**BULK RATE  
POSTAGE & FEES PAID  
NASA Washington, DC  
Permit No. G-27**

**NASA**

**POSTMASTER:**

**If Undeliverable (Section 158  
Postal Manual) Do Not Return.**

---